

UNIVERSITY OF KWAZULU-NATAL



**EVOLUTION OF GALAXY CLUSTER
SCALING RELATIONS OVER HALF A
HUBBLE TIME**

by

Susan Wilson

Submitted in fulfillment of the
academic requirements for the degree of
Doctor of Philosophy (Science)
in the
School of Mathematics, Statistics, and Computer Science,
University of KwaZulu-Natal

Durban

December, 2016

As the candidate's supervisor I have approved this thesis for submission.

Signed: Name: Date:

“A mathematician may say anything he pleases, but a physicist must be at least partially sane.” -

J. Willard Gibbs

ABSTRACT

In this thesis, we observe a sample of 38 galaxy clusters drawn with $0.1 < z < 1$ from the *XMM* Cluster Survey in order to study scaling relations and their evolution. The two scaling relations discussed are the velocity dispersion–temperature (σ_v – T_X) and the mass–temperature relation (M – T_X).

We measure the evolution of the σ_v – T_X for our sample using an orthogonal regression method. This work improves upon previous studies by the use of a homogeneous cluster sample and in terms of the number of high redshift clusters included. We present here new redshift and velocity dispersion measurements for 12 $z > 0.5$ clusters observed with the GMOS instruments on the Gemini telescopes. We find that the slope of the relation is steeper than that expected if clusters were self-similar, and that the evolution of the normalisation is slightly negative, but not significantly different from zero ($\sigma_v \propto T^{0.86 \pm 0.14} E(z)^{-0.37 \pm 0.33}$). We verify our results by applying our methods to cosmological hydrodynamical simulations. The lack of evolution seen in our data is consistent with simulations that include both feedback and radiative cooling.

Since we find no evidence of evolution in the σ_v – T_X relation, and the dynamical mass of the cluster is dependent on σ we can conclude that the M – T_X relation is not evolving. We measure the M^{dyn} – T_X relation for our sample using two methods, an orthogonal regression method

and a Bayesian Gaussian mixture model fitting method, and find a slope of $M_{500} \propto T_X^{2.44 \pm 0.37}$ and $M_{500} \propto T_X^{1.11 \pm 0.97}$, respectively. The expected relation from the self-similar model is $M_{500} \propto T_X^{1.5}$. Although both our fit results are within 3σ of the expected result, the orthogonal method slope is steeper than expected and the Gaussian mixture model fitting method gives a shallower than expected slope. We tested the effectiveness of retrieving a fit from a simulated set of data and found the Gaussian mixture model fitting method to provide a more consistent and reliable result in comparison to the orthogonal method. However, we also found that the steepness of the slope for the orthogonal method is biased high when there is large scatter in the data. The Gaussian mixture model data over-estimates the scatter and therefore in low scatter systems, the slope is under-estimated. The fit for our $M - T_X$ relation was compared to the small population of previous studies and was found to be consistent within 3σ . However, all previous methods fitted their relation using a hydrostatic mass which requires the assumption that the clusters are in hydrostatic equilibrium. A comparison between hydrostatic and dynamical masses is given and the hydrostatic mass bias is discussed.

In order to gain further knowledge about galaxy clusters we consider what information the radio wavelength can provide. The presence of diffuse radio emission, in the form of radio halos, radio relics and mini halos, has been linked to cluster mergers but the exact model for its origin is still not understood. Two competing models exist, but studies of galaxy clusters seem to be more in favour of the primary electron model rather than the hadronic model. Since the presence of a merger will have an effect on the properties of a galaxy cluster, we considered how they will change the known scaling relations. Although literature provides a change in the X-ray luminosity relation, the effect on the $\sigma_v - T_X$ relation has not been studied. To gain some insight into this we compare the position of a sample of clusters with and without radio halos, which are traces of a merger, on the $\sigma_v - T_X$ plane. We find no obvious population difference but a larger, homogeneous sample will be required to validate this result.

We also provide 3 new VLA observations for galaxy clusters from our XCS sample as part of a pilot project to search for radio halos in low mass clusters. Due to an insufficient observation time and corrupted data, the images we obtain have a high rms noise, and no detection of a radio halo is found. The expected average size of a radio halo is 1 Mpc but we discuss the correlation between the radio halo size and the cluster mass. To see if it has an effect on radio power and detections we simulate radio halos of two different sizes, 400 kpc and 1 Mpc. We determine power upper limit estimates at the 3σ level for our 3 clusters, with radio halo sizes of 400 kpc, of: $P_{1.4GHz} < 1.67 \times 10^{24} \text{ W Hz}^{-1}$ in XMMXCS J111515.6+531949.5, $P_{1.4GHz} < 4.15 \times 10^{24} \text{ W Hz}^{-1}$ in XMMXCS J104044.4+395710.4, and $P_{1.4GHz} < 5.88 \times 10^{25} \text{ W Hz}^{-1}$ in XMMXCS J151618.6+000531.3. We compare the positions of our upper limit estimates, to other known radio halo detections and upper limits, on the $P_{1.4GHz} - L_X$ and $P_{1.4GHz} - M_{500}$ plane. Using the reduced simulated halo size, our radio power upper limits are decreased by a factor of 2~10. Although, our upper limits still do not rule out the presence of a radio halo at this smaller size, it does bring into question the accepted method for calculating radio halo upper limits.

The results obtained in this thesis have provided us with more knowledge of scaling relations of galaxy clusters but has also shown us how much there is still left unknown. Further spectroscopic observations of galaxy clusters will allow us to increase our sample size and further constrain the $\sigma_v - T_X$ and $M - T_X$ relation. Radio observations of a large homogeneous selected sample of galaxy clusters will allow us to further investigate the presence of radio halos and their effect on scaling relations.

ACKNOWLEDGMENTS

This research was possible due to funding from the National Research Foundation (NRF) and the Square Kilometer Array South Africa (SKA) through the postgraduate bursary.

This research has made use of the NASA/IPAC Extragalactic Database (NED) which is operated by the Jet Propulsion Laboratory, California Institute of Technology, under contract with the National Aeronautics and Space Administration.

This research has made use of the X-Rays Clusters Database (BAX) which is operated by the Laboratoire d'Astrophysique de Tarbes-Toulouse (LATT), under contract with the Centre National d'Etudes Spatiales (CNES)

This research obtained results based on observations obtained at the Gemini Observatory, which is operated by the Association of Universities for Research in Astronomy, Inc., under a cooperative agreement with the NSF on behalf of the Gemini partnership: the National Science Foundation (United States), the National Research Council (Canada), CONICYT (Chile), the Australian Research Council (Australia), Ministério da Ciência, Tecnologia e Inovação (Brazil) and Ministerio de Ciencia, Tecnología e Innovación Productiva (Argentina).

“Strength doesn’t come from what you can do. It comes from overcoming the things you once thought you couldn’t. - Rikki Rogers

There were often moments when I was completing my thesis, that I thought I would never finish. This is a thank you to everyone who believed in me and encouraged me to continue so I could complete my dream. Special mention must be given to the following people.

My supervisor Dr Matt Hilton - Thank you for giving me the opportunity to work with you and thank you for having with patience me. I really appreciate all your help. You were always available and ready to answer questions and encourage me to think through problems for myself. Thank you for making these last 4 years bearable and interesting. My co-supervisor Dr Nadeem Oozeer - Although I was not able to physically consult you on this project, you were always available to offer help over email. Thank you for the skype conversations and encouragement.

My two best friends:

Nikhita Madhanpall although we have not studied in the same city over the past four years you have been a constant rock and support for me. Thank you for your cheerfulness and belief in me on my disheartening days. I am so grateful to call you my friend. Kenda Knowles thank you for everything you have done in the last four years. Your unwavering support and friendship has helped me to achieve my dream of completing my PhD. From the late night chats, to the constant supply of tea and chocolate, and the extensive grammar checking and proof reading during the last push. You have made these last four years a wonderful journey and now it’s time to celebrate - cheers!

My family: My sisters and brothers-in-law - Thank you for believing in me and loving me even when I was having a bad day. I love you all so much and promise to visit more often now.

My parents - Thank you for your patience and love these last four years. For pushing me to work on days when I didn’t want to, I may not have shown it at the time but I am extremely grateful and love you so much.

PREFACE

The work described in this thesis was carried out in the School of Mathematics, Statistics, and Computer Science, University of KwaZulu-Natal from January 2013 to December 2016. This dissertation was completed under the supervision of Dr M. Hilton, with co-supervision by Dr N. Oozeer.

This study represents original work by the author and has not been submitted in any form for any degree or diploma to any other tertiary institution. Where use was made of the work of others it has been duly acknowledged in the text.

DECLARATION OF NON-PLAGIARISM

I, **Susan Wilson** declare that

1. The research reported in this thesis, except where otherwise indicated, is my original research.
2. This thesis has not been submitted for any degree or examination at any other university.
3. This thesis does not contain other persons' data, pictures, graphs or other information, unless specifically acknowledged as being sourced from other persons.
4. This thesis does not contain other persons' writing, unless specifically acknowledged as being sourced from other researchers. Where other written sources have been quoted, then:
 - (a) Their words have been re-written but the general information attributed to them has been referenced.
 - (b) Where their exact words have been used, then their writing has been placed in italics and inside quotation marks, and referenced.
5. This thesis does not contain text, graphics or tables copied and pasted from the Internet, unless specifically acknowledged, and the source being detailed in the thesis and in the References sections.

Signed in Westville, KwaZulu-Natal: Date:

DECLARATION OF PUBLICATIONS

Details of contribution to publications that form part of and/or include research presented in this thesis:

Chapter 2

SALT spectroscopic observations of galaxy clusters detected by ACT and a type II quasar hosted by a brightest cluster galaxy

Kirk, Brian; Hilton, Matt; Cress, Catherine; Crawford, Steven M.; Hughes, John P.; Battaglia, Nicholas; Bond, J. Richard; Burke, Claire; Gralla, Megan B.; Hajian, Amir; Hasselfield, Matthew; Hincks, Adam D.; Infante, Leopoldo; Kosowsky, Arthur; Marriage, Tobias A.; Menanteau, Felipe; Moodley, Kavilan; Niemack, Michael D.; Sievers, Jonathan L.; Sifón, Cristóbal; Wilson, Susan; Wollack, Edward J.; Zunckel, Caroline (2015), MNRAS, 449, 4010

I contributed to and helped to write the code to determine the method of galaxy cluster membership. This same code, with slight modifications and improvements was used in this thesis.

Chapter 2 & Chapter 3

The XMM Cluster Survey: Evolution of the velocity dispersion – temperature relation over half a Hubble time

Wilson, Susan; Hilton, Matt; Rooney, Philip J.; Caldwell, Caroline; Kay, Scott T.; Collins, Chris

A.; McCarthy, Ian G.; Romer, A. Kathy; Bermeo, Alberto; Bernstein, Rebecca; da Costa, Luiz; Gifford, Daniel; Hollowood, Devon; Hoyle, Ben; Jeltema, Tesla; Liddle, Andrew R.; Maia, Marcio A. G.; Mann, Robert G.; Mayers, Julian A.; Mehrrens, Nicola; Miller, Christopher J.; Nichol, Robert C.; Ogando, Ricardo; Sahlén, Martin; Stahl, Benjamin; Stott, John P.; Thomas, Peter A.; Viana, Pedro T. P.; Wilcox, Harry (2016), MNRAS, 463, 413

I am the main contributor to this work. I undertook the data reduction and the analysis and wrote up the results under the supervision of Dr M. Hilton. The form of the publication has been altered slightly to adhere to the formatting requirements of this thesis.

Signed in Westville, KwaZulu-Natal: Date:

CONTENTS

Abstract	i
Acknowledgments	iv
Preface	vi
Declaration of Non Plagiarism	vii
Declaration of Publications	viii
List of Tables	xvi
List of Figures	xix
1 Introduction	1
1.1 Big Bang Theory	2
1.1.1 Expansion of the Universe	2
1.1.2 Nucleosynthesis of the light elements	6
1.1.3 Origin of the cosmic microwave background radiation	8
1.2 Galaxy Cluster Formation	10

1.3	Galaxy Cluster Detection	16
1.3.1	Optical	17
1.3.2	X-ray	24
1.3.3	Radio	28
1.3.3.1	Detection of diffuse radio emission	30
1.3.3.2	Origin of diffuse radio emission	31
1.3.3.3	Radio relics	32
1.3.3.4	Mini-halos	35
1.3.3.5	Radio halos	36
1.3.4	Sunyaev-Zeldovich Effect	40
1.4	Scaling Relations	45
1.5	Cluster Cosmology	50
1.6	Thesis Outline	52
2	Optical observations and the cluster sample	53
2.1	Origin of the sample	53
2.2	Low redshift sample	56
2.3	High redshift sample	57
2.3.1	Clusters from literature	57
2.3.2	New observations	58
2.3.2.1	Observations	58
2.3.2.2	Spectroscopic data reduction	59
2.3.2.3	Galaxy redshift measurements	63
2.4	Membership determination	63
2.4.1	Cluster redshifts	64
2.4.2	Cluster membership	65
2.4.3	Final samples	65
2.5	Conclusion	67

3	Velocity Dispersion - Temperature scaling relation	74
3.1	Motivation	74
3.2	Velocity dispersion calculation	76
3.3	Fitting the $\sigma_v - T_X$ relation	76
3.4	Results	80
3.4.1	Evolution of the slope and intrinsic scatter	80
3.4.2	Evolution of the normalisation	83
3.5	Discussion	85
3.5.1	Comparison with previous results	85
3.5.2	Comparison with simulations - no evolution	88
3.5.3	The effect of biased slope measurements on the evolution of the normal- isation	91
3.5.4	Comparison with simulations - evolution	93
3.6	Conclusion	95
4	Mass-Temperature scaling relation	97
4.1	History	97
4.2	Galaxy cluster masses	99
4.3	Fitting the Mass – Temperature relation	101
4.3.1	Orthogonal fitting	102
4.3.2	Gaussian mixture model approach to fitting	102
4.4	Results and Analysis	103
4.4.1	Expected slope vs Measured Slope	103
4.4.2	Comparison with previous results	105
4.4.3	Comparison of fitting methods	107
4.4.4	Comparison with simulations	110
4.4.5	Dynamical Mass vs Hydrostatic Mass	112
4.5	Conclusions	113

5	Diffuse radio emission	116
5.1	Diffuse emission and the link to galaxy cluster properties	116
5.2	Effect of mergers and cool cores on scaling relations	120
5.3	Diffuse emission and the $\sigma_v - T_X$ relation	124
5.3.1	Sample	124
5.4	VLA observations	127
5.4.1	Motivation and Proposal	127
5.4.2	VLA data reduction and analysis	128
5.4.2.1	Interferometry and calibration	130
5.4.3	JVLA pipeline	131
5.4.4	Initial analysis	133
5.4.5	Self calibration	137
5.4.6	Upper limit estimation	138
5.5	Conclusion	142
6	Conclusion	145
6.1	Future Work	147
	Appendix	149
A	Redshift catalogue	149
B	Velocity Histograms	203
	Bibliography	206

LIST OF TABLES

1.1	Comparison of selection criteria for Abell and Zwicky catalogs	17
1.2	Classifications of galaxy clusters	18
1.3	Comparison of different wavelength studies	44
2.1	Spectroscopic observations log	60
2.2	Redshifts of galaxies for cluster XMMXCS J025006.4-310400.8	68
2.3	Properties of low redshift sample ($0.0 < z < 0.5$)	70
2.4	Properties of high redshift sample ($0.5 < z < 1.0$)	72
3.1	Calculated properties of low redshift sample ($0.0 < z < 0.5$)	77
3.2	Calculated properties of high redshift sample ($0.5 < z < 1.0$)	77
3.3	Priors on $\sigma_v - T_X$ relation fit parameters	80
3.4	Best-fit $\sigma_v - T_X$ scaling relation parameters	82
3.5	Previous measurements of the velocity dispersion–temperature relation	87
3.6	Best fit values for the parameters in Equation 3.2 obtained from simulations with- out evolution	89
3.7	Best fit values for the parameters in Equation 3.2 with evolution from simulations	96
4.1	Calculated masses of low redshift sample ($0.0 < z < 0.5$)	100

4.2	Calculated masses of high redshift sample ($0.0 < z < 0.5$)	100
4.3	Priors on $M_{\delta}^{dyn} - T$ relation fit parameters	102
4.4	Best-fit $M_{\delta}^{dyn} - T$ scaling relation parameters	104
4.5	Best-fit $M_{200}^{dyn} - T$ scaling relation parameters for the Millennium simulation data	110
4.6	Previous measurements of the $M_{500} - T_X$ relation	115
5.1	Properties of the 3 clusters observed by VLA	128
5.2	Properties of the 3 clusters observed by VLA	137
5.3	Simulated 1 Mpc halo upper limits for the 3 clusters observed by VLA	139
5.4	Simulated 400 kpc halo upper limits for the 3 clusters observed by VLA	140
5.5	Clusters with Mpc diffuse emission	143
5.6	Clusters with no Mpc diffuse emission	144
A.1	XMMXCSJ000013.9-251052.1	150
A.2	XMMXCSJ003430.1-431905.6	151
A.3	XMMXCSJ005603.0-373248.0	152
A.4	XMMXCSJ015315.0+010214.2	153
A.5	XMMXCSJ072054.3+710900.5	155
A.6	XMMXCSJ081918.6+705457.5	156
A.7	XMMXCSJ094358.2+164120.7	157
A.8	XMMXCSJ095957.6+251629.0	158
A.9	XMMXCSJ100047.4+013926.9	159
A.10	XMMXCSJ100141.7+022539.8	161
A.11	XMMXCSJ104044.4+395710.4	162
A.12	XMMXCSJ111515.6+531949.5	163
A.13	XMMXCSJ115112.0+550655.5	164
A.14	XMMXCSJ123144.4+413732.0	164
A.15	XMMXCSJ151618.6+000531.3	166
A.16	XMMXCSJ161132.7+541628.3	167
A.17	XMMXCSJ163015.6+243423.2	170

A.18 XMMXCSJ223939.3-054327.4	174
A.19 XMMXCSJ233757.0+271121.0	174
A.20 XMMXCSJ105659.5-033728.0	176
A.21 XMMXCSJ114023.0+660819.0	177
A.22 XMMXCSJ182132.9+682755.0	178
A.23 XMMXCSJ005656.6-274031.9	181
A.24 XMMXCSJ015241.1-133855.9	183
A.25 XMMXCSJ021734.7-051326.9	184
A.26 XMMXCSJ025006.4-310400.8	186
A.27 XMMXCSJ030205.1-000003.6	188
A.28 XMMXCSJ095940.7+023113.4	190
A.29 XMMXCSJ112349.4+052955.1	192
A.30 XMMXCSJ113602.9-032943.2	194
A.31 XMMXCSJ134305.1-000056.8	196
A.32 XMMXCSJ145009.3+090428.8	198
A.33 XMMXCSJ215221.0-273022.6	200
A.34 XMMXCSJ230247.7+084355.9	202

LIST OF FIGURES

1.1	Hubble (1929) Velocity vs Distance Plot	3
1.2	Time evolution of the knowledge of the Hubble constant	4
1.3	HST Key Project on the Extragalactic Distance Scale Final Results	5
1.4	Abundance of light elements in the early Universe	7
1.5	Cosmic Microwave Background Spectrum	9
1.6	Main components of galaxy clusters	10
1.7	Snap shot from the Millennium Simulation	15
1.8	Bremsstrahlung radiation	25
1.9	Classifications of X-ray sources based on optical and radio observations	26
1.10	Sensitivity versus area for existing X-ray surveys	27
1.11	Synchrotron radiation	28
1.12	Proof of a shock producing a radio relic	34
1.13	Mini radio halos	35
1.14	Radio halo 1E 0657-558	38
1.15	Sunyaev-Zel'dovich Effect	41
1.16	Sunyaev-Zel'dovich Effect images of clusters	42
1.17	Effect of active AGN on the $L_X - T_X$ relation	46

2.1	Sample Selection	55
2.2	Spectra of galaxies in XMMXCS J025006.4-310400.8	64
2.3	Redshift and temperature distributions of the sample	66
3.1	Sketch showing orthogonal regression	78
3.2	The $\sigma_v - T_X$ relation assuming no evolution for both samples	81
3.3	One and two dimensional projections of the posterior probability distributions	82
3.4	The $\sigma_v - T_X$ relation with and without evolution for the combined sample	83
3.5	Evolution of the normalisation of the $\sigma_v - T_X$ relation	84
3.6	$\sigma_v - T_X$ relation for the Millennium Gas Project simulations	90
3.7	$\sigma_v - T_X$ relation for the BAHAMAS simulation data	91
3.8	Histogram showing the distribution of slope values for $\sigma_v - T_X$ obtained from a mock cluster sample	92
3.9	Evolution of the normalisation of the $\sigma_v - T_X$ relation, with $B = 0.5$	93
3.10	Evolution of the normalisation of $\sigma_v - T_X$ relation of the Millennium Gas and BAHAMAS simulations	95
4.1	$M_\delta^{dyn} - T_X$ relation: $\delta = 200, \delta = 500$	104
4.2	Comparison of our fit to previous studies	105
4.3	Best fit lines achieved for simulated data using the orthogonal and Bayesian Gaussian mixture model fitting methods	107
4.4	Histograms showing the distribution of slope and intercept parameter values for the orthogonal and Bayesian Gaussian mixture model fitting method	108
4.5	Histograms showing the distribution of slope and intercept parameter values for the orthogonal fitting method with small scatter	109
4.6	$M_{200}^{dyn} - T_X$ relation: Simulations	111
5.1	Radio halo power – X-ray Luminosity Relation	118
5.2	Radio halo power vs Mass Relation	119
5.3	Radio halo power vs X-ray Temperature Relation	120

5.4	Evolution of galaxy properties during a merger	122
5.5	X-ray luminosity - X-ray Temperature relation for merging clusters	123
5.6	Diffuse emission clusters on the $\sigma_v - T_X$ plane	126
5.7	X-ray images with radio overlays of the clusters observed with VLA	129
5.8	Radio images of J1040	133
5.9	Radio images of J1115	134
5.10	Radio images of J1516	135
5.11	UV coverage of our 3 clusters	136
5.12	Bad spectral windows in our data	136
5.13	Position of our simulated upper limits on the $P_{1.4\text{GHz}} - L_X$ and $P_{1.4\text{GHz}} - M_{500}$ relation	141
B.1	Velocity histograms for the low redshift sample	204
B.2	Velocity histograms for the high redshift sample	205

CHAPTER 1

INTRODUCTION

Clusters of galaxies are the largest coherent gravitationally bound objects in our Universe. By studying galaxy clusters, information can be gained about the formation of galaxies, and the effect of ongoing galaxy processes on the intracluster medium (ICM) such as Active Galactic Nuclei (AGN) feedback. They can also be used as a probe of cosmology by studying the evolution of their number density with mass and redshift (e.g., Vikhlinin et al., 2009; Hasselfield et al., 2013; Reichardt et al., 2013; Planck Collaboration et al., 2015). However, the mass of galaxy clusters is not a quantity that can be directly measured, and therefore it needs to be determined using observable mass tracers such as X-ray properties, e.g., luminosity and temperature (Boldt et al. 1966; Sarazin 1988; Edge and Stewart 1991; Ebeling et al. 1996; White et al. 1997; Bryan and Norman 1998; Reiprich and Böhringer 2002; Ebeling et al. 2007; Finoguenov et al. 2007; Fassbender et al. 2011; Giodini et al. 2013; Rozo et al. 2014; Lovisari et al. 2015; Section 1.3.2), the Sunyaev-Zel'dovich (SZ) effect signal (Sunyaev and Zeldovich 1970b; Sunyaev and Zeldovich 1972; Birkinshaw 1999; Holder et al. 2000; Patel et al. 2000; Motl et al. 2005; Bonamente et al. 2008; Planck Collaboration et al. 2016b, Section 1.3.4), and optical properties, such as richness and the line-of-sight velocity dispersion of member galaxies, as discussed in Section 1.3.1 (Abell 1958; Zwicky et al. 1968; Ortiz-Gil et al. 2004; Vikhlinin et al. 2006a; Rozo et al.

2009; Wen et al. 2009; Sifón et al. 2013; Rines et al. 2013; Nastasi et al. 2014). In this chapter, we give a brief outline of the “Big Bang” model for the formation of the Universe and the formation of galaxy clusters. The various methods of galaxy cluster detection and their importance in determining scaling relations are discussed. Finally, we look at how scaling relations can help us to constrain cosmological parameters in the search for a better understanding of the Universe.

1.1 Big Bang Theory

Cosmology is the study of the Universe as a whole, starting with its origin and extending to its contents, evolution, and finally the large scale structure. Over time different theories and predictions have been made regarding how the Universe began and evolved. Observations and testing have led to the accepted theory we use today known as the Big Bang Theory. By using general relativity and extrapolating the expansion of the Universe backward in time, there would be a finite time in the past, when the Universe had an infinite density and temperature. At this point, known as the singularity, general relativity and all the laws of physics break down, although this may be avoided in cosmic inflation theories. This singularity is considered to be the origin of our Universe (e.g., Roos, 2008). The success of the standard big bang model for the formation of the Universe can be based on four key observations: the expansion of the Universe; nucleosynthesis of the light elements; the formation of galaxies and large scale structure; and the origin of the cosmic background radiation.

1.1.1 Expansion of the Universe

One of the most important cosmological discoveries ever made was that our Universe is expanding. It was first discovered largely due to observations performed by Edwin Hubble in 1924. He determined estimates of distances to galaxies and discovered the presence of Cepheid variable stars in M31 when performing observations using the 100-inch telescope at Mt. Wilson (Hubble, 1925). Lemaître (1927) (translation available in Lemaître 1931) and Robertson (1929) used the

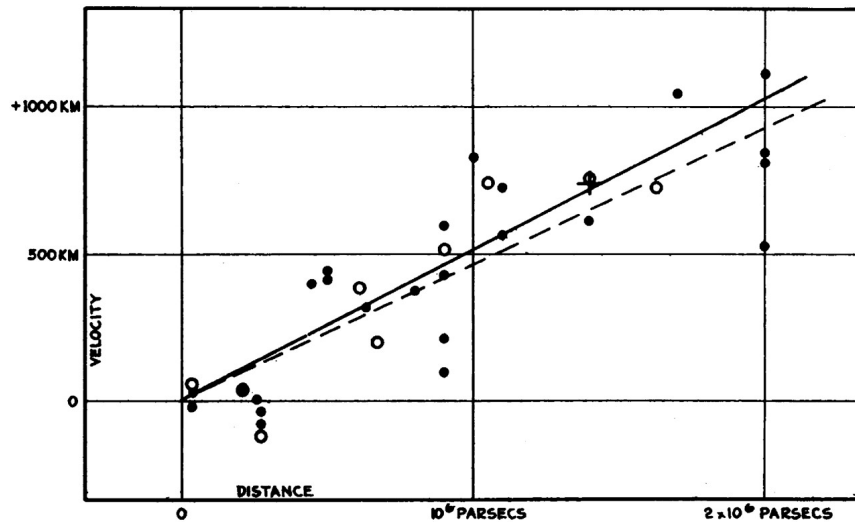


Figure 1.1: The plot from Hubble (1929), showing the velocity and distance to galaxies, which convinced the astronomy community that the Universe was expanding and that a proportionality existed between velocity and distance. Radial velocities, corrected for solar motion, are plotted against distances estimated from evolved stars and mean luminosities of nebulae in a cluster.

data taken by Hubble and were the first to predict the expansion of the Universe. However, Hubble (1929) was able to convince the astronomy community of the finding with his plot showing the proportionality between the velocity, v , and the distance, d (Figure 1.1). This proportionality, $v = H_0 d$, became known as Hubble's law, and the constant of proportionality, H_0 , is known as the Hubble constant. It was initially over-estimated at $500 \text{ km s}^{-1} \text{ Mpc}^{-1}$ (Hubble, 1929).

Controversy over Hubble's constant began almost immediately. The age of the Universe inferred from this value dated the Universe at an age of 2 Gyr, but by the 1930s radioactive dating of rocks by geologists showed that it was 3 Gyrs (Mould et al., 2000). It also raised concerns in the astronomy community because it implied that the Milky Way was much larger than any nearby galaxy, except possibly Andromeda. However, they continued to support and use Hubble's value until the 1950s when Walter Baade discovered Population II stars (Baade, 1956) and re-calibrated the period-luminosity relation for Cepheid variables. It was discovered that what Hubble was observing as individual stars in distant galaxies were actually star clusters, and when corrected, Hubble's constant dropped to a value of $280 \text{ km s}^{-1} \text{ Mpc}^{-1}$ (Baade, 1956).

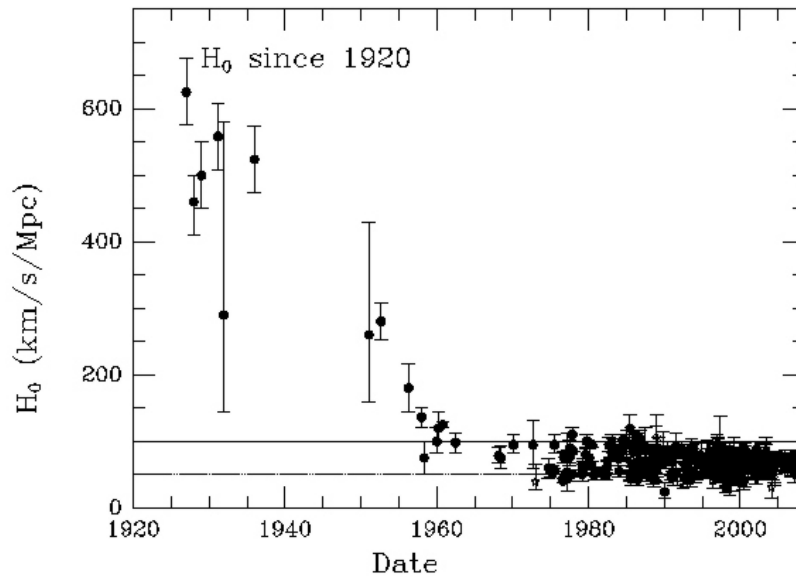


Figure 1.2: This plot, courtesy of John P. Huchra¹, shows how our knowledge of the Hubble constant has changed since it was first measured in 1927.

However, the issue was still not resolved. Hubble's successor at the Mt. Wilson observatory, Allan Sandage, performed further calculations and observations, and by 1956 had further reduced the value to $180 \text{ km s}^{-1} \text{ Mpc}^{-1}$ (Humason et al., 1956). Two years later he published a value of $75 \text{ km s}^{-1} \text{ Mpc}^{-1}$ (Sandage, 1958), and by the 1970s had reduced it to a value of only $55 \text{ km s}^{-1} \text{ Mpc}^{-1}$ (Sandage and Tammann, 1974). During this time, other competitors continually measured values of the order of $100 \text{ km s}^{-1} \text{ Mpc}^{-1}$ (e.g., van den Bergh, 1970, 1972, 1975; de Vaucouleurs and Bollinger, 1979; de Vaucouleurs, 1982a,b). The various values for the Hubble constant can be seen in Figure 1.2. A resolution to this problem was presented in the form of the Hubble Space Telescope (HST).

In the early 1980s a team was formed for a project known as the HST Key Project on the Extragalactic Distance Scale. The primary goal of this project was to decrease the errors in the calibration of the Hubble constant and derive a value which was accurate to 10%. This project ran for many years but they achieved their goal and in 2001 they published their final results

¹<https://www.cfa.harvard.edu/~dfabricant/huchra/hubble/>

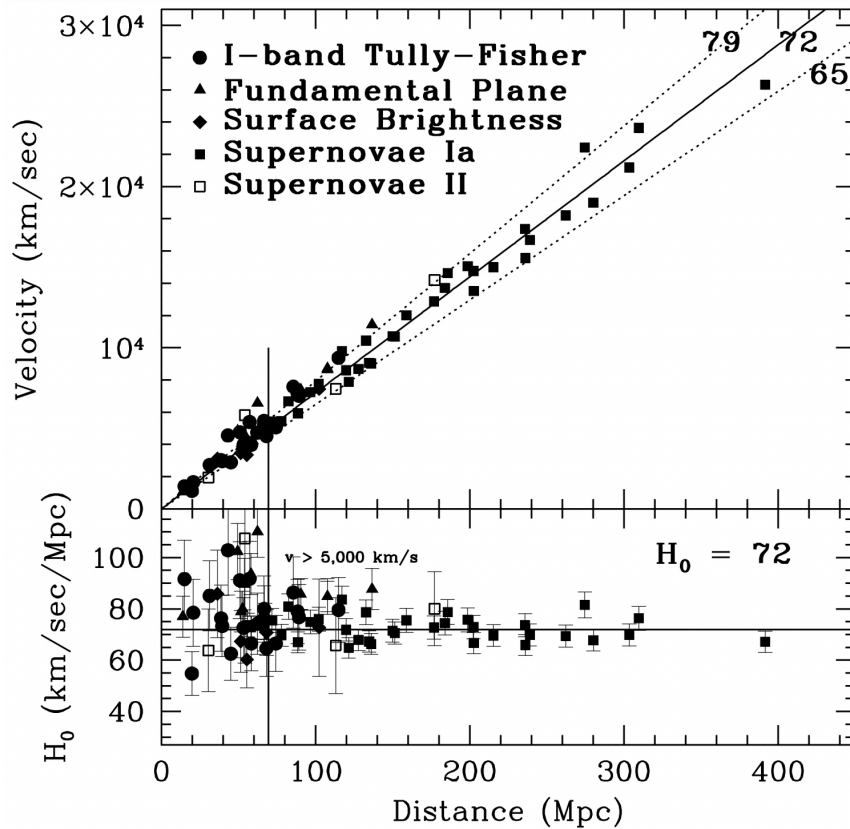


Figure 1.3: Hubble diagram of the distance vs velocity taken from Freedman et al. (2001). This plot shows a summary of the results from this project, with the different methods used for determining distance and velocities. They determined a value of $H_0 = 72 \pm 8 \text{ km s}^{-1} \text{ Mpc}^{-1}$.

(Freedman et al., 2001). Using various methods (Figure 1.3) they were able to determine a value for the Hubble constant, $H_0 = 72 \pm 8 \text{ km s}^{-1} \text{ Mpc}^{-1}$.

Since then numerous studies have worked on improving this value, including the Wilkinson Microwave Anisotropy Probe (WMAP) and the Planck project. WMAP was a NASA Explorer mission which was launched in 2001 with the primary aim to make fundamental measurements of cosmology. The mission was completed in 2012 and the final cosmological results are published in Hinshaw et al. (2013). They inferred $H_0 = 70.0 \pm 2.2 \text{ km s}^{-1} \text{ Mpc}^{-1}$, under the assumption of spatial flatness. Planck was an ESA mission to observe the first light in the Universe. It was launched in 2009 and recorded data until it was deactivated, after 30 months, in October 2013 (Planck Collaboration et al., 2016a). The data has not been completely analysed but the latest

results, combining temperature and lensing data, give a result of $H_0 = 67.8 \pm 0.9 \text{ km s}^{-1} \text{ Mpc}^{-1}$ (Planck Collaboration et al., 2016c). All of these data leads to the conclusion that our Universe is expanding and therefore all objects around us, with the exception of nearby gravitationally bound objects (e.g., our Local Group, van der Marel et al. 2012), are receding.

1.1.2 Nucleosynthesis of the light elements

The abundance of light-elements in our Universe is another important criteria we can use to verify the hypothesis of the Big Bang Theory. The abundance of light elements (deuterium, helium, and lithium) in the early Universe is dependent on the density of the ordinary matter (Figure 1.4). Above a certain threshold we are able to approximate that 24% of the ordinary matter in the Universe is helium.

In the 1950s and 1960s, the predominant theory regarding how the chemical elements in the Universe were formed was due to work done by G. Burbidge, M. Burbidge, Fowler, and Hoyle. Their work became known as the BBFH hypothesis (Hoyle et al. 1956; Burbidge et al. 1957). They suggested the idea that all the elements were made in stellar interiors or during supernova explosions. However, two main faults were present in this theory. Firstly, if the stellar nuclear reactions are the only processes responsible for the production of helium then only a small amount should be seen rather than the observed 25%. Secondly, stellar theory excludes the production of deuterium in stellar interiors and suggests that it is rather destroyed inside stars. Therefore, this theory could not accurately predict the observed abundances of these two elements.

A different theory was needed to explain the observed Helium abundance and, due to work by George Gamow and his collaborators (Gamow, 1946; Alpher et al., 1948), one now exists. This theory is known as Big Bang Nucleosynthesis and encapsulates the following. The very early Universe existed at extremely high temperatures, resulting in all matter being fully ionised and dissociated. Approximately three minutes after the Big Bang, the temperature of the Universe

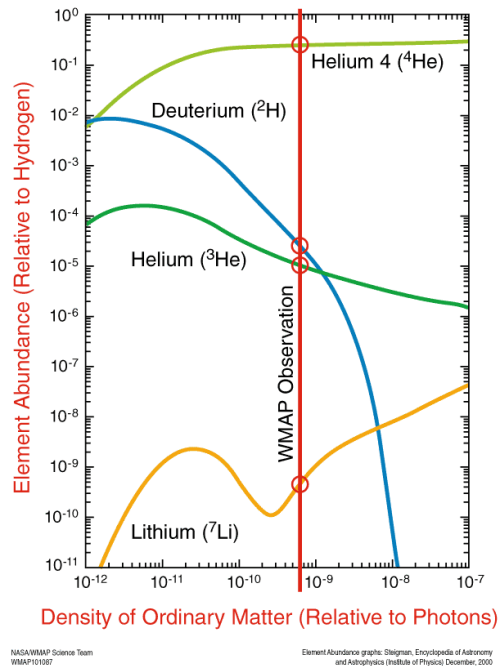


Figure 1.4: This image produced by the WMAP² science team shows how the abundance of light elements in the early Universe depends on the density of ordinary matter. It can easily be seen that above a certain threshold, the yield of helium is insensitive to changes in density. The WMAP satellite is able to measure the density of the ordinary matter, shown by the vertical red line, and they can then predict the abundance of the different elements. They found them to be in good agreement with the observed abundances.

began to cool adiabatically to approximately 10^9 K. At this lower temperature the products of fusion, i.e., deuterium, helium and tritium, are no longer dissociated by high energy photons as soon as they are formed. Lithium was formed due to the collision between tritium and two deuterium nuclei. The heavier elements are only formed much later in the interior of stars. Observations of the Universe have verified the abundances of these light elements and found them to be in excellent agreement, except for Lithium, with the theory of Big Bang Nucleosynthesis (Planck Collaboration et al., 2014b, 2016d; Komatsu et al., 2011; Hinshaw et al., 2013).

²http://map.gsfc.nasa.gov/universe/bb_tests_ele.html

1.1.3 Origin of the cosmic microwave background radiation

In the beginning, approximately 13,8 billion years ago, when the Universe was very young, it was extremely dense and hot, with temperatures greater than 10^{32} K, and filled with hydrogen plasma and radiation (Anderson, 2015). As it expanded, this plasma and radiation cooled. After approximately 380 000 years ($z \sim 1100$) it had cooled sufficiently for neutral hydrogen atoms to form (Sunyaev and Zeldovich, 1970a; Peebles and Yu, 1970; Farhang et al., 2012). This time period is known as the recombination epoch. This resulted in the thermal radiation no longer being able to interact with the background gas, making it transparent and resulting in photon decoupling. During this time the photons were no longer being constantly scattered by the electrons and protons and were able to travel freely through space. These photons have been moving through space ever since, being stretched due to the expansion of the Universe. This stretching caused an increase in wavelength and hence a decrease in the energy of the photons. This is the source of the cosmic microwave background (CMB) radiation (Gawiser and Silk, 2000).

The CMB was first predicted in 1948 by Ralph Alpher and Robert Herman who estimated that the temperature of the CMB was 5 K (Alpher and Herman, 1948). However, it was only recognised as a detectable phenomenon in 1964 when two Soviet astrophysicists released a short paper on the subject (Doroshkevich and Novikov, 1964). Around this time, David Todd Wilkinson and Peter Roll undertook the task to build a Dicke radiometer (Dicke, 1946) to measure the CMB. However, before they could complete their task the CMB was detected by chance at the Bell Telephone Laboratories. Arno Penzias and Robert Woodrow Wilson were using a Dicke radiometer for satellite communications and radio astronomy when they observed an excess 4.2 K antenna temperature which they could not account for (Penzias and Wilson, 1965). Through communications between Wilkinson, Roll and Peebles, they were able to determine that the excess temperature was indeed due to the CMB (Dicke et al., 1965). Penzias and Wilson were awarded the Nobel Prize in Physics for their discovery in 1978.

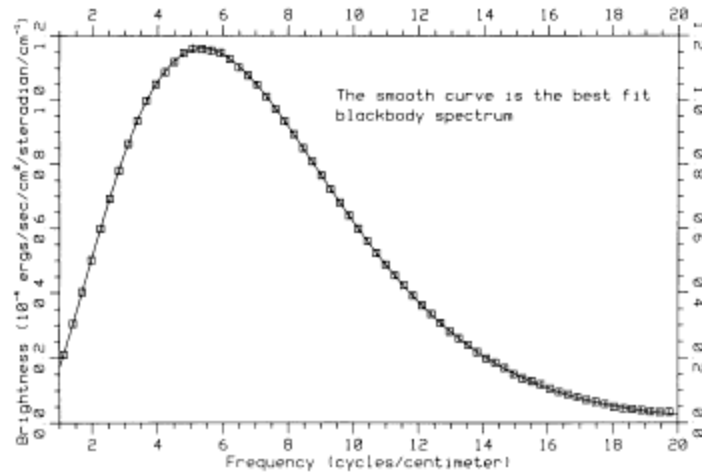


Figure 1.5: This image was taken from Mather et al. (1990) showing the power spectral density of the cosmic microwave background as observed by COBE. It corresponds perfectly to a black body spectrum.

Around this time, the steady state model of the evolution of the Universe was still a popular theory. In this model, the density of matter in the expanding Universe is unchanging due to a continuous creation of matter. Supporters of this model argued that the excess temperature was the result of scattered starlight (Narlikar and Wickramasinghe, 1967). However, new measurements at different frequencies revealed that the spectrum was a thermal, blackbody spectrum (Figure 1.5). This was a result that could not be reproduced by the steady state model, and the consensus that the CMB was a remnant of the Big Bang grew (Peebles et al., 1991).

When observing the CMB with extremely sensitive instruments such as the Cosmic Background Explorer (COBE) satellite and WMAP, tiny fluctuations in the CMB temperature were detected (White, 1999). Studies of these fluctuations allow us to measure the basic parameters describing the Big Bang theory, as well as provide us with information about the origin of galaxies and large scale structures of galaxies (Bennett et al., 2003). The small temperature anisotropies that we see in the CMB are thought to be the seeds of structure formation, and give rise to the formation of galaxies, and eventually clusters of galaxies, that will be discussed in the next section.

1.2 Galaxy Cluster Formation

Galaxy clusters are composed of 3 main components: stars (in both galaxies and the intracluster light [ICL]), the hot ICM, and dark matter (See Figure 1.6). Stellar light is observed with optical telescopes and the hot ICM can be observed via the Sunyaev-Zeldovich effect and X-ray observations. Dark matter can not be observed directly but its presence can be inferred by the observations of gravitational lensing of background galaxies distorted into extended arcs (Kravtsov and Borgani, 2012).

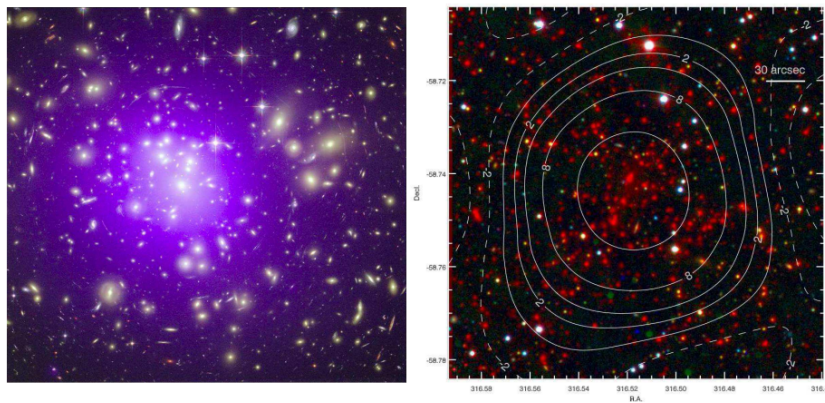


Figure 1.6: This image taken from Kravtsov and Borgani (2012) clearly shows the 3 main components of galaxy clusters. Left panel: This image shows galaxy cluster Abell 1689 at redshift $z=0.18$. The purple haze shows the X-ray emission due to the ICM, and was obtained by the Chandra X-ray Observatory. The galaxies observed in the optical band by the Hubble Space Telescope are shown in yellow. The presence of dark matter can be inferred by the long arcs seen in the optical image which are caused by the gravitational lensing of background galaxies. (Credit:X-ray: NASA/CXC/MIT; Optical: NASA/STScI). Right panel: This image shows galaxy cluster SPT-CL J2106-5844 at $z = 1.133$. This cluster is one of the most massive clusters known at $z > 1$ discovered via its Sunyaev-Zeldovich (SZ) signal. The image shows the optical band as observed by Magellan/LDSS3 and the blue-green-red color channels represent the mid-infrared measurements taken by Spitzer/IRAC. The white contours correspond to the South Pole Telescope SZ significance values, as labelled, where dashed contours are used for the negative significance values.(Adapted from Foley et al. (2011).)

Dark matter was originally postulated by Zwicky (1933). He derived an equation that linked the line of sight radial velocity of galaxies within a cluster to the mass of the cluster using Newton's second law. He considered a system of mutually interacting masses, where r_i is the

position of mass m_i with respect to the system center of mass and F_i is the total force acting on this mass as a result of its interaction with all of the other masses in the system. Then, by applying Newton's second law, he got the following equation:

$$F_i = m_i \frac{d^2 r_i}{dt^2}. \quad (1.1)$$

Scalar multiplication by r_i , summing over all the masses and time averaging then yields,

$$\overline{\frac{1}{2} \frac{d^2}{dt^2} \left(\sum_i m_i r_i^2 \right)} = \overline{\left(\sum_i r_i F_i \right)} + \overline{\left(\sum_i m_i v_i^2 \right)}, \quad (1.2)$$

where v_i is the velocity of the i th mass. He made the further assumption that the overall mass distribution fluctuates about some equilibrium value. Thus the time average of the derivative on the left became zero, leaving,

$$\overline{\left(\sum_i \frac{1}{2} m_i v_i^2 \right)} = -\frac{1}{2} \overline{\left(\sum_i r_i F_i \right)}. \quad (1.3)$$

This equation which links the system's total kinetic energy to its total potential energy became known as the virial theorem and is often written as,

$$2KE + U = 0. \quad (1.4)$$

Zwicky (1933) applied this virial theorem to the Coma cluster to determine its approximate mass. He knew that this cluster consisted of about 1000 galaxies that were distributed in a nearly

spherical pattern and interacting gravitationally. By applying Newton's third law and the Law of Universal Gravitation he was able to simplify the potential energy to have the form,

$$\sum_i r_i F_i = - \sum_i \sum_{j < i} \frac{G m_i m_j}{r_{ij}}. \quad (1.5)$$

Substitution into the virial equation then gives,

$$\overline{\left(\sum_i m_i v_i^2 \right)} = \overline{\sum_i \sum_{j < i} \frac{G m_i m_j}{r_{ij}}}, \quad (1.6)$$

where the left hand side of the equation is simply the total mass of the cluster multiplied by the time and mass averaged squared velocity. Zwicky made the further assumption that the mass is uniformly distributed over a sphere of radius R , which allows the right hand side of the equation to be simplified to,

$$U \approx \frac{GM^2}{R}. \quad (1.7)$$

Using this he got an equation for an approximation of the total mass of the galaxy cluster,

$$M \approx \frac{v^2 R}{G}. \quad (1.8)$$

Since Zwicky knew the redshifts of the galaxies he could calculate line of sight velocities for the galaxies and by assuming spherical symmetry was able to calculate the time and mass averaged squared velocity. He also knew the radius of the Coma cluster and therefore was able to calculate the mass of the Coma cluster. However, when he then calculated the average mass to light ratio

of the galaxies in the Coma cluster, using the average galactic luminosity he found it to be much higher than expected if the mass of the galaxies was only due to stars Zwicky (1937).

One plausible explanation for this discrepancy is dark matter, which contributes to the mass of the galaxies without increasing the galactic luminosity. This observation of dark matter has been confirmed by studies of clusters and the stellar dynamics of their members (e.g., Bridges et al., 2006; Bradford et al., 2011; Tortora et al., 2014; Sweet et al., 2016), and gravitational lensing (e.g., Bartelmann and Schneider, 2001; Benjamin et al., 2007; Tinker et al., 2012; Liu and Hill, 2015). The presence of dark matter is also inferred from observations of spiral galaxy rotation curves (e.g., Rubin et al., 1980; Bosma, 1978, 1981a,b; Begeman, 1987; Persic et al., 1996; van den Bosch and Swaters, 2001; Salucci et al., 2007; Brook and Shankar, 2016).

The theory of cold dark matter was first proposed by Peebles (1982) as a way to solve two major problems: (i) when observing clusters and galaxies they were found to be much more clustered than expected if only baryonic matter was present, and (ii) the baryon density was observed to be too low to result in the total energy of the Universe, since at this time, various studies indicated $\Omega = 0.3$. In this model of structure formation, most of the mass is thought to be made up of massive, weakly-interacting, non-baryonic particles which travel at non-relativistic speeds. Since this matter only interacts with gravity it begins clustering sooner than baryons, resulting in the observed clustering. Cold dark matter is currently the most widely accepted type of dark matter.

The process by which galaxy clusters form is not simple or linear. It involves many different physical phenomena on different scales and therefore, to date, the exact method is not fully understood. The general process is that the tiny density perturbations in the early Universe, caused by inflation, are amplified due to gravity and dark matter. This resulted in a hierarchical sequence of mergers ultimately resulting in galaxy clusters. A review of different galaxy cluster formation models is provided by Kravtsov and Borgani (2012).

One of the main models describing this process was suggested by Kaiser (1986a) and uses baryonic processes to explain observational properties, such as the galaxy cluster temperature. In this model, known as the self-similar model, all galaxy clusters and groups are essentially identical objects which have been scaled up or down (Maughan et al., 2012). Strong self-similarity refers to when galaxy clusters have been scaled by mass and weak self-similarity refers to a scaling due to the changing density of the Universe with redshift (Bower, 1997). This model makes some key assumptions, as described by Kravtsov and Borgani (2012) and Maughan et al. (2012). The first assumption is that the cluster began as a density perturbation that at some point had $\Omega_m > 1$. This perturbation then evolved as a closed Universe independent of the background cosmology. Secondly, gravitational energy as a result of the collapse is the only source of energy to the ICM. By introducing these assumptions we greatly simplify the problem so that properties of the density field depend on only two control parameters: the slope of the power spectrum of the initial perturbations, and its normalisation. The strong self-similarity determines the slope and is not expected to evolve with redshift, while the weak self-similarity is responsible for the evolution of the normalisation since, in this simplified model, it is due only to a change in density with redshift (Bryan and Norman, 1998). This self-similar model is used to predict the values for the slopes of different scaling relations as discussed later in this thesis.

The self-similar scaling relations developed by [Kaiser, 1986] are based on three key assumptions. The first assumption is that the Universe is an Einstein-de Sitter Universe, $\Omega_m = 1$, and that the clusters have formed through gravitational collapse. The next assumption is that the initial perturbations present in the early Universe do not have a pre-set or preferred scale; this allows scale-free or self-similar perturbations (beyond gravitational collapse and shock heating), to evolve and grow. The final, and perhaps most interesting, assumption is that other physical processes, which shape the formation of clusters, do not interfere with formation nor do they introduce their own scaling into the model. These different models can be investigated using simulations. Cosmological simulations are used to model the growth of structure in the Universe. They play a significant role in cosmology because they offer us a way to test and verify models of the origin of the Universe and its evolution. It starts with a specific number of particles and a set

theory that is being tested and scientists watch how it evolves over time (Borgani and Kravtsov, 2011). Therefore, the two main constraints on simulations are the correct initial conditions and that the final distribution mimics what we can observe. Simulations were initially used to solve ‘zoomed-in’ problems where the focus would be on a few galaxies (Vogelsberger et al., 2014), but over time and with the improvement of technology we are now able to start looking at simulations of the Universe as a whole. A thorough review of the advances in simulations is presented by Bertschinger (1998).

One of the most important recent cosmological simulations is the Millennium simulation (Springel et al., 2005). It was carried out by the Virgo Consortium, made up of British, German, Canadian, and US astrophysicists. The original simulation follows approximately 10^{10} particles from redshift $z = 127$ to the present and it uses a cubic region of $500 h^{-1}$ Mpc. In Figure 1.7 we show some snapshots of the simulation showing how galaxy clusters are formed in a hierarchical formation.

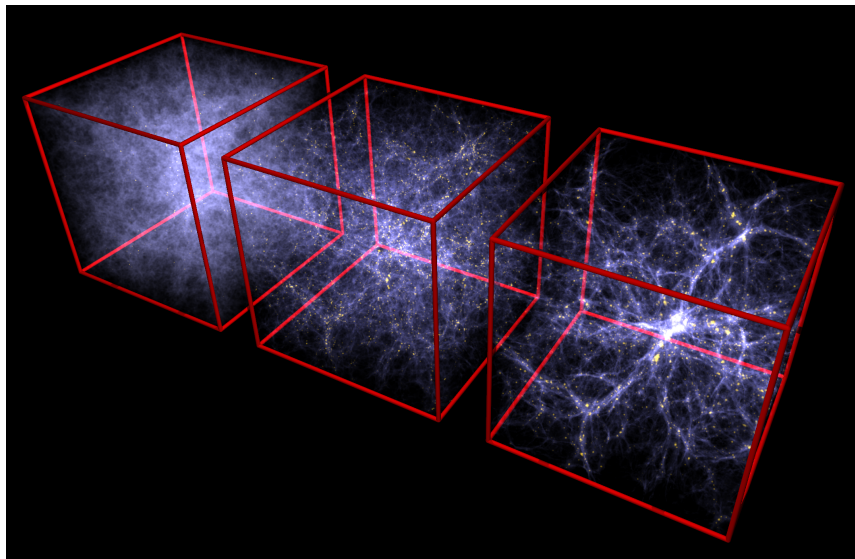


Figure 1.7: Snap shot from the Millennium Simulation to show the formation of large scale structure of the Universe at various redshifts (from left to right: $z = 6$, $z = 2$, and $z = 0$). Credit: Volker Springel (Max-Planck-Institute for Astrophysics.)

Simulations allow us to determine dynamics of clusters and make theoretical predictions of cluster properties. They are used for a variety of different studies including investigating basic cluster properties and the X-ray emission of clusters. The basic models have been improved by adding processes such as the SZ effects (Section 1.3.4), AGN heating, and cold fronts in the ICM (Springel, 2004). They have also been used to study scaling relations, which forms the basis of this thesis and will be discussed in more detail in Section 1.4. However, before any of these studies can be performed we require a sample of galaxy clusters and so we provide a short background on different galaxy cluster detection methods and their importance.

1.3 Galaxy Cluster Detection

In the 18th Century, Charles Messier and F. Wilhelm Herschel each independently produced a catalogue of nebulae and discovered that they had a tendency to cluster (Biviano, 2000; Herschel, 1864; Messier and Niles, 1981). During the 19th and early 20th Century this tendency became more pronounced as larger samples of galaxies were compiled. In the 1920s, Edwin Hubble made the discovery that elliptical and spiral galaxies are real galaxies like the Milky Way but at very large distances, implying the enormous size of clusters of galaxies (Hubble, 1925, 1926).

A few years later galaxies in regions of clusters were studied and measurements of galaxy velocities were made by Hubble and Humason (1931). By using the assumption that the motions of galaxies are in virial equilibrium, the total gravitational mass for clusters like Coma (Zwicky 1933; Zwicky 1937) and Virgo (Smith, 1936) were calculated, leading to the theory of Dark Matter (Section 1.2). This theory resulted in many investigations into the formation and evolution of galaxy clusters, introducing the study of aspects such as the properties and distribution of galaxy clusters and their dynamical status.

Original studies of the night sky were carried out in the optical band, but as technology has improved surveys searching for clusters in the X-ray have been developed and have been ex-

tremely important. Bright clusters have also more recently been discovered using radio, infrared, and sub-millimetre observations. All of these surveys have their own advantages and disadvantages, but by combining the data from different wavelengths we can minimise biases and gain a more complete understanding of galaxy clusters. In this section, we look at the optical, X-ray, and radio wavebands (summarised in Table 1.3) and discuss different surveys and original discoveries made. We also look at other methods of galaxy cluster detection including the SZ effect and gravitational lensing.

1.3.1 Optical

When galaxy clusters were first beginning to be studied, the two largest and most used optical catalogues were compiled by Abell (1958) and Zwicky et al. (1968). Both of these made use of the Palomar Optical Sky Survey (POSS) which was the first photographic survey of the sky (Minkowski and Abell, 1963; Reid et al., 1991). Since there was no standard definition of a galaxy cluster, both Zwicky and Abell visually examined the POSS and defined their own criteria for what would be included, based on magnitude, redshift, and area within which these galaxies fell (Table 1.1).

Table 1.1: Comparison of selection criteria for Abell and Zwicky catalogs (Sarazin and Boller, 1989). In this table m_i refers to the magnitude of the i th brightest galaxy in the cluster and z is the redshift.

Abell	Zwicky
At least 50 galaxies with magnitude in the range m_1 to m_3	At least 50 galaxies in the range m_1 to m_1+3 must fall in the boundary
The galaxies must fall in a circle of radius $R_A = \frac{1.7}{z}$ arcminutes	The boundary of the cluster is the isopleth where the galaxy surface is twice the local background density
$0.02 \leq z \leq 0.20$	No distance criteria

Table 1.2: Classifications of galaxy clusters by different astronomers from Sarazin and Boller (1989) and Abell (1975). Some of these astronomers define the type of cluster based on the galaxies within it, specifically the presence or lack of a cD galaxy. A cD galaxy is a extremely luminous elliptical galaxy found in the centre of an extended surface brightness halo.

Author	Classification	Explanation
Zwicky et al. (1968)	Compact	One pronounced concentration and >10 galaxies in contact
	Medium Compact	One pronounced concentration and >10 galaxies separated by several diameters or several pronounced concentrations
	Open	No pronounced peak of population
Bautz and Morgan (1970)	Type I	Cluster dominated by a cD galaxy
	Type II	Brightest galaxies are between a cD and giant elliptical
	Type III	No dominating galaxies
Rood and Sastry (1971)	cD	Dominated by a central cD galaxy
	B	Binary — dominated by a pair of luminous galaxies
	L	Line — at least 3 of the brightest galaxies appear to be in a straight line
	C	Core — at least 4 of the 10 brightest galaxies form a cluster core
	F	Flat — the brightest galaxies form a flattened distribution across the sky
	I	Irregular — the brightest galaxies have an irregular distribution across the sky
Morgan (1961)	Type I	Contains many spirals
	Type II	Contains a few spirals
Oemler (1974)	Spiral-Rich	Spirals most common
	Spiral-Poor	S0s most common
	cD	Dominated by a cD galaxy and most galaxies are S0 or elliptical

Abell's criteria focused mainly on the magnitude of the galaxies and their redshift, estimated from a velocity-magnitude relation (Abell, 1958), but since neither could be quantitatively measured, this introduced a bias into his catalogue. The Abell catalogue contains a total of 2712 galaxy clusters with an analysed distribution of 1682 of them, and was found to be mostly complete out to $z \sim 0.20$. However, up to 25% of these clusters could be contaminated or be the result of projections (Fesenko 1979; Lucey 1983; Frenk et al. 1990; Lumsden et al. 1992; Dalton et al. 1992; van Haarlem et al. 1997). Zwicky found galaxy clusters by searching for overdensities in the sky, and although this method seems simpler than Abell's, its completeness is extremely dependent on the redshift of the cluster. This is because clusters that have identical richness but are at different redshifts will have different overdensities (Abell, 1975).

In order to try and better understand galaxy clusters, astronomers used these two catalogues to try to find a way to classify galaxy clusters, most of which depended on their content and richness. When studying the content of the galaxy clusters they looked at the different types of galaxies and which were the most dominant. The richness has a variety of definitions, but can generally be classified as a statistical measure of the number of galaxies within a cluster (Abell 1958; Zwicky et al. 1968; Sarazin and Boller 1989; Koester et al. 2007a; Rykoff et al. 2016). A wide variety of classifications were created, the most popular of which we have described in Table 1.2. By studying this table we can see correlations between the different classifications and therefore, by combining them, we can simplify the classification into two main groups: regular and irregular galaxy clusters. The properties of regular clusters include there being a population of greater than 10^3 in the interval of the six brightest magnitudes, a central concentration of galaxies, spherical symmetry, and being dominated by E and S0 galaxies. Irregular galaxy clusters have a varying population from poor to relatively rich, little to no symmetry, no marked concentrations, and contain all types of galaxies.

Gunn et al. (1986) (Gunn, Hoessel and Oke (GHO) survey) were able to make use of this information to come up with a different method of identifying high redshift clusters. They used the photographic plates to search for large, red, central galaxies and marked these as possible

galaxy clusters requiring follow up with deep CCD images. Due to this being a different and novel method of finding galaxy clusters, the completeness of their sample could not be calculated (Yee and Gladders, 2002).

As technology advanced, digitised images and computer algorithms were used to replace visual inspection of the photographic plates. The first examples of this were shown by Heydon-Dumbleton et al. (1989) (Edinburgh-Durham survey) and Maddox et al. (1988) (APM survey) who used plates taken by the UK Schmidt Telescope Unit (UKSTU) to create galaxy catalogues. The plates cover the entire southern sky below a declination of -20° and have a limiting magnitude of 21. The Edinburgh-Durham Survey was the first large-scale machine-based optical galaxy catalogue and used the COSMOS — an automatic measuring machine designed for Schmidt telescopes (Pratt, 1977) — microdensitometer to scan 200 of the UKSTU plates. A mosaic of 60 of these plates around the Southern Galactic Pole had image classification performed on them to provide a galaxy catalogue of 10^6 galaxies. Lumsden et al. (1992) used this catalogue and a peak-finding algorithm to create the Edinburgh-Durham Cluster Catalogue (EDCC). This algorithm involved the binning of the galaxy data into equal square area bins, smoothing using a Shectman filter (Shectman, 1985), subtracting a background sky frame, and applying a threshold to determine possible cluster candidates. They then deblended the data to search for true peaks and used the Abell classifications described in Table 1.2. This gave a catalogue of 737 clusters or groups. Maddox et al. (1988) used the SERC Automatic Plate Measuring (APM) densitometer to study 176 of the UKSTU plates. Their survey discovered 3.6×10^6 galaxies in a 4400 square degree area. Dalton et al. (1992) used this survey and a two-stage process to create a galaxy cluster catalogue. The first stage used a percolation algorithm to locate spots of overdensity with a magnitude above 20.5. The second stage uses these possible candidates and an iterative procedure, involving sorting galaxies by magnitude and weighting them, to find the magnitude of each cluster. They selected a sample of 240 clusters for spectroscopic follow-up.

Further advancements allowed for the release of the Palomar Distant Cluster Survey (PDCS) by Postman et al. (1996). This survey was based on CCD images and was the first objectively

selected, fully automated catalogue of clusters. Although the survey was rather shallow, it did cover six square degrees of the sky and allowed for a substantial cluster survey to be performed. With the main aim of this survey being to reduce the effect of projection contamination seen in all previous studies, they used the more modern cluster finding method known as the matched filter algorithm, described in detail in their paper. This algorithm uses known facts about galaxy clusters from previous studies to aid in identifying real clusters. The properties used in this survey were the luminosity function and the size of the clusters. They found a total of 79 clusters, of which 16 were already known from a survey performed by Gunn et al. (1986). However, since the luminosity function is not very well defined it was found that there was still $\sim 30\%$ contamination from projection effects. Further studies by (Oke et al., 1998) using spectroscopic observations with Keck found that even with this high contamination rate, optical surveys searching for galaxy clusters are successful and important for finding systems with $z < 1$ (Gioia, 2000).

In 1996 Dalcanton (1996) suggested that by looking for surface brightness fluctuations on the sky we could find high redshift clusters. The reasoning behind this is that the fluctuations are caused by the light from unresolved galaxies in the cluster (Gioia, 2000). The advantage of this method is that initial searches can be done with small telescopes with follow-up observations required for confirmation of a galaxy cluster. Two surveys, the Palomar Transit Grism Survey (PTGS) and the LasCampanas Distant Cluster Survey (LCDCS), used this method to search for clusters. The PTGS covered 17.5 square degrees of the northern sky and identified 52 possible cluster candidates. Follow-up spectroscopy and imaging identified 10 of these as real clusters. The LCDCS catalogue is described in Gonzalez et al. (2001). They observed 130 square degrees of the southern sky and have found a total of 1073 possible cluster and group candidates in the redshift range $0.3 < z < 1$. (Zaritsky et al., 2002) describe this unique method in more detail.

Another optical technique for finding galaxy clusters is the cluster red sequence (CRS) method (Gladders and Yee, 2000). The motivation for this method stems from the observation that early-type galaxies in a rich cluster follow a colour-magnitude relation (Visvanathan and Sandage 1977; Bower et al. 1992; Bower et al. 1992; van Dokkum et al. 1998; Gioia 2000;

Baldry et al. 2004; Bernardi et al. 2005; Mei et al. 2009). Although the properties of a cluster will evolve with time, it was found that the red sequence galaxies in the galaxy cluster core occur at a higher number density compared to the red sequence galaxies in the field, and therefore the background contamination is negligible. The searching algorithm uses this population as an indicator that the object may be a cluster candidate. This technique has been used to generate two large surveys, Red-sequence Cluster Survey 1 (RCS-1) and RCS-2. These surveys used mosaic CCD cameras mounted on 4m telescopes to image the sky (Gladders and Yee 2001; Gladders 2002; Gladders and Yee 2005). RCS-1 observed a 90-degree square patch of sky and found a total of 1000 clusters (Yee et al., 2007). RCS-2, described in detail in Gilbank et al. (2011), is a ~ 1000 square degree survey using the square-degree imager, MegaCam, which aims to find 10^4 clusters. The aim of these surveys is to build a large enough catalogue of clusters to allow them to place constraints on cosmological parameters (see Section 1.1).

The Sloan Digital Sky Survey (SDSS) covers a third of the celestial sphere and provides the most complete database for low redshift clusters Alam et al. (2015). This large survey saw first light in 1998 but only started routine operations in 2000. It provides photometry in the five main bands (u,g,r,i and z) and has spectroscopic observations from follow-up studies. Due to the sheer number of objects from this survey, we have the chance to create a large and complete cluster catalogue. Different research groups have tried to do this using various cluster algorithms, a few of which we briefly describe below.

The maxBCG algorithm, a red-sequence cluster-finding algorithm, uses data from SDSS to detect 13,823 clusters (Koester et al., 2007a). This algorithm, first described in Koester et al. (2007b), exploits three known features of galaxy clusters in order to detect them. The first is that the spatial clustering of galaxies is inversely proportional to the radius of the cluster. The second is the position of the galaxies on the colour magnitude diagram, and lastly the brightest galaxy, i.e., the brightest cluster galaxy (BCG), will most likely be found in the centre of the cluster. These are all incorporated into a likelihood function used to detect BCGs and ultimately the clusters they reside in.

In 2009 Wen et al. (2009) used the SDSS Data Release 6 (DR6) to find 39,716 galaxy clusters in the redshift range $0.05 < z < 0.6$. They used a friends-of-friends algorithm and specify that, in order to be classified as a cluster, it must contain more than eight galaxies which fall within 0.5 Mpc of the centre of the cluster, and they must have a magnitude of $M_r < -21$.

The SDSS DR7 was used by Hao et al. (2010) to detect 55,424 rich clusters using the Gaussian Mixture Brightest Cluster Galaxy (GMBCG) algorithm. This algorithm is similar to the maxBCG algorithm and also uses the cluster red-sequence.

Rykoff et al. (2014) also use a red sequence technique to develop the redMaPPer algorithm which they applied to SDSS DR8 data. They found approximately 25,000 clusters in the redshift range $0.08 < z < 0.55$. Their algorithm is iterative and divided into two main stages: the calibration stage and the cluster finding stage. A rough colour calibration is used to identify possible cluster candidates which are then used to improve the calibration of the red sequence and allow for an improved cluster finding run. This process is run multiple times before a final run is made and clusters are identified.

In summary, optical observations provide the largest yield of galaxy clusters per square degree, when compared to other wavelengths. The reason for this is the wide field of view of these surveys and their greater depth. They are also essential for providing photometric redshifts for clusters detected in other wavelengths (Khedekar and Majumdar, 2013). However, optical surveys are vulnerable to projection effects and observations can be contaminated by line of sight foreground or background objects (Yee and Gladders, 2002). X-ray surveys are less vulnerable to these projection effects and therefore can aid in our understanding of galaxy clusters.

1.3.2 X-ray

X-ray studies of clusters of galaxies began in 1966 when Boldt et al. (1966) detected an extended X-ray source of $4^\circ - 5^\circ$ from space when conducting experiments at the Goddard Space Flight Centre. This source had a temperature of 25 keV and was situated at the same position as the Coma Cluster. The spectral flux was measured to be $10^{-2}(\text{cm}^2\text{s keV})^{-1}$ which implies a very large X-ray luminosity, leading to some controversy regarding whether or not this source could, in fact, be linked to the Coma Cluster. Felten et al. (1966) addressed this problem, after making the assumption that this X-ray source is in fact linked to the Coma Cluster, considering two possibilities, namely that the X-rays are produced by

1. the individual galaxies, or
2. the intergalactic medium.

By performing a simple superposition calculation, they were able to quickly dismiss the idea that the galaxies could be responsible for the total observed X-ray flux. They suggested that the X-ray emission may be coming from thermal bremsstrahlung caused by a hot gas filling the area of the cluster between the galaxies.

Bremsstrahlung is a German term that means "braking rays". The gas within a cluster is extremely hot causing it to become ionized. These charged particles are moving past each other and very high speeds. When these particles pass close by each other an electric force causes them to accelerate away from or towards each other resulting in bremsstrahlung radiation as shown in Figure 1.8.

Since the acceleration is not uniform, photons are emitted at various wavelengths resulting in a spectrum forming. The example given in Figure 1.8 is for a single photon, but this can be generalised for a population of electrons with a certain velocity and density distribution. If the population has an uniform temperature then the total emission by all the particles in this population is known as thermal bremsstrahlung, and is given by the equation:

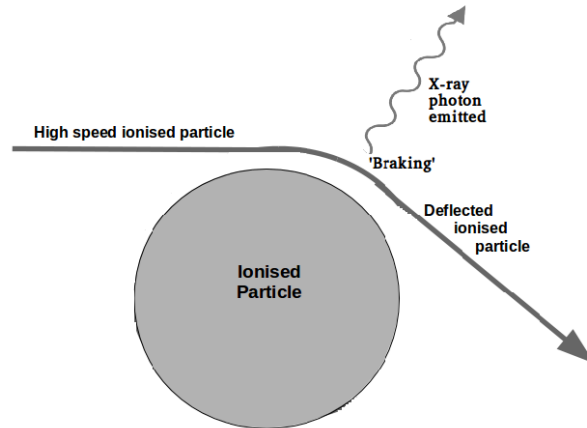


Figure 1.8: Bremsstrahlung radiation occurs when a high speed ionized particle is deflected and slowed down by another particle, resulting in energy being emitted as an X-ray photon.

$$\epsilon_v^{ff} = 6.8 \times 10^{-38} Z^2 n_i^2 T^{-\frac{1}{2}} e^{-\frac{h\nu}{kT}} \text{ erg s}^{-1} \text{ cm}^{-3} \text{ Hz}^{-1}. \quad (1.9)$$

Z is the charge on the ion, n_i is the number density of the ion and T is the temperature of the gas.

This observation, of the X-ray source in Coma, resulted in an increased interest in X-ray observations of galaxy clusters in an attempt to determine if it was a common occurrence or merely an anomaly.

In 1978 the Einstein observatory was launched, carrying X-ray imaging instrumentation, allowing for the Extended Medium Sensitivity Survey (EMSS) to be conducted. It orbited Earth just above 500 km until 1982 when it re-entered the Earth's atmosphere and burnt up. It surveyed an area of 778 square degrees finding a total of 835 sources (Gioia et al., 1990). This survey provided a homogeneous flux-limited sample of X-ray sources which can be used for various studies. Optical and radio follow-up of these sources (Stocke et al., 1991) allowed for classification, as shown in Figure 1.9.

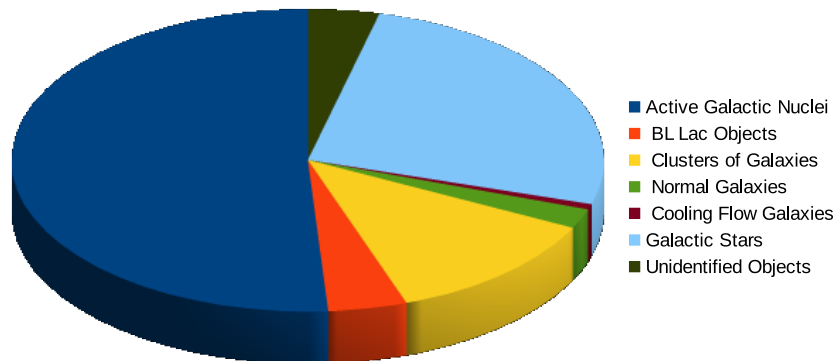


Figure 1.9: In 1978 the EMSS surveyed 835 X-ray sources using X-ray instrumentation on the Einstein observatory. In this pie chart we show the classifications of these objects which were determined using optical and radio follow-up.

After this first survey, it was discovered that X-rays offer some advantages over optical surveys. Galaxy clusters are the second brightest extragalactic sources in the sky, when observed in X-ray, and are easily identified because they are resolved. Projection effects are also minimised in X-ray surveys because the X-ray luminosity scales as the square of the gas density and confusion from background fluctuations is much lower (Voit, 2005). Optical observations are reliant on determining which galaxies belong to a cluster in order to determine velocity dispersions and masses. X-ray masses, however, are dependent on the temperature and density of the gas which we can measure. Finally, the selection criteria for X-rays are objective and quantifiable.

Due to these obvious advantages, many X-ray surveys have taken place. These surveys can be divided into two main types: contiguous area surveys and serendipitous surveys (Gioia, 2000). The contiguous area surveys cover large areas of the sky. Examples of these surveys include the Northern Rosat All-Sky (NORAS) survey (Böhringer et al., 2000), the Rosat ESO Flux Limited X-ray (REFLEX) survey (Böhringer et al., 1998), the ROSAT Brightest Cluster sample (BCS; Ebeling et al., 1998), the RASS1 Bright Sample (RASS1-BS De Grandi et al., 1999), the Massive Cluster Survey (MACS Ebeling et al., 2001), and the North Ecliptic Pole (NEP) survey (Henry et al., 1995). They are used to study the large-scale structure in galaxy clusters but, due

to their shallowness, can not be used to identify large numbers of the more massive clusters at high redshift. The serendipitous surveys use pointed data surveys to search for clusters which have the advantage of higher sensitivity but the disadvantage of a much smaller observation field of view, making identifying large clusters difficult. In Figure 1.10 we show the various X-ray surveys to date and compare their sensitivity and area. The X-ray data used for this thesis were from the XMM Cluster Survey (XCS), a serendipitous survey based on the XMM telescope described by (Romer et al., 2001; Mehrrens et al., 2012) and discussed in greater detail in Chapter 2.

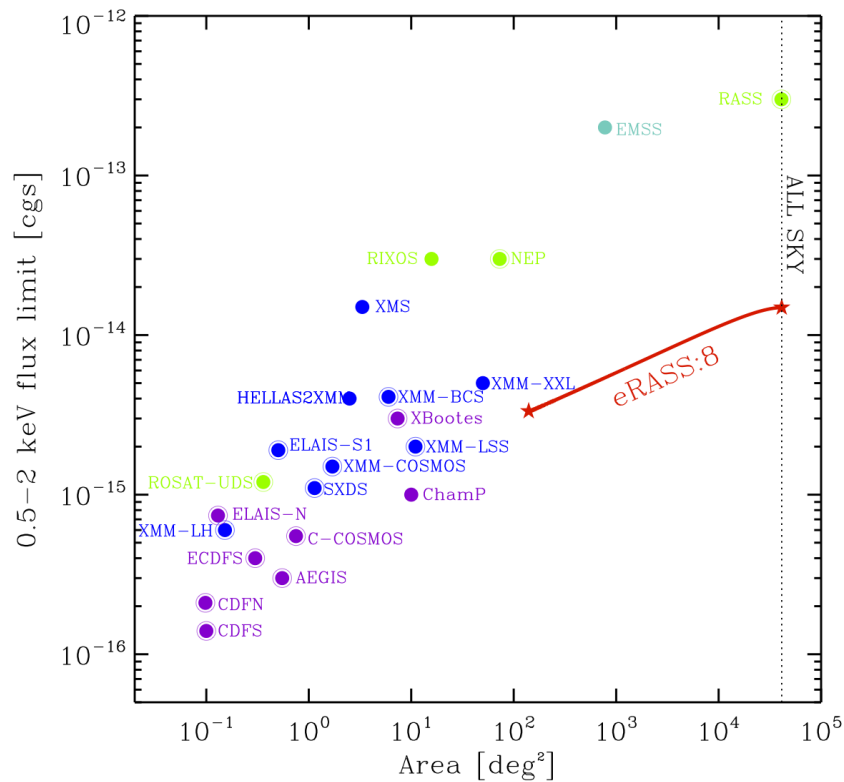


Figure 1.10: This image, taken from Merloni et al. (2012), shows a comparison of sensitivity versus area for existing X-ray surveys. The red line is for the eROSITA All Sky Survey, the cyan dots depict the Einstein surveys, orange is HEAO-1, green shows all the ROSAT surveys, blue is XMM-Newton, and Chandra is shown in purple. The points that have been encircled are contiguous surveys.

1.3.3 Radio

Mills (1960) and van den Bergh (1961) discovered a link between radio sources and galaxy clusters in the beginning of the 1960s. They discovered that radio emission could be attributed to individual galaxies or pairs of galaxies in the cluster. A year later this was confirmed by van den Bergh when he studied radio galaxies from the 3rd Cambridge (3C) catalogue (Edge et al., 1959; Bennett, 1962) and compared them to the positions of rich galaxy clusters. The emission from these galaxies is known to be due to synchrotron radiation (Sarazin and Boller, 1989).

The acceleration of relativistic particles by a magnetic field causes synchrotron radiation. For non-relativistic particles, this process is known as cyclotron radiation, and the frequency at which the radiation is emitted is known as the frequency of gyration. For relativistic particles, the frequency spectrum is more complex and the frequency is many times greater than the gyration frequency. The particle will undergo a combination of circular and uniform motion along the magnetic field which results in a helical motion as shown in Figure 1.11.

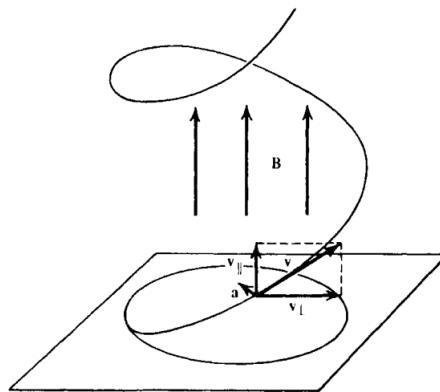


Figure 1.11: Synchrotron radiation occurs when charged particles are accelerated in a circular pattern. In this image, taken from Rybicki and Lightman (1986), we see a charged particle moving at velocity v in a magnetic field B . The velocity can be split into components, parallel ($v_{||}$) and perpendicular (v_{\perp}) to the magnetic field. If we study $v_{||}$ we see that $v_{||} \times B = 0$ and therefore $v_{||} = \text{constant}$. The acceleration, a , is perpendicular to the magnetic field and $v_{||}$. This results in motion of constant velocity along the magnetic field direction and circular motion about it, i.e., the helical motion shown above.

Hill and Lilly (1991) studied radio galaxies at $z \sim 0.5$. They found that radio sources at higher redshift ($z > 3$) are normally in the centres of rich proto-clusters (Bremer et al. 1997; Pentericci et al. 1999). This was proven by various observational indicators such as extended luminous X-ray emission, overdensities and spectroscopic studies (Gioia, 2000). Therefore, by performing observations around high redshift radio galaxies we can search for distant clusters as shown in recent studies (e.g., Burns et al., 1993; Blanton, 2000; Blanton et al., 2003; Baker et al., 2005; Paterno-Mahler et al., 2016). These searches can then be followed up with studies in optical or X-ray to confirm. Radio studies, however, do not provide a complete sample or any information regarding the selection function. The radio sources in galaxy clusters can be divided into two main types: single radio galaxies and diffuse radio emission.

If the radio galaxy existed in the field it would generally be symmetric with a simple structure. When radio sources are present in a galaxy cluster they take on a more complex structure which lacks symmetry. This is due to the confinement of the radio source by the surrounding ICM. The two main types are Wide Angle Tails (WAT), and Narrow Angle Tails (NAT) or Head-Tail (HT) galaxies (Miley, 1980). WATs are double-lobed but the lobes are not aligned with the nucleus. They are generally associated with the optically dominant galaxies and are more luminous than the HT galaxies (Douglass et al. 2016; Mao et al. 2010; Gómez et al. 1997; O'Donoghue et al. 1993; O'Donoghue et al. 1990; Owen and Rudnick 1976). For an HT galaxy, all the emission lies in a tail on one side and the galaxy forms the head. They are often not associated with cD galaxies (O'Dea and Owen 1985; Jones and Owen 1979; Rudnick and Owen 1976; Bliton et al. 1998; Mao et al. 2009).

For this thesis, we focus on the diffuse radio emission and will go into detail regarding its detection and origin.

1.3.3.1 Detection of diffuse radio emission

Extended radio emission was first detected in the Coma cluster by Large et al. (1959). They were observing an area of the sky, which included the Coma cluster, using the 250-ft radio telescope at Jodrell Bank at 408 MHz. They detected an extended source with an angular diameter of 45' in the middle of the cluster, later classified as a radio halo (Section 1.3.3.5). Further observations with single dish telescopes, and at lower frequencies, were able to confirm this extended size and show that the source had a steep spectrum (Costain and Smith 1960; Kenderdine 1963; Erickson and Cronyn 1965; Roger et al. 1969; Bridle 1969). However, it wasn't until Willson (1970) performed interferometric observations, using the Cambridge One Mile telescope, that it was confirmed to be diffuse emission and not linked to any specific cluster galaxy. Since then, high sensitivity radio observations have revealed many diffuse, non-thermal radio sources in clusters that are linked to the ICM rather than a specific cluster galaxy (e.g., Miley, 1980; Ensslin et al., 1998; Blasi and Colafrancesco, 1999; Liang et al., 2000; Petrosian, 2001; Govoni et al., 2001; Ferrari et al., 2008; Venturi et al., 2008; Brunetti et al., 2008; Giovannini et al., 2009; Feretti et al., 2012; ZuHone et al., 2013; Knowles et al., 2016).

Unlike the thermal gas emitting in X-rays which are detected in all clusters, this non-thermal emission is more elusive. Giovannini et al. (1999) presents the results of a search for diffuse radio emission in the NRAO VLA Sky Survey (NVSS). They inspected a sample of 205 X-ray bright Abell type sources taken from Ebeling et al. (1996) and found only 29 candidates. This proved that these diffuse sources are not present in all galaxy clusters. The low detection rate may also be attributed to the very low surface brightness of this diffuse emission. The Very Large Array (VLA), Westerbork Synthesis Radio Telescope (WSRT), and the Giant Metrewave Radio Telescope (GMRT) have proved very effective at detecting diffuse radio emission due to their compromise between high angular resolution and sensitivity to low brightness sources (Feretti et al., 2012).

Since the first detection of diffuse radio emission in Coma, many studies were launched to try to see if this was an anomaly. By 1982, diffuse emission had been found in 10 other clusters, with the most prominent evidence found for Abell 2255, Abell 2256 and Abell 2319 (Hanisch, 1982). By 2012, diffuse emission had been detected in 80 galaxy clusters at 1.4 GHz, with varying sizes, positions in the cluster and evolutionary conditions (Feretti et al., 2012) and this amount has not vastly changed since then.

1.3.3.2 Origin of diffuse radio emission

Diffuse radio emission found in radio halos and relics are extended synchrotron radio sources and therefore, in order for them to exist, relativistic particles must be present. There are two main models describing the origin of the relativistic electrons and hence the diffuse radio emission: the primary electron model and the hadronic (secondary electrons) model. In both models, relativistic particles are present in the cluster because they were injected at some point in the cluster's history by AGN activity or star formation (Jaffe 1977; Brunetti et al. 2001). Over time these electrons lose energy and radiation due to inverse Compton radiation and synchrotron radiation, and therefore would be unable to produce the large-scale diffuse radio emission observed (Schlickeiser et al., 1987). This is where the models begin to differ. In the primary electron model, the electrons are re-accelerated due to a transfer of energy from the cluster ICM. This occurs in two main ways: cluster turbulence (Brunetti and Lazarian, 2011) and cluster shocks (Keshet et al., 2004). In the hadronic model, inelastic nuclear collisions occur between the relativistic protons and the thermal intracluster medium, producing relativistic electrons. These secondary electrons are then injected into the cluster (Dennison 1980; Blasi and Colafrancesco 1999; Dolag and Enßlin 2000). This method means that the electrons can continuously be made *in situ* and distributed throughout the cluster. Colafrancesco and Mele (2001) also suggested that these electrons could have been formed by the decay of secondary products of the neutralino annihilation in the dark matter halos. The variances in the models describe different aspects of the diffuse radio emission and are dependent on the type of emission present.

Diffuse radio emission is typically grouped into three main categories depending on their position in the cluster and the cluster type: radio halos, mini-halos, and radio relics. All diffuse radio emission has been found to have a steep radio spectrum but the clear distinction between relics and halos is the polarisation. In this section, we will discuss each of these types of diffuse radio emission.

1.3.3.3 Radio relics

Radio relics are large diffuse extended sources (≥ 1 Mpc), with a low surface brightness and a steep spectrum³. They are found on the outer edges of a cluster and are strongly polarised. Jaffe and Rudnick (1979) were the first to unknowingly detect a radio relic. They used the Green Bank 300-ft telescope to map 32 clusters, including Coma, at 610 MHz to search for diffuse radio emission, similar to that found by Large et al. (1959). They found a second extended source, 1253+275, located approximately 70' South West from the centre of the Coma cluster. Due to a lack of strong discrete radio sources in this region they linked this emission to the galaxy 3C 277.3 at $z = 0.086$ (Schmidt, 1965), rather than the Coma cluster ($z = 0.023$). Ballarati et al. (1981) observed this same source with the Northern Cross Radio Telescope, and due to the better resolution, were able to determine that it was an extended source with a size of $22' \times 10'$. They suggested that it belonged to the Coma cluster but was not linked to any specific galaxy within the cluster, and classified it as a radio halo. It wasn't until 1985 that a different interpretation was offered. Giovannini et al. (1985) and Hanisch et al. (1985) suggested that it was rather a relic radio galaxy but differed on the parent radio galaxy. Hanisch et al. (1985) performed observations using the WSRT at 608 and 1400 MHz, and identified a 16 magnitude galaxy in the centre of one of the lobes and identified this as the parent source. Giovannini et al. (1985), however, believed it was linked to IC 3900 which is a Coma cluster galaxy located 3' from the centre of 1253+275. Giovannini et al. (1991) rejected both of these observations. They found that the galaxy detected by Hanisch et al. (1985) showed no presence of radio emission and IC 3900 was

³ $\alpha > 1$, where the flux depends on a power law spectral index: $S_\nu \propto \nu^\alpha$.

radio quiet. They instead used evidence of a bridge joining the halo source at the centre of Coma and 1253+275 (Kim et al., 1989), to suggest that it was part of the extended radio source. This led to the concept of the radio relic.

Many theories regarding the origin of these radio relics were proposed. However, their position in the peripheral region of the cluster offers support to the primary electron model rather than the hadronic model. The reason for this is because on the outer edges there are insufficient protons to make a continuous supply of electrons, and therefore there would be no secondary electrons supplied to the cluster and no diffuse emission. Therefore, the origin models discussed below are in line with the primary model. The first theory, proposed by Enßlin et al. (1998), suggests that shock waves could cause the acceleration of relativistic electrons. These shocks are caused by large scale structure formation such as mergers or steady state accretion on to galaxies. They showed that the spectral index and polarisation observed in 1253+275 could have been caused by an accretion shock. This theory was further tested by Roettiger et al. (1999). They studied Abell 3667 and simulated a recent merger event to show that the resulting shocks could be responsible for the observed radio relic. Enßlin and Gopal-Krishna (2001) realised that shocks are present in almost all clusters but radio relics are rare and that, therefore, there must be a second requirement for their formation. They offered an alternative model based on the theory of radio ghosts (Enßlin, 1999).

When the central engine of the AGN in a radio galaxy stops ejecting plasma, the radio galaxy becomes undetectable. However, the plasma, made up of relativistic electrons and magnetic fields, remains present in a cocoon known as a radio ghost. Enßlin and Gopal-Krishna (2001) postulate that these radio ghosts could be revived by the shock waves present in the clusters, providing sufficient relativistic electrons to produce the emission detected. Through calculations they showed that these radio ghosts could be revived up to 2 Gyr after they ‘died’. Studies of galaxy clusters in the X-ray showed cavities in the surface brightness, providing substantial evidence for radio ghosts (Boehringer et al. 1993; Wilson et al. 2000; McNamara et al. 2001; Dunn et al. 2005; Machacek et al. 2011). Hoeft et al. (2004) used N-body simulations to test both these

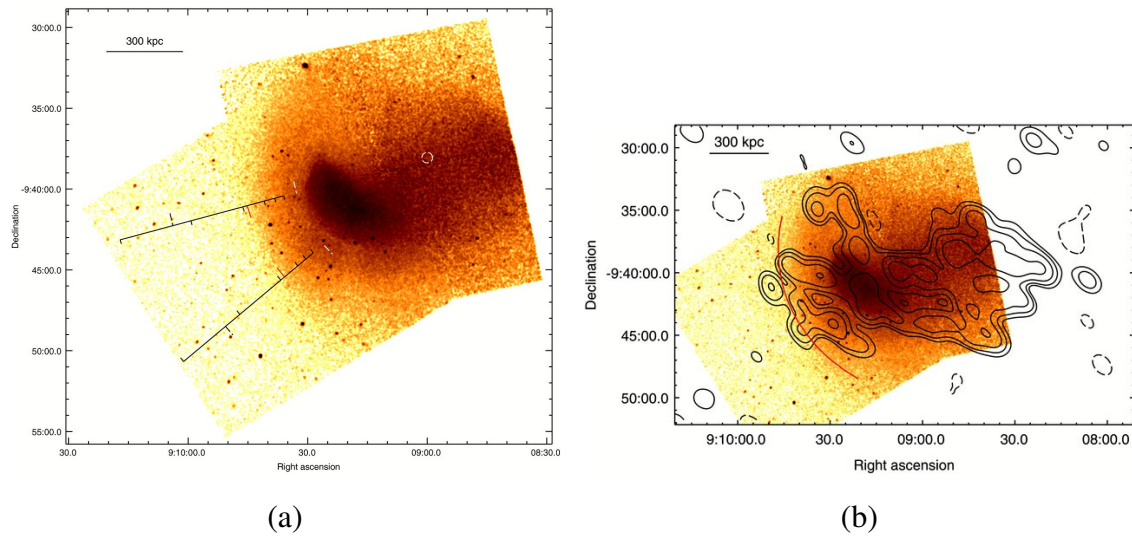


Figure 1.12: In these images taken from Macario et al. (2011) we show the shock detected using Chandra in Abell 754 (a). The radio relic contours as observed with GMRT are overlaid on this shock in (b) showing that it may have been responsible for its formation.

theories and determined that they were both insufficient and that the radio ghosts could only be revived if the thermal pressure is much higher than the magnetic field pressure. This requirement provided an explanation as to the cause of the relics being situated on the outer edges of a cluster. In the centre of the cluster the shock waves are too weak to overcome the magnetic field, but as they move past the cooler outer regions they steepen. Due to the low gas density in the outer regions of these clusters, they have a low X-ray brightness making shocks very hard to detect. Therefore, proving these shocks are the cause of radio relics is difficult. However, some detections near relics have been made either directly (e.g., Solovyeva et al., 2008; Macario et al., 2011; Akamatsu et al., 2012b,a; Akamatsu and Kawahara, 2013) or by identifying density and/or temperature drops (e.g., Markevitch et al., 2002; Krivonos et al., 2003; Markevitch et al., 2005; Finoguenov et al., 2010). Figure 1.12 shows an example of one of these detections in Abell 754 taken from Macario et al. (2011).

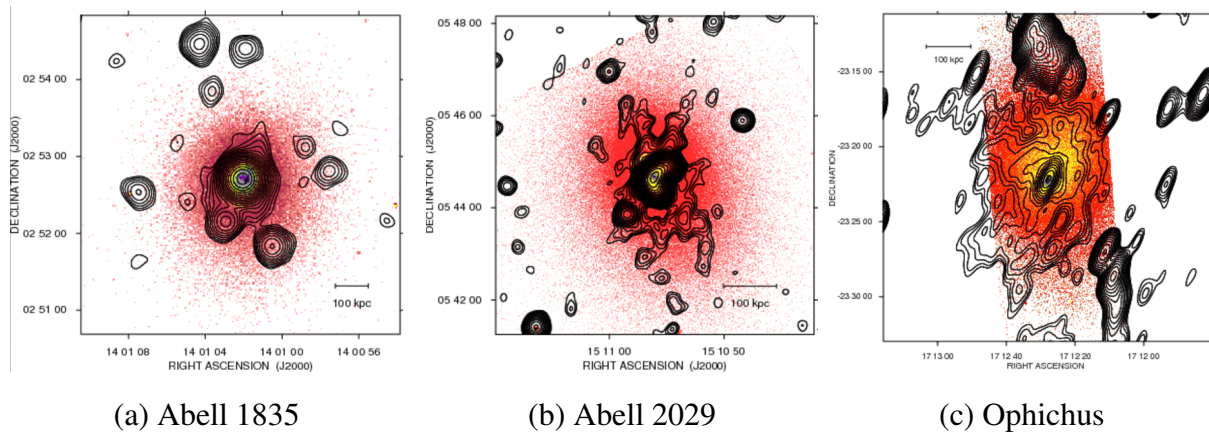


Figure 1.13: In these three images we show the three mini halos detected by Govoni et al. (2009). Each image shows VLA 1.4 GHz radio contours overlaid on the Chandra X-ray image in the 0.5-4 keV band.

1.3.3.4 Mini-halos

Mini-halos are smaller sources (≤ 500 kpc) found in cool core clusters. They are linked to powerful radio galaxies in the centre of the cooling region, have a steep radio spectrum, and a low surface brightness. Govoni et al. (2009) performed VLA observations in search of diffuse emission in relaxed, cool-core clusters and made detections in three clusters: Abell 1835, Abell 2029, and Ophiuchus. In each cluster they found a dominant radio galaxy surrounded by diffuse low-brightness emission (Figure 1.13).

However, mini radio halos have been found in two clusters which may not be relaxed: Abell 2142 and RXJ 1347.5-1145. Abell 2142 has both a massive cooling flow (Peres et al., 1998) and signatures of recent merger events (Markevitch et al., 1998b). However, Markevitch et al. (2000) studied this cluster in more detail and determined that the merger was unequal and had disturbed, but not destroyed, the cooling flow. RXJ 1347.5-1145 is an extremely X-ray luminous galaxy cluster with one of the largest and most prominent cooling flows observed (Gitti and Schindler, 2004). However, the strength of the cooling flow suggests that it has been undisturbed for a long time (1-2 Gyr)(Ferrari et al., 2008). Other minor mergers have been detected in the clusters with mini halos but these are all located outside the cooling region (e.g., Mohr et al., 1996; Ettori

et al., 1998; Furusho et al., 2001; Allen et al., 2001). Due to the small size of these mini halos and the strong emission from the central radio galaxy they are extremely hard to detect. Therefore, identifying their origin and the causes of the different properties seen are still unclear. The link to radio halos, if it exists, is also still not certain.

1.3.3.5 Radio halos

Radio halos are extended (~ 1 Mpc) diffuse radio sources located in the centre of the cluster. Similarly to radio relics, they have a low surface brightness and a steep spectrum. However, unlike relics, they are unpolarised. Radio halos have a regular morphology which seems to coincide with the X-ray emitting thermal gas (Feretti et al., 2012). Since the first detection of a radio halo in the Coma cluster (Section 1.3.3.1) and the increase in more sensitive telescopes, a number of radio halos have been found. A few of the well studied observations are mentioned here.

Diffuse emission in the cluster centre of Abell 665 was first detected by Moffet and Birkinshaw (1989). They were using the VLA to survey the fields of this cluster to search for radio sources which might contaminate observations of the SZ effect and instead found a faint steep spectrum extended source in the centre of the cluster. The detection was verified by Jones and Saunders (1996) who obtained images at 1.4 GHz using the VLA and 151 MHz with the Cambridge Low-Frequency Synthesis telescope. Using the curvature of the radio spectrum and an estimation of the magnetic field, they were able to estimate the age of the halo to be less than 0.12 Gyr. Abell 665 also formed part of the NRAO VLA Sky Survey and was detected by Giovannini et al. (1999). Further observations by Giovannini and Feretti (2000) detected an elongation of the radio halo in the SE-NW direction. They also found that it was asymmetric with the respect to the centre of the cluster and was brighter and more extended towards the NW. X-ray observations show a similar X-ray brightness asymmetry suggesting a link between the radio and X-ray emission. Studies by Markevitch (1996) and Gómez et al. (2000) suggest the cluster is in an ongoing or post-merger state. White et al. (1997), through a X-ray image deprojection analysis

of Einstein Observatory imaging data, found that Abell 665 contained no cooling flow. Recent deep Chandra images taken by Dasadia et al. (2016) detected a strong shock (Mach ~ 3.0) and two cold fronts. They also detected the presence of possible further diffuse emission to the North of the shock which requires further investigation.

Abell 2163 is one of the richest and hottest Abell clusters with a temperature of ~ 15 keV (Arnaud et al., 1992). X-ray studies have shown that the gas distribution in the cluster is non-isothermal and strong temperature variations exist in the central regions suggesting that a recent merger occurred (e.g., Markevitch et al., 1994; Markevitch, 1996; Govoni et al., 2004; Ota et al., 2014). The radio halo was first detected by Herbig et al. (1995) using VLA observations. Feretti et al. (2001) confirmed the detection using VLA observations in various configurations at 20 cm. They also detected a relic in the outer edges of the cluster. Follow-up observations by Feretti et al. (2004) at 90 cm determined that the spectral index was steepening as the distance from the centre increased. Optical analysis of the cluster by Maurogordato et al. (2008) determined a northern component, A2163-B. They suggest that the main cluster has already undergone a merger but that A2163-B is falling into the cluster and soon another merger will occur. Allen (2000) found no cooling flow present which also suggests the cluster is not in a relaxed state. Giovannini et al. (2009) found the size of the radio halo in Abell 2163 to be 2.28 Mpc making it one of the most extended radio halos found.

One of the most well known clusters which hosts a radio halo is 1E 0657-558, also known as the ‘bullet cluster’ (Figure 1.14). It is made up of two colliding clusters of galaxies and provides the best evidence of the presence of dark matter through gravitational lensing studies (Clowe et al. 2004, Markevitch et al. 2004). The radio halo at its centre was first detected by Liang et al. (2000) using the Molonglo Observatory Synthesis Telescope (MOST). The detected radio morphology was similar to the known X-ray morphology. Markevitch et al. (2002) identified a clear shock front propagating in front of a gas cloud exiting the disrupted cluster core of 1E 0657-558. This gas cloud, shaped like a bullet, appears to be the remnants of a cooling flow that was present in the cluster and was disrupted by the merger. Shimwell et al. (2014) performed

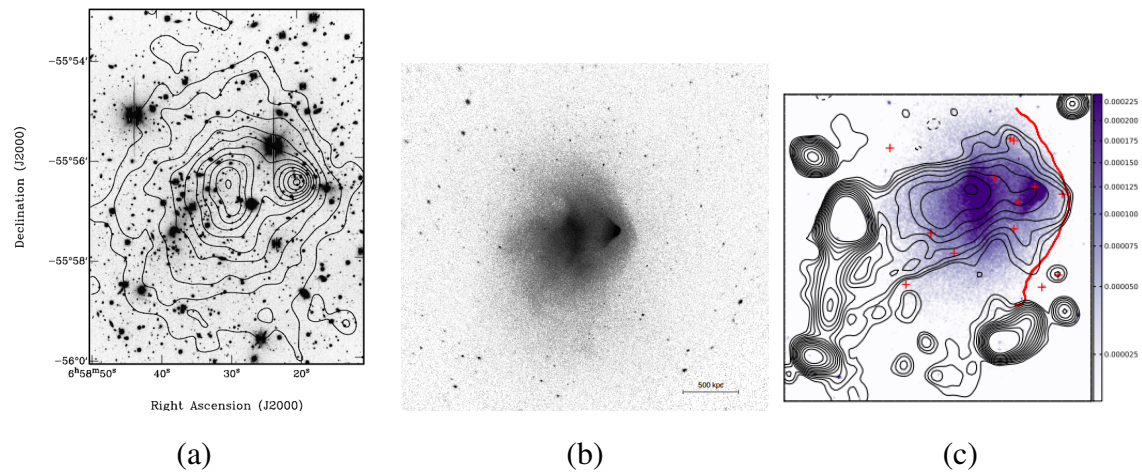


Figure 1.14: Images of the well-known ‘bullet’ cluster, 1E 0657-558. In (a) we show the first detection of the radio halo in this cluster taken from Liang et al. (2000). In (b) we show the bow shock detected in the X-ray (Markevitch, 2006) and how it links to the radio halo in (c). The contours of the radio halo are overlaid on the Chandra X-ray image and the red line shows the position of the shock.

deep radio observations of this cluster using the Australia Telescope Compact Array and found that the western edge of the radio halo lines up with the bow shock. They also found evidence that the radio, like the X-ray, may consist of two components. These observations suggest that shocks and turbulence influence the formation of radio halos.

Just considering these 3 well-known clusters, there appears to be a link between radio halos and galaxy cluster mergers - identified by the presence of X-ray substructure, X-ray temperature gradients or weak (absent) cooling flows. This connection was suggested and discussed in early works on the topic (e.g., Tribble, 1993; Feretti, 1999; Roettiger et al., 1999; Burns et al., 2000; Giovannini and Feretti, 2000; Markevitch and Vikhlinin, 2001) but the first analysis of the dynamical state of clusters was performed by Buote (2001). They studied clusters containing radio halos and found that radio halos only appear in clusters that are experiencing large departures from their virialised state. Cassano et al. (2010) recently confirmed this link using a sample of 67 galaxy clusters taken from the GMRT Radio Halo Survey (Venturi et al. 2007, Venturi et al. 2008). They classified the state of the cluster using three parameters; power ratio, the centroid shift and the X-ray brightness concentration parameter. The power ratio is a dimensionless

measure of substructure in the cluster described in Buote and Tsai (1995) and has been used in previous studies (e.g., Buote and Tsai, 1995; Ventimiglia et al., 2008; Böhringer et al., 2010). The centroid shift, w , is the standard deviation of the projected separation between the peak and the centroid and is a robust measure of plane-of-the-sky structure in the cluster (Poole et al. 2006, Maughan et al. 2008). The X-ray brightness concentration parameter, c , is defined as the ratio of the peak over the ambient surface brightness, S (Santos et al., 2008). This parameter allows for the identification of cool-core clusters by identifying if the gas in the centre of the core is compact (i.e., not disturbed by a recent merger) or has a spread distribution (i.e., core has been disturbed). Clusters with and without radio halos can be clearly differentiated by their dynamical state. Clusters containing a radio halo are normally dynamically disturbed and those without are usually more relaxed. However, there has also been a non-detection of a radio halo in a cluster which is known to be undergoing a merger (Russell et al., 2011) and more recently a radio halo found in a massive cool core cluster (Bonafede et al., 2014). The general trend of the presence of mergers in clusters hosting a radio halo is evidence in favour of the re-acceleration model for their formation.

Cluster mergers cause turbulence throughout the cluster. Electrons are re-accelerated by this turbulence resulting in a transfer of energy from the ICM to the non-thermal emission (Brunetti et al. 2001, Petrosian 2001, Cassano and Brunetti 2005, Xu et al. 2010). This turbulent re-acceleration is linked with random processes and therefore, not extremely efficient. The process is effective for a short time (10^8 years) so it must therefore be linked to ongoing or recent mergers (Feretti et al. 2004, Brown et al. 2011, Enßlin et al. 2011). Further support of this model is found when observing the radio spectra. Feretti et al. (2012) study the link between spectral index and the temperature of the cluster and find that the hotter the cluster, the flatter the spectrum. Hotter clusters are more massive and undergoing more mergers. This results in more re-acceleration of the electrons and more energy being supplied to the non-thermal emission, causing the flatter spectra observed. The rarity of radio halos is also proof of the primary model, since without re-acceleration, the electrons responsible for the diffuse emission will lose their energy via inverse Compton losses and the halo will have a short lifetime (Kuo et al., 2004). In the secondary

model the relativistic electrons, injected into the plasma causing the diffuse emission, are due to collisions between the relativistic protons, accumulated during cluster formation and the ICM. Therefore, they should be present in all clusters. This model also requires that the magnetic field is larger than a few μG , otherwise the steep spectra are not observed (Feretti et al., 2012).

Studies have found that the clusters that host radio halos all have merger activity present but not all merging clusters host radio halos. Cassano et al. (2011) identified 4 such clusters: Abell 141, Abell 781, Abell 2631 and MACS J2228.5+2036. VLA observations at 1400 and 325 MHz by Govoni et al. (2011) later found very low surface brightness diffuse emission in Abell 781, but nothing has yet been detected in the other three. Another well-known merging cluster without a radio halo is Abell 119 (Giovannini and Feretti, 2000). Feretti et al. (2012) and Russell et al. (2011) suggest that there is more to the model of the origin of radio halos than we currently know and suggest that the radio halos may only be present in clusters above a certain mass threshold.

1.3.4 Sunyaev-Zeldovich Effect

The thermal Sunyaev-Zel'dovich (SZ) effect occurs when CMB photons encounter a cluster of galaxies on their path towards us from the last scattering surface (Sunyaev and Zeldovich 1970b; Sunyaev and Zeldovich 1972). The gas within the cluster is hot and ionised and causes inverse Compton scattering of the CMB photons. This causes a boost in their energy resulting in a change of the intensity of the microwave background (see Figure 1.15). Galaxy clusters can, therefore, be detected by searching for this distortion.

The first detections of the SZ effect were completed using a single dish radio telescope at centimetre wavelengths (Gull and Northover 1976; Uson 1986). However, they were unreliable due to their large systematic errors. With advances in technology and the introduction of beam switching techniques, the results improved. The pioneering work of the time was done by Birkinshaw et al. (1978a), Birkinshaw et al. (1978b) and Birkinshaw et al. (1991). They observed known galaxy clusters discovered in the X-ray to determine whether or not the SZ effect

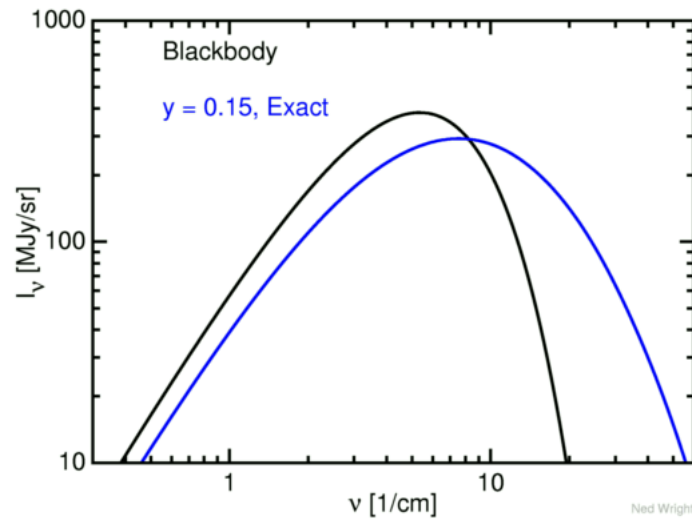


Figure 1.15: In this image, courtesy of Ned Wright⁴, the black line represents the undistorted CMB background while the blue line represents the distorted CMB due to the SZ effect. This effect has been increased by 1000 to make it more easily noticeable.

was real. Further studies by Herbig et al. (1995), Myers et al. (1997), and Mason et al. (2001) produced very reliable results for nearby clusters. The first millimetre measurements of the SZ effect were carried out using a 140 GHz bolometer array for the Sunyaev-Zel'dovich Infrared Experiment (SuZIE). Using a drift scanning technique, described by Holzapfel et al. (1997), this experiment was able to produce high signal-to-noise maps of the SZ emission in several clusters. It was used by Mauskopf et al. (2000) in combination with X-ray results to determine Hubble's constant. These bolometric detectors have very high sensitivity and therefore are excellent in detecting the SZ effect.

Another way to observe the SZ effect is to use interferometers. Due to their stability and good spatial filtering, interferometers provide high-quality images of the SZ effect. Jones et al. (1993) used the Ryle telescope to make the first SZ effect detection using an interferometer. The Ryle telescope consisted of eight 13 m telescopes and was located in Cambridge, England. The Owens Valley Radio Observatory (OVRO) and Berkeley-Illinois-Maryland-Association (BIMA) SZ effect imaging project mounted 30 GHz receivers on the OVRO and BIMA mm-wave arrays

⁴<http://astro.ucla.edu/~wright/SZ-spectrum.html>

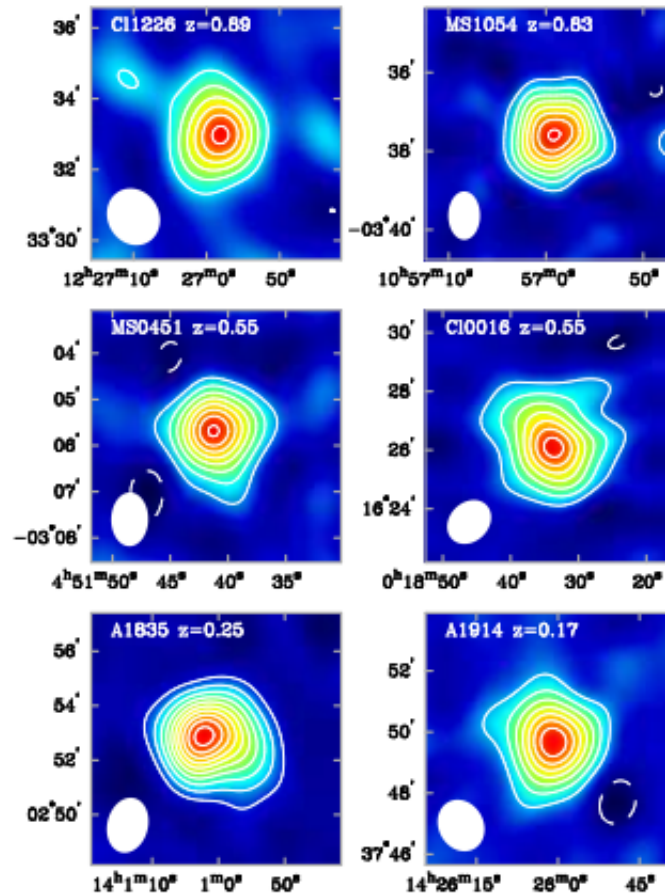


Figure 1.16: In this image, taken from Carlstrom et al. (2002), we show the deconvolved interferometric SZ effect images for a sample of galaxy clusters. These clusters have redshifts varying from 0.17 to 0.89. The contours depict the SZ effect signal and are shown in multiples of 2σ . The clusters are all of similar X-ray luminosity and have similar SZ effect signals despite the wide range of redshifts. This shows the independence of the SZ effect on redshift.

in California. The data from the project was used by many collaborations (Carlstrom et al. 1996; Carlstrom et al. 2000; Patel et al. 2000; Grego et al. 2000; Grego et al. 2001; Reese et al. 2000; Reese et al. 2002; Joy et al. 2001; LaRoque et al. 2002) and has produced SZ images for over 60 clusters, a few of which can be seen in Figure 1.16.

Due to the huge advances in the technology and telescopes, high sensitivity images of large patches of the sky can be obtained to allow for SZ searches of galaxy clusters (e.g., Planck Collaboration et al., 2016b; Bleem et al., 2015; Sifón et al., 2015). This is allowing us to build up a

cluster catalogue which has a well-known selection function (Melin et al., 2005). This catalogue can be used for studies of large-scale structure as well as a probe of cosmology (Carlstrom et al., 2002). SZ signal is not discussed in this thesis but was included for completeness of the subject and for allowance of explanation of future studies.

Table 1.3: Here we summarise the uses, advantages and disadvantages of optical, x-ray and radio studies for detecting galaxy clusters.

Wavelength	Surveys	Advantages	Disadvantages	Uses
Optical	Spectroscopic Imaging	Wide field of view Good depth Large yield	Projection effects Contamination	Redshifts Velocity Dispersions Dynamical Masses
X-ray	Spectroscopic Imaging	Easily identifiable Minimal projection effects Selection criteria quantifiable	Current instruments have a small field of view Few high M clusters at high z	Temperature Luminosity Hydrostatic Mass
Radio	Interferometry Single dish	Can be performed any time Not affected by atmosphere High redshift clusters	Incomplete sample Poor resolution Radio Pollution	Signs of mergers Information about the ICM Dynamical state

1.4 Scaling Relations

The scaling relations of interest to this thesis are simple power law relationships between galaxy cluster properties such as X-ray luminosity, X-ray temperature, mass, and velocity dispersion. The self-similar model described in Section 1.2 can be used to predict these scaling relations. However, studies have found that this self-similar model does not always agree with observational data.

One of the most studied scaling relations is that between the X-ray luminosity and the X-ray temperature ($L_X - T_X$). The self-similar model predicts $L_X \propto T^2$ but it has been found through various studies that this slope is more of the order of $\sim 2.5 - 3$ (e.g., Edge and Stewart, 1991; Markevitch et al., 1998a; Vikhlinin et al., 2002; Maughan et al., 2006; Hilton et al., 2012). The reason for this is thought to be due to the fact that non-gravitational processes are not included in the self-similar model. This would increase the temperature of the clusters relative to their luminosity, specifically the lower mass systems, causing a steepening of the slope to what is seen through observations. Specific examples of this include the addition of cool core clusters, AGN, and merging clusters.

Cool core clusters are formed due to the fact that, in the dense cluster core, thermal energy is radiated as X-ray emission resulting in the gas cooling and condensing. Therefore, these clusters are cooler and brighter than their self-similar predicted counterparts. Since radiative cooling is not included in the self-similar model, it causes a bias in the scaling relation. One way of working around this is to remove the core regions from luminosity and temperature measurements (e.g., Markevitch et al., 1998a; Lumb et al., 2004).

Many cool core clusters also host AGN in the central galaxy, which have jets of relativistic material which interacts with the surrounding X-ray plasma. The exact mechanisms of this process are not understood but it is thought that it might play some part in counteracting the cooling process. However, similarly to the cool core clusters, the energy input from these AGN is not in-

cluded in the self-similar model. Croston et al. (2005) studied the $L_X - T_X$ relation for low mass clusters for a variety of clusters with active and inactive AGN and found that the active AGN were hotter and resulted in a steeper slope than expected (Figure 1.17). This effect is likely to have less of an effect on the higher mass clusters due to their large gravitational energy, resulting in the shallower slope of the $L_X - T_X$ relation.

In the self-similar model one of the main assumptions is that the clusters form in a single collapse but, as discussed in Section 1.2, this is not true because they form in a hierarchical manner. Mergers cause a spike in the temperature and luminosity of the ICM (Ritchie and Thomas, 2002). However, these spikes are short-lived compared to the mass of the newly formed cluster (Rowley et al., 2004). It is hard to make an observational comparison for mergers since these relations hold for clusters in hydrostatic equilibrium and therefore the exact effect is not known.

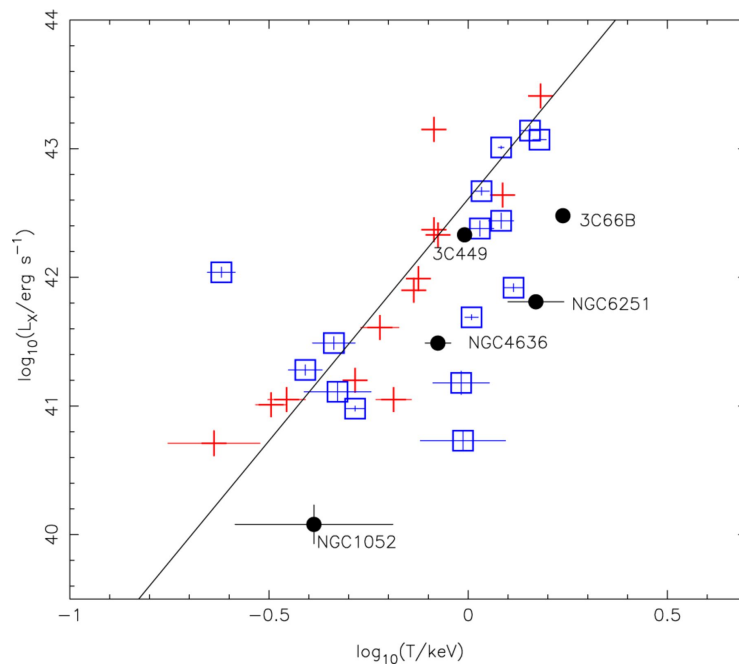


Figure 1.17: Image taken from Croston et al. (2005) to show how active AGN increase the temperature of clusters and cause a steepening of the $L_X - T_X$ relation for low mass clusters. The hollow squares represent the active AGN and the crosses represent the inactive AGN. The black dots represent studies of radio galaxy environments observed with XMM by Croston et al. (2003) and Evans et al. (2005).

Even through these many studies, no consensus has been reached on whether the $L_X - T_X$ relation evolves with redshift. One may expect that the scaling relation would evolve with redshift when one of the variables being studied is the temperature of the cluster. This is due to the increase of star formation and AGN activity at high redshift (e.g., Silverman et al., 2005; Mag-nelli et al., 2009), or due to the increase in frequency of galaxy cluster mergers with increasing redshift (e.g., Cohn and White, 2005; Kay et al., 2007; Mann and Ebeling, 2012). Galaxy cluster mergers are among the most energetic events in the Universe, and simulations have shown that these could result in the boosting of cluster X-ray temperatures (e.g., Ritchie and Thomas, 2002; Randall et al., 2002; Poole et al., 2007). All of these processes add energy into the ICM, and so we might expect to see an overall increase in the average temperatures of galaxy clusters above that expected from the self-similar case at a given redshift.

Self-similarity predicts that the evolution of the normalisation will be of the order $(1 + z)^{1.5}$. Some studies have found results consistent with this prediction (e.g., Vikhlinin et al., 2002; Lumb et al., 2004; Maughan et al., 2006), while other studies have found zero or negative evolution (e.g., Ettori et al., 2004; Branchesi et al., 2007; Hilton et al., 2012; Maughan et al., 2012; Clerc et al., 2012, 2014). The presence of cool core clusters may bias the evolution of this relation since they sit on a higher normalisation $L_X - T_X$ relation (Pratt et al., 2009).

In this thesis, we focus on the lesser studied scaling relation between the velocity dispersion of member galaxies (σ_v) and the X-ray temperature (T_X) of the intracluster medium (ICM). The velocity dispersion of a galaxy cluster is a statistical dispersion of the velocities of the cluster members about the mean velocity of the cluster. The velocity dispersion is a measure of the kinetic energy of the galaxies in the cluster, and the temperature is related to the kinetic energy of the gas, therefore both the gas and galaxies are tracers of the gravitational potential (Quintana and Melnick, 1982; Kaiser, 1986b; Voit, 2005). Since the self-similar model is based on the assumption that only gravitational forces are acting it stands to reason that we can use this model to predict the form of this relation, by applying it to the virial theorem.

If we consider a monatomic gas of temperature T , the average kinetic energy per particle will have the form:

$$\langle KE_i \rangle = \frac{3}{2}kT. \quad (1.10)$$

The total kinetic energy of all N particles will then have the form:

$$KE \propto NkT \propto M_{\text{gas}}kT. \quad (1.11)$$

For self-similar models the mass of the gas M_{gas} is proportional to the total mass of the system, M_{total} , and therefore we get:

$$KE \propto NkT \propto M_{\text{total}}kT. \quad (1.12)$$

If we combine Equation 1.12 with Equation 1.7, for the total gravitational potential energy and substitute into the equation for the virial theorem (Equation 1.4), we get the following:

$$kT \propto \frac{M_{\text{total}}}{R}. \quad (1.13)$$

Substitution of this into Equation 1.8 we can get the expected relationship between the temperature and the velocity dispersion, $\sigma_V \propto T^{0.5}$.

The reason for choosing this relation over the $L_X - T_X$ is due to fewer selection effects. In the $L_X - T_X$ relation the higher luminosity clusters are easier to detect at higher redshift, and therefore it can introduce a bias into the scaling relation. Since the XCS clusters are selected on L_X and $L_X \propto T_X^3$ we might expect that this would cause us to miss the lower temperature clusters at higher redshift compared to lower redshift. However, the calculation of the T_X is not a straightforward process. As shown in Lloyd-Davies et al. (2011), it is easier to measure temperatures for lower temperature clusters as they require fewer counts. So although, we may have selected higher temperature clusters at high redshift compared to at lower redshift values, these higher temperature clusters may not make it into the sample due to insufficient counts for an accurate temperature measurement. Therefore, although some selection effects may be present we do not believe them to play as critical a role as in the $L_X - T_X$ relation. In order to do a complete analysis a full selection function for XCS incorporating these effects is required. However, this has not yet been computed, and so any correction of possible selection effects is deferred to future studies.

The velocity dispersion is also used to calculate the mass of the cluster so that the relationship between the mass and temperature can be studied. By extending the derivation of the $\sigma_v - T_X$ relation we can also the expected relation between the mass and temperature of the cluster.

Starting with Equation 1.13, we can remove the dependence of the radius by expressing it in terms of the mean density of the cluster, $R \propto M_{TOT}^{\frac{1}{3}} \rho^{-\frac{1}{3}}$ and re-arrange to obtain:

$$M_{TOT} \propto (kT)^{\frac{3}{2}} \rho^{-\frac{1}{2}}. \quad (1.14)$$

By definition the mean density of the cluster within radius, R , is $\rho = \Delta\rho = \Delta \frac{3H^2}{8\pi G}$. The Hubble constant, H , is dependent on the redshift of the cluster and can therefore be written as $H = E(z)H_0$ where $E(z) = \sqrt{\Omega_m(1+z)^3 + \Omega_\Lambda}$. Combining this information with Equation

1.15 we get:

$$M_{TOT} \propto (kT)^{\frac{3}{2}} E(z)^{-1}. \quad (1.15)$$

Accurate understanding of these scaling relations will help us to determine if they are evolving with redshift, which will ultimately help to constrain cosmological parameters and provide a better understanding of our Universe.

1.5 Cluster Cosmology

Although the concept of the Big Bang Theory has been the accepted model of the origin of the Universe for a long time, the parameters in the model were only recently measured with any degree of certainty and consistency. Some of these parameters are the density of matter, its equation of state, and a curvature parameter to describe the geometry of the Universe.

Since galaxy clusters are the largest gravitationally bound objects in the Universe it is reasonable to assume that by studying them we may learn valuable information regarding the Universe's formation and evolution. Galaxy cluster surveys have been shown to be particularly good at constraining two very important cosmological parameters, σ_8 and Ω_m (Vikhlinin et al., 2009). σ_8 refers to the RMS dispersion of the mass field after the application of smoothing on a scale of $8 h^{-1}$ Mpc, while Ω_m is the mean mass density of the present Universe. These parameters are constrained by studying the evolution of the number density of these galaxy clusters, above a given mass, with redshift. This data could also allow us to constrain Ω_w , the energy density component of dark energy and the equation of state. Combining this data with information gathered from CMB studies and observations of Type Ia supernovae can only improve these constraints (Allen et al., 2011). There are three important things to consider when using galaxy clusters as

a means of constraining cosmological parameters: the selection function of the survey, cluster scaling relations, and the dispersion in the mass function. All of these contribute to predicting the cluster numbers as a function of redshift and temperature and allow for the studying of their evolution (Sahlén et al., 2009).

Recent studies in the optical and X-ray bands have proved their power for constraining cosmological parameters. Vikhlinin et al. (2009) observed a large sample of X-ray selected clusters with Chandra and was able to determine a new robust cluster mass function at both high and low redshift. The evolution of this mass function was then used to constrain the dark energy equation of state parameter to a value of $w_0 = -1.14 \pm 0.21$. Combining their data with CMB anisotropy studies, baryonic acoustic oscillation measurements, and supernovae data they further constrained this value to $w_0 = -0.991 \pm 0.005$. Similar studies were conducted by Rozo et al. (2009), Mantz et al. (2010b) and Rozo et al. (2010).

A newer technique involves exploiting the SZ effect to detect galaxy clusters and constrain cluster cosmology. Since the SZ signal is not diminished by the luminosity distance of the cluster, it is nearly redshift independent allowing us to probe the high redshift population (Kitayama, 2014). The SZ signal is also proportional to the thermal energy of the ICM and can therefore be used to estimate the total cluster mass (Amodeo et al., 2017). Numerical simulations done by Kravtsov et al. (2006), for example, show a tight correlation between the Compton signal, Y , and the mass. This allows us to extend the current samples obtained via optical and X-ray studies. Studies with SZ were conducted with various instruments including the South Pole Telescope (SPT; Vanderlinde et al., 2010); the Atacama Cosmology Telescope (ACT; Sehgal et al., 2011), and the Planck satellite (Planck Collaboration et al., 2015).

With the increase of large surveys of galaxy clusters, we are gaining vast amounts of knowledge and improving our understanding of the Universe, its origin, and its evolution. This thesis serves as a small component of that increasing knowledge.

1.6 Thesis Outline

In this thesis we study a sample of 38 galaxy clusters drawn from the *XMM* Cluster Survey. We study two important scaling relations, namely the velocity dispersion–temperature ($\sigma_v - T_X$) and mass–temperature ($M_{\text{dyn}}-T$) relations. We also study the evolution of the $\sigma_v - T_X$ relation. We make comparisons to previous studies and give examples of improvements we offer. We consider what information can be gained from studying galaxy clusters in the radio wavelength and discuss what effect it may have on our scaling relations.

This thesis comprises six chapters. The layout of each is summarised below:

- Chapter 2: In this chapter, we describe our sample chosen for this study. We look at galaxy cluster member classification and the calculation of the redshift of each cluster.
- Chapter 3: This chapter presents the velocity dispersion–temperature relation. We show the method used to calculate the velocity dispersion and discuss the Markov Chain Monte-Carlo (MCMC) analysis that was used provide a fit for our data. We make comparisons to previous studies and simulations of the $\sigma_v - T_X$. We also study the evolution of this relation.
- Chapter 4: Here we present the mass–temperature scaling relation determined using our sample of galaxy clusters and the same MCMC analysis used in Chapter 3. We make comparisons to previous studies and compare X-ray and dynamical masses. We also look at mass ratios and discuss the hydrostatic mass bias.
- Chapter 5: We discuss radio observations of clusters in this chapter. We discuss the background of radio halos and their possibility of being linked to mergers of galaxy clusters. We also present new VLA observations of 3 galaxy clusters from our sample.
- Chapter 6: This chapter includes a conclusion to this thesis and possible future work.

We assume a cosmology with $\Omega_m = 0.27$, $\Omega_\Lambda = 0.73$, and $H_0 = 70 \text{ km s}^{-1} \text{ Mpc}^{-1}$ throughout.

CHAPTER 2

OPTICAL OBSERVATIONS AND THE CLUSTER SAMPLE

For this thesis, the velocity dispersion and mass of a sample of clusters will be calculated and the relation between these properties and temperature will be studied. In order to determine the velocity dispersion of a cluster the cluster members and their redshifts are required. Therefore, in this chapter, we discuss cluster membership and obtain a sample of 38 clusters, broken up into two samples - a low redshift sample and a high redshift sample.

2.1 Origin of the sample

The cluster sample for this work is drawn from the XMM Cluster Survey (XCS), a serendipitous X-ray cluster survey being conducted using archival *XMM-Newton* data. Data Release 1 (DR1) of the XCS is described in Mehtens et al. (2012). The overall aims of the XCS project are to measure cosmological parameters through the evolution of the cluster mass function with redshift (Sahlén et al., 2009), study the evolution of galaxies in clusters (Collins et al., 2009; Hilton et al., 2009, 2010; Stott et al., 2010), and investigate the X-ray scaling relations as a way to study

the evolution of the cluster gas with redshift (Hilton et al., 2012).

The XCS Automated Pipeline Algorithm (XAPA) described in Lloyd-Davies et al. (2011) was used to search the XMM archive for cluster candidates. Mehrrens et al. (2012) describes confirmation of a subset of these candidates as clusters using the combination of data from the literature and optical follow-up observations. This left a final sample of 503 X-ray-confirmed galaxy clusters, 255 which were previously unknown and 356 of which were new X-ray detections. Of these, 464 have redshift estimates, and 402 have temperature measurements.

For XCS-DR1 the cluster-averaged X-ray temperatures (T_X) were measured using an automated pipeline described in detail in Lloyd-Davies et al. (2011). In summary this pipeline operates as follows. First, spectra were generated in the 0.3 – 7.9 keV band using photons in the XAPA source ellipse, which corresponds to 0.08 – 0.56 of R_{500} , with a median value of 0.36 R_{500} . R_{500} is calculated using Equation 2 and Table 2 from Arnaud et al. (2005)). An in-field background subtraction method was used before fitting a model. Finally, the model fitting was carried out using the XSPEC software (Schafer, 1991), using an absorbed MEKAL model (Mewe and Schrijver, 1986) and Cash statistics (Cash, 1979). In the fit, the hydrogen column density was fixed to the Dickey (1990) value and the metal abundance to 0.3 times the Solar value.

For this thesis, we have updated the T_X values compared to Mehrrens et al. (2012). The pipeline is very similar to that described in Lloyd-Davies et al. (2011), but using updated versions of the XMM calibration and XSPEC. The median X-ray count for all the clusters in our final sample was 1919 with a minimum count of 220. We note that the X-ray counts used for the spectral analysis are less than 300 for only one of the clusters in our sample. This is the minimum threshold defined by Lloyd-Davies et al. (2011) for reliable, i.e., with a fractional error of < 0.4 , T_X measurements at $T_X > 5$ keV (see Figure 16 from Lloyd-Davies et al. 2011). This low-count cluster was fit using 220 counts, however it still has an expected fractional error of ~ 0.4 due to its temperature value of 3.5 keV.

The low and high redshift samples required were both constructed from XCS DR1, except for XMMXCSJ113602.9-032943.2. This cluster, which belongs to our high redshift sample, is a previously unreported XCS detection. The method used to determine our sample is described in schematic form in Figure 2.1.

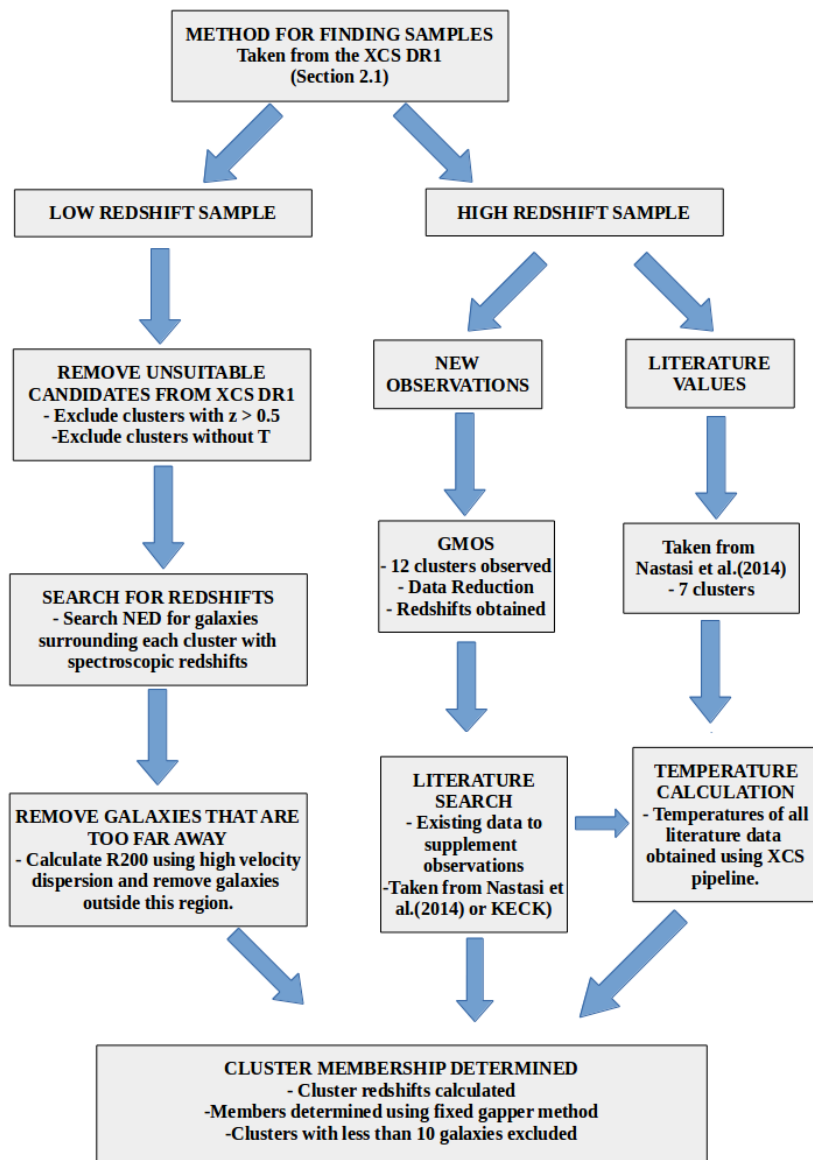


Figure 2.1: Schematic showing how the sample used in the analysis of this thesis is selected.

2.2 Low redshift sample

The low redshift sample contains 19 clusters whose properties can be found in Table 2.3. In order to obtain this sample we used the following steps:

Step 1: All clusters from the DR1 sample that did not have temperatures or which had a redshift $z > 0.5$ were excluded, leaving us with a sample of 320 clusters.

Step 2: We performed a search in NED¹ for galaxies surrounding each cluster. We included only clusters which had spectroscopic redshifts, resulting in our sample size being decreased from 320 to 296. Since NED collects data from many different sources the reliability of the redshifts can not be guaranteed. Hence, where possible we use only one source of redshifts per cluster to ensure homogeneity. These redshifts are specified to the 4th decimal place but unfortunately for most an uncertainty is not included in the original sample and we therefore assumed an accuracy of 1%. This corresponds to an error in peculiar velocity between $3 \times 10^5 \text{ m.s}^{-1}$ and $1.5 \times 10^6 \text{ m.s}^{-1}$ depending on the redshift.

Step 3: We excluded galaxies located at a projected radial distance greater than R_{200} (the radius within which the mean density is 200 times the critical density of the Universe at the cluster redshift) as such galaxies are unlikely to be cluster members. R_{200} was calculated using,

$$R_{200} \text{ (Mpc)} = 2.47 \frac{\sigma_v}{1000 \text{ km s}^{-1}} \frac{1}{\sqrt{\Omega_\Lambda + \Omega_0(1+z)^3}}. \quad (2.1)$$

Here σ_v is the line of sight velocity dispersion (see Section 1.4 with the calculation discussed in Section 3.2) and z is the redshift of the cluster. To ensure we did not exclude possible members,

¹This research has made use of the NASA/IPAC Extragalactic Database (NED) which is operated by the Jet Propulsion Laboratory, California Institute of Technology, under contract with the National Aeronautics and Space Administration.

for this initial step R_{200} was calculated using a fiducial velocity dispersion of 2000 km s^{-1} following Finn et al. (2005). Equation 2.1 assumes that the galaxy velocity distribution follows an isothermal sphere dark matter profile. The fiducial R_{200} values span the range 2–4 Mpc.

Step 4: The final cluster members are chosen using the process discussed in Section 2.4.

2.3 High redshift sample

The high redshift sample is made up of 19 clusters whose properties can be found in Table 2.4. This sample is composed of data taken from new observations and previous literature studies.

2.3.1 Clusters from literature

Seven clusters in our sample used data obtained from Nastasi et al. (2014), who drew on both new observations and on existing data. Three of the Nastasi et al. (2014) clusters that form part of our sample were previously observed. XMMXCS J105659.5-033728.0 also known as MS1054-03 was observed with Keck for 8.6 hours (Tran et al., 1999). XMMXCS J114023.0+660819.0 was observed with Keck (Donahue et al., 1999). XMMXCS J182132.9+682755.0 also known as RXJ1821.6+6827 was observed with CFHT, Keck and the 2.2 m telescope at the University of Hawaii (Gioia et al., 2004).

The observations of the other four clusters were presented for the first time in Nastasi et al. (2014). These four were discovered independently (to XCS) by the XMM Newton Distant Cluster Project (XDCCP; Fassbender et al., 2011) and were observed with the VLT–FORIS2 spectrograph. Nastasi et al. (2014) also presented galaxy redshift data for another six XDCCP clusters, however we have not used those in this thesis because there are insufficient galaxies to derive an accurate velocity dispersion².

²The methodology described in Section 2.4 was applied to these six clusters before they were excluded.

For all seven of the included clusters from Nastasi et al. (2014), new temperatures were obtained using XCS pipelines. The Nastasi et al. (2014) cluster redshifts were used to confirm membership using the process discussed in Section 2.4.

2.3.2 New observations

Galaxy clusters from XCS with $z > 0.5$ and temperatures measured with 300 counts were chosen for spectroscopic follow-up. Observations of 12 of these clusters were obtained using the Gemini Multi Object Spectrographs (GMOS) on both the *Gemini* telescopes from 2010 to 2012.

2.3.2.1 Observations

The nod-and-shuffle mode (Glazebrook and Bland-Hawthorn, 2001) was used to allow better sky subtraction and shorter slit lengths when compared to conventional techniques. For all observations the R400 grating and OG515 order blocking filter were used, giving wavelength coverage of 5400 – 9700 Å. The GMOS field of view samples out to R_{200} at the redshifts of our sample Sifón et al. (2013). A total of 30 masks were observed with a varying number of target slitlets. Each slitlet had length 3'' and width 1''. Target galaxies were selected to be fainter than the brightest cluster galaxy (which was also targeted in the slit masks), on the basis of *i*-band pre-imaging obtained from *Gemini*. We also used colour or photo-*z* information, where available, to maximise our efficiency in targeting cluster members. For five clusters which had *r*, *z*-band photometry from the National Optical Astronomy Observatory–XMM Cluster Survey (NXS; described in Mehrrens et al., 2012), we preferentially selected galaxies with *r* – *z* colours expected for passively evolving galaxies at the cluster redshift (see Mehrrens et al., 2012, for details). For four clusters, we used photometric redshifts for galaxies from SDSS DR7 (Abazajian et al., 2009). For XMMXCS J113602.9-032943.2, we used galaxy photo-*z*'s that were measured from our own *riz* photometry obtained at the William Herschel Telescope (WHT) on May 5, 2011.

Observations at three different central wavelengths (7500, 7550 and 7600 Å) were used to obtain coverage over the gaps between the GMOS CCDs. For all observations, an 85 percentile image quality and 50 percentile sky transparency were requested. The details of the individual observations are given in Table 2.1.

2.3.2.2 Spectroscopic data reduction

The data were reduced in a similar manner to Hilton et al. (2010), using PYRAF and the *Gemini* IRAF³ package. We used the tools from this package to subtract bias frames, make flat fields, apply flat field corrections, and create mosaic images. We then applied nod-and-shuffle sky subtraction using the `gnsskysub` task. Wavelength calibration was determined from arc frames taken between the science frames, using standard IRAF tasks. All data were then combined using a median, rejecting bad pixels using a mask constructed from the nod-and-shuffle dark frames. Finally, we combined the pairs of spectra corresponding to each nod position, and extracted one-dimensional spectra using a simple boxcar algorithm.

³IRAF is distributed by the National Optical Astronomy Observatories, which are operated by the Association of Universities for Research in Astronomy, Inc., under cooperative agreement with the National Science Foundation.

Table 2.1: Spectroscopic observations log. For all observations the R400 grating and the OG515 filter was used.

Cluster Name	Mask	Slits	Airmass Range	Observation Date	Frames (s)	Seeing (//)
XMMXCS J005656.6-274031.9	GS2012B-Q-011-03	33	1.22	2012-10-19	1 x 1830	
"	"		1.48 - 1.76	2012-10-16	2 x 1830	
"	"		1.01 - 1.04	2012-10-15	3 x 1830	0.76 - 0.80
"	GS2012B-Q-011-04	35	1.05 - 1.35	2012-11-14	4 x 1830	
XMMXCS J015241.1-133855.9	GS2011B-Q-050-01	33	1.05 - 1.21	2011-12-02	6 x 1830	
"	GS2011B-Q-050-02	34	1.05 - 1.65	2011-12-03	6 x 1830	
XMMXCS J021734.7-051326.9	GS2012B-Q-011-06	34	1.14 - 1.48	2012-12-05	4 x 1830	
XMMXCS J025006.4-310400.8	GS2012B-Q-011-09	32	1.11 - 1.20	2012-11-24	2 x 1830	
"	"		1.01 - 1.19	2012-11-21	4 x 1830	
"	GS2010B-Q-046-06	35	1.06 - 1.12	2010-11-14	2 x 1830	0.50 - 0.60
"	"		1.06 - 1.44	2010-11-13	5 x 1830, 1 x 762	1
XMMXCS J030205.1-000003.6	GS2011B-Q-050-03	32	1.17	2011-12-01	1 x 1830	
"	"		1.18	2011-11-20	1 x 1098	
"	"		1.17 - 1.45	2011-11-18	4 x 1830	
"	GS2011B-Q-050-04	32	1.32	2011-12-31	1 x 1098	
"	"		1.23 - 1.74	2011-12-30	4 x 1830	0.85 - 1.40
"	GS2011B-Q-050-05	33	1.27 - 1.57	2012-01-17	2 x 1830	0.7
XMMXCS J095940.7+023113.4	GS2010B-Q-046-02	35	1.19 - 1.23	2011-01-09	3 x 1830	
"	"		1.19 - 1.25	2011-01-08	4 x 1830	
"	GS-2012A-Q-46-01	35	1.19 - 1.29	2012-03-18	4 x 1830	

Continued on next page

Table 2.1 – continued from previous page

Cluster Name	Mask	Slits	Airmass Range	Observation Date	Frames (s)	Seeing (//)
"	"		1.19 – 1.23	2012-03-02	2 x 1830	
"	GS-2012A-Q-46-02	34	1.20 – 1.35	2012-03-27	3 x 1830	
"	"		1.23 – 1.46	2012-03-23	3 x 1830	0.8
"	GS-2012A-Q-46-03	34	1.21 – 1.54	2012-03-22	6 x 1830	0.65 – 0.70
XMMXCS J112349.3+052956.8	GS-2012A-Q-46-05	33	1.23 – 1.33	2012-04-22	5 x 1830	
"	"		1.47	2012-04-21	1 x 1830	
"	GS-2012A-Q-46-06	32	1.25 – 1.65	2012-05-15	4 x 1830	0.63 – 0.76
"	"		1.45 – 1.66	2012-04-22	2 x 1830	
"	GS2010B-Q-046-03	33	1.26	2011-01-31	1 x 1830	
"	"		1.35 – 1.64	2011-01-29	2 x 1525, 1 x 975	
"	"		1.23 – 1.24	2011-01-27	2 x 1830	
XMMXCS J113602.9-032943.2	GS-2012A-Q-46-07	36	1.14	2012-05-24	1 x 1830	
"	"		1.12	2012-05-23	1 x 1830	
"	"		1.12 – 1.16	2012-05-20	3 x 1830	
"	"		1.12	2012-05-19	1 x 1830	
"	GS-2012A-Q-46-08	33	1.48 – 1.76	2012-07-15	2 x 1830	
"	"		1.41 – 1.80	2012-07-11	3 x 1830	0.50 – 0.70
"	"		1.5	2012-07-10	1 x 1830	
XMMXCS J134305.1-000056.8	GS-2012A-Q-46-10	36	1.16 – 1.23	2012-05-24	4 x 1830	
"	"		1.24	2012-05-21	1 x 1830	
"	GS-2012A-Q-46-11	34	1.25	2012-07-10	1 x 1830	
"	"		1.16 – 1.19	2012-07-09	2 x 1830	
"	"		1.2	2012-07-06	1 x 1830	
"	"		1.54 – 1.84	2012-06-22	2 x 1830	
XMMXCS J145009.3+090428.8	GN2012A-Q-070-05	32	1.02 – 1.05	2012-07-09	2 x 1800	1.15

Continued on next page

Table 2.1 – continued from previous page

Cluster Name	Mask	Slits	Airmass Range	Observation Date	Frames (s)	Seeing (//)
"	"		1.11 – 1.62	2012-06-26	4 x 1800	0.84 – 0.98
"	GN2012A-Q-070-06	34	1.02 – 1.04	2012-07-07	2 x 1800	
"	"		1.09 – 1.17	2012-07-06	2 x 1800	
"	"		1.48 – 1.79	2012-06-27	2 x 1800	
"	GN2012A-Q-070-07	33	1.22 – 1.59	2012-07-22	3 x 1800	
"	"		1.04 – 1.16	2012-07-08	3 x 1800	1
XMMXCS J215221.0-273022.6	GS2010B-Q-046-04	36	1.14 – 1.24	2010-11-12	2 x 1830	
"	"		1.02 – 1.21	2010-09-14	4 x 1830	
"	GS2011B-Q-050-06	34	1.07 – 1.15	2011-10-05	2 x 1830	
"	"		1.12 – 1.56	2011-09-18	4 x 1830	0.60 – 1.00
"	GS2011B-Q-050-07	34	1.00 – 1.10	2011-10-24	4 x 1830	
"	"		1.05 – 1.12	2011-10-16	2 x 1830	
XMMXCS J230247.7+084355.9	GN2012A-Q-070-10	34	1.37	2012-08-08	1 x 1800	0.60 – 0.68
"	"		1.02 – 1.11	2012-07-30	5 x 1800	0.43 – 0.86
"	GN2012A-Q-070-11	33	1.18 – 1.31	2012-08-13	2 x 1800	
"	"		1.02 – 1.08	2012-08-09	3x1800	0.60 – 0.68
"	"		1.19	2012-08-08	1 x 1800	1

2.3.2.3 Galaxy redshift measurements

We measured galaxy redshifts from the spectra by cross-correlation with SDSS spectral templates⁴ using the RVSAO/XCSAO package for IRAF (Kurtz and Mink, 1998). XCSAO implements the method described by Tonry and Davis (1979). The spectra were compared to six different templates over varying redshifts with the final redshift measurement being determined after visual inspection. Redshifts were assigned a quality flag according to the following scheme: $Q = 3$ corresponds to two or more strongly detected features; $Q = 2$ refers to one strongly detected or two weakly detected features; $Q = 1$ indicates one weakly detected feature; and $Q = 0$ applies when no features could be identified.

The features used were spectral lines, with the most commonly identified being [OII] 3727 Å, H, K, H β , and the [OIII] 4959, 5007 Å lines. Only galaxies with a quality rating of $Q \geq 2$ were used in this study because these have reasonably secure redshifts. Fig.2.2 shows spectra of some member galaxies of the cluster XMMXCS J025006.4-310400.8 as an example. Tables of redshifts for galaxies in each cluster field as well as histograms depicting the included/excluded members and the best-fit Gaussian can be found in Appendix A. Table 2.2, found at the end of this chapter, lists the galaxy redshifts for cluster XMMXCS J025006.4-310400.8, and is shown in Figure 2.2 as an example.

2.4 Membership determination

In this section we describe the methodology used to determine cluster membership based on the redshifts of the galaxies in the cluster and take a look at our final samples. This method is based on the code developed for use in Kirk et al. (2015).

⁴<http://www.sdss.org/dr7/algorithms/spectemplates/index.html>

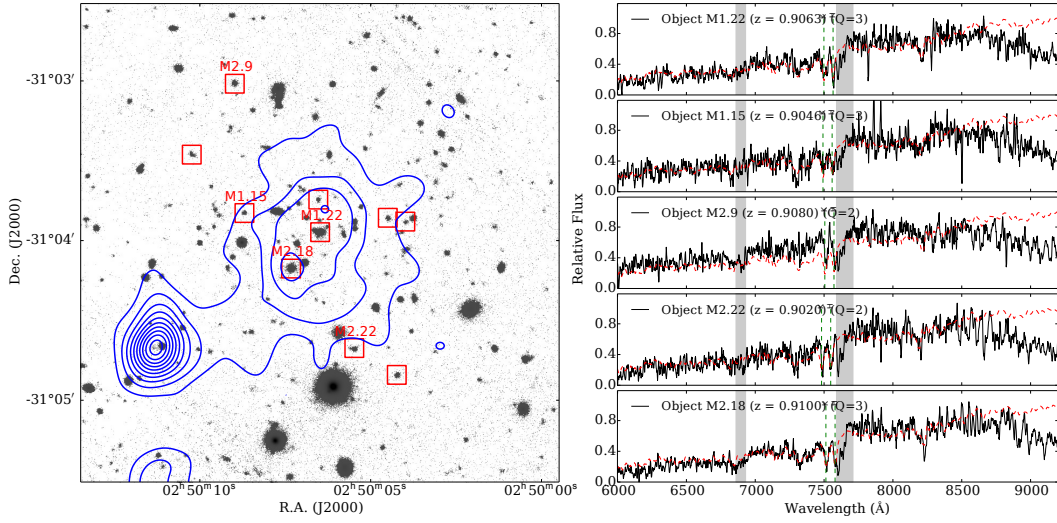


Figure 2.2: The $z=0.91$ cluster XMMXCS J025006.4 – 310400.8. The left hand panel shows the *Gemini* *i*-band image overlaid with the X-ray contours in blue. The red squares represent possible galaxy cluster members. Each possible member is labelled Mx.y, where x is the mask number and y is the object ID. The right hand panel shows the *Gemini* spectra (black lines) for a subset of these galaxies. The grey bands indicate regions affected by telluric absorption lines. The red line is the best fit SDSS template. The green dotted vertical lines show the positions of the H and K lines at the galaxy redshift.

2.4.1 Cluster redshifts

For all of the clusters an estimate of the redshift is known either from the literature or from previous observations and this is used as a starting point. The peculiar velocity of each of the galaxies is calculated relative to this redshift estimate using

$$v_i = c \times \frac{z_i - \bar{z}}{1 + \bar{z}}, \quad (2.2)$$

where v_i is the peculiar velocity of the i th galaxy, z_i is the redshift of the i th galaxy, \bar{z} is the redshift of the cluster, and c is the speed of light. Extreme foreground and background sources were removed by applying a 3000 km s^{-1} cut with respect to the cluster redshift and then the redshift was recalculated using the biweight location method described by Beers et al. (1990). This process was iterated until the redshift converged. The redshift errors were then calculated via

bootstrap resampling. Bootstrapping is a statistical technique in which we do random sampling with replacement and calculate confidence intervals on our samples.

2.4.2 Cluster membership

A fixed gapper method, similar to that of Fadda et al. (1996) and Crawford et al. (2014), was applied to determine which galaxies are cluster members. The reasoning behind this method is that by studying a histogram of the redshifts of possible members there should be a clear distinction between the cluster and the fore/background galaxies. Therefore, we can exclude interlopers by finding the velocity difference between adjacent galaxies and setting a fixed gap that should not be exceeded. De Propriis et al. (2002) found this optimum gap to be 1000 km s^{-1} , which avoids the merging of subclusters but also prevents the breaking up of real systems into smaller groups. The peculiar velocity for each galaxy was calculated relative to the cluster redshift, assuming they are cluster members using Equation 2.2. The galaxies were then sorted by peculiar velocity and the difference between all adjacent pairs was calculated. Any galaxies which had a difference between adjacent galaxies of greater than 1000 km s^{-1} were considered interlopers and were removed. This process was iterated until the number of galaxies converged. Redshift histograms with overlaid Gaussians for each cluster are given in Appendix A. These plots show that all of our clusters are virialised and suggest no evidence of substructure. Sifón et al. (2015) found that if you probe out to a reasonable fraction of R_{200} when determining velocity dispersions, then your mass calculations will not be biased by the spatial distribution of the clusters. Combining our plots with these findings allows us to proceed with confidence with our mass calculations.

2.4.3 Final samples

Once the final members had been determined for each cluster, all clusters which had less than 10 galaxies were excluded. Beers et al. (1990) tested a variety of velocity dispersion estimators on three sample sizes, tiny ($N=5$), medium ($N=10$) and intermediate ($20 < N < 50$). They found

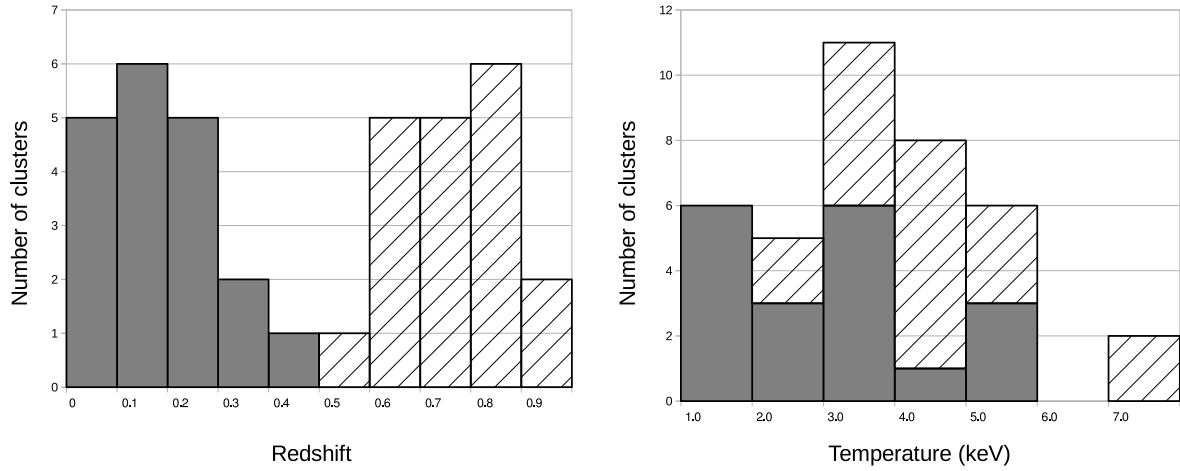


Figure 2.3: The redshift and temperature distributions of the low and high redshift cluster samples used in this work. The solid grey marks the low redshift sample ($z < 0.5$) and the diagonally shaded region marks the high redshift sample ($z > 0.5$). Note that the high redshift sample ($T_{\text{median}} = 4.5$ keV) contains more high temperature clusters than the low redshift sample ($T_{\text{median}} = 3.0$ keV).

that for tiny sample sizes the bi-weight estimator could not be used but for the medium and intermediate samples it produced the best results. Therefore, clusters with 10 or more galaxies will be sufficient for accurate velocity dispersion calculations. This cut resulted in both the low and high redshift samples each containing 19 clusters.

Fig. 2.3 shows the redshift and temperature distributions of the two samples. The high redshift sample contains more high temperature clusters than the low redshift sample, which may be due to selection effects which result in higher luminosity, and hence higher temperature clusters, being chosen at higher redshift. The effect of this on our fitting will be discussed in Section ??.

In Tables 2.3 and 2.4, found at the end of this chapter, we give the calculated redshifts of each cluster and compare them to literature values. We also include the total number of galaxies determined to be members of each cluster.

2.5 Conclusion

In this chapter we introduced the samples used in our studies. We chose a set of two samples, both of which were taken from the XCS DR1, split by redshift. For the low redshift sample ($z < 0.5$) we used NED to determine redshifts for galaxies surrounding our clusters. The high redshift sample ($z > 0.5$) used spectroscopic results taken with the *Gemini* telescopes to identify redshifts. A fixed gapper method was applied to both these samples to determine which galaxies belonged to each cluster and to obtain a final redshift of each cluster.

Table 2.2: We depict the galaxy redshifts for the cluster XMMXCS J025006.4-310400.8. Column 1 gives an arbitrary ID for each galaxy, columns 2 and 3 give the right ascension and declination respectively, and column 4 gives the redshift of the galaxy. Column 5 gives the quality flag as explained in Section 2.3.2.3 and column 6 shows whether or not the galaxy was included as a member for the determination of the velocity dispersion.

ID	Mask	RA(J2000)	Dec(J2000)	z	Quality	Member
1	GS-2010B-Q-46-06	02 ^h 50 ^m 22.92 ^s	-31°03'53.0"	0.8337	3	
8	GS-2010B-Q-46-06	02 ^h 50 ^m 15.25 ^s	-31°03'33.5"	0.7263	3	
9	GS-2010B-Q-46-06	02 ^h 50 ^m 13.27 ^s	-31°03'35.7"	0.6168	3	
10	GS-2010B-Q-46-06	02 ^h 50 ^m 12.05 ^s	-31°03'08.0"	0.7146	3	
14	GS-2010B-Q-46-06	02 ^h 50 ^m 06.63 ^s	-31°03'13.7"	0.8496	3	
15	GS-2010B-Q-46-06	02 ^h 50 ^m 08.70 ^s	-31°03'49.7"	0.9052	3	✓
16	GS-2010B-Q-46-06	02 ^h 50 ^m 03.78 ^s	-31°03'51.5"	0.3533	3	
17	GS-2010B-Q-46-06	02 ^h 50 ^m 06.89 ^s	-31°03'51.5"	0.9217	3	✓
18	GS-2010B-Q-46-06	02 ^h 50 ^m 05.48 ^s	-31°03'53.0"	0.6972	3	
19	GS-2010B-Q-46-06	02 ^h 50 ^m 04.50 ^s	-31°03'51.5"	0.9149	3	✓
21	GS-2010B-Q-46-06	02 ^h 50 ^m 02.79 ^s	-31°04'04.9"	0.9831	3	
22	GS-2010B-Q-46-06	02 ^h 50 ^m 06.48 ^s	-31°03'56.9"	0.9069	3	✓
23	GS-2010B-Q-46-06	02 ^h 50 ^m 09.04 ^s	-31°04'06.3"	0.7567	3	
25	GS-2010B-Q-46-06	02 ^h 50 ^m 03.83 ^s	-31°04'34.0"	0.8988	3	✓
26	GS-2010B-Q-46-06	02 ^h 50 ^m 04.24 ^s	-31°04'50.6"	0.9095	3	✓
28	GS-2010B-Q-46-06	02 ^h 50 ^m 04.59 ^s	-31°05'41.7"	0.6197	3	
34	GS-2010B-Q-46-06	02 ^h 50 ^m 04.26 ^s	-31°07'05.2"	0.1261	3	
1	GS-2012B-Q-011-09	02 ^h 50 ^m 22.92 ^s	-31°03'53.0"	0.5924	2	
2	GS-2012B-Q-011-09	02 ^h 50 ^m 18.11 ^s	-31°03'10.5"	0.9326	2	
4	GS-2012B-Q-011-09	02 ^h 50 ^m 16.05 ^s	-31°03'23.1"	1.0077	2	
5	GS-2012B-Q-011-09	02 ^h 50 ^m 14.89 ^s	-31°03'32.1"	0.7245	3	
6	GS-2012B-Q-011-09	02 ^h 50 ^m 14.94 ^s	-31°02'56.8"	0.9927	2	

Continued on next page

Table 2.2 – continued from previous page

ID	Mask	RA(J2000)	Dec(J2000)	z	Quality	Member
9	GS-2012B-Q-011-09	02 ^h 50 ^m 08.98 ^s	-31°03'01.1"	0.9086	3	✓
10	GS-2012B-Q-011-09	02 ^h 50 ^m 10.24 ^s	-31°03'27.8"	0.9056	3	✓
11	GS-2012B-Q-011-09	02 ^h 50 ^m 07.01 ^s	-31°01'00.9"	0.5204	3	
13	GS-2012B-Q-011-09	02 ^h 50 ^m 06.54 ^s	-31°03'44.7"	0.9126	3	✓
17	GS-2012B-Q-011-09	02 ^h 50 ^m 03.99 ^s	-31°03'53.0"	0.9176	3	✓
18	GS-2012B-Q-011-09	02 ^h 50 ^m 07.33 ^s	-31°04'10.6"	0.9106	3	✓
19	GS-2012B-Q-011-09	02 ^h 50 ^m 02.67 ^s	-31°03'26.0"	0.9797	3	
20	GS-2012B-Q-011-09	02 ^h 50 ^m 07.38 ^s	-31°05'28.7"	0.6494	2	
21	GS-2012B-Q-011-09	02 ^h 49 ^m 58.10 ^s	-31°03'39.6"	0.8696	3	✓
22	GS-2012B-Q-011-09	02 ^h 50 ^m 05.48 ^s	-31°04'40.5"	0.9026	2	
27	GS-2012B-Q-011-09	02 ^h 49 ^m 58.68 ^s	-31°05'25.8"	0.6274	3	
28	GS-2012B-Q-011-09	02 ^h 49 ^m 59.99 ^s	-31°05'07.8"	0.8816	2	
29	GS-2012B-Q-011-09	02 ^h 49 ^m 58.60 ^s	-31°04'59.2"	0.9216	3	✓
30	GS-2012B-Q-011-09	02 ^h 50 ^m 00.51 ^s	-31°04'44.5"	0.5654	3	
31	GS-2012B-Q-011-09	02 ^h 50 ^m 04.26 ^s	-31°07'05.2"	0.9827	3	

Table 2.3: Low redshift sample ($0.0 < z < 0.5$): column 1 gives the name of the XCS Cluster, columns 2 and 3 give its J2000 right ascension and declination. Column 4 gives the redshift, with the uncertainty found using bootstrapping. Column 5 and 6 give the redshift from the literature and its corresponding reference. Column 7 gives the temperature of the cluster as given by the XCS pipeline and column 8 gives the number of confirmed members for each cluster. Column 9 gives the number of sources that the redshifts were taken from.

Cluster Name	RA (J2000)	DEC (J2000)	z	z_{lit}	z_{lit} Reference	T_X keV	No.	Sources
XMMXCS J000013.9-251052.1	00 ^h 00 ^m 13.9 ^s	-25°10'52.1''	0.0845 ± 0.0004	0.08	Mehrtens et al. (2012)	$1.8^{+0.40}_{-0.2}$	19	3
XMMXCS J003430.1-431905.6	00 ^h 34 ^m 30.1 ^s	-43°19'05.6''	0.3958 ± 0.001	0.4	Mehrtens et al. (2012)	$3.5^{+0.20}_{-0.2}$	22	2
XMMXCS J005603.0-373248.0	00 ^h 56 ^m 03.0 ^s	-37°32'48.0''	0.1659 ± 0.0009	0.16	Cappi et al. (1998)	$5.2^{+0.30}_{-0.2}$	22	2
XMMXCS J015315.0+010214.2	01 ^h 53 ^m 15.0 ^s	+01°02'14.2''	0.0593 ± 0.0002	0.06	Yoon et al. (2008)	$1.08^{+0.02}_{-0.02}$	12	4
XMMXCS J072054.3+710900.5	07 ^h 20 ^m 54.3 ^s	+71°09'00.5''	0.2309 ± 0.0005	0.23	Mulchaey et al. (2006)	$2.9^{+0.50}_{-0.4}$	29	2
XMMXCS J081918.6+705457.5	08 ^h 19 ^m 18.6 ^s	+70°54'57.5''	0.2298 ± 0.0005	0.23	Vikhlinin et al. (1998)	$3^{+0.80}_{-0.6}$	19	1
XMMXCS J094358.2+164120.7	09 ^h 43 ^m 58.2 ^s	+16°41'20.7''	0.2539 ± 0.0005	0.25	Mehrtens et al. (2012)	$1.5^{+0.40}_{-0.2}$	27	1
XMMXCS J095957.6+251629.0	09 ^h 59 ^m 57.6 ^s	+25°16'29.0''	0.0523 ± 0.0005	0.08	Takey et al. (2013)	$1.4^{+0.05}_{-0.05}$	15	3
XMMXCS J100047.4+013926.9	10 ^h 00 ^m 47.4 ^s	+01°39'26.9''	0.2202 ± 0.0006	0.22	Finoguenov et al. (2007)	$3.3^{+0.20}_{-0.2}$	16	5
XMMXCS J100141.7+022539.8	10 ^h 01 ^m 41.7 ^s	+02°25'39.8''	0.1233 ± 0.0005	0.12	Takey et al. (2011)	$1.43^{+0.06}_{-0.03}$	26	3

Continued on next page

Table 2.3 – continued from previous page

Cluster Name	RA (J2000)	DEC (J2000)	z	z_{lit}	z_{lit} Reference	T_X keV	No.	Sources
XMMXCS J104044.4+395710.4	10 ^h 40 ^m 44.4 ^s	+39°57'10.4"	0.1389 ± 0.0007	0.16	Hao et al. (2010)	3.54 ^{+0.03} _{-0.03}	17	5
XMMXCS J111515.6+531949.5	11 ^h 15 ^m 15.6 ^s	+53°19'49.5"	0.4663 ± 0.001	0.47	Hennawi et al. (2008)	5.4 ^{+1.50} _{-0.9}	16	2
XMMXCS J115112.0+550655.5	11 ^h 51 ^m 12.0 ^s	+55°06'55.5"	0.0791 ± 0.0003	0.08	Struble and Rood (1999)	1.66 ^{+0.04} _{-0.04}	16	2
XMMXCS J123144.4+413732.0	12 ^h 31 ^m 44.4 ^s	+41°37'32.0"	0.1735 ± 0.0009	0.18	Burenin et al. (2007)	2.7 ^{+0.60} _{-0.4}	10	1
XMMXCS J151618.6+000531.3	15 ^h 16 ^m 18.6 ^s	+00°05'31.3"	0.12 ± 0.0005	0.13	Koester et al. (2007a)	5.4 ^{+0.10} _{-0.1}	35	4
XMMXCS J161132.7+541628.3	16 ^h 11 ^m 32.7 ^s	+54°16'28.3"	0.3372 ± 0.0013	0.33	Takey et al. (2011)	4.6 ^{+1.20} _{-0.8}	12	1
XMMXCS J163015.6+243423.2	16 ^h 30 ^m 15.6 ^s	+24°34'23.2"	0.0625 ± 0.0003	0.07	Mullis et al. (2003)	3.5 ^{+0.60} _{-0.4}	62	3
XMMXCS J223939.3-054327.4	22 ^h 39 ^m 39.3 ^s	-05°43'27.4"	0.2451 ± 0.0003	0.24	Mullis et al. (2003)	2.8 ^{+0.20} _{-0.2}	68	1
XMMXCS J233757.0+271121.0	23 ^h 37 ^m 57.0 ^s	+27°11'21.0"	0.1237 ± 0.0007	0.12	Sakelliou and Merrifield (1998)	3.4 ^{+0.60} _{-0.4}	12	4

Table 2.4: High redshift sample ($0.5 < z < 1.0$): column 1 gives the name of the XCS Cluster, columns 2 and 3 give its J2000 right ascension and declination. Column 4 gives the redshift, with the uncertainty found using bootstrapping. Column 5 and 6 give the redshift from the literature and its corresponding reference. Column 7 gives the temperature of the cluster as given by the XCS pipeline. Column 8 gives whether this is a new detection (N) or whether the data is from the literature (L). Column 9 gives the number of confirmed members for each cluster.

Cluster Name	RA (J2000)	DEC (J2000)	z	z_{lit}	z_{lit} Reference	T_X keV	Observation	No.
XMMXCS J000216.1-355633.8	00 ^h 02 ^m 16.1 ^s	-35°56'33.8''	0.7709 ± 0.0021	0.77	Nastasi et al. (2014)	$4.83^{+1.01}_{-0.76}$	L	13
XMMXCS J005656.6-274031.9	00 ^h 56 ^m 56.6 ^s	-27°40'31.9''	0.5601 ± 0.0007	0.56	Scharf et al. (1997)	$3.30^{+0.94}_{-0.63}$	N	15
XMMXCS J015241.1-133855.9	01 ^h 52 ^m 41.1 ^s	-13°38'55.9''	0.8268 ± 0.0010	0.82	Mehrtens et al. (2012)	$3.23^{+0.38}_{-0.31}$	N	29
XMMXCS J021734.7-051326.9	02 ^h 17 ^m 34.7 ^s	-05°13'26.9''	0.6467 ± 0.0012	0.65	Adami et al. (2011)	$2.23^{+0.90}_{-0.44}$	N	12
XMMXCS J025006.4-310400.8	02 ^h 50 ^m 06.4 ^s	-31°04'00.8''	0.9100 ± 0.0024	0.90	Scharf et al. (1997)	$4.50^{+1.33}_{-0.88}$	N	13
XMMXCS J030205.1-000003.6	03 ^h 02 ^m 05.1 ^s	-00°00'03.6''	0.6450 ± 0.0007	0.65	Šuhada et al. (2011)	$5.82^{+2.09}_{-1.32}$	N	16
XMMXCS J095417.1-173805.9	09 ^h 54 ^m 17.1 ^s	-17°38'05.9''	0.8272 ± 0.0017	0.82	Nastasi et al. (2014)	$3.65^{+0.62}_{-0.51}$	L	10
XMMXCS J095940.7+023113.4	09 ^h 59 ^m 40.7 ^s	+02°31'13.4''	0.7291 ± 0.0005	0.72	Bellagamba et al. (2011)	$5.02^{+0.68}_{-0.55}$	N	25
XMMXCS J105659.5-033728.0	10 ^h 56 ^m 59.5 ^s	-03°37'28.0''	0.8336 ± 0.0013	0.82	Gioia and Luppino (1994)	$7.57^{+0.43}_{-0.40}$	L	29
XMMXCS J112349.4+052955.1	11 ^h 23 ^m 49.4 ^s	+05°29'55.1''	0.6550 ± 0.0007	0.65	Mehrtens et al. (2012)	$4.62^{+1.55}_{-0.95}$	N	17

Continued on next page

Table 2.4 – continued from previous page

Cluster Name	RA (J2000)	DEC (J2000)	z	z_{lit}	z_{lit} Reference	T_X keV	Observation	No.
XMMXCS J113602.9-032943.2	11 ^h 36 ^m 02.9 ^s	-03°29'43.2''	0.8297 ± 0.0011			3.32 ^{+1.20} _{-0.78}	N	21
XMMXCS J114023.0+660819.0	11 ^h 40 ^m 23.9 ^s	+66°08'19.0''	0.7855 ± 0.0015	0.78	Gioia and Luppino (1994)	7.47 ^{+0.92} _{-0.77}	L	22
XMMXCS J124312.2+131307.2	12 ^h 43 ^m 12.2 ^s	13°13'07.2''	0.7910 ± 0.0014	0.80	Nastasi et al. (2014)	4.92 ^{+2.93} _{-1.54}	L	11
XMMXCS J134305.1-000056.8	13 ^h 43 ^m 05.1 ^s	-00°00'56.8''	0.6894 ± 0.0011	0.67	Basilakos et al. (2004)	4.49 ^{+0.72} _{-0.57}	N	23
XMMXCS J145009.3+090428.8	14 ^h 50 ^m 09.3 ^s	+09°04'28.8''	0.6412 ± 0.0007	0.60	Mehrtens et al. (2012)	3.84 ^{+0.66} _{-0.55}	N	22
XMMXCS J182132.9+682755.0	18 ^h 21 ^m 32.9 ^s	+68°27'55.0''	0.8166 ± 0.0011	0.82	Gioia et al. (2004)	4.49 ^{+0.79} _{-0.56}	L	19
XMMXCS J215221.0-273022.6	21 ^h 52 ^m 21.0 ^s	-27°30'22.6''	0.8276 ± 0.0011	0.82	Mehrtens et al. (2012)	2.18 ^{+0.67} _{-0.45}	N	15
XMMXCS J230247.7+084355.9	23 ^h 02 ^m 47.7 ^s	+08°43'55.9''	0.7187 ± 0.0014	0.72	Perlman et al. (2002)	5.29 ^{+0.59} _{-0.50}	N	22
XMMXCS J235616.4-344144.3	23 ^h 56 ^m 16.4 ^s	-34°41'44.3''	0.9391 ± 0.0012	0.94	Nastasi et al. (2014)	4.57 ^{+0.48} _{-0.41}	L	10

CHAPTER 3

VELOCITY DISPERSION - TEMPERATURE SCALING RELATION

In this chapter, we study the velocity dispersion (σ_v) - temperature (T_X) relation which was described in Chapter 1. In Chapter 2 we described our cluster sample and how cluster membership and redshift were determined. In this chapter we use these redshifts to calculate the velocity dispersion for each of our clusters and use the Metropolis algorithm to fit for the above scaling relation, implementing a Markov Chain Monte-Carlo (MCMC) method. We make comparisons to both previous results and simulations and test for the evolution of the normalisation of the $\sigma_v - T_X$ relation.

3.1 Motivation

Clusters of galaxies provide us with the opportunity to learn about a variety of different processes happening on small scales, such as within galaxies, but also allows us to constrain cosmology and learn about the Universe as a whole. The advancement of science relies on the predicting and testing of models, and for astronomy and cosmology it is no different. Many different models

exist regarding the formation of galaxy clusters as well as the processes occurring within them. As discussed in Chapter 1, one of the more popular models is that of self-similarity. This model allows us to predict the relationships between various observables of galaxy clusters. This model can then be tested, shortfalls can be identified, and it can be improved to further our understanding of the Universe.

As shown in Section 1.4, we can use the self-similar model and the virial theorem to derive the relationship between the velocity dispersion of a cluster and its temperature to be $\sigma_v \propto T^{0.5}$. This relation is not as well studied as the X-ray luminosity – temperature ($L_X - T_X$) relation and therefore provides us with a good opportunity to provide new insights into scaling relations. One of the first points of interest is that similarly to studies of the $L_X - T_X$ relation almost all previous studies of the $\sigma_v - T_X$ relation have found a steeper power-law slope than expected (see Table 3.5). The reasons for this are the same as for the $L_X - T_X$ relation, mainly, the exclusion of non-gravitational effects in the self-similar model as discussed in Section 1.4.

The other interesting part of studying scaling relations is to determine if they are evolving with redshift. Due to selection effects, this is an extremely difficult task when studying the $L_X - T_X$ relation. However, as discussed in Section 1.4 we assume negligible selection effects on our measurement of the $\sigma_v - T_X$. The self-similar model predicts that the $\sigma_v - T_X$ relation will not evolve with redshift but to date this has been tested only by Wu et al. (1998) and Nastasi et al. (2014). Even then, all but four clusters in the Wu et al. (1998) sample are at $z < 0.5$. Nastasi et al. (2014) made a measurement of the relation at $0.6 < z < 1.5$ using a sample of 12 clusters, obtaining results consistent with previous studies at low redshift. In our study, as discussed in Chapter 2, we use a sample of 38 clusters ranging in redshift from 0.1 to 0.9 and therefore used a larger sample spanning this z range than previous studies, except for Wu et al. (1998). However, we offer an improvement over this work because we have 19 clusters with $z > 0.5$ compared to their sample which only contained 4.

3.2 Velocity dispersion calculation

We used our confirmed galaxy cluster members (Chapter 2) to calculate an initial estimate of the velocity dispersion of each cluster using the biweight scale method described in Beers et al. (1990). We then calculated R_{200} using Equation 2.1, and excluded all galaxies located at projected cluster-centric radial distances outside R_{200} . The velocity dispersion of each cluster was then recalculated and the error found via bootstrap resampling. This final radial cut did not remove more than two galaxies from the final sample for each cluster. Tables 3.1 and 3.2 list the velocity dispersions and R_{200} values for the low and high redshift samples, respectively.

3.3 Fitting the $\sigma_v - T_X$ relation

To determine the scaling relation between σ_v and T_X , we fitted a power law of the form

$$\log \left(\frac{\sigma_v}{1000 \text{ km s}^{-1}} \right) = A + B \log \left(\frac{T}{5 \text{ keV}} \right) + C \log E(z). \quad (3.1)$$

Here, 5 keV and 1000 km s^{-1} are the pivot temperature and velocity dispersion, respectively, for our fit. These were chosen to reduce the covariance between the normalisation A and the slope B , and for ease of comparison to previous studies. In the above, evolution of the normalisation is parametrised as $E(z)^C$, where $E(z) = \sqrt{\Omega_m(1+z)^3 + \Omega_\Lambda}$ describes the redshift evolution of the Hubble parameter. The evolution is normalised using the Hubble parameter as this is the evolution expected for the self-similar case which we are using for comparison and which gives $B = 0.5$ and $C = 0$.

Table 3.1: Calculated properties of the low redshift sample ($0.0 < z < 0.5$): column 1 gives the name of the XCS Cluster. Columns 2 and 3 give the measured velocity dispersion and R_{200} respectively. Column 4 and 5 give the temperature of the cluster and the number of members (Taken from Table 2.3 for convenience of comparison).

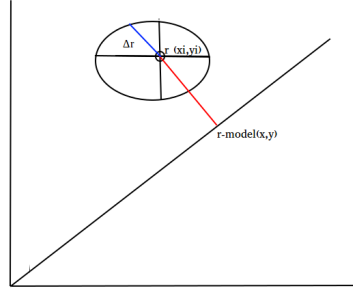
Cluster Name	σ_v (km s^{-1})	R_{200} (Mpc)	T_X (keV)	No.
XMMXCS J000013.9-251052.1	410± 80	1.11	1.8 ^{+0.40} _{-0.2}	19
XMMXCS J003430.1-431905.6	920±150	1.96	3.5 ^{+0.20} _{-0.2}	22
XMMXCS J005603.0-373248.0	900±140	2.06	5.2 ^{+0.30} _{-0.2}	22
XMMXCS J015315.0+010214.2	240± 80	0.55	1.08 ^{+0.02} _{-0.02}	12
XMMXCS J072054.3+710900.5	550± 60	1.2	2.9 ^{+0.50} _{-0.4}	29
XMMXCS J081918.6+705457.5	410± 70	0.83	3 ^{+0.80} _{-0.6}	19
XMMXCS J094358.2+164120.7	590± 90	1.54	1.5 ^{+0.40} _{-0.2}	27
XMMXCS J095957.6+251629.0	510±220	1.79	1.4 ^{+0.05} _{-0.05}	15
XMMXCS J100047.4+013926.9	560±140	1.41	3.3 ^{+0.20} _{-0.2}	16
XMMXCS J100141.7+022539.8	590±130	1.05	1.43 ^{+0.06} _{-0.03}	26
XMMXCS J104044.4+395710.4	860±150	2.12	3.54 ^{+0.03} _{-0.03}	17
XMMXCS J111515.6+531949.5	910±310	1.75	5.4 ^{+1.50} _{-0.9}	16
XMMXCS J115112.0+550655.5	330±100	1.5	1.66 ^{+0.04} _{-0.04}	16
XMMXCS J123144.4+413732.0	480±100	1.26	2.7 ^{+0.60} _{-0.4}	10
XMMXCS J151618.6+000531.3	870±220	2.01	5.4 ^{+0.10} _{-0.1}	35
XMMXCS J161132.7+541628.3	790±150	1.69	4.6 ^{+1.20} _{-0.8}	12
XMMXCS J163015.6+243423.2	710±130	2.2	3.5 ^{+0.60} _{-0.4}	62
XMMXCS J223939.3-054327.4	560± 70	1.32	2.8 ^{+0.20} _{-0.2}	68
XMMXCS J233757.0+271121.0	460±110	1.49	3.4 ^{+0.60} _{-0.4}	12

Table 3.2: Calculated properties of the high redshift sample ($0.5 < z < 1.0$). All columns are as explained in Table 3.1.

Cluster Name	σ_v (km s^{-1})	R_{200} (Mpc)	T_X (keV)	No.
XMMXCS J000216.1-355633.8	1100±191	1.77	4.83 ^{+1.01} _{-0.76}	13
XMMXCS J005656.6-274031.9	380± 60	0.66	3.3 ^{+0.94} _{-0.63}	15
XMMXCS J015241.1-133855.9	840±150	1.33	3.23 ^{+0.38} _{-0.31}	29
XMMXCS J021734.7-051326.9	620±210	1.11	2.23 ^{+0.9} _{-0.44}	12
XMMXCS J025006.4-310400.8	1120±260	1.66	4.5 ^{+1.33} _{-0.88}	13
XMMXCS J030205.1-000003.6	610±180	1.04	5.82 ^{+2.09} _{-1.32}	16
XMMXCS J095417.1-173805.9	940±310	1.42	3.65 ^{+0.62} _{-0.51}	10
XMMXCS J095940.7+023113.4	470± 90	0.88	5.02 ^{+0.68} _{-0.55}	25
XMMXCS J105659.5-033728.0	1010±120	1.57	7.57 ^{+0.43} _{-0.4}	29
XMMXCS J112349.4+052955.1	600±210	1.05	4.62 ^{+1.55} _{-0.95}	17
Continued on next page				

Table 3.2 – continued from previous page

Cluster Name	σ_v (km s ⁻¹)	R_{200} (Mpc)	T_X (keV)	No.
XMMXCS J113602.9-032943.2	700±110	1.06	3.32 ^{+1.2} _{-0.78}	21
XMMXCS J114023.0+660819.0	950±100	1.51	7.47 ^{+0.92} _{-0.77}	22
XMMXCS J124312.2+131307.2	790±460	1.19	4.92 ^{+2.93} _{-1.54}	11
XMMXCS J134305.1-000056.8	920±170	1.72	4.49 ^{+0.72} _{-0.57}	23
XMMXCS J145009.3+090428.8	630± 90	1.07	3.84 ^{+0.66} _{-0.55}	22
XMMXCS J182132.9+682755.0	860±130	1.34	4.49 ^{+0.79} _{-0.56}	19
XMMXCS J215221.0-273022.6	530±150	0.86	2.18 ^{+0.67} _{-0.45}	15
XMMXCS J230247.7+084355.9	1010±130	1.6	5.29 ^{+0.59} _{-0.5}	22
XMMXCS J235616.4-344144.3	670±260	0.91	4.57 ^{+0.48} _{-0.41}	10

**Figure 3.1:** This sketch shows how $r - r_{\text{model}}$ and Δr are calculated for the orthogonal method.

Similarly to Hilton et al. (2012), the best fit values for these parameters were found using Markov Chain Monte-Carlo (MCMC) with the Metropolis algorithm. Both orthogonal and bi-sector regression methods were used. For the orthogonal method, the probability for a given cluster to be drawn from the model scaling relation is

$$P_{\text{model}} = \frac{1}{\sqrt{2\pi(\Delta r^2 + \Delta S^2)}} \exp \left[\frac{-(r - r_{\text{model}})^2}{2(\Delta r^2 + S^2)} \right], \quad (3.2)$$

where $r - r_{\text{model}}$ is the orthogonal distance of the cluster from the model relation, Δr is the error on the orthogonal distance, and S is the intrinsic scatter orthogonal to the model relation. Δr is calculated from the projection in the direction orthogonal to the model line of the ellipse

defined by the errors on $\log \sigma_v$ and $\log T$, chosen according to the position of a given point relative to the model fit line as shown in Figure 3.1.

For the bisector method, the intrinsic scatter and measurement errors are treated independently for each axis. Therefore, in the equation for P_{model} , r_{model} is replaced by

$$y_{\text{model}} = \log \left(\frac{\sigma_v}{1000 \text{ km s}^{-1}} \right) - \left[A + B \log \left(\frac{T}{5 \text{ keV}} \right) + C \log E(z) \right], \quad (3.3)$$

and

$$x_{\text{model}} = \log \left(\frac{T}{5 \text{ keV}} \right) - \left[\frac{\log \left(\frac{\sigma_v}{1000 \text{ km s}^{-1}} \right) - A - C \log E(z)}{B} \right], \quad (3.4)$$

where r and Δr are replaced by x , Δx or y , Δy as appropriate in Equation 3.2. The intrinsic scatter S is replaced by two parameters S_x and S_y . For this work, the covariance between S_x and S_y is negligible since it is very unlikely that there will be any correlation between σ_v , which is measured using galaxy velocity measurements, and T , which is measured from X-ray spectroscopy.

For both methods, the likelihood \mathcal{L} of a given model is simply the product of P_{model} for each cluster in the sample, i.e., in the orthogonal case

$$\mathcal{L}(\sigma_v, T_X | A, B, C, S) \propto P_{\text{prior}}(A, B, C, S) \prod_i P_{\text{model},i}, \quad (3.5)$$

where we assume generous, uniform log priors on each parameter, as listed in Table 3.3.

Table 3.3: Priors on $\sigma_v - T_X$ relation fit parameters

Parameter	Uniform Prior	Notes
A	(-5.0,5.0)	-
B	(0.0,2.0)	-
C	(-1.0,1.0)	-
S	(0.01,1.0)	Orthogonal method only
S_x	(0.01,1.0)	Bisector method only
S_y	(0.01,1.0)	Bisector method only

3.4 Results

In this section we look at the results of our MCMC algorithm and discuss the implications of the different measured values.

3.4.1 Evolution of the slope and intrinsic scatter

For the model given in Equation 3.1, it is assumed that the slope (parameter B) is not evolving with redshift. To test this, the $\sigma_v - T_X$ relation was fitted with $C = 0$ in two redshift bins, $0.0 < z < 0.5$ and $0.5 < z < 0.9$, with 19 clusters in each bin. The parameters A , B , and S were obtained using the MCMC method described above for the high and low redshift samples individually. The results for this are shown in Figures 3.2 and 3.3 and Table 3.4.

Using the orthogonal method we found $B = 1.12 \pm 0.41$ for the high redshift sample and $B = 0.89 \pm 0.16$ for the low redshift sample. However, we found that the slope of the relation for the high redshift sample is driven by the prior and future work will look at fitting for $B(z)$. We assume for the remainder of this paper that the slope does not evolve with redshift, though clearly either a larger sample or more accurate measurements of individual clusters are needed to confirm this assumption.

The samples were also tested to see if the results may be biased by selection effects resulting in more high temperature clusters in the high redshift sample. To do this, all clusters with $T < 2keV$ were removed from the low redshift sample, so that the temperature distribution was

similar in both the high and low redshift samples, and fitting was re-done. The results for the low redshift sample were found it be consistent within 1σ to those with the low temperature clusters included. Therefore, this suggests that selections effects do not play a significant role in the $\sigma_v - T_X$ relation for this sample.

The intrinsic scatter is $S = 0.05 \pm 0.02$ for the low redshift sample and $S = 0.08 \pm 0.04$ for the high redshift sample. As these values are consistent within their errors, there is no evidence that the intrinsic scatter varies with redshift.

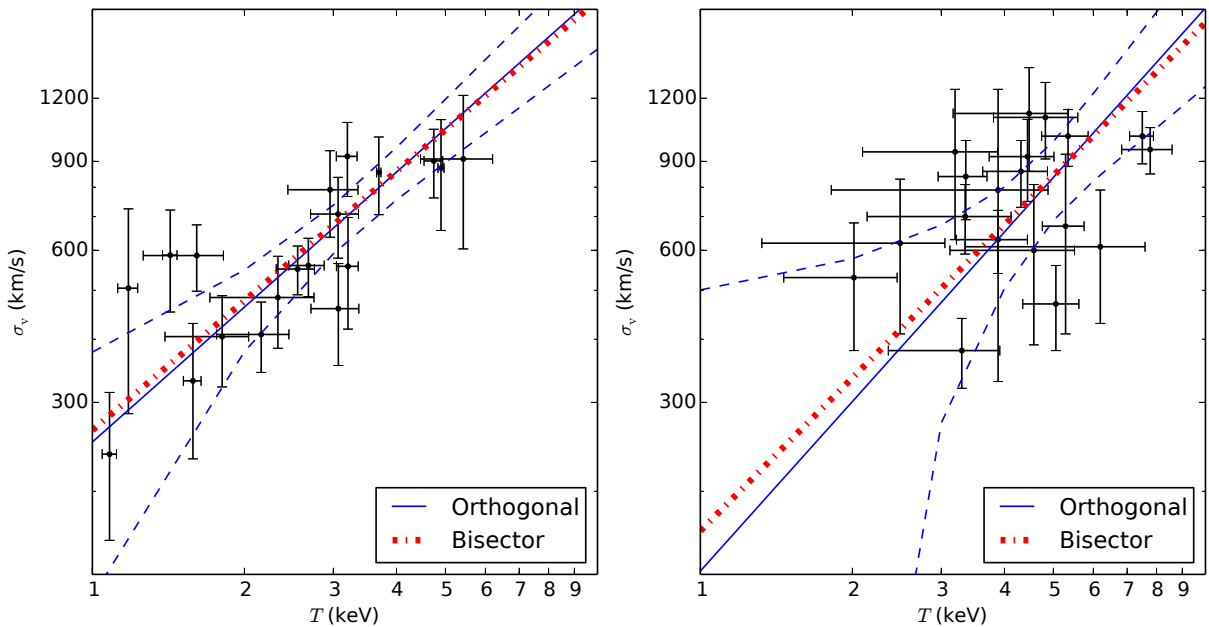


Figure 3.2: The $\sigma_v - T_X$ relation assuming no evolution, i.e., $C = 0$ in Equation 3.1, for low ($0.0 < z < 0.5$; left panel) and high ($0.5 < z < 0.9$; right panel) redshift samples. The solid blue line shows an orthogonal regression fit to the data with the dashed lines representing the 95% confidence interval. The thick, red, dot-dashed line shows a bisector regression fit to the data (see Section 3.3). A model of the form seen in Equation 3.1 was used in the Metropolis algorithm to determine a line of best fit (see Section 3.4.1).

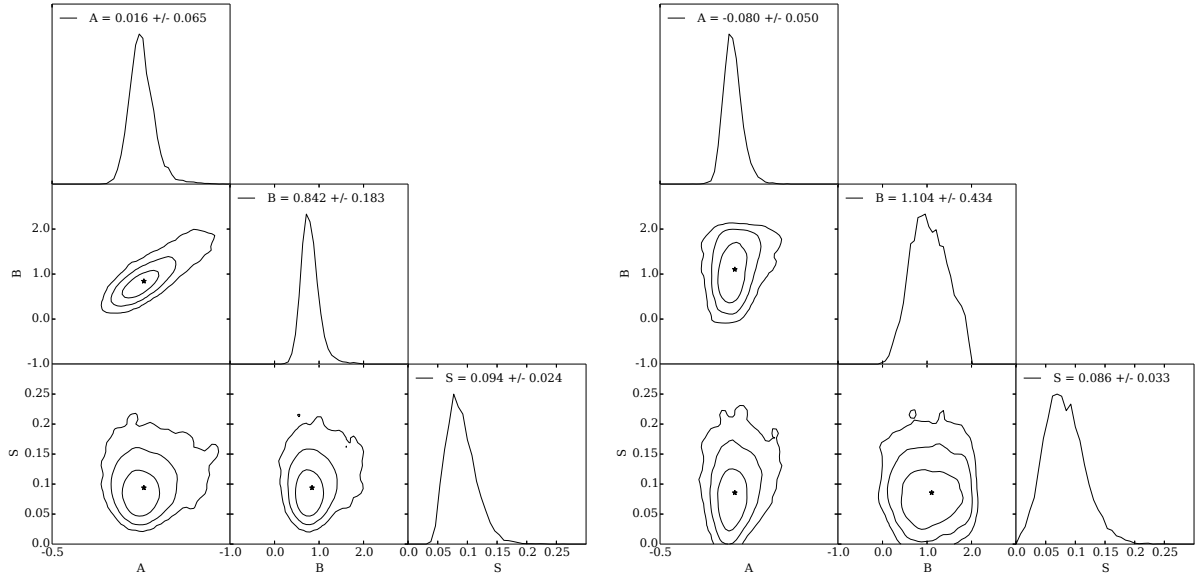


Figure 3.3: Corner plots for the low (left - $0.0 < z < 0.5$) and high (right- $0.5 < z < 0.9$) redshift sample showing all the one and two dimensional projections of the posterior probability distributions of the three parameters when using the orthogonal method. The values of each parameter are given in the top centre. The histograms show the one dimensional marginalised distribution for each parameter and the other plots show the 2 dimensional version, where the contours show 1, 2, and 3 σ . The contour plot for the B parameter for the high redshift sample is slightly flattened due to it being driven by the prior (Section 3.4.1)

Table 3.4: Best-fit $\sigma_v - T_X$ scaling relation parameters using both the orthogonal and bisector regression methods (see Section 3.3).

Method	Parameter	Low Redshift	High Redshift	Combined (no evolution)	Combined (with evolution)
Orthogonal	A	0.02 ± 0.07	-0.08 ± 0.05	-0.05 ± 0.04	0.02 ± 0.05
	B	0.84 ± 0.18	1.10 ± 0.43	0.72 ± 0.12	0.83 ± 0.14
	S	0.09 ± 0.02	0.09 ± 0.03	0.06 ± 0.03	0.06 ± 0.03
	C	0	0	0	-0.42 ± 0.27
Bisector	A	0.02 ± 0.04	-0.07 ± 0.03	-0.04 ± 0.02	0.02 ± 0.04
	B	0.85 ± 0.11	1.01 ± 0.17	0.77 ± 0.08	0.86 ± 0.09
	S_x	0.15 ± 0.03	0.19 ± 0.03	0.15 ± 0.02	0.14 ± 0.02
	S_y	0.07 ± 0.03	0.12 ± 0.04	0.09 ± 0.02	0.09 ± 0.02
	C	0	0	0	-0.49 ± 0.25

3.4.2 Evolution of the normalisation

To test for the evolution of the normalisation (parameter A in Equation 3.1), the low and high redshift samples were combined and C was allowed to vary in the MCMC analysis. The results obtained are shown by the scaling relation plot in Fig. 3.4. We found $C = -0.42 \pm 0.27$, meaning that for a given σ_v , a higher T_X is obtained at higher redshift. However, the no evolution relation falls within the 95 per cent confidence interval and therefore we conclude that there is no significant evidence in favour of evolution.

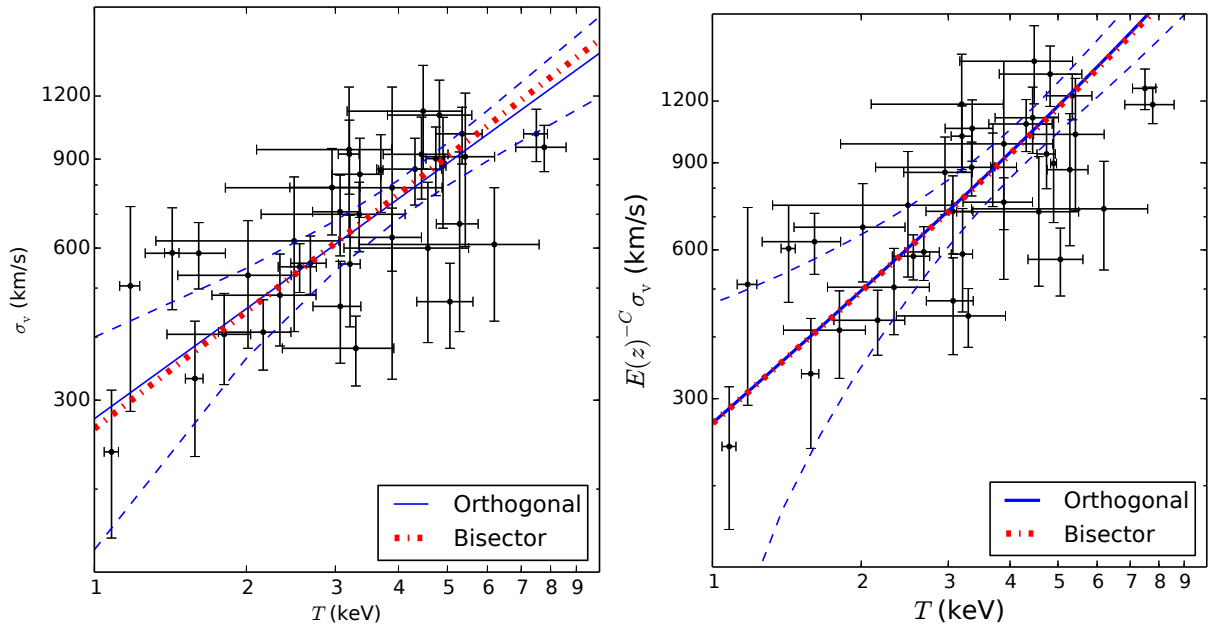


Figure 3.4: *Left:* The $\sigma_v - T_X$ relation assuming no evolution, i.e., $C = 0$ in Equation 3.1, for the combined sample. *Right:* The $\sigma_v - T_X$ relation for the combined sample with varying evolution, i.e., C is a free parameter in Equation 3.1. The velocity dispersion is scaled to take into account the evolution by multiplying by $E(z)^{-C}$. All lines are as explained in Fig. 3.2.

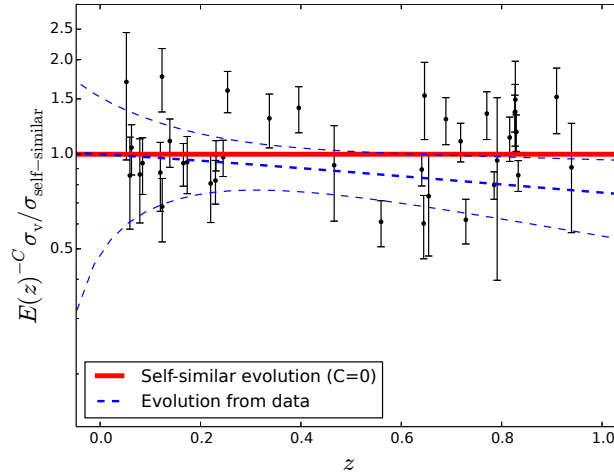


Figure 3.5: Plot showing the evolution of the normalisation of the $\sigma_v - T_X$ relation obtained for the data with the 95% confidence intervals (blue dashed lines), as compared to the self similar relation which predicts no evolution which is shown as the solid red line. The black points show our sample data.

We also applied a statistical test known as the Akaike information criterion (AIC) to determine whether the model with or without evolution (Fig. 3.4) was preferred. The AIC estimates the quality of each model relative to each other and is therefore a means of model selection. It is defined by (Burnham and Anderson, 2002) as

$$\text{AIC} = 2k - 2\ln(\mathcal{L}), \quad (3.6)$$

where \mathcal{L} is the maximised likelihood function (Equation 3.5) and k is the number of free parameters. The AIC includes a penalty for using extra parameters as a way to discourage over-fitting and rewards goodness of fit based on the likelihood function. When modelling data there will always be some information lost, but we are trying to find the model that minimises the data loss. We can calculate the probability that a model will minimise the information loss compared to another model using the relative likelihood as shown below:

$$\exp((\text{AIC}_{min} - \text{AIC}_i)/2), \quad (3.7)$$

where AIC_{min} is the lowest AIC values of all your models and AIC_i is the model you comparing it too.

For the combined sample with the no evolution model the AIC value was -64.6 and when the fourth parameter for evolution (C) was included this increased to -62.1. The relative likelihood is then calculated to be 0.08. This means that the model with evolution is 0.08 times as probable as the model without evolution to minimise information loss. Therefore, combining this with the results from the $\sigma_v - T_X$ relation fit, it can be concluded that the preferred model is the one with no evolution.

3.5 Discussion

3.5.1 Comparison with previous results

Table 3.4 and Figs.3.2–3.4 present the results of applying the orthogonal and bisector fitting methods to the low redshift, high redshift, and combined samples. We see that the bisector and orthogonal methods give very similar results, especially for our total sample without evolution. Hogg et al. (2010) suggests that the bisector method should be avoided as, by simply finding the difference between a forward and reverse fitting method, large systematic errors will be introduced. Maughan et al. (2006) also suggests that the orthogonal method is preferable as it avoids biases that are inherent in the bisector regression when doing a fit with intrinsic scatter. However, the bisector method has been widely used for scaling relation measurements in the past and is therefore included for completeness.

Results from previous studies of the $\sigma_v - T_X$ relation are collected in Table 3.5. All of these studies, except for Edge and Stewart (1991) and the low redshift sample of Wu et al. (1998), obtained a slope steeper than the expected self-similar slope of $\sigma_v \propto T^{0.5}$. We measured $B = 0.72 \pm 0.12$ using the orthogonal fitting method and $B = 0.77 \pm 0.08$ using the bisector fitting method for our combined sample. Therefore, both the orthogonal and bisector slopes are in agreement with each other and the previous values in the literature, except for the result obtained by Edge and Stewart (1991), which is only consistent with the orthogonal result. The temperature range for previous studies varies but most are consistent with $0 < T < 10$ except

for studies by Wu et al. (1998), Wu et al. (1999) and Nastasi et al. (2014) which probe out to $T > 15$ keV. Xue and Wu (2000) only probe a small temperature range of $T < 2$ keV. Most of these studies are reliant on data from literature, like our low cluster sample. However, unlike our study they don't calculate the velocity dispersion in a consistent way, but instead rely on previous velocity dispersion measurements. Our study therefore, offers an improvement in the calculation of velocity dispersions and hence a more reliable $\sigma_v - T$ relation.

With the exception for work done by Wu et al. (1998) and Nastasi et al. (2014), all the previous results were obtained for low redshift samples and no test for evolution was performed. Wu et al. (1998) divided their sample into two groups, $z < 0.1$ and $z \geq 0.1$, and found no significant evolution, however their sample included only four clusters in the redshift range $0.5 < z < 1.0$. Nastasi et al. (2014) had a sample of 12 galaxy clusters and found a very large error of more than 50 per cent on their slope. They concluded that their sample size was too small to accurately measure evolution. We conclude that the data presented in this paper — a homogeneous cluster sample that is larger than those used in previous studies at $z > 0.5$ — are consistent with previous results.

Table 3.5: Previous measurements of the velocity dispersion–temperature relation. Here the relation is in the form $\sigma_v = 10^A T^B$, where σ_v is measured in km s^{-1} and T_X is measured in keV.

Paper	Number of clusters	A	B	Redshift range	Fitting method	Temperature Range
Edge and Stewart (1991)	23	2.60 ± 0.08	0.46 ± 0.12	$z < 0.1$	Least squares	$2 < T < 10$
Lubin and Bahcall (1993)	41	2.52 ± 0.07	0.60 ± 0.11	$z < 0.2$	χ^2	$2 < T < 10.5$
Bird et al. (1995)	22	2.50 ± 0.09	0.61 ± 0.13	$z < 0.1$	Bisector	$1.4 < T < 9$
Girardi et al. (1996)	37	2.53 ± 0.04	0.61 ± 0.05	$z < 0.2$	Bisector	$0 < T < 11$
Ponman et al. (1996)	27	2.54 ± 0.04	0.55 ± 0.05	$z < 0.15$	Bisector	$0 < T < 1.5$
White et al. (1997)	35	2.53 ± 0.08	0.60 ± 0.10	$z < 0.2$	Orthogonal	$0 < T < 14$
Wu et al. (1998)	94	2.47 ± 0.06	0.67 ± 0.09	$z < 0.9$	Orthogonal	$1 < T < 17$
Wu et al. (1998)	110	2.57 ± 0.03	0.49 ± 0.05	$z < 0.1$	Orthogonal	$1 < T < 17$
Wu et al. (1998)	39	2.57 ± 0.08	0.56 ± 0.09	$0.1 < z < 0.9$	Orthogonal	$1 < T < 17$
Wu et al. (1999)	92	2.49 ± 0.03	0.64 ± 0.02	$z < 0.45$	Orthogonal	$2.5 < T < 15$
Xue and Wu (2000)	109	2.53 ± 0.03	0.58 ± 0.05	$z < 0.2$	Orthogonal	$0 < T < 2$
Nastasi et al. (2014)	12	2.47 ± 0.19	0.64 ± 0.34	$0.64 < z < 1.46$	Bisector	$2.5 < T < 15$
This work	38	3.00 ± 0.59	0.72 ± 0.12	$0.1 < z < 1.0$	Orthogonal	$0 < T < 10$
This work	38	3.22 ± 0.41	0.77 ± 0.08	$0.1 < z < 1.0$	Bisector	$0 < T < 10$

3.5.2 Comparison with simulations - no evolution

Comparing observational results to simulations is important for two main reasons. Firstly, we can determine if there is any bias due to sample selection, as the simulations provide both a larger temperature and larger redshift range. It also allows us to compare different simulation models and learn about the nature of the non-gravitational physics through their effect on the gas temperature.

The Millennium Gas Project is a set of hydrodynamical simulations described in Short et al. (2010) which uses the same initial perturbations as the Millennium Simulation (Springel et al., 2005). These simulations include a variety of models, including gravity only; energy injection with radiative cooling; and feedback only. For comparison to the data presented in this paper, the feedback only model (FO) in a volume of $250 h^{-1} \text{ Mpc}^3$ was used. This model includes supernova and AGN feedback using a semi-analytic galaxy formation model. Heating due to supernovae, AGN, and the star formation rate are obtained using the model of De Lucia and Blaizot (2007). The AGN feedback model used is described in Bower et al. (2008), which is dependent on the matter accreted by the central black hole and the efficiency with which the matter is converted to energy near the event horizon, with the upper limit being at two per cent of the Eddington rate.

As a comparison to the velocity dispersion of the cluster, two proxies were considered: the velocity dispersion of the galaxies (σ_{Gal}), and that obtained from the dark matter particles (σ_{DM}). The temperatures from the simulation were spectroscopic-like temperatures (T_{sl} ; Mazzotta et al., 2004). To ensure that only clusters similar to those in our sample were included, we excluded all groups from the simulation with M_{200} less than $10^{14} M_{\odot}$. We also included a temperature cut, $1 < T(\text{keV}) < 11$, and a redshift cut, $0 < z < 1$, to match our sample.

We also tested our fitting method on the BAHAMAS hydrodynamical simulation (McCarthy et al. (2016) and Caldwell et al., in prep.) and compared it to the fit for our data. Here, a $400 h^{-1} \text{Mpc}^3$ box is used, with initial conditions based on Planck 2013 cosmological parameters (Planck Collaboration et al., 2014c), and both AGN and supernovae feedback models as described by Le Brun et al. (2014). A galaxy mass lower limit of $5 \times 10^9 M_\odot$ and a cluster mass lower limit of $10^{14} M_\odot$ were implemented. This simulation reproduces a large number of X-ray, SZ, and optical scaling relations of groups and clusters. However, unlike previous simulations, the new simulation also reproduces the observed galaxy stellar mass function remarkably well over a wide range of stellar masses. The velocity dispersion is traced by galaxies and is calculated using the gapper technique described by Beers et al. (1990). The temperatures used from the simulation were spectroscopic (T_s).

For both sets of simulations the orthogonal fitting method described in Section 3.3 was applied with $C = 0$. The parameters A , B , and S for both the Millennium Gas Project and BAHAMAS simulations are shown in Table 3.6. The $\sigma_v - T_X$ relation for the Millennium Gas Project with the two different σ_v proxies are shown in Fig. 3.6. The slope is slightly steeper for the stars ($B = 0.62 \pm 0.01$) than for the dark matter ($B = 0.55 \pm 0.08$), but both are consistent with previous studies of the $\sigma_v - T_X$ relation and the results obtained from our data.

Table 3.6: Best fit values for the parameters in Equation 3.2 (slope B , intercept A and scatter S) for the various models obtained from simulations without evolution. For the Millennium Gas Project we use dark matter (DM) and stars as the tracers for the velocity dispersion. The BAHAMAS simulation uses galaxies. The Millennium Gas simulations use spectroscopic like temperatures (T_{sl}) and the BAHAMAS simulation use spectroscopic temperatures (T_s). Caldwell et al., (in prep) present a different method for determining the $\sigma_v - T_X$ relation as discussed in Section 3.5.2, the results of which are also shown below.

Simulation	σ_{tracer}	T_{model}	A	B	S
Millennium Gas	DM	T_{sl}	-0.011 ± 0.002	0.553 ± 0.008	0.028 ± 0.001
Millennium Gas	Galaxies	T_{sl}	-0.034 ± 0.003	0.621 ± 0.010	0.034 ± 0.001
BAHAMAS	Galaxies	T_s	-0.055 ± 0.003	0.848 ± 0.012	0.055 ± 0.001
Caldwell et al., in prep	Galaxies	T_s	-0.133	0.545	—

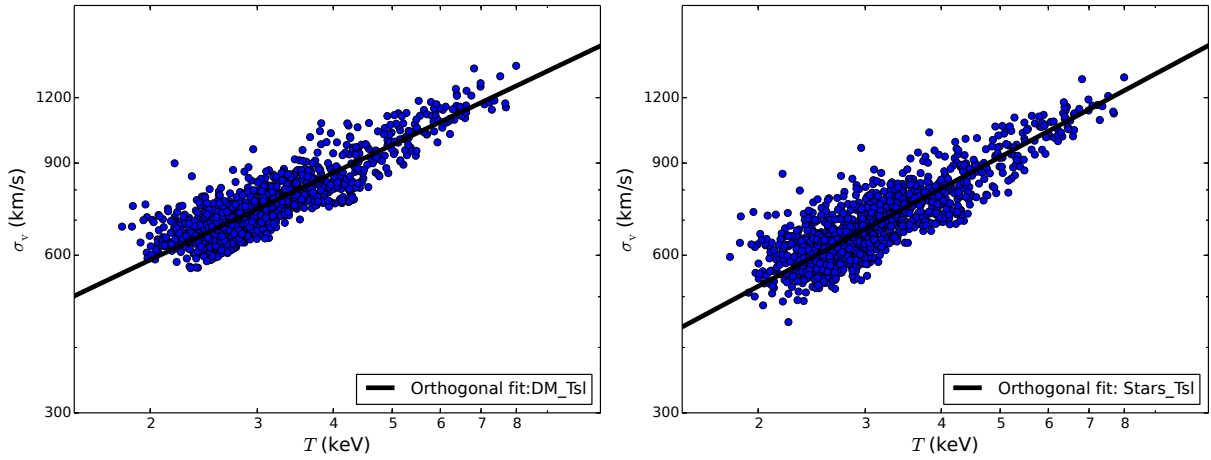


Figure 3.6: The $\sigma_v - T_X$ relation for the Millennium Gas Project simulations using dark matter (left panel) and galaxies (right panel) as proxies for the velocity dispersion. The blue dots are the data obtained from the simulation and the solid black line shows the fit using the orthogonal regression method. The slope is slightly steeper for the galaxies ($B = 0.62 \pm 0.01$) than for the dark matter ($B = 0.55 \pm 0.08$) but both are consistent with previous studies of the $\sigma_v - T_X$ relation and the results obtained from our data.

Fig. 3.7 shows that the orthogonal fit to the full BAHAMAS sample systematically overestimates the average velocity dispersion at $T_X > 5$ keV. This may be due, in part, to the model not being a complete description of the data: as can be seen in Fig. 3.7, the intrinsic scatter decreases with increasing temperature for the BAHAMAS sample. This is not captured in our orthogonal regression model (Equation 3.2), i.e., S is constant with both T_X and z . However, we found that this bias is mostly due to the temperature distribution of the sample. Choosing a subset of the BAHAMAS sample with a uniform temperature distribution, ie. a sample with the same number of clusters in each 0.01 keV bin, we obtained $B = 0.55 \pm 0.01$ using the orthogonal fitting method. We note that there is no single method which gives the underlying ‘true’ scaling relation in the presence of errors on both variables and intrinsic scatter: the recovered slope and normalisation depend upon the details of the method used.

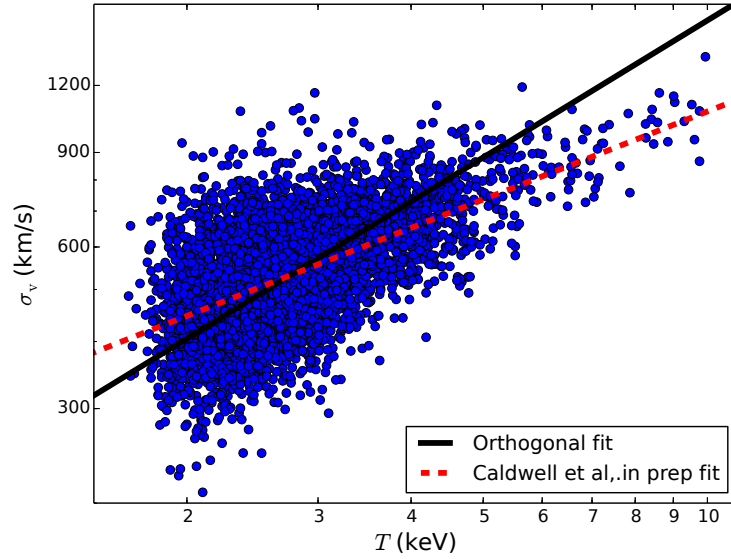


Figure 3.7: Plot showing the $\sigma_v - T_X$ relation for the BAHAMAS simulation data. The blue circles represent the data points from the simulation. An error of 1% was assumed on both the velocity dispersion and temperature as this was not calculated by the simulation. The solid line is the fit obtained using the orthogonal method and the dashed line is the fit obtained using the method described in Section 3.5.2 and performed by Caldwell et al., in prep. From this it can be seen that the orthogonal fit over-estimates the velocity dispersion at $T_X > 5$ keV (see Section 3.5.2).

3.5.3 The effect of biased slope measurements on the evolution of the normalisation

Having seen, using the BAHAMAS simulation, that the temperature distribution of the sample can affect the slope recovered using the orthogonal regression method, we now discuss the potential impact of a biased slope measurement on our conclusions regarding the observed cluster sample in Section 3.5.1. To investigate this, we generated 1000 mock samples (each containing 38 clusters) from the BAHAMAS simulation with the same temperature distribution as the observed sample, and applied the orthogonal regression method. Fig. 3.8 shows the distribution of recovered slope values. The average is $B = 0.69 \pm 0.13$, which is 2σ higher than the slope obtained from the uniform T_X distribution sub-sample of BAHAMAS (Section 3.5.2). Therefore, if the BAHAMAS sample is representative of the real cluster population, then we would conclude that the slope we have measured for the observed cluster sample is biased high.

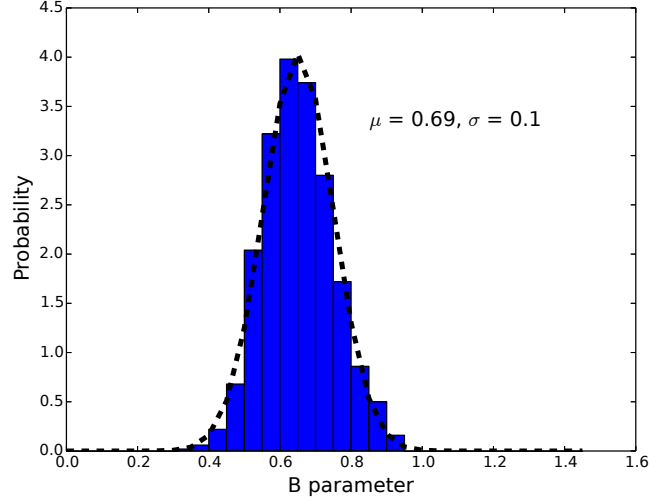


Figure 3.8: This histogram shows the probability of getting a specific value for the slope of the best-fit $\sigma_v - T_X$ relation given a mock cluster sample, drawn from BAHAMAS with temperature distribution matched to the observed cluster sample. We chose various sub-samples from the BAHAMAS simulation which had the same T_X distribution as our sample and calculated the slope for each. The mean slope obtained is $B = 0.69 \pm 0.13$, which is within 2σ of the value obtained from the uniform T_X sample shown in Figure 3.7, so there is a slight bias from the distribution of the sample.

To check if such a biased slope estimate affects our conclusions regarding the lack of significant evidence for evolution of the normalisation of the relation (Section 3.4.2), we fixed the slope to $B = 0.5$ and re-ran the orthogonal fit for the observed cluster sample. We found $C = 0.15 \pm 0.28$, which is consistent with no evolution (Fig. 3.9). Therefore, even if the slope value of $B = 0.86 \pm 0.14$ that we measured was biased high for any reason, this does not affect our conclusion that we do not see significant evidence in favour of evolution.

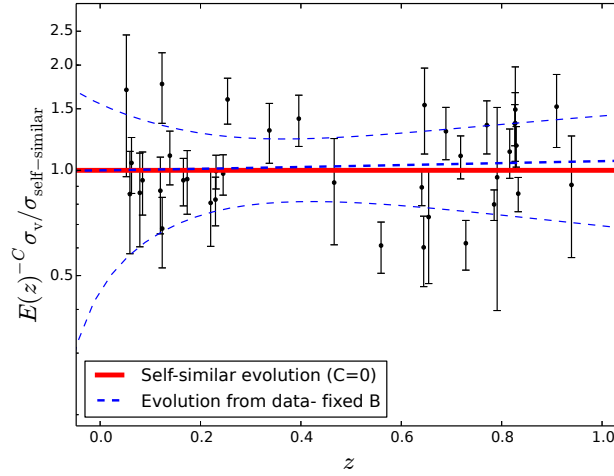


Figure 3.9: Plot showing the evolution of the normalisation of the $\sigma_v - T_X$ relation, with $B = 0.5$, obtained for the observed cluster sample with the 95% confidence intervals in the blue dashed lines, as compared to the self similar relation which predicts no evolution, shown as the red solid line. The black points show the measurements for the clusters in our sample.

3.5.4 Comparison with simulations - evolution

We now investigate evolution in the normalisation of the $\sigma_v - T_X$ relation in the simulations by fitting for the value of C , as we did for the observed sample (see Section 3.4.2). The results are shown in Table 3.7 and graphically in Fig. 3.10. The BAHAMAS simulation with free or fixed slope ($B = 0.5$) is consistent with zero evolution. However, the simulations from the Millennium Gas Project show small but significant positive evolution ($C = 0.273 \pm 0.013$ for σ_{Gal} and T_{sl}). To see the reason for this, we can re-write the $\sigma_v - T_X$ relation in terms of the $\sigma_v - M$ and $T - M$ relations, where M is the cluster mass (see, e.g., Maughan, 2014). We define

$$\sigma_v = 10^{A_{\sigma_v T}} \left(\frac{T}{5 \text{ keV}} \right)^{B_{\sigma_v T}} E(z)^{C_{\sigma_v T}}, \quad (3.8)$$

where

$$\begin{aligned} B_{\sigma_v T} &= B_{\sigma_v M} / B_{TM}, \\ A_{\sigma_v T} &= A_{\sigma_v M} - A_{TM} B_{\sigma_v T}, \text{ and} \\ C_{\sigma_v T} &= C_{\sigma_v M} - C_{TM} B_{\sigma_v T}. \end{aligned} \quad (3.9)$$

Here, A , B , and C have the same meaning as before, and the subscripts indicate the corresponding relation (e.g., B_{TM} indicates the slope of the $T - M$ relation). If we set $C_{\sigma_v M} = \frac{1}{3}$, $C_{TM} = \frac{2}{3}$, and $B_{\sigma_v T} = \frac{1}{2}$ as predicted by the self-similar relation, then we obtain $C_{\sigma_v T} = 0$ as expected.

We performed fits to determine the values of $C_{\sigma_v M}$, C_{TM} , and $B_{\sigma_v T}$ in the Millennium Gas simulation at $z = 0$ and $z = 0.5$. We found that $C_{\sigma_v M} = \frac{1}{3}$ when using either σ_{Gal} or σ_{DM} as the measure of σ_v , and that $B_{\sigma_v T}$ varied from 0.55–0.6, depending on whether spectroscopic-like or mass-weighted temperature estimates were used. This is slightly higher than the self-similar value, but not by enough to explain the positive evolution measured in the $\sigma_v - T_X$ relation. This leads to the conclusion that the evolution is driven by the value of C_{TM} , and it was found that the measured value for the dark matter was $C_{TM} = \frac{2}{3}$ as expected, but that this decreased to values between 0–0.2 for the gas. Therefore, in the Millennium Gas simulation, the lack of redshift evolution in the $T - M$ relation drives the positive evolution in the $\sigma_v - T_X$ relation.

The most likely explanation for the lack of redshift evolution in the $T - M$ relation in the Millennium Gas simulation is the absence of radiative cooling. When both cooling and feedback are included in simulations (as in BAHAMAS), the feedback acts as a regulation mechanism, heating the surrounding dense gas and expelling it from the cluster core. This in turn leads to higher-entropy gas flowing inwards. In the Millennium Gas simulation, the feedback model heats the gas and directly increases its entropy, which is eventually distributed throughout the cluster. This builds up over time as more and more energy is pumped into the gas from the growing black holes, and has the effect of slowing down the evolution of the $T - M$ relation (compared to the evolution expected due to the decreasing background density with redshift). This in turn leads to the positive evolution of the $\sigma_v - T_X$ relation. It is likely that the more sophisticated feedback model used in BAHAMAS, where the entropy evolution is driven by radiative cooling, is the more realistic of the two.

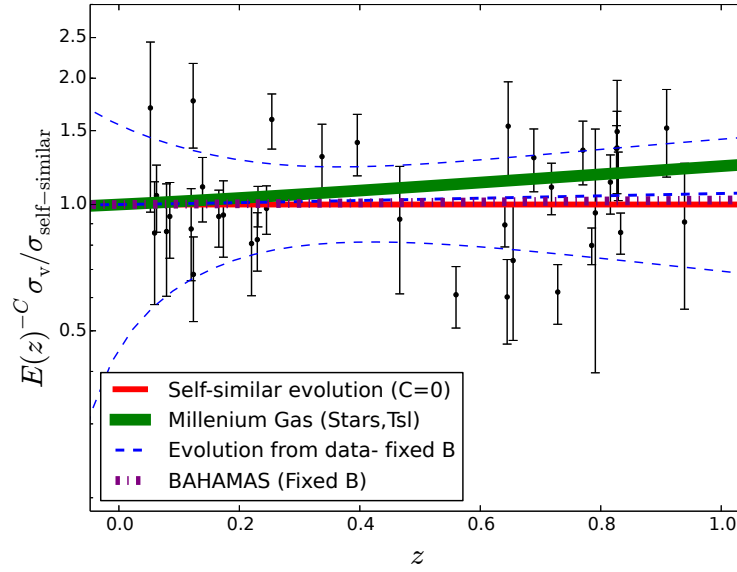


Figure 3.10: We compared the evolution of the normalisation of $\sigma_v - T_X$ relation of the Millenium Gas and BAHAMAS simulations with the self similar relation and that found from our data using a fixed slope. The red solid line shows the line representing the self-similar relation i.e., $C = 0$, the dot-dashed line represents the BAHAMAS simulation results with a fixed B to avoid bias due to the sample distribution, and the solid thick green line represents the result from the Millennium Gas simulation. The blue dashed line, and corresponding 95% confidence interval, and black points are our orthogonal fit and observed sample, respectively.

3.6 Conclusion

In this chapter we studied the $\sigma_v - T_X$ relation. We discussed the importance of this relation in terms of astronomy and cosmology. We calculated the velocity dispersion of each of the clusters in our sample and presented the method that was used to fit the scaling relation. We compared our results to previous studies and simulations. We determined that the slope for our $\sigma_v - T_X$ relation was consistent with previous results and slightly steeper than the self-similar model predicts. We also tested for evolution of the normalisation of the $\sigma_v - T_X$ relation and found it to be slightly negative but not significantly different from the expected result of no evolution.

Table 3.7: Best fit values for the parameters in Equation 3.2 (slope B , intercept A , scatter S and evolution C) for the various models obtained from simulations. All abbreviations are as in Table 3.6.

Simulation	σ_{tracer}	T_{model}	A	B	S	C
Millennium Gas	DM	T_{sl}	-0.031 ± 0.002	0.551 ± 0.006	0.0220 ± 0.0010	0.371 ± 0.014
Millennium Gas	Galaxies	T_{sl}	-0.056 ± 0.002	0.619 ± 0.009	0.0295 ± 0.0010	0.397 ± 0.019
BAHAMAS (fixed B)	Galaxies	T_s	-0.135 ± 0.002	0.545	0.0390 ± 0.0010	0.046 ± 0.016
BAHAMAS (varying B)	Galaxies	T_s	-0.071 ± 0.005	0.779 ± 0.014	0.0570 ± 0.0010	-0.029 ± 0.024

CHAPTER 4

MASS-TEMPERATURE SCALING RELATION

This chapter follows a similar arrangement to Chapter 3, however here we study a cluster mass – temperature scaling relation. We show the calculation for two types of masses: a dynamical mass, which is an optical-based measurement, and an X-ray-determined mass. In each case we fit for a scaling relation between the mass and the X-ray temperature using two Bayesian methods: the orthogonal method described in Chapter 3, and one implementing a Gaussian mixture model likelihood. We compare our results to previous studies and simulations and make a comparison between hydrostatic and dynamical masses.

4.1 History

As previously mentioned, galaxy clusters can be used as a probe of cosmology, but this requires a knowledge of the mass of the galaxy clusters. As discussed in Chapter 1, the mass of a galaxy cluster is not a directly measurable quantity and therefore we rely on observable cluster measurements, such as X-ray properties, the SZ effect, shear due to gravitational lensing, and optical properties, as mass tracers.

By using X-ray properties of galaxy clusters and the assumption that they are in hydrostatic equilibrium, a hydrostatic mass estimate can be calculated, using the following equation (Sarazin, 1988),

$$M(r) = -\frac{kT_g(r)r}{\mu m_p G} \left(\frac{d \ln n_e}{d \ln r} + \frac{d \ln T_g(r)}{d \ln r} \right). \quad (4.1)$$

In this equation, the cluster mass, $M(r)$, within radius r , is dependent on the gas density, n_e , and the temperature profile, $T_g(r)$. Both the temperature and gas density are found by spectral fitting and the X-ray surface brightness, respectively. The mass is only weakly dependent on the gas density, as it only enters into the equation as a logarithmic derivative, but is strongly dependent on the temperature profile.

Since we have studied the $\sigma_X - T_X$ relation, making comparisons to previous studies and simulations, and were able to constrain our velocity dispersion measurements efficiently, we use this relation to calculate a dynamical mass (M_δ^{dyn}) for each cluster in our sample. A comparison between this and the aforementioned hydrostatic mass method will be given in Section 4.4.5. The dynamical mass can then be tested by determining the mass-temperature relation and comparing it to previous results and models.

The self-similar model discussed in Chapter 1 predicts that the mass-temperature relation will take the form $E(z)M_\delta^{dyn} = A_\delta \left(\frac{T}{5\text{keV}}\right)^{\frac{3}{2}}$, if the clusters are in hydrostatic equilibrium. A_δ is dependent on the internal structure of the clusters Arnaud et al. (2005). Although several previous studies have been done, no consensus has yet been reached regarding whether or not this prediction is correct (see, e.g. Maughan et al., 2006; Mantz et al., 2010a; Vikhlinin et al., 2006b; Castillo-Morales and Schindler, 2003; Ettori et al., 2002; Finoguenov et al., 2001; Nevalainen et al., 2000). In this chapter, we provide the results from the fit of the scaling relation and compare the results to previous studies and simulations.

4.2 Galaxy cluster masses

For this thesis we calculated two different masses: the dynamical mass, M_{200}^{dyn} , and the X-ray mass, M_{200X} . The dynamical masses were calculated using the scaling relation obtained from simulations by Munari et al. (2013). They use subhalos and galaxies to get a relation of the form

$$\sigma \text{ (km s}^{-1}\text{)} = A \left(\frac{0.7 E(z) M_{200}^{dyn}}{10^{15} M_{\odot}} \right)^{\alpha}, \quad (4.2)$$

where $A = (1177 \pm 4.2) \text{ km s}^{-1}$, $\alpha = 0.364 \pm 0.0021$, $E(z) = \sqrt{\Omega_m(1+z)^3 + \Omega_{\Lambda}}$, and the 0.7 factor accounts for the fact that we assume $H_0 = 70 \text{ km s}^{-1} \text{ Mpc}^{-1}$. A and α are, respectively, the normalisation and slope obtained by Munari et al. (2013) when using a cosmological hydrodynamical simulation which included a model for AGN feedback and used galaxies as the velocity tracers.

The X-ray masses were calculated using the scaling relation obtained by Arnaud et al. (2005). They studied the $M_{200X} - T_X$ relation at various densities for 10 relaxed, nearby clusters, with temperatures in the range 2-9 keV. The masses are calculated using the hydrostatic mass equation (Eqn. 4.1) and a NFW-type model, described in Navarro et al. (1997), who studied density profiles of dark matter halos using high-resolution N-body simulations. Arnaud et al. (2005) found that the $M_{200X} - T_X$ relation was consistent and well-constrained over a variety of densities, and was of the form,

$$E(z) M_{200X} = A_{200} \left[\frac{kT}{5 \text{ keV}} \right]^{\alpha}, \quad (4.3)$$

where $A_{200} = (5.34 \pm 0.22) 10^{14} M_{\odot}$, $\alpha = 1.72 \pm 0.10$, and $E(z)$ is the Hubble constant normalised to its local value and it is used to correct for the evolution expected in the self-similar relation.

Tables 4.1 and 4.2 give the two masses for each cluster in the low and high redshift samples, respectively.

Table 4.1: Calculated masses of the low redshift sample ($0.0 < z < 0.5$). Column 1 gives the name of the XCS Cluster. Columns 2 and 3 give the calculated dynamical and X-ray masses, respectively.

Cluster Name	M_{200}^{dyn} ($10^{14}M_{\odot}$)	M_{200X} ($10^{14}M_{\odot}$)
XMMXCS J000013.9-251052.1	0.76 ± 0.41	0.89 ± 0.26
XMMXCS J003430.1-431905.6	5.90 ± 2.64	2.01 ± 0.16
XMMXCS J005603.0-373248.0	6.31 ± 2.69	4.49 ± 0.33
XMMXCS J015315.0+010214.2	0.18 ± 0.16	0.37 ± 0.02
XMMXCS J072054.3+710900.5	1.57 ± 0.47	1.49 ± 0.22
XMMXCS J081918.6+705457.5	0.71 ± 0.33	1.12 ± 0.31
XMMXCS J094358.2+164120.7	1.89 ± 0.79	0.67 ± 0.21
XMMXCS J095957.6+251629.0	1.40 ± 1.66	0.43 ± 0.03
XMMXCS J100047.4+013926.9	1.66 ± 1.14	2.23 ± 0.19
XMMXCS J100141.7+022539.8	2.02 ± 1.22	0.58 ± 0.03
XMMXCS J104044.4+395710.4	5.64 ± 2.70	2.96 ± 0.05
XMMXCS J111515.6+531949.5	5.49 ± 5.14	4.79 ± 1.33
XMMXCS J115112.0+550655.5	0.42 ± 0.35	0.71 ± 0.05
XMMXCS J123144.4+413732.0	1.13 ± 0.64	1.32 ± 0.20
XMMXCS J151618.6+000531.3	5.91 ± 4.09	4.87 ± 0.12
XMMXCS J161132.7+541628.3	4.07 ± 2.09	1.81 ± 0.49
XMMXCS J163015.6+243423.2	3.47 ± 1.74	2.24 ± 0.42
XMMXCS J223939.3-054327.4	1.66 ± 0.56	1.61 ± 0.22
XMMXCS J233757.0+271121.0	1.02 ± 0.67	2.17 ± 0.40

Table 4.2: Calculated masses of the high redshift sample ($0.0 < z < 0.5$). Column 1 gives the name of the XCS Cluster. Columns 2 and 3 give the calculated dynamical and X-ray masses, respectively.

Cluster Name	M_{200}^{dyn} ($10^{14}M_{\odot}$)	M_{200X} ($10^{14}M_{\odot}$)
XMMXCS J000216.1-355633.8	7.94 ± 3.68	3.26 ± 1.05
XMMXCS J005656.6-274031.9	0.48 ± 0.20	1.92 ± 0.34
XMMXCS J015241.1-133855.9	3.67 ± 1.74	1.69 ± 0.32
XMMXCS J021734.7-051326.9	1.76 ± 1.60	1.12 ± 0.24
XMMXCS J025006.4-310400.8	7.71 ± 4.75	2.64 ± 0.66
XMMXCS J030205.1-000003.6	1.69 ± 1.33	5.41 ± 0.86
Continued on next page		

Table 4.2 – continued from previous page

Cluster Name	M_{200}^{dyn} ($10^{14}M_{\odot}$)	M_{200X} ($10^{14}M_{\odot}$)
XMMXCS J095417.1-173805.9	5.00 ± 4.39	1.55 ± 0.30
XMMXCS J095940.7+023113.4	0.79 ± 0.40	3.63 ± 0.79
XMMXCS J105659.5-033728.0	6.06 ± 1.92	6.71 ± 0.63
XMMXCS J112349.4+052955.1	1.61 ± 1.50	3.19 ± 0.89
XMMXCS J113602.9-032943.2	2.22 ± 0.93	1.68 ± 0.35
XMMXCS J114023.0+660819.0	5.27 ± 1.48	7.35 ± 1.44
XMMXCS J124312.2+131307.2	3.16 ± 4.91	2.22 ± 0.55
XMMXCS J134305.1-000056.8	5.09 ± 2.52	2.97 ± 0.74
XMMXCS J145009.3+090428.8	1.85 ± 0.71	2.43 ± 0.66
XMMXCS J182132.9+682755.0	3.94 ± 1.59	2.62 ± 0.65
XMMXCS J215221.0-273022.6	1.03 ± 0.78	0.70 ± 0.13
XMMXCS J230247.7+084355.9	6.47 ± 2.23	4.02 ± 0.73
XMMXCS J235616.4-344144.3	1.85 ± 1.91	3.46 ± 0.56

4.3 Fitting the Mass – Temperature relation

To determine the scaling relation between the cluster mass and X-ray temperature, we need to fit a power law of the form

$$\log \left(\frac{E(z)M_{\delta}^{dyn}}{10^{14}M_{\odot}} \right) = \log A_{\delta} + B \log \left(\frac{T}{5 \text{ keV}} \right). \quad (4.4)$$

Here, 5 keV and $10^{14}M_{\odot}$ are the pivot temperature and pivot mass for our fit, and $E(z) = \sqrt{\Omega_m(1+z)^3 + \Omega_{\Lambda}}$. M_{δ} refers to the mass being calculated in a radius R_{δ} , where the mean density is δ times the critical density of the Universe at the cluster redshift. In this work, we make use of $\delta=200$ and $\delta=500$. The M_{200} dynamical masses shown in Tables 4.1 and 4.2 are converted to M_{500} , for ease of comparison to other work, using the $c - M$ relation given in Duffy et al. (2008). We consider two methods for fitting this power law: the orthogonal method used in Chapter 3, and the Bayesian Gaussian mixture model of Kelly (2007).

Table 4.3: Priors on $M_\delta^{\text{dyn}} - T$ relation fit parameters

Parameter	Uniform Prior
A	(0.0, 1.0)
B	(0.0, 5.0)
S	(0.01, 1.0)

4.3.1 Orthogonal fitting

Similarly to Chapter 3, the best fit values for A and B were found using Markov Chain Monte-Carlo (MCMC) with the Metropolis algorithm, using both the orthogonal and bisector fitting methods. However, for the $M - T_X$ relation we only consider the orthogonal method.

The probability for a given cluster to be drawn from the model scaling relation is the same as in Equation 3.2. However, Δr is now defined by the errors on $\log(E(z)M_\delta)$ and $\log T$. Priors for the fit are listed in Table 4.3, with the likelihood, \mathcal{L} , given in Equation 3.5, now having the following form:

$$\mathcal{L}(E(z)M_\delta^{\text{dyn}}, T_X | A, B, S) \propto P_{\text{prior}}(A, B, S) \prod_i P_{\text{model},i}. \quad (4.5)$$

4.3.2 Gaussian mixture model approach to fitting

Kelly (2007) uses a Bayesian Gaussian mixture model to account for measurement errors when performing linear regression. A detailed account is provided in their paper - in this section we highlight the key points and reference the relevant equations.

In this fitting procedure, linear regression of y on x is performed when measurement errors are present in both variables. The likelihood function, which describes the regression, is given by Equations 16-18 in Kelly (2007). The regression assumes the following:

$$\eta = \alpha + \beta \times x_i + \epsilon, \quad (4.6)$$

where $x = x_i + x_{err}$ and $y = \eta + y_{err}$. α and β are the regression coefficients and ϵ is the intrinsic random scatter. The measurement error in x and y are given by x_{err} and y_{err} , respectively. The distribution of the independent variable, x_i , is estimated using a mixture of Gaussian functions.

To determine the best fit values, Bayesian interference is used. A Markov chain is developed using a Gibbs sampler (Geman and Geman, 1984) based on the model parameters, the observed data, and the missing data. After each iteration the model parameters and missing data are re-determined. This process continues until convergence which is monitored using the potential scale reduction factor (R.hat, Gelman et al. 2004). The process is said to have reached convergence when $R.hat < 1.1$.

To apply this fitting method, we use the python implementation by Joshua Meyers¹. This method of fitting was not used in our analysis of the $\sigma_v - T_X$ relation in Chapter 3 because it has not been adapted to include the possibility of evolution. However, we were able to show using the orthogonal method and simulations that no evolution was present in the $\sigma_v - T_X$ relation. Therefore, since the mass is calculated from σ_v , we can assume that the $M - T_X$ relation is not evolving and can use this Bayesian Gaussian mixture model to the fitting.

4.4 Results and Analysis

4.4.1 Expected slope vs Measured Slope

We fitted both the $M_{200}^{dyn} - T_X$ and the $M_{500}^{dyn} - T_X$ relation using the orthogonal and Bayesian Gaussian mixture model methods described in Section 4.3. Both M_{200}^{dyn} and M_{500}^{dyn} are included here to allow for comparison with previous studies and simulations. However, they are not independent results as M_{500}^{dyn} is a scaled result of M_{200}^{dyn} . Our best-fit results are shown in Table 4.4 and Figure 4.1. For the orthogonal approach, the slope for both the $M_{200}^{dyn} - T_X$ and the

¹Code available at: <https://github.com/jmeyers314/linmix>

$M_{500}^{dyn} - T_X$ relations are much steeper than the expected value of $B = 1.5$, however, they both fall within 3σ of this value. The Bayesian Gaussian mixture model method results in a shallower than expected slope, but it is more consistent with the expected result than the orthogonal result as it falls within 2σ of $B = 1.5$.

Table 4.4: Best fit values for the parameters in Equation 4.4 (slope B , intercept A , and scatter S) for different values of δ and the two different methods.

Method	δ	$A(\times 10^{14})$	B	S
Orthogonal	200	7.13 ± 1.21	2.43 ± 0.30	0.11 ± 0.03
Orthogonal	500	6.03 ± 1.27	2.44 ± 0.37	0.12 ± 0.03
Kelly (2007)	200	3.70 ± 1.17	1.30 ± 0.28	0.25 ± 0.05
Kelly (2007)	500	2.76 ± 1.17	1.11 ± 0.29	0.26 ± 0.05

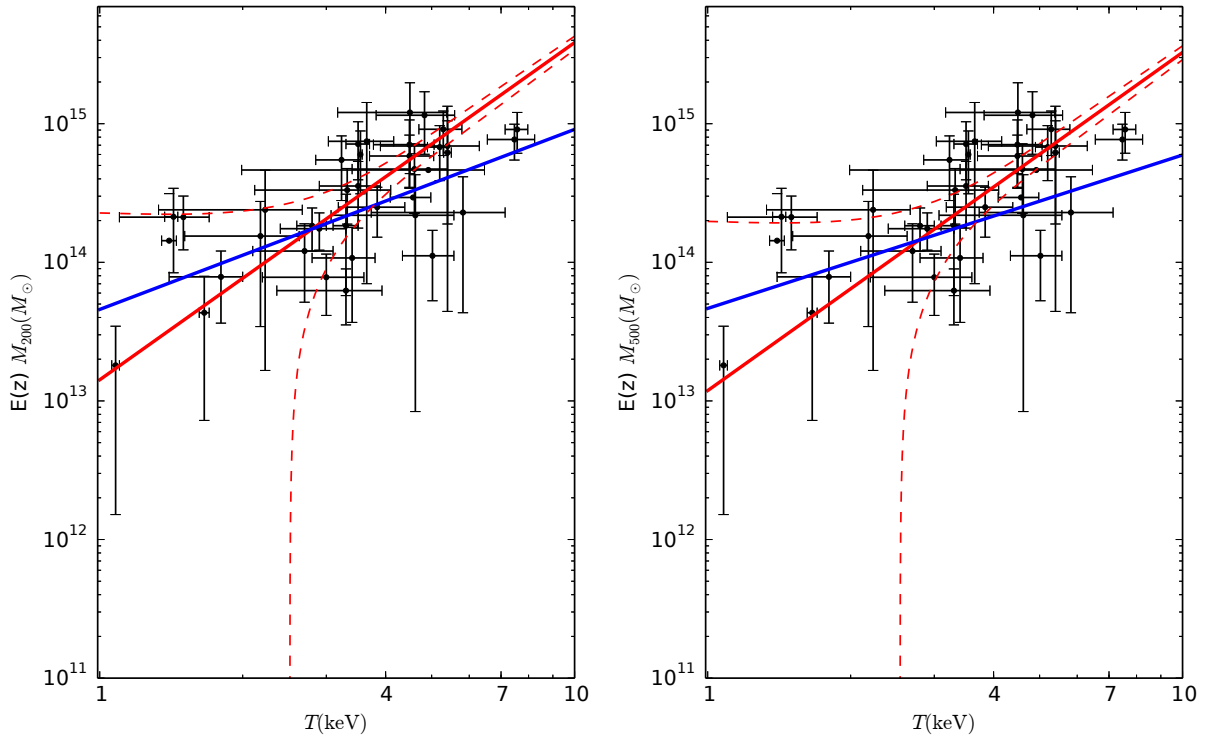


Figure 4.1: The $M_{\delta}^{dyn} - T_X$ relation for $\delta = 200$ and $\delta = 500$. The solid red line shows the orthogonal regression fit to the data with the dotted red line showing the 95 % confidence interval. The solid blue line represents the fit obtained using the Bayesian Gaussian mixture model described by Kelly (2007). The best fit parameter values are given in Table 4.4.

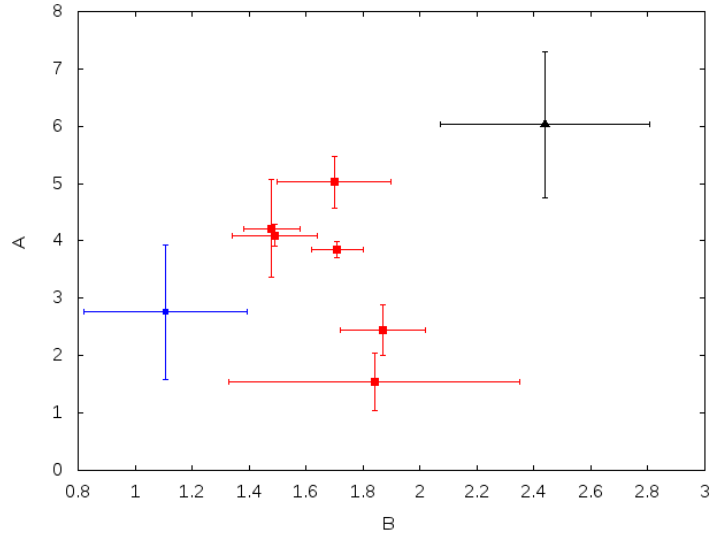


Figure 4.2: This is a summary plot of A and B parameter values in the $M_{500} - T_X$ relation for previous studies shown as red squares. It is noted that these studies used hydrostatic masses and not dynamical masses like our work. We also plot our fitted values as a black triangle for the orthogonal MCMC method and the blue square for the Bayesian Gaussian mixture model method derived by Kelly (2007).

4.4.2 Comparison with previous results

Some studies of the $M_\delta - T_X$ relation have been done previously, (see, e.g., Castillo-Morales and Schindler, 2003; Ettori et al., 2002; Finoguenov et al., 2001; Nevalainen et al., 2000), but it is still unclear if it follows the expected slope of $B = 1.5$. Most of these studies use $\delta = 500$ or higher, so for ease of comparison to previous measurements we will use the results obtained for the $M_{500} - T_X$ relation. Results of these previous studies are shown in Table 4.6 at the end of this chapter. Other studies, such as Maughan et al. (2006) and Mantz et al. (2010a) calculate the $M_\delta - T_X$ relation in a different manner or with a different δ and are therefore not studied here. We show a comparison between previous studies and our results graphically in Figure 4.2. Unlike our work, where we calculate the dynamical mass based on the velocity dispersion, all the previous studies calculate a hydrostatic mass estimate using the X-ray temperature and surface brightness profiles as described in Section 4.1. The differences between these masses will be discussed in Section 4.4.5.

Finoguenov et al. (2001) suggest that discrepancies in the slope may be caused by the inclusion of low mass or low temperature systems. They performed three separate studies to test these suggestions and compare their results to the expected value of $B = 1.5$ and the value obtained with their complete sample of 39 clusters ($B = 1.78 \pm 0.09$). In the first test they removed all galaxy groups from their sample ($M_{500} < 5 \times 10^{13} M_{\odot}$) and found that the slope decreased to $B = 1.58 \pm 0.07$, which is consistent with the expected value. They also tested the effect of the temperature on the sample by performing a fit for all clusters with $T_X > 3.0$ keV and $T_X < 4.5$ keV. They found a much steeper relation of $B = 1.87 \pm 0.15$ for the cooler clusters. This steeper slope is in agreement with studies by Nevalainen et al. (2000) and Arnaud et al. (2005), who also include low temperature clusters in their sample and get slopes of $B \sim 1.70 - 1.84$. Arnaud et al. (2005) also find a decrease in the slope ($B = 1.49 \pm 0.154$) when they exclude the lowest temperature clusters. A study by Castillo-Morales and Schindler (2003), however, contradicts this finding by obtaining a slope of $B = 1.70 \pm 0.20$ when using a sample with clusters with $T_X > 4.7$ keV.

For our sample, our temperature is in the range $1.0 < T_X < 9.0$ keV. Our sample size of 38 clusters offers an improvement on all previous studies except that of Finoguenov et al. (2001). From our fits we obtain $B = 2.44 \pm 0.37$ and $B = 1.11 \pm 0.29$ for the orthogonal and Bayesian Gaussian mixture model fits, respectively. The orthogonal slope is much higher than found in all other previous literature but is within 3σ of the expected value. The Bayesian Gaussian mixture model fit appears to be in good agreement with the expected value but is less than that determined by previous studies. Due to the small sample of previous measurements, we can not definitively determine which of our two methods is performing the fit better, and therefore we compare them using simulated data for which the slope is known. We again note that as we are using dynamical masses instead of X-ray hydrostatic masses for these comparisons, we expect some variation in the results.

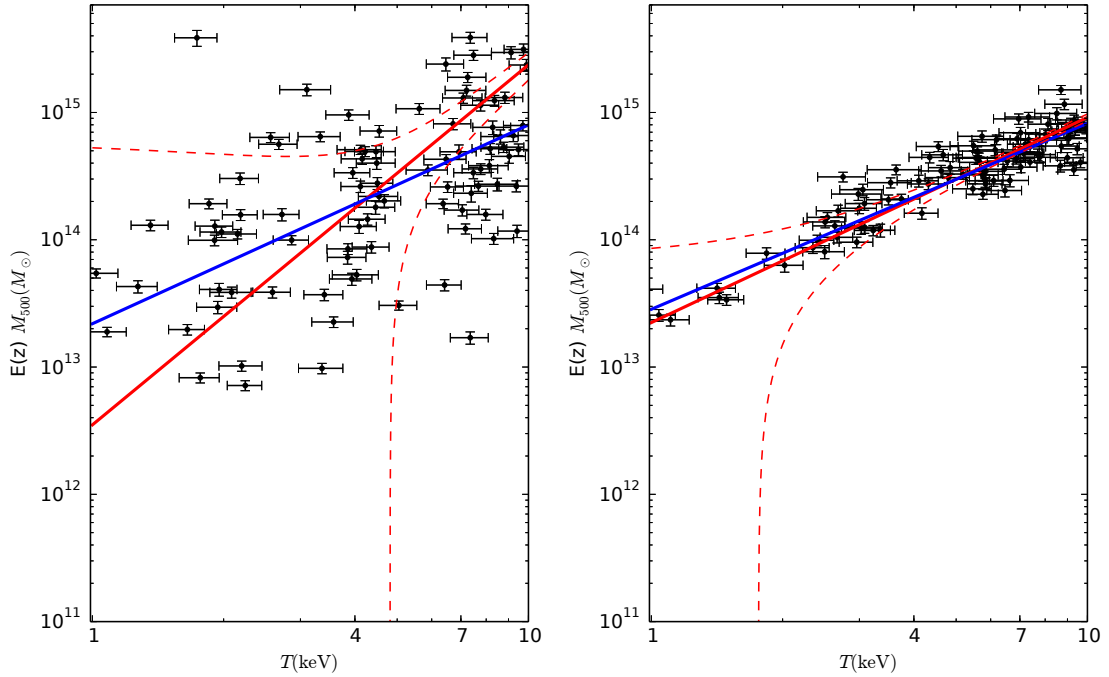


Figure 4.3: In this plot we show a set of simulated data (black points), with the red solid (blue dashed) best fit line obtained using the orthogonal (Bayesian Gaussian mixture model) fitting method. The red dashed lines show the 95% confidence interval for the orthogonal fit. The image on the left has an intrinsic scatter, $S = 0.3$ and the image on the right has an intrinsic scatter, $S = 0.05$. For the image on the left, the orthogonal fit has a much higher slope than that from the Bayesian Gaussian mixture model fitting method, resulting in an under-estimation of the mass at low T_X values and an over-estimation at high T_X values. For the image on the right, the orthogonal and Bayesian Gaussian mixture model are in agreement and accurately recover the slope and normalisation.

4.4.3 Comparison of fitting methods

To create our mock data, we simulated 100 random points with the same temperature range as our sample and calculated the corresponding M_{500} values based on a correlation with slope $B = 1.5$, intercept $A = 3.16$ and scatter $S = 0.3$. Errors of 10% are then added onto both M and T . Both fitting methods were then used to determine best fit values for the parameters, an example of which is shown in Figure 4.3. This process was repeated 1000 times to produce the posterior distribution of the recovered fit parameters. We calculated the mean and the standard deviation of this distribution and retrieved the values for the parameters. For the orthogonal method the fit was found to have the form $M_{500}^{dyn} = (3.81 \pm 0.61) \times 10^{14} \left(\frac{2.78 \pm 0.07}{5 \text{ keV}} \right)$ and for the Bayesian

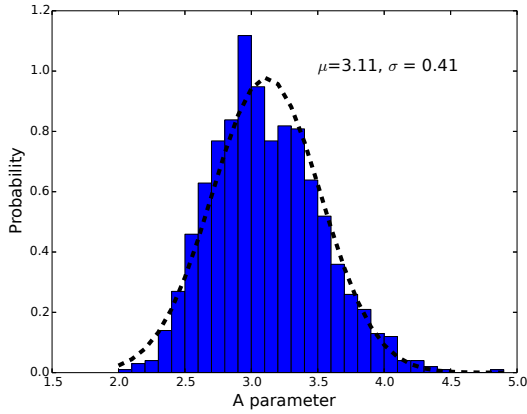
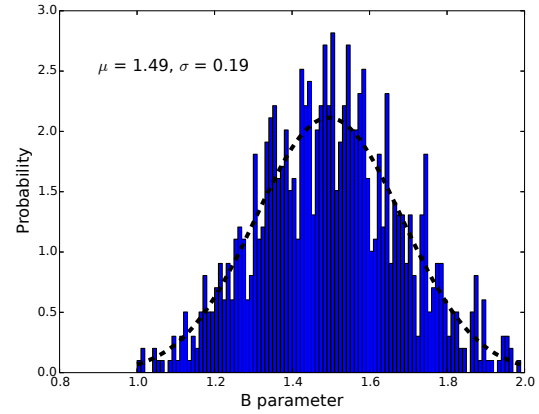
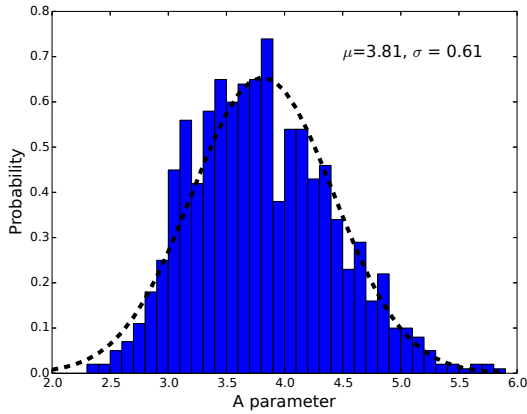
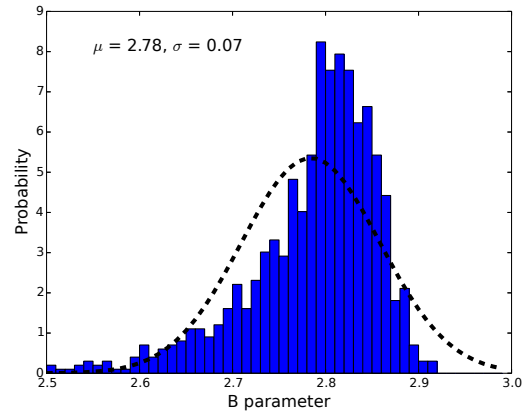
(a) Bayesian Gaussian-mixture-model-based fitting for A (b) Bayesian Gaussian-mixture-model fitting for B (c) Orthogonal fitting for A (d) Orthogonal fitting for B

Figure 4.4: We show the distribution of the two fit parameter values, A and B , for the Bayesian Gaussian mixture model (a and b) and orthogonal (c and d) fitting method. The value for A was well fitted by the Bayesian Gaussian mixture model but was higher than the input parameter ($A = 3.16$) for the orthogonal fitting method. The input value ($B = 1.5$) for B was well recovered by the Bayesian Gaussian mixture model fitting method, but was much steeper for the orthogonal fitting method.

Gaussian mixture model it was $M_{500}^{dyn} = (3.11 \pm 0.41) \times 10^{14} \left(\frac{1.49 \pm 0.19}{5\text{keV}} \right)$. The histograms with parameter values are shown Figure 4.4.

Due to the high value for the orthogonal fit, we investigated further to try to determine the cause of the high bias. We varied the values for the scatter when making our simulated data

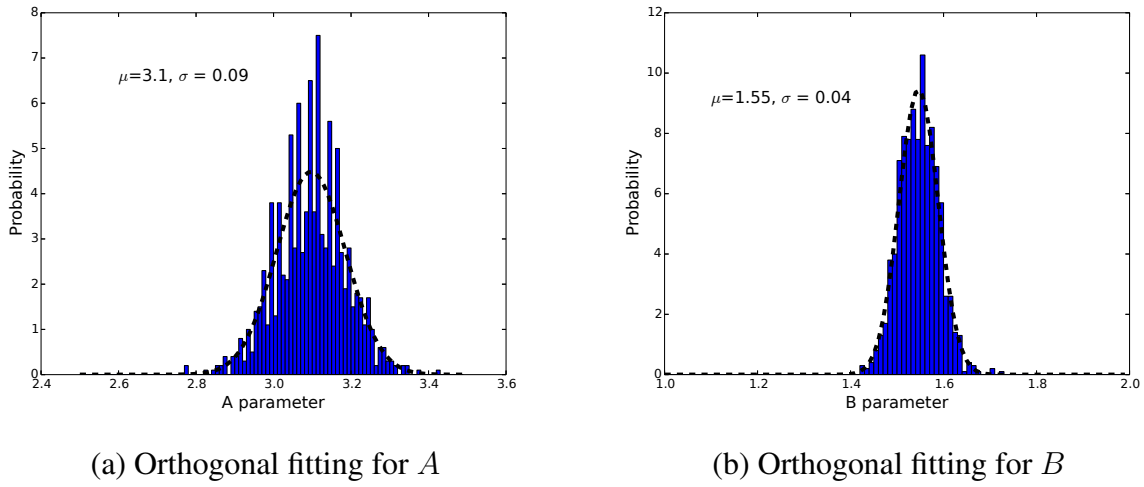


Figure 4.5: We show the distribution of the two fit parameter values, A (a) and B (b), for the orthogonal fitting method when the intrinsic scatter is reduced to $S = 0.05$. For this small intrinsic scatter we were able to accurately recover both the slope and normalisation when using the orthogonal method.

and found that if the scatter was decreased to $S = 0.05$ then the slope was recovered accurately (Figure 4.5). When a plot has high scatter, the orthogonal method under-estimates it producing an over-estimated slope. Therefore, the higher the scatter the higher the bias on the slope.

This concern regarding the inability of the orthogonal method to accurately recover the slope of a fit, resulted in us re-examining the $\sigma_v - T$ results. However, we found that the intrinsic scatter in our $\sigma_v - T$ relation for all of our orthogonal fits was ~ 0.05 . Therefore we believe that our fitting for the $\sigma - T$ relation is not affected. Also, if we consider the qualitative sense of the result of a biased fit by the orthogonal regression it means the slope value may be biased. However, we showed in Chapter 3, that a biased slope value doesn't affect the conclusion that there is no significant evolution.

The Bayesian Gaussian mixture model, over-estimates the scatter, resulting in the very slight under estimation of the slope we observe. From these results, we can conclude that the Bayesian Gaussian mixture model fitting method is preferable over the orthogonal method for testing the $M - T_X$ scaling relation when there is large scatter in the data. The most likely reason for

Table 4.5: Best fit values for the parameters in Equation 4.4 (slope B , intercept A , and scatter S) for the two different methods when fitting to the Millennium simulation data.

Method	Tracer	$A (\times 10^{14})$	B	S
Orthogonal	DM	7.80 ± 1.01	1.644 ± 0.016	0.072 ± 0.001
Kelly (2007)	DM	7.11 ± 1.01	1.455 ± 0.018	0.069 ± 0.001
Orthogonal	Galaxies	6.95 ± 1.02	1.895 ± 0.040	0.047 ± 0.001
Kelly (2007)	Galaxies	5.98 ± 1.01	1.587 ± 0.024	0.094 ± 0.002

this is due to the more descriptive likelihood method used in the Bayesian Gaussian mixture model fitting, allowing for a more precise model. We can not conclude if this will always be true, as further studies and different relations would be required. An important point to note is that the success of the Bayesian Gaussian model fitting method is affected by the choice of the independent variable, and this should be taken under consideration when using this fitting procedure. This choice is not always a simple one to make and can therefore negatively impact the obtained results. The method described by Kelly (2007) does have the advantage that if the selection function for your data is known, it can be added into the fit to decrease its effects. This is currently unavailable for our sample as the selection function for XCS is unknown.

4.4.4 Comparison with simulations

As a further check for our work, we use our two fitting methods to determine the $M_{\delta}^{dyn} - T_X$ relation for the Millennium Gas Project simulations used in Chapter 3 for the $\sigma - T$ relation. The results for this fitting are shown in Table 4.5. When using galaxies as the tracer we found that the slope was steeper than expected for both the orthogonal and Bayesian Gaussian mixture model method. This is expected as the $\sigma_v - T$ was also high for the galaxies. When using dark matter as the tracer we find results that are more consistent with the expected result. For the orthogonal fitting method, we obtain $B = 1.644 \pm 0.016$, which is steeper than the expected slope but in agreement with the previous studies, given in Table 4.6, using the same temperature range. The Bayesian Gaussian mixture model method gives a value of $B = 1.455 \pm 0.018$, which is lower than previous literature studies. Figure 4.6 shows these fits plotted with the data from the Millennium Gas simulations. Due to the small scatter in this plot the orthogonal method is producing a

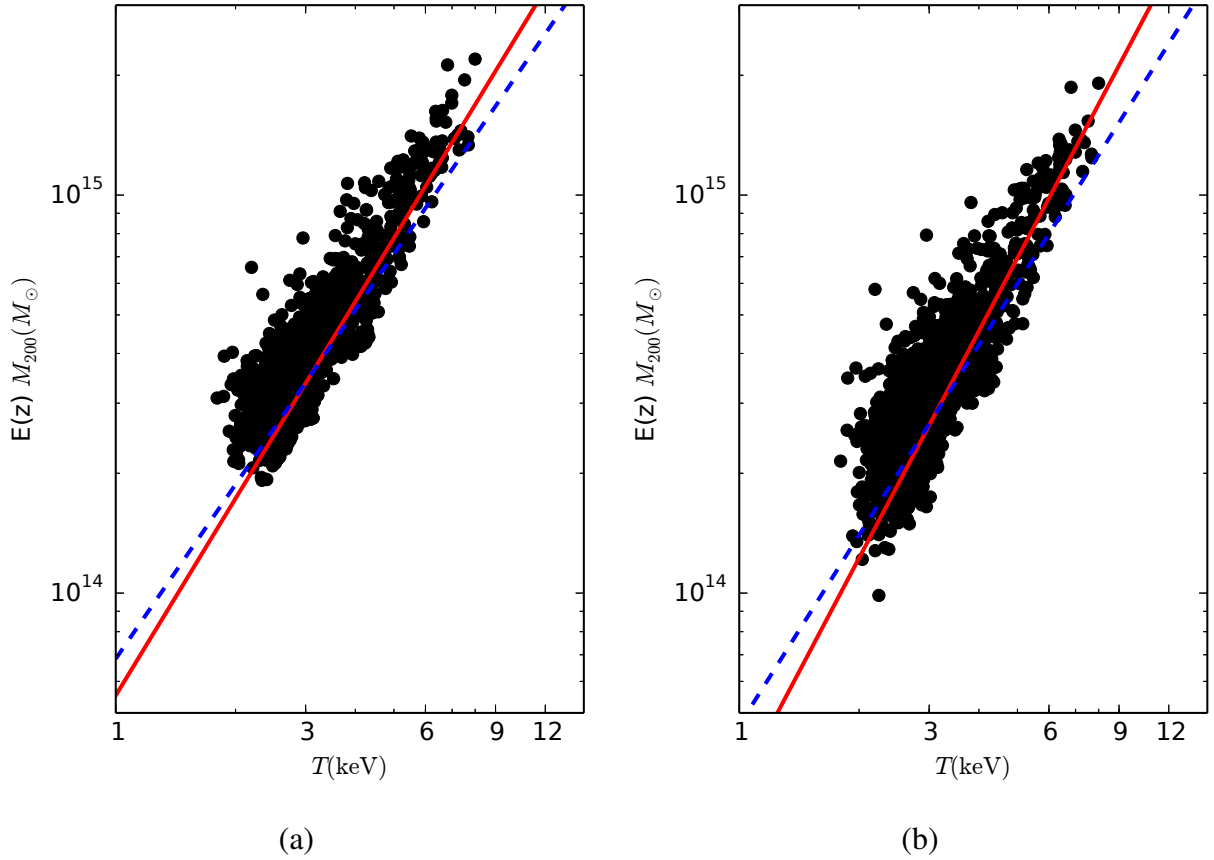


Figure 4.6: We compare the best fit $M_{200}^{dyn} - T_X$ relation for the Millennium Gas Project Simulations for the two fitting methods using both dark matter (a) and galaxies (b) as our tracer. The black points are the simulated data with the red solid line representing the best fit obtained using the orthogonal fitting method. The blue dashed line shows the best fit line obtained for the Bayesian Gaussian mixture model fitting.

reliable result, compared to the Bayesian Gaussian mixture model which is over-estimating the scatter and obtaining an under-estimated relation.

The masses for this simulation are calculated using R_{200} and thus, for easy comparison and to avoid bias possibly introduced by the conversion to M_{500}^{dyn} , we offer a comparison here to our M_{200}^{dyn} relation. In this case, the slope obtained for our data is $B = 2.64 \pm 0.38$, which is steeper than the result obtained for either fit to the simulation data. This steeper than expected slope was also observed in the $\sigma_v - T_X$ relation and it was discussed in detail in Sections 3.5.2 and 3.5.3. We believe that the steepness observed here can be attributed to the same reasoning.

4.4.5 Dynamical Mass vs Hydrostatic Mass

Since all the previous works we use for comparison calculate the mass using the hydrostatic equation rather than dynamically, we wanted to make a comparison between dynamical and X-ray hydrostatic masses. A comprehensive review of the comparisons between mass estimates is given by Sadat (1997). Here we summarise the main findings.

The hydrostatic mass has three main advantages over the dynamical mass we calculated. Firstly, the accuracy at which the hydrostatic mass is calculated is not dependent on the number of galaxies in the cluster, and can be improved by observing the cluster for longer to obtain more X-ray counts (Girardi et al., 1998). The correct method for determining cluster membership also plays a major role with regards to this, and the inclusion of foreground or background sources can cause a bias dynamical mass calculations. This leads to the second advantage which is that X-ray observations are not as greatly affected by foreground galaxies or projection effects (Voit, 2005). It also allows for the detection of substructure which may affect the result. Lastly, since the gas in a cluster is a collisional fluid, the velocities of the particles are isotropically distributed. However, galaxies are collisionless, resulting in velocity anisotropies which can have a negative effect on mass calculations, therefore the mass calculated from the gas, i.e., the hydrostatic mass is better. (Wojtak et al., 2009).

Although the above properties lend support for using hydrostatic masses over dynamical values, there are two very large disadvantages of the hydrostatic mass: the measurement of the temperature profile, and the assumption of hydrostatic equilibrium. The hydrostatic mass is dependent on the density and temperature of the gas within a cluster (Equation 4.1). The density can be measured with relative ease from the surface brightness of the cluster (Croston et al., 2006), but temperatures require sufficient photon statistics to fit and build a spectrum (Leccardi and Molendi, 2008). This requires very long observation times and therefore the temperature profiles are not determined with the same resolution as the density profiles. There is also the added complication by the density squared dependence (n_e^2) on the X-ray emission and the steep

drop in X-ray surface brightness as you move away from the cluster centre (Pratt et al., 2007).

The assumption of hydrostatic equilibrium is a requirement for calculating hydrostatic masses. In order for this to be true, the cluster must be stationary, have no forces except gas pressure and gravity acting on it, and any motions in the gas must be travelling at speeds less than the speed of sound Sarazin (1988). However, clusters are dynamic and active and their state is significantly different from the equilibrium position, resulting in hydrostatic masses under-estimating the mass of the cluster Lau et al. (2013). Therefore the hydrostatic mass bias is one of the largest sources of uncertainty in cluster cosmology (Allen et al. 2008, Vikhlinin et al. 2009, Planck Collaboration et al. 2014d). It is therefore essential to constrain this bias. Without a complete sample, calculating a mass bias is not accurate and therefore we rely on results from simulations.

Simulations have found the hydrostatic bias to be 10%. (see, e.g., Nagai et al., 2007; Jeltema et al., 2008; Piffaretti and Valdarnini, 2008; Meneghetti et al., 2010; Burns et al., 2010; Lau et al., 2013). If this is true for our sample, it implies that our dynamical mass calculation may be over-estimating the mass of the clusters, which can be seen in most of our clusters when a comparison is made between the hydrostatic and dynamical masses. This would cause a steeper than expected $M - T_X$ relation, which is what we observe.

4.5 Conclusions

In this chapter we discussed the importance of the $M - T_X$ relation in terms of astronomy and cosmology. We performed a fit using two methods, the orthogonal method discussed in Chapter 3 and a Bayesian Gaussian mixture model described in Kelly (2007). The orthogonal fit resulted in a steeper than expected slope but which was consistent within 3σ while the Bayesian Gaussian mixture model method provided an improved, but shallower than expected slope. We compared our fitted results to previous studies and found that the Bayesian Gaussian mixture model method gave a consistent result. The slope obtained from the orthogonal method was much higher than all previous studies. We tested the validity of both methods by using a set

of simulated data and determining which recovered the simulated slope most accurately. The Bayesian Gaussian mixture model method was found to be the most consistent over a set of 1000 runs. Upon investigation it was discovered that the slope for the orthogonal method is biased high due to an under-estimation of the scatter. This bias increases for data with larger scatter. The Bayesian Gaussian mixture model over-estimates the scatter, resulting in an under-estimation of the slope. This is clearly seen when determining the fit for Millennium simulation data. Due to the small scatter, the orthogonal result returns the better fit. Previous studies of this relation used hydrostatic masses rather than the dynamical masses used here and therefore we offered a comparison between the two, listing the differences. We also discussed the hydrostatic mass bias and calculated it for our data, finding a bias a little higher than expected. This suggests an over estimation in the masses of our clusters. The correct method for the measurement of the mass of galaxy clusters is still a highly debated topic, with each method having its own set of advantages and disadvantages. This results in high systematic errors in constraining cluster cosmology.

Table 4.6: Previous measurements of the $M_{500} - T_X$ relation. Here the relation is in the form $M_{500} = A \left(\frac{T}{5\text{keV}} \right)^B$, where M_{500} is measured in $10^{14}M_{\odot}$ and T_X is measured in keV.

Paper	Number of clusters	Redshift Range	$A(\times 10^{14})$	B	Temperature Range (keV)
Arnaud et al. (2005)	10	$0.04 < z < 0.15$	3.84 ± 0.14	1.71 ± 0.09	2.0-9.0
Arnaud et al. (2005)	10	$0.04 < z < 0.15$	4.10 ± 0.19	1.49 ± 0.15	3.5-9.0
Castillo-Morales and Schindler (2003)	10	$0.03 < z < 0.09$	5.03 ± 0.45	1.70 ± 0.20	4.7-9.4
Ettori et al. (2002)	20	$0.01 < z < 0.10$		1.89 ± 0.20	3.0-10.0
Finoguenov et al. (2001)	39	$0.01 < z < 0.07$	4.22 ± 0.85	1.48 ± 0.10	3.0-10.0
Finoguenov et al. (2001)	39	$0.01 < z < 0.07$	2.45 ± 0.44	1.87 ± 0.15	0.0-4.5
Nevalainen et al. (2000)	9	$0.01 < z < 0.08$	1.55 ± 0.50	1.84 ± 0.51	0.0-10.0
Vikhlinin et al. (2006b)	13	$0.01 < z < 0.23$	6.19 ± 1.03	1.58 ± 0.11	0.7-9.0'

CHAPTER 5

DIFFUSE RADIO EMISSION

As mentioned in the introduction, the realisation that radio sources and galaxy clusters can be linked occurred in the 1960s. Since then many studies have been performed in the radio wavelength of sources both within the field and clusters. It was discovered that two main types of radio sources exist: diffuse radio emission and compact radio sources. In this chapter, we will focus on the diffuse radio emission and its link to different galaxy cluster properties. Since it was shown that diffuse emission is often a sign of a merger, we will also look at what effect mergers, have on scaling relations. We also present new VLA observations of three of the clusters in our sample. We will also look at where clusters with radio halos lie on the $\sigma_v - T_X$ plane and how they differ from clusters without radio halos.

5.1 Diffuse emission and the link to galaxy cluster properties

The properties of the diffuse emission are linked to the properties of the galaxy cluster. The most well studied is the link between the detection of diffuse emission and its X-ray luminosity. Giovannini et al. (1999) identified that diffuse radio emission is detected more often in clusters with a high X-ray luminosity. They only found this emission in 6-9% of clusters with $L_X < 10^{45}$ erg s⁻¹, but found them to be present in 27-44% of clusters with $L_X > 10^{45}$ erg s⁻¹, depend-

ing on the type of diffuse emission. Cassano et al. (2011) were able to prove statistically that radio halos are found in 30% of clusters with $L_X > 5 \times 10^{44}$ erg s⁻¹. Giovannini and Feretti (2002) find that radio relics occur in approximately 25% of clusters with this same luminosity level. This suggests that diffuse radio emission is only found in the most X-ray luminous clusters.

Liang et al. (2000) used data for the 10 known radio halos, at the time, and compared the radio power of the halo to the X-ray luminosity. They became the first to detect a power-law relationship between these two quantities. This correlation was confirmed in studies by Feretti et al. (2000) and Govoni et al. (2001). Bacchi et al. (2003) added 6 new radio halo detections and re-examined the relationship finding that $P_{1.4\text{GHz}} \propto L_X^{1.68 \pm 0.15}$. Extrapolation of this correlation to below the threshold of $L_X = 10^{45}$ erg s⁻¹ finds that the radio power of the halos would be of the order 10^{23} W Hz⁻¹. If a radio halo with a size of 1 Mpc contained this much power the radio surface brightness would be below the limits of current telescopes. This could be the reason why radio halos are only detected in the most luminous clusters. However, it may be wrong to assume that the halos of lower luminosity would be as large as 1 Mpc, as observations find them to be smaller. Feretti et al. (2012) compiled a list of all known radio halos and relics up to 2011 with their relevant radio powers and X-ray luminosities. They determined that $P_{1.4\text{GHz}} \propto L_X^2$ for radio halos and $P_{1.4\text{GHz}} \propto L_X^{1.2}$ for radio relics. Figure 5.1 shows these correlations and also combines them in (c). From this plot we can see that at high radio powers and X-ray luminosities, halos and relics show a similar relation with small dispersion. As we look towards the lower X-ray luminosities the dispersion increases for both halos and relics. This suggests a link between the origin of both of these sources of diffuse emission. Another interesting point to note is the presence of more relic sources at low X-ray luminosities than than halo sources. This could provide us with more information about the differences between the two types.

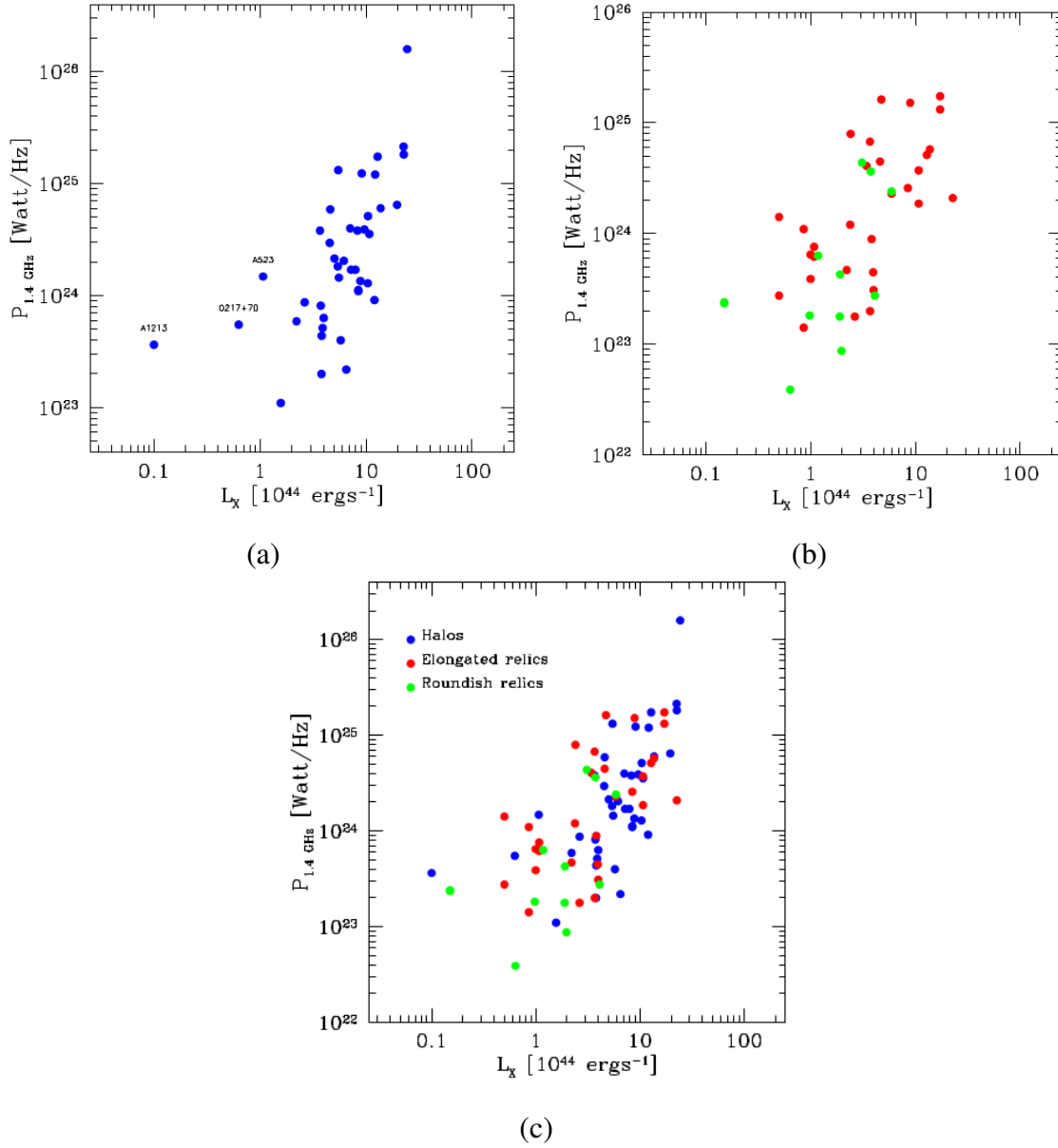


Figure 5.1: These three images show the correlation between the radio power of the diffuse emission, in halos (a), relics (b), and combined, and the X-ray luminosity as determined in Feretti et al. (2012).

Since the X-ray luminosity is a tracer of the mass of a cluster, the correlation could be extended to that between the radio power and the mass. Govoni et al. (2001) first determined this relation using only 6 galaxy clusters containing radio halos and found a well fitted power law of the order $P_{1.4\text{GHz}} \propto M_{500}^{2.2}$. Feretti (2003) add 4 more galaxy clusters and find the relation to be

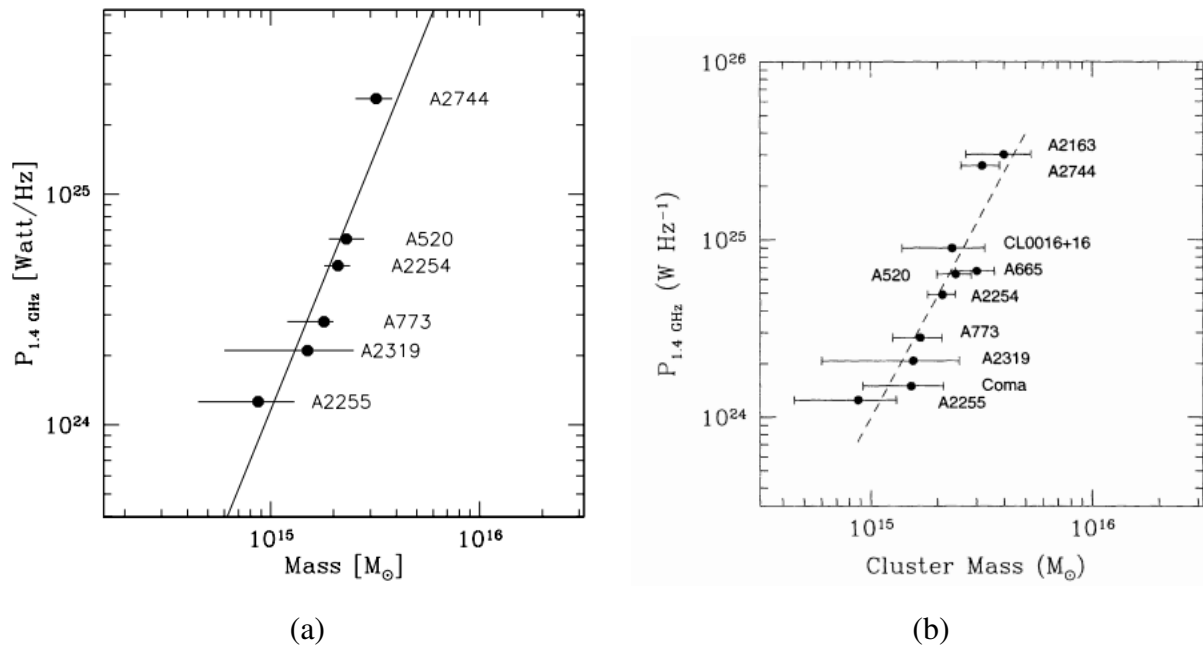


Figure 5.2: These two images show the correlation between the radio power of the diffuse emission in halos as determined by Govoni et al. (2001) in (a) and Feretti (2003) in (b).

$P_{1.4\text{GHz}} \propto M_{500}^{2.3}$ (Figure 5.2). Theoretical predictions by Kempner and Sarazin (2001) predict $P_{1.4\text{GHz}} \propto M_{500}^{2.5}$, showing good agreement to observations.

Since the cluster temperature is also linked to the X-ray luminosity we also expect a relation between the radio power and the X-ray temperature of the cluster. Colafrancesco (1999) and Liang (1999) both determined a correlation between the radio power of halos and their X-ray temperature. Colafrancesco (1999) fitted the relation and obtained $P_{1.4\text{GHz}} \propto T_X^{0.16 \pm 0.08}$. Liang et al. (2000) confirmed this relation when adding 6 additional radio halos. The steepness of this relation shown in Figure 5.3 suggests that radio halos are only easily detectable in galaxy clusters with a high X-ray temperature and moderate redshift. The halo brightness rapidly diminishes with redshift, making detection difficult. However, at low redshift they are also difficult to detect because they can be resolved out in interferometric maps.

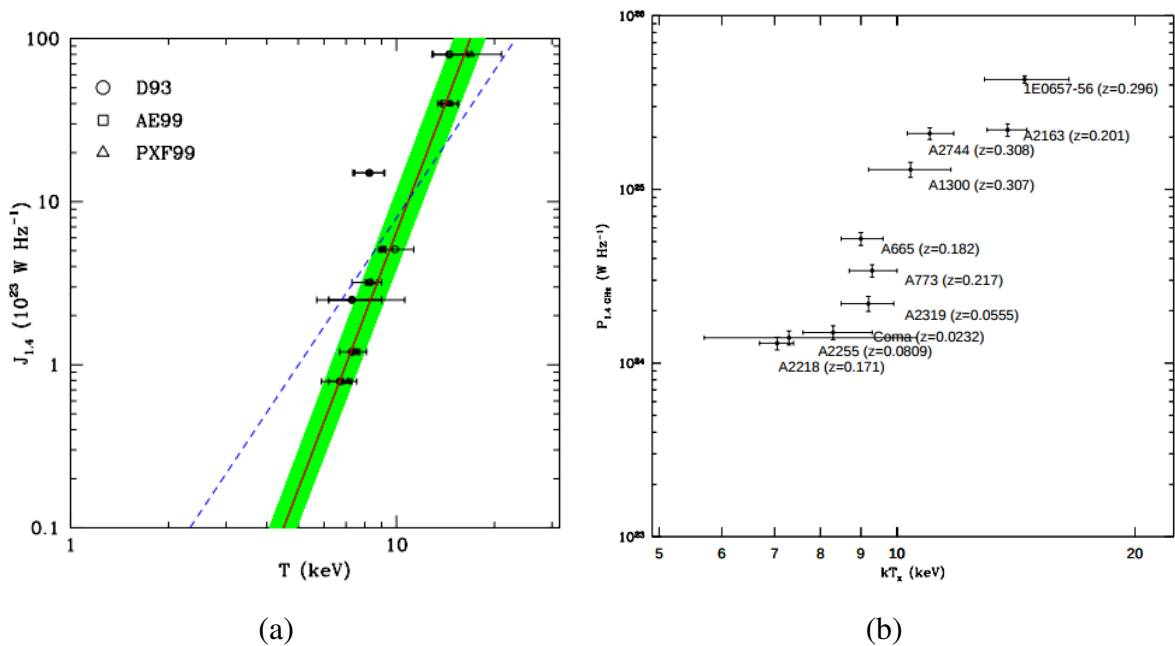


Figure 5.3: These three images show the correlation between the radio power of the diffuse emission in halos by (a), Colafrancesco (1999) and (b) Liang et al. (2000).

We can conclude from this section that the thermal X-ray emission and the non-thermal radio emission must be linked in clusters containing both radio halos and relics. This suggests a similarity between the two types of diffuse radio emission, that is not yet fully understood. However, we do know that halos are usually found in disturbed clusters containing recent or on-going mergers, and relics can be found in disturbed or relaxed clusters, containing a cooling core. Therefore, we will now look at what effect mergers and cooling flows have on scaling relations.

5.2 Effect of mergers and cool cores on scaling relations

Since scaling relations are important tools for understanding the formation of large scale structure and cosmology (Section 1.4) it is necessary that we understand any instances which may cause scatter or affect the relation. Examples of this include cooling flows and mergers. Fabian (1994) and Markevitch et al. (1998b) studied the scatter in the $L_X - T_X$ relation and found that it was linked to cooling flows in the central regions of the clusters. McCarthy et al. (2004) showed that the position of a cluster on the $L_X - T_X$ and $M - T_X$ relations was dependent on the entropy

of the central region and hence the morphology of the cluster core. They found that clusters with a cool-core tend to have a high luminosity and a low temperature and those without have a low luminosity and a low mass. O'Hara et al. (2006) identified that the scatter in clusters with a cool core was larger than in clusters without. However, by removing the cores of both types during analysis they were able to determine that they became indistinguishable, identifying the morphology of the cluster core as a key issue.

Balogh et al. (2006) confirm this theory by ruling out dark matter structure and uncertainty in cosmological models as causes of the scatter. They suggest that instead it could be related to variations in the efficiency of heating and cooling in the cluster centre. They offer little explanation as to the cause of this variation, except to mention that they do not believe it is caused by mergers. Their reasoning is that previous theoretical models of mergers show that they cause systems to evolve parallel to observed scaling relations (Rowley et al., 2004). Smith et al. (2005) show the opposite results, finding that the scatter in the scaling relation is dominated by the unrelaxed systems. They also find that the disturbed clusters are $\sim 40\%$ hotter than similar sized relaxed clusters and conclude that the scatter is caused by merger-induced boosts to the X-ray temperature and luminosity. Therefore, the exact effect of mergers on scaling relations is still a hot topic for debate.

This has resulted in many authors removing the central core of clusters before performing cosmological studies but Poole et al. (2007) realised that by not excluding the cores, they could determine valuable information regarding the processes which shape them. These processes – including but not limited to mergers, AGN, and pre-heating – change the entropy of the core and hence its morphology. Poole et al. (2007) use simulations to focus on the effect of mergers on the scaling relations. They found that the X-ray properties of a cluster follow an evolutionary sequence when undergoing a merger. They found that these properties, specifically L_X and T_X , initially have a large increase as the cores begin to interact. The expansion of the primary system then causes these values to drop, followed by a second spike when accretion begins. Once the cluster has returned to its relaxed state, the properties increase again as a cooling flow is

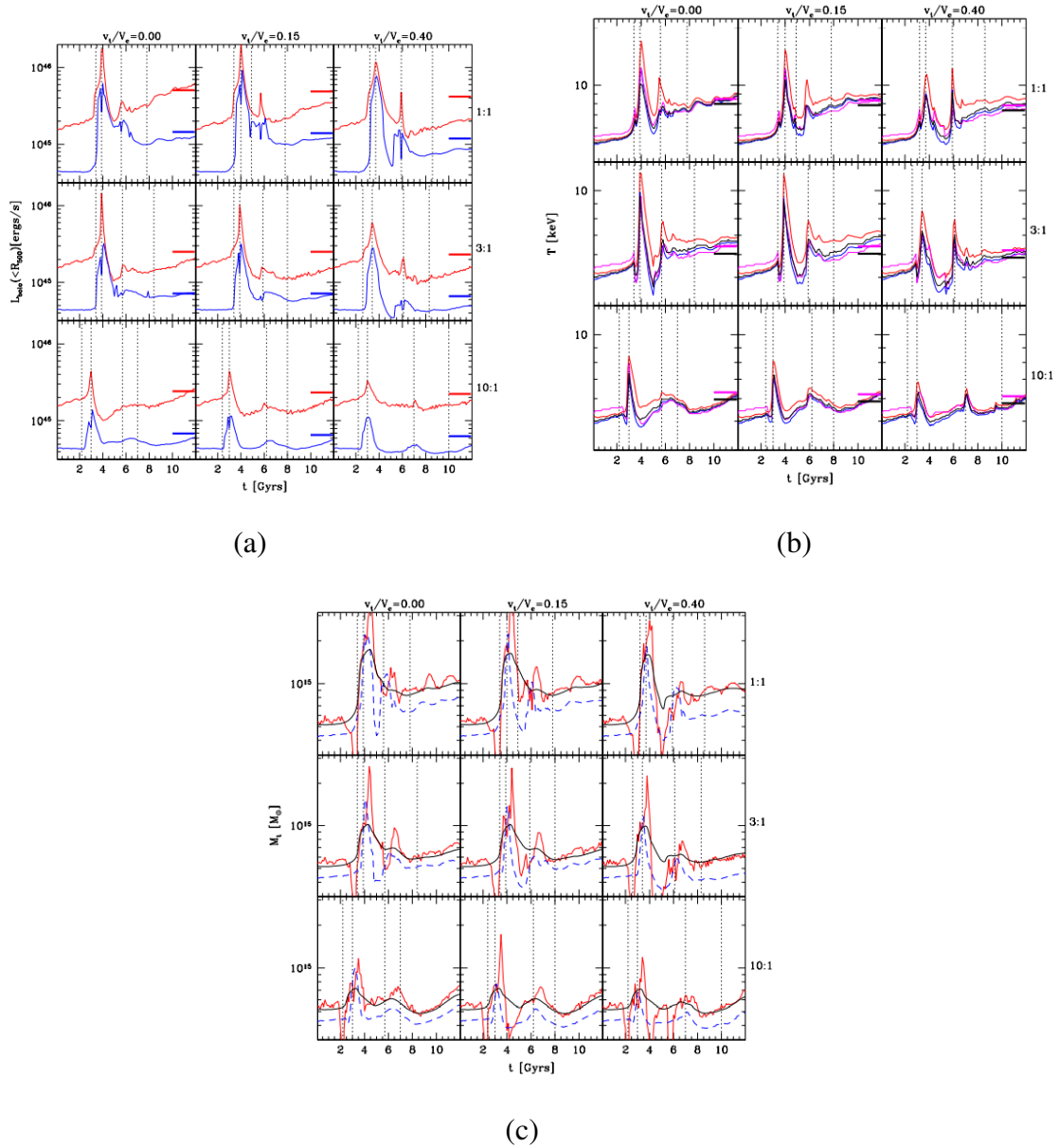


Figure 5.4: These three images taken from Poole et al. (2007) show how the X-ray luminosity (a), X-ray temperature (b), and mass of a cluster (c) vary during a merger event. The values in bold on the edges of each image identify the mass ratio of the clusters involved in the merger and the type of merger (head-on or two different off-axis collisions). The vertical dotted lines indicate the time of first crossing, core interaction, accretion, and when the cluster is back in a relaxed state. In (a) the blue line follows the evolution when the core has been removed and the red line shows the evolution with the core present. In (b) the various lines indicate the types of temperature. Red is the emission-weighted temperature, black is spectrally fit temperatures and blue is the spectroscopic like temperatures. In (c) the various lines indicate types of masses measured. The solid black line is the actual total mass, the red line is the hydrostatic equilibrium mass and the blue line is the isothermal β model mass.

re-developed and accretion of displaced material occurs. The mass of the clusters tends to evolve in the same way. In Figure 5.4, we show this evolution for L_X , T_X , and the cluster mass for different mass ratios of the merging clusters and different types of collisions, including head-on and off-axis. This results in the mergers evolving in a specific way along the scaling relations. At first they follow the relation, then they drift due to the merger and once relaxed again, go back onto the relation. Therefore, Poole et al. (2007) conclude that a typical merger can not account for the scatter in the scaling relations.

Hartley et al. (2008) focus specifically on the $L_X - T_X$ relation using Millennium Gas Simulations. They found that mergers boost a cluster's temperature and luminosity. They identify that the brightest clusters are therefore near the peak of a merger, while those of low temperature and low luminosity are just beginning the merger. They obtain a slope for this relation which is slightly below the mean $L_X - T_X$ relation slope (Figure 5.5).

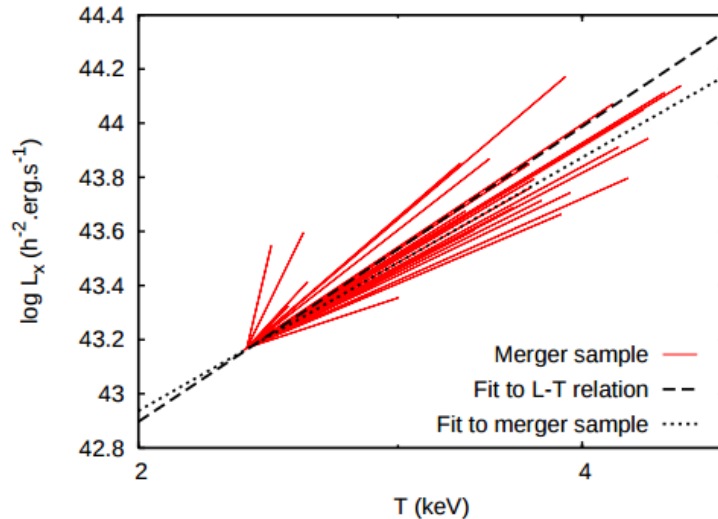


Figure 5.5: This image, taken from Hartley et al. (2008), shows the relative motion of different mergers on the $L_X - T_X$ plane using red lines. The dashed line represents the mean $L_X - T_X$ relation and the dotted line represents this relation for the sample containing merging clusters.

From these studies, we can conclude that mergers and cooling flows can have a significant affect on the various scaling relations. This in turn affects cosmology parameter calculations and

can therefore result in inconsistencies in our understanding. To improve on this we need to gain a better knowledge of these events. Since radio halos are thought to be caused by merger events, by studying them in relation to scaling relations, we may learn more.

5.3 Diffuse emission and the $\sigma_v - T_X$ relation

In Section 5.2, we reviewed how mergers cause a change in the $L_X - T_X$ and $M - T_X$ relations but to date no study has been done on their effect on the $\sigma_v - T_X$ relation. In this section we look at known radio halos, which show the presence of a merger, and compare their position on the $\sigma_v - T_X$ plane to clusters without a halo.

5.3.1 Sample

A recent study by Cuciti et al. (2015) searched for the presence of radio halos in a SZ selected sample of clusters from Planck (Planck Collaboration et al., 2014a). They wanted to determine if the occurrence of radio halos was dependent on their host cluster mass. Due to the close relationship between the SZ signal, Y_{500} , and the cluster mass, M_{500} , this provided an unbiased sample that was almost mass-selected. This sample consists of 1227 objects, 861 of which are confirmed clusters. It spans the cluster range from 0.1 to $1.6 \times 10^{15} M_\odot$ and goes out to a redshift of approximately 1. Cuciti et al. (2015) selected all the clusters within this sample which had $M_{500} > 6 \times 10^{14} M_\odot$ and a redshift range of $0.08 < z < 0.33$. The mass selection was put in place to exclude poor clusters and groups (Basu, 2012) and the redshift range was chosen to mimic where the most radio halos have been found. Since they wanted to search for diffuse radio emission using the GMRT RH survey (GRHS), its extension (EGRHS), and NVSS they had to include a declination limit. For clusters with $z > 0.2$, the limit was $\delta > -31^\circ$, for lower redshifts it was $\delta > -40^\circ$, resulting in a sample of 54 clusters with $z > 0.2$ and 21 clusters in the range $0.08 < z < 0.2$. Of the 54, 34 belonged to EGRHS and had deep radio data and a further 2 had literature information. In the low redshift sample, data for 14 of the clusters was taken from

literature and the other 7 were studied with data from NVSS. The total sample size was therefore 57 clusters. They detected diffuse radio emission in the form of radio halos, relics or mini-halos in 35 of these clusters, with suspected emission in a further 4. No radio halo was detected in the remaining 18, but upper limits were found for 11 clusters.

They also provided a dynamical study of these clusters using X-ray data. 50 out of the 57 clusters had Chandra archival data and 24 of these already had dynamical information based on this data (Cassano et al., 2010). Cuciti et al. (2015) used the data to image the remaining 26 clusters and determine their dynamical state. They found that all the clusters that hosted a radio halo or relic and 10 out of the 18 without a halo had evidence of merger activity. All 9 clusters hosting a mini-halo were found in a relaxed cluster as expected (Section 1.3.3.4). The clusters with X-ray morphology suggesting a merger that lack a radio halo can be explained by the primary model for their origin. Since the generation of turbulence and its subsequent dissipation are not instantaneous, the relativistic electrons may not be re-accelerated straight-away, resulting in an ‘off-phase’. During this time the X-ray will show a disturbance in the cluster but the radio halos will be undetected (Donnert et al., 2013). Their work has provided us with a good sample for studying where clusters with diffuse emission lie on the $\sigma_v - T_X$ plane in relation to those which do not.

We combined the radio halos and relics together to form a sample of clusters with Mpc diffuse emission and the mini-halos and non-detections together to form a sample without Mpc diffuse emission. For both samples, we performed a literature search to determine reliable values for σ_v and T_X and made extensive use of the Base de Données Amas de Galaxies, an X-ray galaxy cluster database (Sadat et al., 2004). The results are shown in Tables 5.5 and 5.6 at the end of this chapter.

In Figure 5.6 we plot the two samples on the $\sigma_v - T_X$ plane. We further separate the sample with no diffuse emission into clusters which show evidence of merging and those which do not. Due to the small sample size, we are not able to fit the data to obtain a $\sigma_v - T_X$ relation.

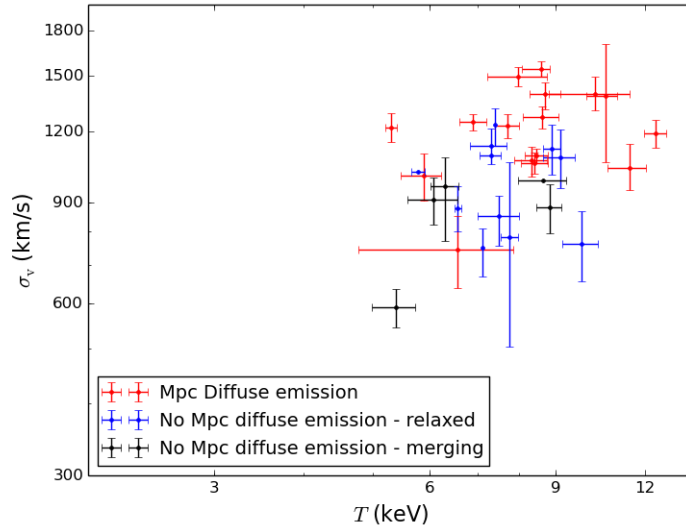


Figure 5.6: In this image we plot the velocity dispersions and temperatures of the clusters in our two samples. The sample of cluster hosting diffuse emission are shown in red. We separate the sample with no diffuse emission into relaxed (blue) and merging (black) systems. Due to the small sample size we are unable to fit the two samples, but analysis shows that the scatter is slightly increased for clusters with diffuse emission and clusters without diffuse emission but that show signs of merging when compared to relaxed clusters with no diffuse emission.

However, we calculated the intrinsic scatter of each sample around our best-fit $\sigma_v - T_X$ from our combined sample (Chapter 3). We find the following: For clusters with 1 Mpc diffuse emission $S = 0.116 \pm 0.021$, for clusters without 1 Mpc diffuse emission that show signs of merging $S = 0.117 \pm 0.022$ and for relaxed clusters without diffuse emission $S = 0.096 \pm 0.019$. The scatter in the relaxed cluster is slightly less, as expected, but since all the results are consistent within 1σ there is no obvious split in the samples. Therefore, we can tentatively conclude that the presence of diffuse radio emission does not result in an obvious deflection from the $\sigma_v - T_X$ relation. In order to improve on this we need to increase our sample size and therefore we present here 3 new VLA observations of XCS clusters.

5.4 VLA observations

5.4.1 Motivation and Proposal

The turbulent re-acceleration model, if responsible for the origin of radio halos, suggests that the presence of a radio halo is dependent on the cluster merging rate and the mass of the clusters. Both these properties affect the the amount of energy available for the re-acceleration of the relativistic particles. The models predict that the spectra of the radio halos will steepen at a frequency that depends on how energetic the merger is, and hence the cluster's mass. Therefore, the more massive and energetic the merger, the greater the probability of detecting a radio halo (Cassano and Brunetti, 2005). The less massive and less energetic mergers are thought to produce ultra-steep spectrum radio emission, which become difficult to detect at higher frequencies (Cassano et al. 2006, Brunetti et al. 2008, Dallacasa et al. 2009, Cuciti et al. 2015). In 2015, we submitted a proposal to VLA to observe 3 low mass galaxy clusters, using the VLA D configuration, to see if we could detect a radio halo. In the D configuration all the telescopes are located within 0.6 km of the central core, resulting in the shortest baselines and hence the best sensitivity to large scale structure. This is particularly important for our pilot study because due to the low redshift, if a halo is present, it will appear large on the sky. However, a lack of long baselines will result in a lower resolution image which we will discuss in Section 5.4.6. A non-detection would offer proof that the turbulent re-acceleration model may be correct. This was a pilot project with a small sample size, that if successful could lead to further studies.

We proposed to observe 3 clusters, XMMXCS J151618.6+000531.3; XMMXCS J104044.4+395710.4 and XMMXCS J111515.6+531949.5 (hereafter J1516, J1040, and J1115, respectively), from our XCS sample (Chapter 2). All these clusters have dynamical information as well as X-ray temperature and luminosity measurements. By observing them in the radio, we can provide a multi-wavelength study of these clusters. The 3 chosen clusters have a low mass, $M_{500} \sim 4 \times 10^{14} M_{\odot}$, and a low redshift since almost all radio halos have been found in clusters with $z < 0.35$ (Cassano et al., 2010). The properties of these 3 clusters are given in Table 5.1.

Table 5.1: Properties of the 3 clusters observed by VLA. The M_{500} value was taken from our dynamical calculation in Chapter 4 and the right ascension, declination, and redshift (columns 2, 3, and 4 respectively) are taken from Chapter 2. The bolometric X-ray luminosity as calculated by XCS is given in column 7, with their corresponding 0.1-2.4 keV band luminosities estimated using Böhringer et al. (2004) provided in column 8.

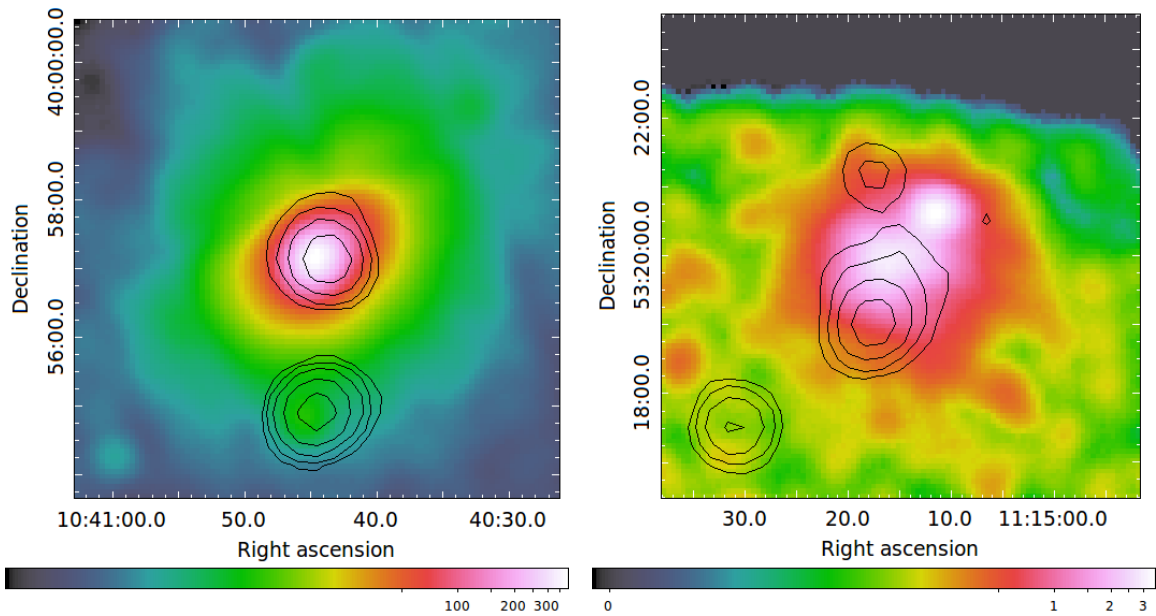
Cluster Name	RA (J2000)	DEC (J2000)	z	M_{500}^{dyn} [$10^{14} M_{\odot}$]	L_X [$10^{44} \text{ erg s}^{-1}$]	$L_{[0.1-2.4]\text{keV}}$ [$10^{44} \text{ erg s}^{-1}$]
J1040	10 ^h 40 ^m 44.5 ^s	39°57'10.4"	0.14	5.64 ± 2.70	8.89 ± 0.03	5.01 ± 0.02
J1115	11 ^h 15 ^m 15.6 ^s	53°19'49.5"	0.47	5.49 ± 5.15	18.13 ± 0.52	8.24 ± 0.24
J1516	15 ^h 16 ^m 18.6 ^s	00°0'31.3"	0.12	5.91 ± 4.09	4.51 ± 0.01	2.05 ± 0.01

All three of these clusters have previous VLA observations (NVSS and FIRST) and the NVSS images for J1115 show potential diffuse emission. The X-ray images and preliminary analysis for these clusters (Figure 5.7) show that they are likely to be dynamically disturbed or merging systems. Therefore, they are good candidates for hosting a radio halo.

We proposed to observe these three XCS Clusters at 1.4 GHz with the VLA configuration D for a total time of 25 minutes per source. For these integration times we do not have to worry about being confusion limited as the confusion limit for VLA D configuration in L-band is 89 $\mu\text{Jy}/\text{beam}$ (Witz, Stephan W. , 2015). After the observations were completed, we found that the on source time was not sufficient to get proper uv-coverage. Therefore the results we present here are just preliminary findings and will require further follow up study. A further improvement could be made by including data from the VLA configuration C. This would help to reduce confusion noise and help with the detection and removal of point sources.

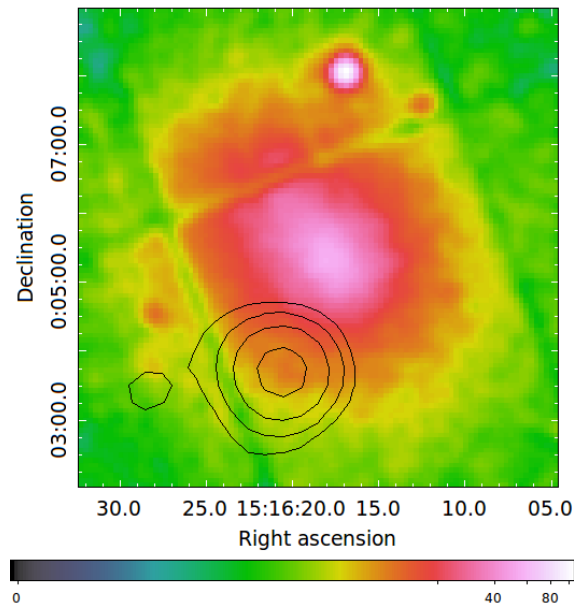
5.4.2 VLA data reduction and analysis

The three clusters were observed in October 2015 (PI: S Wilson, ID: VLA/15B-102). In this section we look at the analysis of these data.



(a) J1040

(b) J1115



(c) J1516

Figure 5.7: Here we show the smoothed X-ray images for each of our clusters with NVSS contours (black) overlaid. The X-ray images are smoothed with a Gaussian filter of $\text{FWHM} = 26''$ for J1040, and $\text{FWHM} = 13''$ for J1115 and J1516. The contour levels are at $[3, 6, 12, 24, 48, 96] \times 0.5 \text{ mJy beam}^{-1}$ for all radio images. The units on the colour bars are counts.

5.4.2.1 Interferometry and calibration

Radio interferometers are made up of N antennas that can be broken up into $\frac{N(N-1)}{2}$ antenna pairs. To explain the process by which a signal is obtained we consider the simplest case of two antenna separated by a baseline distance b . Antenna 1, V_1 and antenna 2, V_2 , will both record a signal, but the signal received by V_2 will experience a phase shift of τ_g , which is dependent on the viewing direction and b . To produce a single amplitude and phase measurement the two signal are multiplied and averaged. The position of this signal on the uv -plane is determined by the projected baseline through a Fourier relationship. A single baseline can fill up more than one space on the uv -plane by using the rotation of the Earth to produce multiple projected baselines.

The signals recorded by the radio interferometers represent the intensity of the true sky as a Fourier transformed complex visibilities described by amplitude and phase components. Corrupting effects, such as the ionosphere, pointing errors, system noise and radio frequency interference (RFI) as well as antenna responses change the true sky density, therefore in order to reconstruct it corrections must be made for these modifications. After this it is Fourier transformed back into the image plane. This is the basic principle on which radio data reduction is formed (Thompson et al., 2001).

We need to model and correct for these effects that modify the intensity in order to be able to Fourier transform them into an image. To model for the antenna response to the sky we observe a bright and compact calibrator source for which the flux is known. This can be used to determine a flux scale for the uncalibrated sources and determine phase solutions for applications to the target data.

Many software programs exist to reduce radio data using the same core principles. They require two calibrators: the primary calibrator, a well-studied bright source, to be used to determine the flux scale and primary phase calibrators and a second weaker calibrator closer to the source to apply accurate phase solutions. The Common Analysis Software for Astronomy pack-

age (CASA; McMullin et al. 2007) was developed by NRAO, NAOJ, Penticton, and U. Calgary for the ALMA and EVLA observatories and Version 4.4.0 was used to reduce our JVLA data. The VLA calibration pipeline is an automated data reduction pipeline for Stokes I continuum data (Chandler, 2016) that was applied to these data (Version 1.3.4).

5.4.3 JVLA pipeline

In this section we give the steps followed by the pipeline with an explanation of the most important tasks. Before any data reduction can be done the model visibilities for calibrators are set, either from point source visibilities or visibilities from previous images or known flux densities. An antenna which will be stable for most of the pipeline is also automatically chosen. Then the process takes the following steps:

1. Hanning smoothing - If a sharp frequency jump, caused by removing a single channel with strong RFI, is Fourier transformed it can result in the Gibbs phenomenon (Gibbs, 1898), which produces ripples in the image. Hanning smoothing causes the edges of the flagged region to become more attenuated and hence reduces the ripple effect (Tukey, 1977).
2. Auto flagging - During this stage, flags that were generated during observations are applied. The time based flags include online flags, shadowed data, zeroes, pointing scans, and quacking. The channel based flags include removing the end 5% of channels of each spectral window and the 10 end channels at the edges of basebands. Shadowed data is due to close proximity of dishes to one another, resulting in them casting shadows on the nearby dishes and blocking the signal. Quacking removes the first 5% of each scan to eliminate data when some antennas are still slewing to the scan target.
3. Prior calibration - Previously known calibration quantities, such as antenna gain curves, atmospheric models, delays, and antenna position offsets are pre-applied. The elevation of a telescope affects the amplitude of the signal the antenna receives. Since antennas are not absolutely rigid, their effective collecting area and net surface accuracy vary as gravity

deforms the surface. Gain curves help to compensate for these effects. Since the antennas for VLA can move, it is important to check for and apply off-sets.

4. Test calibration - In this step bandpass and delay calibrations are tested by solving for the relative gain of the system over the frequency channels.
5. Flag bad deformatters and RFI - The signal on each antenna is converted from electronic to optical before it can be sent along the optic fiber link. When it arrives at the correlator it is deformatted back to an electronic signal. Sometimes the timing on the deformatter is mis-aligned resulting in phase and amplitude peaks, which may in turn result in bad spectral windows. In this step, these bad deformatter and RFI are flagged in the bandpass amplitude and phase tables. Any RFI on the bandpass calibrator is also flagged.
6. Semi-final delay and bandpass calibrations - Repeat of step 4. Since the spectral index has not yet been determined, this is not the final set of calibration performed.
7. Flagging; re do bandpass calibration - The previous flags are applied to the calibrator and further flagging is performed.
8. Determine optimal solution interval to calculate time-dependent gain solutions for scan-average equivalent.
9. Flux density bootstrapping - The flux density scale is established in this process. If only some of the calibrators have known flux densities then the gain solutions are re-scaled and flux densities of secondary calibrators are derived.
10. Apply calibration - The calibration is applied to all sources and checked.
11. Final flagging - One last round of automated flagging is run.

The final steps of the pipeline are to calculate data weights based on the standard deviation within each spectral window and make final *uv*-plots for visual inspection. These plots, combined with the QA2 scores for each primary step, can be used to gauge how well the pipeline ran on the input data before initial analysis can begin. A QA2 score is either Pass, Partial, or Fail

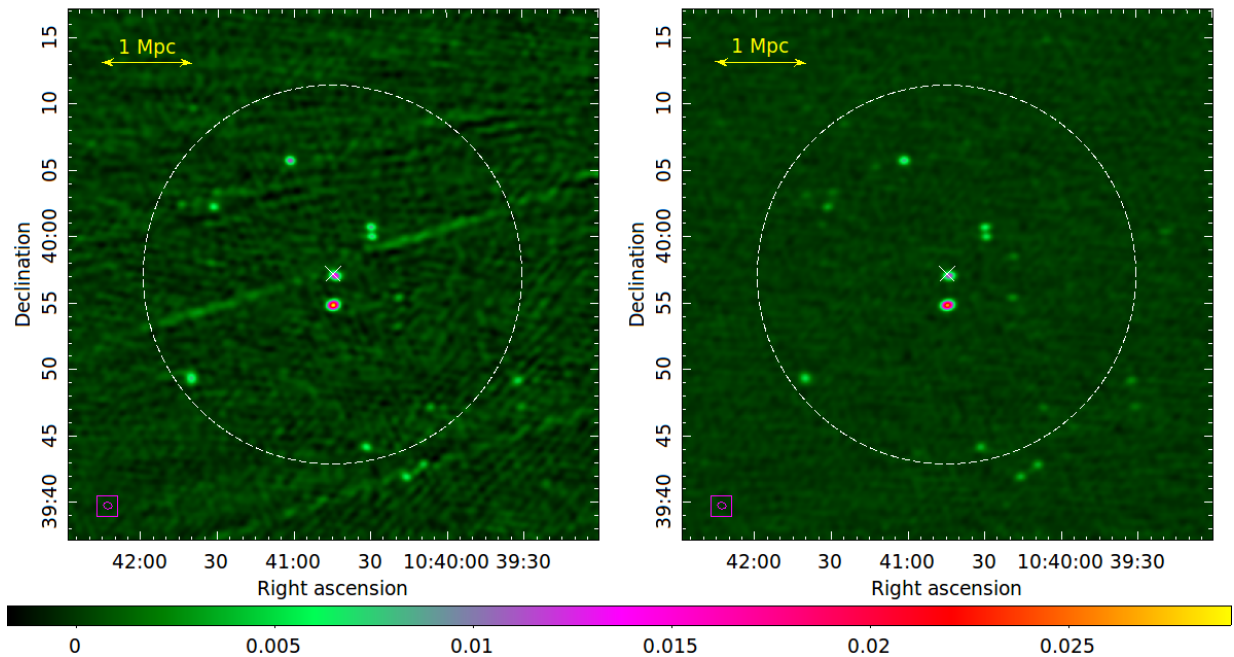


Figure 5.8: Here we show the VLA images of J1040. *Left:* Image obtained after running the VLA calibration pipeline and doing some manual flagging. The 1σ rms is $0.55 \text{ mJy beam}^{-1}$, with a beam size of $38.0'' \times 30.9''$, 83.6° . There are several stripe artifacts running appearing close to the phase centre of the image. *Right:* Final image obtained after several rounds of self-calibration. The image noise is much improved, with a 1σ rms of $0.19 \text{ mJy beam}^{-1}$. There is a slight decrease in resolution ($41.6'' \times 31.4''$, -84.0°) owing to some of the longer baselines being affected by the calibration. The white cross indicates the position of the cluster X-ray peak, with the optically determined R_{200} region shown by the dashed white circle. The beams for each image are shown by the magenta boxed ellipse. The colour scaling is the same for both images, with the colourbar in units of Jy beam^{-1} .

and is a quality measurement automatically generated for the pipeline as a whole and for each step along the way. The final QA2 score is equal to the worst score reached for any step of the pipeline.

5.4.4 Initial analysis

After running the pipeline on each of our three datasets, we achieved a final ‘Pass’ QA2 score in each case. However, we proceeded to check the calibrated target data visually for any remaining bad data, which we manually flagged before imaging. The target data is used to produce

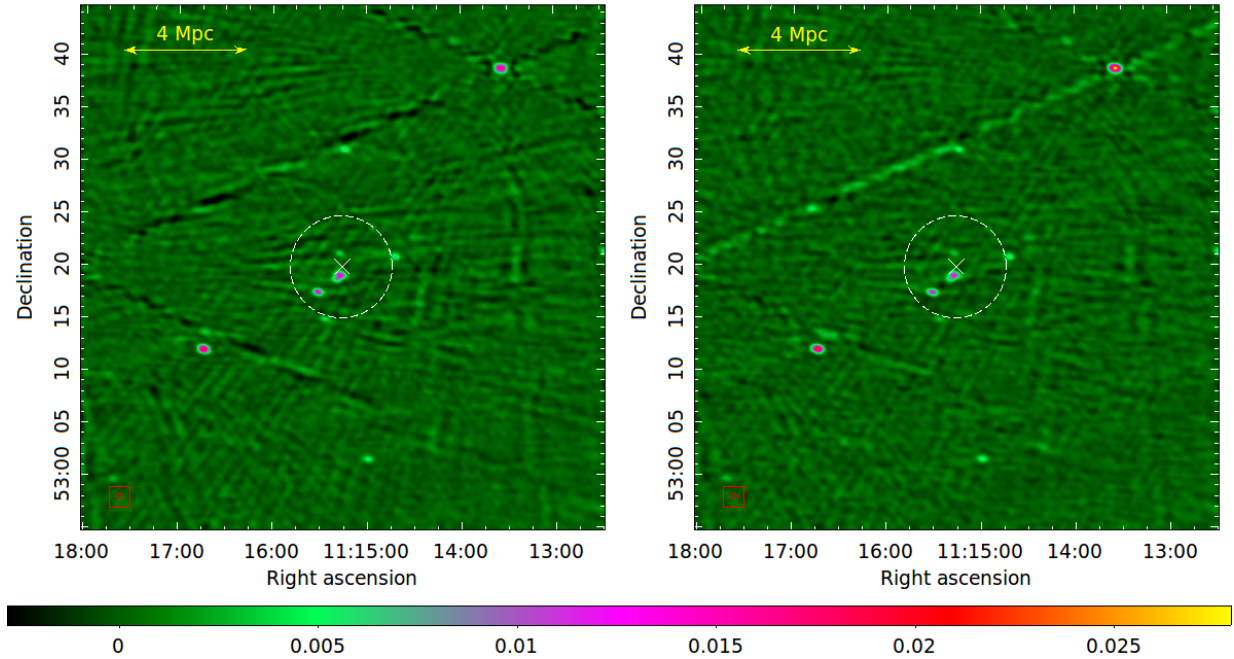


Figure 5.9: Here we show the VLA images of J1115. *Left:* Image obtained after running the VLA calibration pipeline and doing some manual flagging. The 1σ rms is $0.52 \text{ mJy beam}^{-1}$, with a beam size of $48.3'' \times 31.5''$, 76.0° . There are several negative bores and striping in the image, indicating residual RFI or poor calibration. *Right:* Final image obtained after several rounds of self-calibration. The image noise is only slightly improved, with a 1σ rms of $0.45 \text{ mJy beam}^{-1}$, and a strong linear artifacts remains. There is also a slight decrease in resolution ($48.3'' \times 32.1''$, 78.1°) owing to some of the longer baselines being affected by the calibration. The white cross indicates the position of the cluster X-ray peak, with the optically determined R_{200} region shown by the dashed white circle. The beams for each image are shown by the red boxed ellipse. The colour scaling is the same for both images, with the colourbar in units of Jy beam^{-1} .

an initial image via a deconvolution algorithm known as CLEAN (Högbom, 1974). The initial images for J1040, J1115, and J1516 are shown in the left panels of Figures 5.8, 5.9, and 5.10 respectively. Although point sources are detected in all initial images, the 1σ rms noise thresholds are fairly high, being $0.55 \text{ mJy beam}^{-1}$, $0.52 \text{ mJy beam}^{-1}$, and $4.96 \text{ mJy beam}^{-1}$ for J1040, J1115, and J1516 respectively. Artifacts are also clearly evident in these initial images, either from residual RFI or poor calibration solutions.

The high noise values are to some extent unavoidable given the sparse uv -coverage, as shown in figure 5.11. This is due to the short observing time and large amounts flagging (see Table

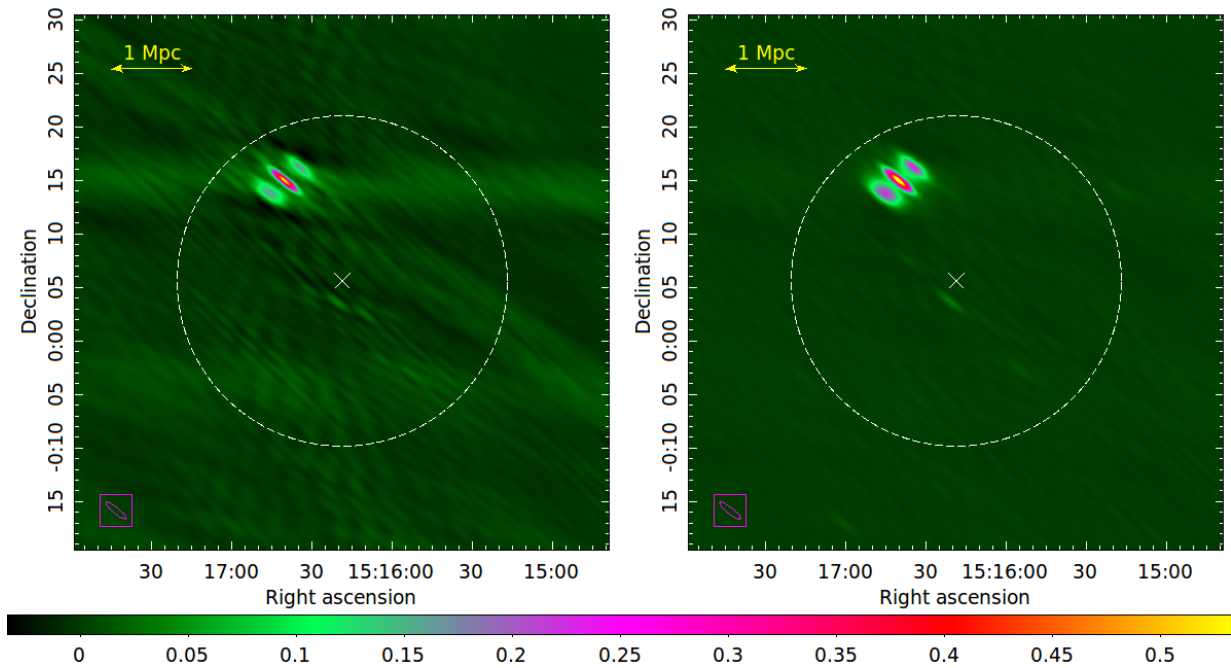


Figure 5.10: Here we show the VLA images of J1516. *Left:* Image obtained after running the VLA calibration pipeline and doing some manual flagging. The 1σ rms is quite high at $4.96 \text{ mJy beam}^{-1}$ and the image has a highly elongated beam ($140.6'' \times 32.0''$, 50.6°). *Right:* Final image obtained after several rounds of self-calibration. The image noise has improved by a factor of 5, with a 1σ rms of $0.98 \text{ mJy beam}^{-1}$. As for the other clusters, there is a slight decrease in resolution ($41.6'' \times 31.4''$, -84.0°). The white cross indicates the position of the cluster X-ray peak, with the optically determined R_{200} region shown by the dashed white circle. The beams for each image are shown by the magenta boxed ellipse. The colour scaling is the same for both images, with the colourbar in units of Jy beam^{-1} .

5.2). In general, flagging is done to remove bad data caused by antenna problems, RFI, or other telescope issues. Since target data is calibrated by the primary and phase calibrators, if the data on these sources is bad it results in the loss of a fair amount of target data. For all three clusters, over 80% of the calibrator data was flagged. This is particularly high and after investigation we find the following. For clusters J1040 and J1115, which were observed in the same schedule block and therefore shared the same primary calibrator, large amounts of calibrator data ($\sim 60\%$) were flagged during the first step of the process for an antenna not being on source. Furthermore, while checking for bad deformatters or RFI in the primary calibrator data (step 5), the pipeline identified spectral windows 8 and 9 as corrupted (Figure 5.12) and the entire windows were flagged for all baselines. Cluster J1516 was observed one day prior to the

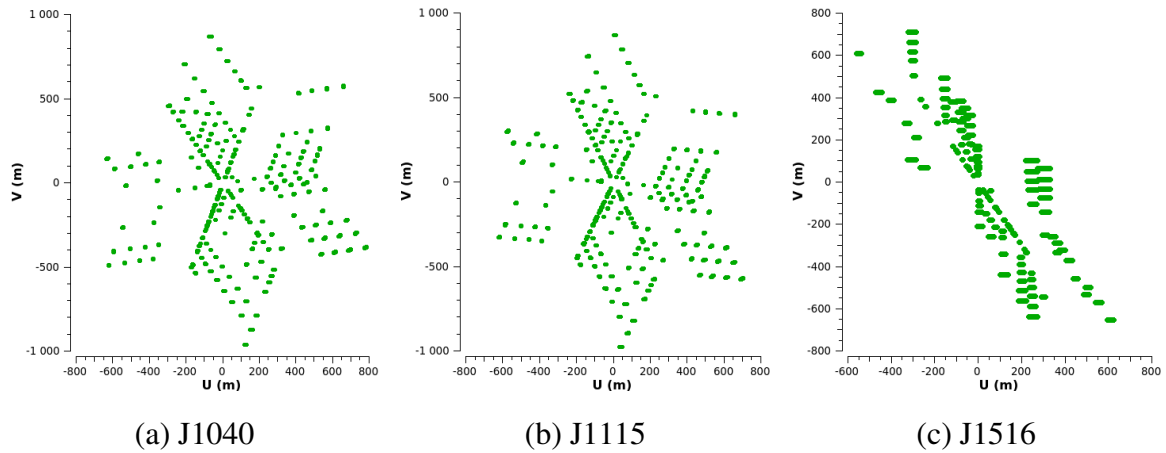


Figure 5.11: In this plot, we show the uv -coverage for each of our three clusters after applying the pipeline and performing manual flagging. The uv -coverage for all three is very sparse, specifically for cluster J1516, which also shows an elongation along one direction. Due to the short baselines offered by the VLA D-configuration, we are able to resolve large scale structure. By considering the smallest available UV distance we were able to determine the largest scales we are sensitive to for each cluster. For J1040, J1115 and J1516 the largest structure we can resolve is $15'$, $28'$ and $25'$ respectively.

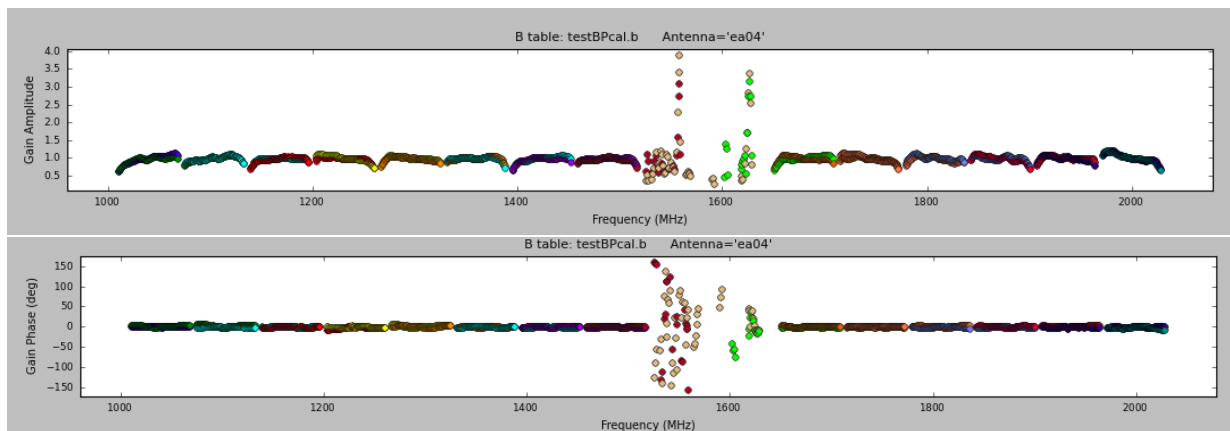


Figure 5.12: This image shows an example of the bad spectral windows in our data in both the amplitude (top panel) and phase (bottom panel). These bad spectral windows are caused by RFI or bad deformaters.

other clusters. Similarly to the other dataset, large amounts of calibrator data were removed due to corrupted spectral windows and antennas not being on source. However, an additional $\sim 17\%$ was flagged due to shadowing (step 1) as the observed coordinates were further from zenith than during the other observations. For all three clusters the large amount of data flagged, has greatly

Table 5.2: Properties of the 3 clusters observed by VLA. Column 1 gives the name of the cluster. Columns 2 and 3 give the rms noise of the initial and post-selfcal images, respectively. Column 4 gives the size of the synthesised beam size for the post-selfcal image. Columns 5, 6, and 7 give the percentage of data flagged in the primary calibrator, phase calibrator, and the target data, respectively.

Cluster Name	σ_{initial} (mJy/beam)	σ_{final} (mJy/beam)	Beam size (" \times ", $^\circ$)	Primary Cal % Flagged	Phase Cal % Flagged	Target % Flagged
J1516	4.96	0.98	146 \times 36, 51	88.9	90.9	86.6
J1040	0.55	0.19	42 \times 31, -84	85.5	85.3	63.1
J1115	0.52	0.45	48 \times 32, 78	86.1	80.4	69.4

reduced the amount of target data, and negatively affected our imaging. However, with further calibration techniques we may be able to improve the quality of the images.

5.4.5 Self calibration

A major contributor to the high image noise levels are the artifacts remaining after the initial calibrations. These artifacts may be reduced or removed by the implementation of second generation calibration techniques, namely self-calibration (selfcal; Cornwell and Wilkinson, 1981). Self-calibration is when calibration solutions are determined and applied based on the target data itself, iterating until the skymodel converges.

For all our datasets, we first applied a gain phase calibration using the target data in decreasing integration times, starting at 20 minutes and ending at 1 minute intervals. This was repeated with a combined amplitude-and-phase calibration. After each calibration step, we re-imaged using CLEAN to ensure we had good solutions and that we were not introducing further artifacts into the images. Once the results had converged we created final images for each cluster. The final images for J1040, J1115, and J1516 are shown in the right panels of Figures 5.8, 5.9, and 5.10 respectively. There is a marked improvement in both the noise levels and image quality for both J1040 and J1516 — the noise improves by 65% and 80%, respectively. In both cases, most of the artifacts have been removed completely or suppressed below the noise limit. There is a smaller noise improvement of only 13% for J1115, with some artifacts still present after selfcal.

The 1σ rms noise levels and synthesised beam for each post-selfcal image are given in Table 5.2, along with the final percentages of flagged data for each calibrator and target source. A further technique which could be used to further improve the data is point source removal but this is left for future studies.

5.4.6 Upper limit estimation

Upper limits for radio halos are usually determined by injecting a simulated radio halo into the uv -data and re-imaging at various levels to determine at what flux the halo can just not reliably be recovered. This process is explained in detail by Brunetti et al. (2007), Venturi et al. (2008), Kale et al. (2013) and Knowles (2015).

In the literature, the simulated halos are assumed to be 1 Mpc in diameter Brunetti et al. (2007), the typical size for a giant radio halo. Given our chosen cosmology and the cluster redshifts, this is equivalent to an angular size of $6.73'$, $2.8'$ and $7.68'$ for J1040, J1115 and J1516 respectively. The injected halos are therefore all smaller than the largest angular size to which our observations are sensitive, i.e., $15'$, $28'$ and $25'$ for J1040, J1115 and J1516 respectively.

For each cluster we first injected a simulated halo of flux 30 Jy and lowered this flux until we could not recover the injected halo emission. The flux upper limit was taken to be that flux at which we could just not reliably detect the halo. These flux upper limits are given in Table 5.3. To determine where our cluster upper limits lie on the well known $P_{1.4\text{GHz}} - L_X$ and $P_{1.4\text{GHz}} - M_{500}$ relations we convert our flux to a k-corrected radio power using the following equation:

$$\left(\frac{P_{1.4\text{GHz}}}{\text{WHz}^{-1}}\right) = 4\pi \left(\frac{D_L}{\text{m}}\right)^2 \left(\frac{S_{1.4\text{GHz}}}{\text{m}^{-2}\text{WHz}^{-1}}\right) (1+z)^{-1}, \quad (5.1)$$

where D_L is the luminosity distance at the redshift, z , of the cluster, and $S_{1.4\text{GHz}}$ is the flux

Table 5.3: In this table, we present the the upper flux limits determined from the simulation of a 1 Mpc halo in column 2 (see Section 5.4.6 for more details). This is converted to a radio power given in column 4 by using Equation 5.1 and the luminosity distance given in column 3. Column 5 gives the bolometric X-ray luminosity as calculated by XCS.

Cluster Name	$S_{1.4\text{GHz}}$ [$10^{-28}\text{m}^{-2}\text{WHz}^{-1}$]	D_L [10^{25}m]	$P_{1.4\text{GHz}}$ [10^{24}WHz^{-1}]	L_X [10^{44}erg s^{-1}]
J1040	12.0	1.94	5.00	8.89 ± 0.03
J1115	10.0	7.33	46.13	18.13 ± 0.52
J1516	15.0	1.67	88.24	4.51 ± 0.01

upper limit. These values are shown in Table 5.3. In addition, as the majority of the literature clusters were observed with Chandra, the observed $P_{1.4\text{GHz}} - L_X$ correlation is based on luminosities in the 0.1 – 2.4 keV band. We therefore convert our cluster bolometric X-ray luminosities to luminosities in this band by using a scaling factor as determined by Böhringer et al. (2004). Both luminosities for our clusters are given in Table 5.1. We also note that the observed $P_{1.4\text{GHz}} - M_{500}$ relation uses SZ masses from either Planck or ACT. Unfortunately not all of our clusters have an available SZ mass value, and we therefore use our dynamical masses calculated in Chapter 4. Sifón et al. (2015) compare dynamical masses, also determined via the Munari relation, with SZ masses from ACT. They leave determining a scaling relation between the two types of masses for future work. However, based on Figure 6 in Sifón et al. (2015), we note that for the range of masses of our three clusters, they find that the dynamical masses are slightly higher than the SZ values, but are consistent with each other within 2σ . Therefore, we do not expect significant horizontal movement of our upper limits on the $P_{1.4\text{GHz}} - M_{500}$ plane when using future SZ masses.

In Figure 5.13 we show the position of each cluster upper limit in the $P_{1.4\text{GHz}} - L_X$ (left panel) and $P_{1.4\text{GHz}} - M_{500}$ (right panel) planes. The upper limits for all three clusters are much higher than the known radio halo upper limits from the literature. Given our poor data quality, this is not unexpected.

Table 5.4: In this table, we present the the upper flux limits determined from the simulation of a 400 kpc halo in column 2 (see Section 5.4.6 for more details). This is converted to a radio power given in column 4 by using Equation 5.1 and the luminosity distance given in column 3. Column 5 gives the bolometric X-ray luminosity as calculated by XCS.

Cluster Name	$S_{1.4\text{GHz}}$ [$10^{-28}\text{m}^{-2}\text{WHz}^{-1}$]	D_L [10^{25}m]	$P_{1.4\text{GHz}}$ [10^{24}WHz^{-1}]	L_X [10^{44}erg s^{-1}]
J1040	4.0	1.94	1.67	8.89 ± 0.03
J1115	0.9	7.33	4.15	18.13 ± 0.52
J1516	10.0	1.67	58.82	4.51 ± 0.01

Although, previous studies use a generic 1 Mpc halo size for simulations, radio halo sizes can vary significantly from this value. Cassano et al. (2007) found an observational connection between the size of the radio halo (R_H) and the cluster virial radius (R_V) of $R_H \propto R_V^{2.63 \pm 0.50}$ (Figure 11). This equates to a decrease in halo size with a decrease in cluster mass. Based on this relation and our cluster properties we expect to find $R_H \lesssim 300$ kpc in our clusters, significantly smaller than the standard simulated size of 1 Mpc. For the same halo flux, and therefore radio halo power, it would be easier to detect the halo with the smaller expected size due to its higher surface brightness. Given that the synthesised beam for each dataset is $\sim 1'$, we simulate a slightly larger halo, i.e., 400 kpc, so that the simulated halo is not smaller than the beam. These upper limits are given in Table 5.4 and shown by the open red, green and blue triangles in Figure 5.13. Using this reduced simulated halo size, our radio power upper limits are decreased by a factor of 2~10. Our upper limits do not rule out the presence of a radio halo as they are all above or in the region of the correlation. More sensitive data, with slightly better resolution to enable the removal of point sources, to probe the flux levels at which we might expect a detection. No upper limit study has as yet been done using variable halo sizes, but our results may be an indication that the accepted method for calculating radio halo upper limits may need to be revised.

With respect to the $P_{1.4\text{GHz}} - L_X$ relation, after correcting for the band luminosity, we note that the 400 kpc halo upper limits for J1040 and J1115 are consistent with the scaling relation as they lie within the scatter. The J1516 upper limit is well above the correlation given the cluster's low luminosity, even after adjusting for the smaller simulated halo. The uv -coverage (Figure

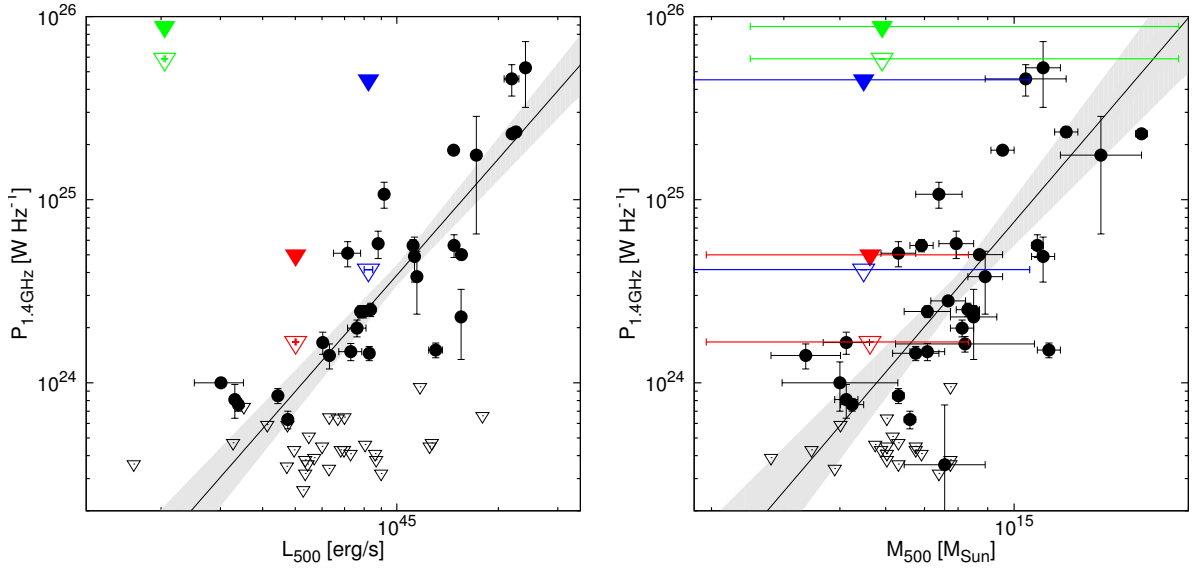


Figure 5.13: In this plot we show the position of our simulated upper limits on the well-known $P_{1.4\text{GHz}} - L_X$ (left panel) and $P_{1.4\text{GHz}} - M_{500}$ (right panel) relations (Cassano et al., 2013). Radio halos from the literature are shown as filled black circles. The literature upper limits are shown as empty black triangles. All literature values are taken from Cassano et al. (2013). The literature values use SZ M_{500} masses and X-ray luminosities measured in the 0.1 - 2.4 keV band. The 1 Mpc (400 kpc) simulated halo upper limits for J1040, J1115, and J1516 are shown by red, blue, and green filled (open) triangles, respectively. We use dynamical masses calculated in chapter 4 as not all of our clusters have SZ masses. Our bolometric XCS luminosities have been converted into 0.1 - 2.4 keV band luminosities for accurate comparison with the literature values. Error bars are plotted for both our L_X and M_{500} values. The best fit to the GRH detections and associated 95% confidence interval is from Cassano et al. (2013) and are shown by the black line and grey shaded region, respectively.

5.11) for this source is more elongated in one direction when compared to the other two sources. This causes a stretching of the beam resulting in the major axis being much larger than the minor axis. This asymmetrical pattern was due to the low elevation ($14^\circ - 17^\circ$) of the source in the sky, which resulted in the apparent array size being shortened in one direction but not the other. This low elevation and the short base lines would have resulted in shadowing, which resulted in extra flagging as discussed in Section 5.4.4. J1516 does indeed have the highest noise level of our 3 cluster images and this contributes to the high radio power upper limit.

The $P_{1.4\text{GHz}} - M_{500}$ relation is less constrained than the $P_{1.4\text{GHz}} - L_X$ relation and our clusters, allowing for their large mass uncertainties, are consistent with the scatter of the $P_{1.4\text{GHz}} - M_{500}$ relation. To improve the interpretation of our upper limits, we would require better constrained dynamical masses or SZ mass measurements for our clusters.

5.5 Conclusion

In this chapter, we focused on observing galaxy clusters in the radio wavelength and specifically on the diffuse radio emission that is found within clusters. Since mergers are thought to be the driving force behind this diffuse emission, we discuss the effect of mergers on scaling relations. We also extract a sample of clusters from literature with known diffuse emission and non-detections, that have velocity dispersions and temperatures. We plot these clusters on the $\sigma_v - T_X$ plane and show that there is no difference in the two populations. We also present 3 new observations with the VLA D array of clusters from our XCS sample. Due to insufficient observing time and large amounts of corrupted data, the rms noise obtained for these images was high. We determined upper limit estimations but due to the insufficient sensitivity of our maps we were unable to reach the expected halo flux from the scaling relations and therefore can not rule out the presence of radio halos with theoretically predicted powers. However, given the the observed positive correlation between R_H and R_v and the mass of our clusters we simulated 400 kpc as well as 1 Mpc halos. Based on these 3σ upper limits we can make the following conclusions for the 400 kpc halos: in J1115 we rule out the presence of a radio halo with power $P_{1.4\text{GHz}} = 4.15 \times 10^{24} \text{ W Hz}^{-1}$, in J1040 we rule out the presence of a radio halo with power $P_{1.4\text{GHz}} = 1.67 \times 10^{24} \text{ W Hz}^{-1}$, and in J1516 we rule out the presence of a radio halo with power $P_{1.4\text{GHz}} = 5.88 \times 10^{25} \text{ W Hz}^{-1}$. We plotted these limits on the $P_{1.4\text{GHz}} - L_X$ and $P_{1.4\text{GHz}} - M_{500}$ plane and found that they fit the correlation within the scatter and that more sensitive observations could reveal a lower power radio halo detection.

Table 5.5: List of clusters with Mpc diffuse radio emission taken from Cuciti et al. (2015) with velocity dispersions and temperatures taken from literature.

Name	RA (J2000)	Dec (J2000)	z	σ_v (km s ⁻¹)	Reference	T (keV)	Survey	Reference
A0115	00 55 59.5	+26 19 14.0	0.197	1219 ⁺⁷² ₋₇₁	Haines et al. (2015)	5.3 ^{+0.1} _{-0.1}	Chandra	Maughan et al. (2012)
A0209	01 31 53.0	-13 36 34.0	0.206	1394 ⁺⁸⁸ ₋₉₉	Mercurio et al. (2003)	10.2 ^{+1.2} _{-1.4}	Chandra	Mercurio et al. (2003)
A0520	04 54 19.0	+02 56 49.0	0.203	1066 ⁺⁶⁷ ₋₆₁	Girardi et al. (2008)	8.3 ^{+0.4} _{-0.5}	ASCA	Allen (2000)
A0521	04 54 09.1	-10 14 19.0	0.248	1002 ⁺⁹⁵ ₋₉₅	Sifón et al. (2015)	5.9 ^{+0.3} _{-0.4}	ASCA	Allen (2000)
A0665	08 30 45.2	+65 52 55.0	0.182	1227 ⁺⁵⁹ ₋₅₉	Haines et al. (2015)	7.7 ^{+0.3} _{-0.3}	XMM	Peterson et al. (2003)
A0697	08 42 53.3	+36 20 12.0	0.282	1268 ⁺⁵⁷ ₋₅₈	Haines et al. (2015)	8.6 ^{+0.5} _{-0.5}	ASCA	White (2000)
A0773	09 17 59.4	+51 42 23.0	0.217	1394 ⁺⁸⁴ ₋₆₈	Barrena et al. (2007)	8.7 ^{+0.4} _{-0.4}	ASCA	Saunders et al. (2003)
A1300	11 31 56.3	-19 55 37.0	0.308	1034 ⁺⁸⁹ ₋₁₀₄	Girardi and Mezzetti (2001)	11.4 ^{+0.6} _{-0.8}	ASCA	Pierre et al. (1999)
A1689	13 11 29.5	-01 20 17.0	0.183	1541 ⁺⁴⁶ ₋₄₆	Haines et al. (2015)	8.6 ^{+0.2} _{-0.5}	ASCA	Ikebe et al. (2002)
A1758a	13 32 32.1	+50 30 37.0	0.280	744 ⁺¹⁰⁷ ₋₁₀₇	Sifón et al. (2015)	6.6 ^{+1.3} _{-1.8}	ASCA	Rizza et al. (1998)
A1914	14 26 03.0	+37 49 32.0	0.171	1055 ⁺⁴⁴ ₋₄₄	Haines et al. (2015)	8.4 ^{+0.4} _{-0.4}	ASCA	Ikebe et al. (2002)
A2142	15 58 16.1	+27 13 29.0	0.089	1086 ⁺³¹ ₋₃₁	Sifón et al. (2015)	8.5 ^{+0.3} _{-0.3}	ASCA	Ikebe et al. (2002)
A2163	16 15 46.9	-06 08 45.0	0.203	1381 ⁺³²⁴ ₋₃₂₄	Martini et al. (2007)	10.6 ^{+0.4} _{-0.6}	ASCA	Ikebe et al. (2002)
A2218	16 35 51.6	+66 12 39.0	0.171	1245 ⁺⁴² ₋₄₂	Haines et al. (2015)	6.9 ^{+0.3} _{-0.3}	Chandra	Machacek et al. (2002)
A2219	16 40 21.1	+46 41 16.0	0.228	1189 ⁺⁶⁵ ₋₆₅	Sifón et al. (2015)	12.4 ^{+0.4} _{-0.5}	ASCA	Allen (2000)
A2744	00 14 18.8	-30 23 00.0	0.307	1497 ⁺⁵⁷ ₋₅₇	Owers et al. (2011)	8.0 ^{+0.8} _{-0.8}	Chandra	Merten et al. (2011)

Table 5.6: List of clusters with no Mpc diffuse radio emission taken from Cuciti et al. (2015) with velocity dispersions and temperatures taken from literature. The clusters whose temperatures are listed as coming from ROSAT have been calculated from the $L_X - T_X$ relation. The clusters with an * next to the name are those clusters where merging is evident in X-ray observations. † The full name for RXJ1720 is RXJ1720.1+2368.1

Name	RA (J2000)	Dec (J2000)	z	σ_v (km s ⁻¹)	Reference	T (keV)	Survey	Reference
A0478	04 13 20.7	+10 28 35.0	0.088	1088	Coziol et al. (2009)	7.3 ^{0.3}	Chandra	Cavagnolo et al. (2008)
A1132	10 58 19.6	+56 46 56.0	0.134	749 ⁸⁰ ₆₁	Rines et al. (2013)	7.1	ROSAT	Ebeling et al. (1998)
A1413	11 55 18.9	+23 24 31.0	0.143	881 ⁸¹ ₈₁	Sifón et al. (2015)	6.6 ^{0.1} _{0.1}	XMM	Planck Collaboration et al. (2011)
A1423*	11 57 22.5	+33 39 18.0	0.214	590 ⁴⁵ ₄₅	Lemze et al. (2013)	5.4 ^{0.4} _{0.4}	ASCA	Horner (2001)
A1437	12 00 22.3	+03 20 33.9	0.134	1233 ¹⁰² ₈₁	Rines et al. (2013)	7.4	ROSAT	Ebeling et al. (1996)
A1576*	12 37 59.0	+63 11 26.0	0.302	983	Coziol et al. (2009)	8.7 ^{0.7} _{0.7}	ASCA	Novicki et al. (2002)
A1763	13 35 17.2	+40 59 58.0	0.228	1130 ⁸¹ ₈₁	Sifón et al. (2015)	7.3 ^{0.5} _{0.5}	ASCA	White (2000)
A1835	14 01 02.3	+02 52 48.0	0.253	762 ¹⁰⁶ ₁₀₆	Sifón et al. (2015)	9.8 ^{0.6} _{0.6}	Chandra	Cavagnolo et al. (2008)
A2104	15 40 08.2	-03 18 23.0	0.153	1081 ¹²⁶ ₁₂₆	Sifón et al. (2015)	9.1 ^{0.5} _{0.5}	ASCA	White (2000)
A2204	16 32 45.7	+05 34 43.0	0.151	782 ²⁷⁸ ₂₇₈	Sifón et al. (2015)	7.8 ^{0.2} _{0.2}	XMM	Planck Collaboration et al. (2011)
A2261*	17 22 17.1	+32 08 02.0	0.224	882 ⁸⁶ ₈₆	Sifón et al. (2015)	8.8 ^{0.4} _{0.4}	ASCA	Allen (2000)
A2390	21 53 34.6	+17 40 11.0	0.234	1120 ¹¹³ ₁₁₃	Sifón et al. (2015)	8.9 ^{0.2} _{0.2}	XMM	Planck Collaboration et al. (2011)
A2537*	23 08 23.2	-02 11 31.0	0.297	909 ⁸⁵ ₈₅	Sifón et al. (2015)	6.1 ^{0.5} _{0.5}	ASCA	Horner (2001)
A2631	23 37 40.6	+00 16 36.0	0.278	851 ⁹⁶ ₇₂	Rines et al. (2013)	7.5 ^{0.5} _{0.5}	XMM	Reichert et al. (2011)
A2667*	23 51 40.7	-26 05 01.0	0.226	960 ¹⁹⁰ ₁₂₀	Covone et al. (2006)	6.3 ^{0.3} _{0.3}	ASCA	Horner (2001)
RXJ1720†	17 20 10.1	+26 37 29.5	0.164	1019	Miller et al. (2005)	5.8 ^{0.1} _{0.1}	XMM	Planck Collaboration et al. (2011)

CHAPTER 6

CONCLUSION

Galaxy clusters offer a unique opportunity to study astrophysical processes as well as gain information about the Universe. They allow us to test the underlying cosmological model and learn more about the Big Bang Theory and the evolution of the Universe. The galaxies within the cluster let us explore the formation of structure and the processes, such as AGN feedback, which effect the intracluster medium. Galaxy clusters can be detected via a variety of methods including optical, X-ray, radio, and SZ. Each wavelength study providing us with different properties and allow us to form a complete picture of the workings of the Universe. There are simple power laws which exist between these properties which can be estimated via models, such as the self-similar model, based on our current knowledge of structure formation. By comparing the theoretical relations to observational data, we can re-analyse the models and improve them and thereby allow us to constrain parameters describing our Universe.

In Chapter 2, we introduced a homogeneous cluster sample drawn from the XCS to be used in the study of scaling relations. We present new Gemini data obtained for 12 $z > 0.5$ XCS clusters, and discuss a method for membership determination. We obtain new redshift measurements for these clusters, and include a further 16 clusters with spectroscopic redshift literature data to obtain a final sample of 38 clusters.

In Chapter 3, we studied the velocity dispersion–temperature ($\sigma_v - T_X$) relation for our sample of clusters. Using an orthogonal regression method we found the slope of the relation to be consistent with the findings of previous studies, i.e., slightly steeper than expected from self-similarity. Under the assumption that the slope of the relation does not evolve with redshift, we measured the evolution of the normalisation of the relation and found it to be slightly negative but not significantly different from the self-similar solution ($\sigma_v \propto T^{0.86 \pm 0.14} E(z)^{-0.37 \pm 0.33}$). We applied the same scaling relation analysis methods to the BAHAMAS and Millennium Gas cosmological hydrodynamical simulations and found no evolution in BAHAMAS but positive evolution with the Millennium Gas simulation. The difference is most likely due to the inclusion of self-consistent modelling of radiative cooling in BAHAMAS, which is absent in the Millennium Gas simulation. While this work has improved upon previous studies in terms of the number of high redshift clusters included, we note that the uncertainties on the scaling relation parameters are still rather large, and a combination of better measurements of individual cluster properties and a larger sample are required to make further progress.

In Chapter 4, we studied the mass-temperature ($M - T_X$) by measuring dynamical masses based on our velocity dispersions. We used the orthogonal regression method for $\sigma_v - T_X$ relation, as well as a Gaussian mixture model, to fit for the slope. The Gaussian mixture model method was not included in the $\sigma_v - T_X$ relation fitting as it has not been adapted to include evolution. The regression method returns a steeper than expected slope ($B = 1.5$ for the self-similar model) for the orthogonal method and a shallower slope for the Gaussian mixture model method. To test which method performs better we simulated data and ran the fitting code for both models. The Gaussian mixture model method was able to retrieve the slope of the simulated data but the orthogonal method, once again obtained a steeper than expected result. Since previous results obtained their fits using hydrostatic masses, we offer a comparison between the two masses and identify that the dynamical mass estimate may be over-estimating the mass of the cluster.

In the final chapter, we studied galaxy clusters in the radio wavelength, focusing on diffuse radio emission. We highlight the relationship between diffuse emission and mergers and identify the effect of mergers on scaling relations. We obtain a known sample of galaxy clusters, from literature, which are known to host diffuse emission or have a non detection. We identify their position on the $\sigma_v - T_X$ relation and find no notable difference between the two populations, although the sample size is small. We also present 3 new observations with the VLA of clusters from our XCS sample as part of a pilot study to search for radio halos in low mass clusters. We obtained images for these clusters but they had a high rms noise due to corrupt data and insufficient observing time making the possibility of obtaining a detection extremely low. Hence, we simulated upper limit estimations. We plotted these limits on the $P_{1.4\text{GHz}} - L_X$ and $P_{1.4\text{GHz}} - M_{500}$ plane and found that they fit the correlation within the scatter. We discuss the correlation between the radio halo size and the cluster mass as a further possibility of the discrepancies we observe. We simulate a smaller radio halo of 400 kpc also plot these limits on the $P_{1.4\text{GHz}} - L_X$ and $P_{1.4\text{GHz}} - M_{500}$ plane. Using this reduced simulated halo size, our radio power upper limits are decreased by a factor of 2~10. Although, our upper limits still do not rule out the presence of a radio halo at this smaller size, it does bring into question the accepted method for calculating radio halo upper limits.

6.1 Future Work

Radio, optical and X-ray observations provide complementary data which allows us to gain a better understanding of galaxy clusters. However, some key information is still missing, particularly in relation to the calculations of the masses of clusters, which is extremely important for constraining cosmological parameters. Therefore, an extension to this work includes collecting SZ, hydrostatic and dynamical masses for a large sample of galaxy clusters and providing a full statistical comparison. Other mass estimates such as those from weak lensing must also be considered.

Since one of the main focuses of this thesis was scaling relations, we also need to look at ways to better constrain the fitting parameters. One way of doing this is to include evolution in the Gaussian mixture model fitting method, so that it can be applied to the $\sigma_v - T_X$ relation, since it offers an improvement over the orthogonal fitting method. This method also has the capability to include the effect of selection functions. This can be added once a selection function for XCS exists.

We were unable to draw a concrete conclusion on whether the presence of a radio halo in a cluster lies in a different part of the $\sigma_v - T_X$ when compared to clusters without a radio halo, due to our small sample size. Therefore, future work may include performing a more concise literature review of all known data on clusters with and without radio halos. If sufficient redshifts are available, we can use our methodology to calculate velocity dispersions. A large homogeneous selected cluster sample could aid in this investigation as well as providing us with a tool to learn more about diffuse emission in galaxy clusters. There are still many unanswered questions in this field, such as the effect of the $R_H - R_v$ relation on the calculation of upper limits, that will require follow-up observations and further studies.

APPENDIX A

REDSHIFT CATALOGUE

In this appendix we provide the redshifts of the member galaxies for each cluster used for the redshift and velocity dispersion measurements.

Galaxy Name	RA (J2000)	Dec (J2000)	z	Reference
GALEXASC J000046.26-251058.3	00 ^h 00 ^m 46.26 ^s	-25°10'59.9"	0.0821	Colless et al. (2003b)
GALEXASC J000057.30-250623.9	00 ^h 00 ^m 57.23 ^s	-25°06'25.9"	0.0821	Colless et al. (2003b)
2dFGRS S134Z161	23 ^h 59 ^m 32.60 ^s	-25°13'02.2"	0.0823	Colless et al. (2003b)
GALEXASC J235957.50-250120.7	23 ^h 59 ^m 57.51 ^s	-25°01'20.5"	0.0823	Colless et al. (2003b)
2dFGRS S134Z139	00 ^h 00 ^m 25.25 ^s	-25°20'48.2"	0.0834	Colless et al. (2003b)
2MASX J00002408-2510371	00 ^h 00 ^m 24.10 ^s	-25°10'38.0"	0.0837	Colless et al. (2003b)
2MASX J00004212-2512080	00 ^h 00 ^m 42.12 ^s	-25°12'08.1"	0.0837	Jones et al. (2009)
2MASX J00002446-2516181	00 ^h 00 ^m 24.45 ^s	-25°16'18.3"	0.0839	Colless et al. (2003b)
AM 2357-252 NED01	00 ^h 00 ^m 13.28 ^s	-25°11'08.1"	0.0841	Coziol et al. (2009)
2dFGRS S134Z105	00 ^h 01 ^m 02.68 ^s	-25°08'59.4"	0.0844	Colless et al. (2003b)
2MASX J00000684-2515021	00 ^h 00 ^m 06.85 ^s	-25°15'02.0"	0.0847	Colless et al. (2003b)

Continued on next page

Table A.1 – continued from previous page

Galaxy Name	RA (J2000)	Dec (J2000)	z	Reference
2MASX J00001841-2510051	00 ^h 00 ^m 18.43 ^s	-25°10'04.9"	0.0847	Colless et al. (2003b)
AM 2357-252 2MASX J00000093-2521313	00 ^h 00 ^m 13.70 ^s 00 ^h 00 ^m 00.94 ^s	-25°11'10.0" -25°21'31.8"	0.0847 0.0848	Colless et al. (2003b) Colless et al. (2003b)
AM 2357-252 2dFGRS S134Z131	00 ^h 00 ^m 14.06 ^s 00 ^h 00 ^m 28.86 ^s	-25°11'12.6" -25°07'11.2"	0.0851 0.0854	Jones et al. (2009) Colless et al. (2003b)
2MASX J00003358-2509120	00 ^h 00 ^m 33.59 ^s	-25°09'12.1"	0.0857	Colless et al. (2003b)
2MASX J00000817-2512181	00 ^h 00 ^m 08.16 ^s	-25°12'18.1"	0.0864	Colless et al. (2003b)
2MASX J00004617-2515090	00 ^h 00 ^m 46.18 ^s	-25°15'09.3"	0.0869	Colless et al. (2003b)

Table A.1: XMMXCSJ000013.9-251052.1: Column 1 gives the name of the galaxy, column 2 and 3 give the right ascension and declination respectively, and column 4 gives the redshift of the galaxy. Column 5 gives the reference from which the redshift was taken.

Galaxy Name	RA (J2000)	Dec (J2000)	z	Reference
GALEXMSC J003407.05-432228.7	00 ^h 34 ^m 06.97 ^s	-43°22'30.2"	0.3877	Feruglio et al. (2008)
SWIRE3 J003407.30-432152.8	00 ^h 34 ^m 07.29 ^s	-43°21'52.9"	0.3880	Sacchi et al. (2009)
SWIRE3 J003400.83-432122.5	00 ^h 34 ^m 00.77 ^s	-43°21'22.5"	0.3890	Sacchi et al. (2009)
SWIRE3 J003408.87-432244.6	00 ^h 34 ^m 08.87 ^s	-43°22'44.7"	0.3890	Sacchi et al. (2009)
SWIRE3 J003405.07-431742.3	00 ^h 34 ^m 05.06 ^s	-43°17'42.3"	0.3910	Sacchi et al. (2009)
IRAC 236852 SWIRE3 J003425.16-431912.1	00 ^h 34 ^m 27.40 ^s 00 ^h 34 ^m 25.15 ^s	-43°18'59.6" -43°19'12.2"	0.3925 0.3930	Feruglio et al. (2008) Sacchi et al. (2009)
SWIRE3 J003422.50-431550.8	00 ^h 34 ^m 22.49 ^s	-43°15'51.0"	0.3940	Sacchi et al. (2009)
SWIRE3 J003428.37-431704.2	00 ^h 34 ^m 28.36 ^s	-43°17'04.4"	0.3940	Sacchi et al. (2009)
SWIRE3 J003444.36-431806.2	00 ^h 34 ^m 44.37 ^s	-43°18'06.4"	0.3940	Sacchi et al. (2009)

Continued on next page

Table A.2 – continued from previous page

Galaxy Name	RA (J2000)	Dec (J2000)	z	Reference
SWIRE3 J003413.21-431727.4	00 ^h 34 ^m 13.20 ^s	-43°17'27.5"	0.3960	Sacchi et al. (2009)
SWIRE3 J003417.67-431909.8	00 ^h 34 ^m 17.67 ^s	-43°19'09.9"	0.3960	Sacchi et al. (2009)
SWIRE3 J003424.77-432117.8	00 ^h 34 ^m 24.78 ^s	-43°21'18.2"	0.3960	Sacchi et al. (2009)
SWIRE3 J003430.66-431956.6	00 ^h 34 ^m 30.65 ^s	-43°19'56.8"	0.3960	Sacchi et al. (2009)
SWIRE3 J003419.36-432157.4	00 ^h 34 ^m 19.35 ^s	-43°21'57.6"	0.3970	Sacchi et al. (2009)
SWIRE3 J003426.75-431854.7	00 ^h 34 ^m 26.74 ^s	-43°18'54.6"	0.3970	Sacchi et al. (2009)
SWIRE3 J003407.33-432141.6	00 ^h 34 ^m 07.33 ^s	-43°21'41.7"	0.3980	Sacchi et al. (2009)
SWIRE3 J003417.78-431928.4	00 ^h 34 ^m 17.77 ^s	-43°19'28.5"	0.3980	Sacchi et al. (2009)
ESIS J003412.63-431705.5	00 ^h 34 ^m 12.63 ^s	-43°17'05.5"	0.3990	Sacchi et al. (2009)
SWIRE3 J003425.85-432057.8	00 ^h 34 ^m 25.86 ^s	-43°20'58.0"	0.3990	Sacchi et al. (2009)
SWIRE3 J003424.03-431914.9	00 ^h 34 ^m 24.02 ^s	-43°19'15.0"	0.4010	Sacchi et al. (2009)
SWIRE3 J003442.95-431727.6	00 ^h 34 ^m 42.94 ^s	-43°17'27.2"	0.4020	Sacchi et al. (2009)

Table A.2: XMMXCSJ003430.1-431905.6: All columns are as explained in Table A.1.

Galaxy Name	RA (J2000)	Dec (J2000)	z	Reference
Name	RA(J2000)	Dec(J2000)	z	Reference
Cl 0053-37:[CHM98] 12	00 ^h 55 ^m 55.56 ^s	-37°32'19.7"	0.1613	Guzzo et al. (2009)
Cl 0053-37:[CHM98] 14	00 ^h 55 ^m 57.74 ^s	-37°32'22.6"	0.1613	Guzzo et al. (2009)
Cl 0053-37:[CHM98] 08	00 ^h 55 ^m 58.90 ^s	-37°33'00.7"	0.1617	Cappi et al. (1998)
(GSB2009) J005552.68-373143.0	00 ^h 55 ^m 52.68 ^s	-37°31'43.0"	0.1626	Guzzo et al. (2009)

Continued on next page

Table A.3 – continued from previous page

Galaxy Name	RA (J2000)	Dec (J2000)	z	Reference
2MASX J00555916-3732186	00 ^h 55 ^m 59.11 ^s	-37°32'18.2"	0.1631	Cappi et al. (1998)
APMUKS(BJ) B005339.96-374945.2	00 ^h 56 ^m 01.56 ^s	-37°33'32.0"	0.1633	Guzzo et al. (2009)
CI 0053-37:[CHM98] 15	00 ^h 55 ^m 59.32 ^s	-37°32'35.2"	0.1636	Cappi et al. (1998)
APMUKS(BJ) B005340.88-374818.8	00 ^h 56 ^m 02.42 ^s	-37°32'04.6"	0.1638	Cappi et al. (1998)
CI 0053-37:[CHM98] 20	00 ^h 55 ^m 56.26 ^s	-37°31'48.0"	0.1649	Cappi et al. (1998)
2XMM J005557.1-373237	00 ^h 55 ^m 56.74 ^s	-37°32'35.4"	0.1653	Cappi et al. (1998)
CI 0053-37:[CHM98] 09	00 ^h 56 ^m 02.76 ^s	-37°33'03.9"	0.1654	Cappi et al. (1998)
2MASX J00560639-3733176	00 ^h 56 ^m 06.41 ^s	-37°33'17.6"	0.1661	Guzzo et al. (2009)
CI 0053-37:[CHM98] 21	00 ^h 56 ^m 09.54 ^s	-37°31'49.0"	0.1663	Cappi et al. (1998)
(GSB2009) J005559.52-373343.2	00 ^h 55 ^m 59.52 ^s	-37°33'43.2"	0.1665	Guzzo et al. (2009)
APMUKS(BJ) B005339.81-374854.8	00 ^h 56 ^m 01.34 ^s	-37°32'40.9"	0.1673	Cappi et al. (1998)
APMUKS(BJ) B005343.30-374914.5	00 ^h 56 ^m 04.82 ^s	-37°33'00.0"	0.1682	Guzzo et al. (2009)
(GSB2009) J005552.42-373131.8	00 ^h 55 ^m 52.42 ^s	-37°31'31.8"	0.1686	Guzzo et al. (2009)
CI 0053-37:[CHM98] 04	00 ^h 56 ^m 09.71 ^s	-37°33'39.9"	0.1691	Cappi et al. (1998)
2MASX J00560925-3733595	00 ^h 56 ^m 09.28 ^s	-37°33'59.3"	0.1694	Cappi et al. (1998)
APMUKS(BJ) B005348.77-375021.3	00 ^h 56 ^m 10.23 ^s	-37°34'07.9"	0.1720	Cappi et al. (1998)
CI 0053-37:[CHM98] 11	00 ^h 56 ^m 04.75 ^s	-37°32'51.0"	0.1721	Cappi et al. (1998)
CI 0053-37:[CHM98] 03	00 ^h 56 ^m 07.07 ^s	-37°33'49.4"	0.1722	Cappi et al. (1998)

Table A.3: XMMXCSJ005603.0-373248.0: All columns are as explained in Table A.1.

Galaxy Name	RA (J2000)	Dec (J2000)	z	Reference
2MASX J01530967+0102002	01 ^h 53 ^m 09.69 ^s	+01°02'00.3''	0.0579	Berlind et al. (2006)
2MASX J01531414+0103443	01 ^h 53 ^m 14.16 ^s	+01°03'44.4''	0.0579	Abazajian et al. (2003)
2MASX J01531014+0101302	01 ^h 53 ^m 10.13 ^s	+01°01'30.5''	0.0586	Abazajian et al. (2003)
2MASX J01530528+0059092	01 ^h 53 ^m 05.29 ^s	+00°59'09.2''	0.0588	Stoughton et al. (2002)
2MASX J01531034+0105562	01 ^h 53 ^m 10.37 ^s	+01°05'56.7''	0.0590	Abazajian et al. (2003)
2MASX J01530827+0101502	01 ^h 53 ^m 08.29 ^s	+01°01'50.7''	0.0594	Berlind et al. (2006)
SDSS J015251.27+010705.4	01 ^h 52 ^m 51.28 ^s	+01°07'05.4''	0.0595	Stoughton et al. (2002)
SDSS J015316.74+010139.4	01 ^h 53 ^m 16.75 ^s	+01°01'39.5''	0.0596	Berlind et al. (2006)
2MASX J01530347+0101232	01 ^h 53 ^m 03.49 ^s	+01°01'23.0''	0.0596	Abazajian et al. (2003)
2MASX J01531521+0102203	01 ^h 53 ^m 15.24 ^s	+01°02'20.7''	0.0598	Abazajian et al. (2003)
SDSS J015249.63+010023.3	01 ^h 52 ^m 49.61 ^s	+01°00'22.6''	0.0600	Goto et al. (2003)
2MASX J01532128+0055143	01 ^h 53 ^m 21.27 ^s	+00°55'14.6''	0.0607	Stoughton et al. (2002)

Table A.4: XMMXCSJ015315.0+010214.2: All columns are as explained in Table A.1.

Galaxy Name	RA (J2000)	Dec (J2000)	z	Reference
(MLF2006) J072049.93+710856.6	07 ^h 20 ^m 49.93 ^s	+71°08'56.6''	0.2270	Mulchaey et al. (2006)
1RXS J072049.0+710724	07 ^h 20 ^m 47.35 ^s	+71°07'15.4''	0.2274	Jeltema et al. (2007)
(MLF2006) J072103.45+710906.0	07 ^h 21 ^m 03.45 ^s	+71°09'06.0''	0.2274	Mulchaey et al. (2006)
(MLF2006) J072044.89+710845.5	07 ^h 20 ^m 44.89 ^s	+71°08'45.5''	0.2275	Mulchaey et al. (2006)
(MLF2006) J072039.75+710950.8	07 ^h 20 ^m 39.75 ^s	+71°09'50.8''	0.2277	Mulchaey et al. (2006)

Continued on next page

Table A.5 – continued from previous page

Galaxy Name	RA (J2000)	Dec (J2000)	z	Reference
(MLF2006) J072046.96+710922.8	07 ^h 20 ^m 46.96 ^s	+71°09'22.8''	0.2285	Jeltema et al. (2007)
(MLF2006) J072059.93+710932.2	07 ^h 20 ^m 59.93 ^s	+71°09'32.2''	0.2288	Mulchaey et al. (2006)
(JML2007) J072044.89+710930.9	07 ^h 20 ^m 44.89 ^s	+71°09'30.9''	0.2294	Jeltema et al. (2007)
(JML2007) J072048.69+711123.2	07 ^h 20 ^m 48.69 ^s	+71°11'23.2''	0.2299	Jeltema et al. (2007)
GALEXASC J072040.85+711127.4	07 ^h 20 ^m 40.46 ^s	+71°11'27.9''	0.2300	Jeltema et al. (2007)
(MLF2006) J072053.73+710859.6	07 ^h 20 ^m 53.73 ^s	+71°08'59.6''	0.2300	Jeltema et al. (2007)
(MLF2006) J072114.17+711028.0	07 ^h 21 ^m 14.17 ^s	+71°10'28.0''	0.2304	Mulchaey et al. (2006)
(MLF2006) J072054.47+710857.4	07 ^h 20 ^m 54.47 ^s	+71°08'57.4''	0.2305	Mulchaey et al. (2006)
(JML2007) J072045.08+711118.1	07 ^h 20 ^m 45.08 ^s	+71°11'18.1''	0.2306	Jeltema et al. (2007)
(JML2007) J072046.39+711005.0	07 ^h 20 ^m 46.39 ^s	+71°10'05.0''	0.2307	Jeltema et al. (2007)
(MLF2006) J072103.43+710917.7	07 ^h 21 ^m 03.43 ^s	+71°09'17.7''	0.2308	Mulchaey et al. (2006)
GALEXMSC J072113.65+710952.5	07 ^h 21 ^m 13.26 ^s	+71°09'49.8''	0.2314	Mulchaey et al. (2006)
(MLF2006) J072109.63+710903.3	07 ^h 21 ^m 09.63 ^s	+71°09'03.3''	0.2315	Mulchaey et al. (2006)
(MLF2006) J072109.09+710922.1	07 ^h 21 ^m 09.09 ^s	+71°09'22.1''	0.2320	Mulchaey et al. (2006)
(JML2007) J072039.35+710730.9	07 ^h 20 ^m 39.35 ^s	+71°07'30.9''	0.2323	Jeltema et al. (2007)
GALEXASC J072111.89+710857.1	07 ^h 21 ^m 11.40 ^s	+71°08'57.2''	0.2325	Mulchaey et al. (2006)
(MLF2006) J072048.06+711037.5	07 ^h 20 ^m 48.06 ^s	+71°10'37.5''	0.2326	Jeltema et al. (2007)
(MLF2006) J072058.02+710916.2	07 ^h 20 ^m 58.02 ^s	+71°09'16.2''	0.2328	Jeltema et al. (2007)
(MLF2006) J072050.33+710925.7	07 ^h 20 ^m 50.33 ^s	+71°09'25.7''	0.2329	Jeltema et al. (2007)
(JML2007) J072056.17+711105.1	07 ^h 20 ^m 56.17 ^s	+71°11'05.1''	0.2331	Jeltema et al. (2007)

Continued on next page

Table A.5 – continued from previous page

Galaxy Name	RA (J2000)	Dec (J2000)	z	Reference
(JML2007) J072055.02+710815.0	07 ^h 20 ^m 55.02 ^s	+71°08′15.0″	0.2335	Jeltema et al. (2007)
(MLF2006) J072046.75+710904.4	07 ^h 20 ^m 46.75 ^s	+71°09′04.4″	0.2337	Jeltema et al. (2007)
GALEXMSC J072016.54+710943.2	07 ^h 20 ^m 16.53 ^s	+71°09′42.6″	0.2340	Mulchaey et al. (2006)
(MLF2006) J072044.19+710854.1	07 ^h 20 ^m 44.19 ^s	+71°08′54.1″	0.2347	Mulchaey et al. (2006)

Table A.5: XMMXCSJ072054.3+710900.5: All columns are as explained in Table A.1.

Galaxy Name	RA (J2000)	Dec (J2000)	z	Reference
(VMF98) 049:[BBS2002] 021	08 ^h 19 ^m 42.12 ^s	+70°54′32.1″	0.2272	Balogh et al. (2002)
(VMF98) 049:[BBS2002] 040	08 ^h 19 ^m 11.99 ^s	+70°55′43.8″	0.2274	Balogh et al. (2002)
(VMF98) 049:[BBS2002] 027	08 ^h 19 ^m 01.38 ^s	+70°54′51.6″	0.2277	Balogh et al. (2002)
(VMF98) 049:[BBS2002] 002	08 ^h 18 ^m 48.72 ^s	+70°52′55.8″	0.2278	Balogh et al. (2002)
(VMF98) 049:[BBS2002] 026	08 ^h 19 ^m 22.86 ^s	+70°54′44.9″	0.2280	Balogh et al. (2002)
(VMF98) 049:[BBS2002] 033	08 ^h 19 ^m 17.75 ^s	+70°55′01.0″	0.2289	Balogh et al. (2002)
(VMF98) 049:[BBS2002] 013	08 ^h 19 ^m 46.92 ^s	+70°53′53.9″	0.2294	Balogh et al. (2002)
(VMF98) 049:[BBS2002] 025	08 ^h 18 ^m 56.12 ^s	+70°54′39.4″	0.2296	Balogh et al. (2002)
(VMF98) 049:[BBS2002] 029	08 ^h 18 ^m 54.03 ^s	+70°54′52.6″	0.2297	Balogh et al. (2002)
(VMF98) 049:[BBS2002] 011	08 ^h 19 ^m 07.76 ^s	+70°53′37.7″	0.2304	Balogh et al. (2002)
2MASX J08191836+7055042	08 ^h 19 ^m 18.31 ^s	+70°55′04.2″	0.2304	Balogh et al. (2002)
(VMF98) 049:[BBS2002] 036	08 ^h 19 ^m 23.75 ^s	+70°55′24.3″	0.2304	Balogh et al. (2002)
(VMF98) 049:[BBS2002] 015	08 ^h 19 ^m 35.25 ^s	+70°54′02.4″	0.2305	Balogh et al. (2002)

Continued on next page

Table A.6 – continued from previous page

Galaxy Name	RA (J2000)	Dec (J2000)	z	Reference
(VMF98) 049:[BBS2002] 047	08 ^h 19 ^m 23.60 ^s	+70°56'30.8''	0.2306	Balogh et al. (2002)
(VMF98) 049:[BBS2002] 012	08 ^h 19 ^m 37.97 ^s	+70°53'49.5''	0.2309	Balogh et al. (2002)
(VMF98) 049:[BBS2002] 037	08 ^h 19 ^m 05.95 ^s	+70°55'34.5''	0.2310	Balogh et al. (2002)
(VMF98) 049:[BBS2002] 043	08 ^h 19 ^m 12.64 ^s	+70°56'05.8''	0.2313	Balogh et al. (2002)
(VMF98) 049:[BBS2002] 006	08 ^h 19 ^m 06.49 ^s	+70°53'04.1''	0.2319	Balogh et al. (2002)
(VMF98) 049:[BBS2002] 016	08 ^h 19 ^m 04.37 ^s	+70°53'55.0''	0.2320	Balogh et al. (2002)

Table A.6: XMMXCSJ081918.6+705457.5: All columns are as explained in Table A.1.

Galaxy Name	RA (J2000)	Dec (J2000)	z	Reference
SDSS J094400.28+164011.1	09 ^h 44 ^m 00.29 ^s	+16°40'11.2''	0.2487	Verdugo et al. (2008)
SDSS J094334.06+164035.7	09 ^h 43 ^m 34.06 ^s	+16°40'35.7''	0.2500	Verdugo et al. (2008)
SDSS J094353.35+163958.8	09 ^h 43 ^m 53.35 ^s	+16°39'58.8''	0.2511	Verdugo et al. (2008)
SDSS J094345.51+164130.4	09 ^h 43 ^m 45.52 ^s	+16°41'30.5''	0.2514	Verdugo et al. (2008)
SDSS J094353.48+164022.7	09 ^h 43 ^m 53.49 ^s	+16°40'22.7''	0.2516	Verdugo et al. (2008)
SDSS J094358.03+164116.5	09 ^h 43 ^m 58.03 ^s	+16°41'16.6''	0.2520	Verdugo et al. (2008)
2MASX J09435839+1641091	09 ^h 43 ^m 58.33 ^s	+16°41'09.1''	0.2527	Verdugo et al. (2008)
SDSS J094351.68+164144.7	09 ^h 43 ^m 51.68 ^s	+16°41'44.7''	0.2529	Verdugo et al. (2008)
SDSS J094353.53+164142.6	09 ^h 43 ^m 53.53 ^s	+16°41'42.7''	0.2529	Verdugo et al. (2008)
SDSS J094333.62+163906.3	09 ^h 43 ^m 33.62 ^s	+16°39'06.3''	0.2530	Verdugo et al. (2008)
SDSS J094338.73+163854.9	09 ^h 43 ^m 38.74 ^s	+16°38'55.0''	0.2533	Verdugo et al. (2008)

Continued on next page

Table A.7 – continued from previous page

Galaxy Name	RA (J2000)	Dec (J2000)	z	Reference
SDSS J094401.36+163800.9	09 ^h 44 ^m 01.37 ^s	+16°38'01.0''	0.2536	Verdugo et al. (2008)
SDSS J094352.54+164439.4	09 ^h 43 ^m 52.54 ^s	+16°44'39.5''	0.2538	Verdugo et al. (2008)
SDSS J094358.77+164001.9	09 ^h 43 ^m 58.78 ^s	+16°40'01.9''	0.2538	Verdugo et al. (2008)
SDSS J094332.40+164000.5	09 ^h 43 ^m 32.41 ^s	+16°40'00.6''	0.2539	Verdugo et al. (2008)
SDSS J094359.68+163729.9	09 ^h 43 ^m 59.69 ^s	+16°37'29.9''	0.2542	Verdugo et al. (2008)
SDSS J094348.66+164038.8	09 ^h 43 ^m 48.67 ^s	+16°40'38.8''	0.2546	Verdugo et al. (2008)
SDSS J094355.86+164035.5	09 ^h 43 ^m 55.86 ^s	+16°40'35.6''	0.2551	Verdugo et al. (2008)
SDSS J094336.77+164102.3	09 ^h 43 ^m 36.78 ^s	+16°41'02.3''	0.2552	Verdugo et al. (2008)
SDSS J094356.38+163650.7	09 ^h 43 ^m 56.38 ^s	+16°36'50.8''	0.2552	Verdugo et al. (2008)
SDSS J094358.90+163921.7	09 ^h 43 ^m 58.90 ^s	+16°39'21.7''	0.2561	Verdugo et al. (2008)
SDSS J094405.00+163834.3	09 ^h 44 ^m 05.00 ^s	+16°38'34.4''	0.2561	Verdugo et al. (2008)
SDSS J094359.32+164109.4	09 ^h 43 ^m 59.33 ^s	+16°41'09.4''	0.2570	Verdugo et al. (2008)
SDSS J094342.95+164034.1	09 ^h 43 ^m 42.96 ^s	+16°40'34.1''	0.2573	Verdugo et al. (2008)
SDSS J094403.16+163948.1	09 ^h 44 ^m 03.17 ^s	+16°39'48.1''	0.2574	Verdugo et al. (2008)
SDSS J094337.95+163932.2	09 ^h 43 ^m 37.95 ^s	+16°39'32.3''	0.2574	Verdugo et al. (2008)
SDSS J094340.06+163923.2	09 ^h 43 ^m 40.06 ^s	+16°39'23.3''	0.2578	Verdugo et al. (2008)

Table A.7: XMMXCSJ094358.2+164120.7: All columns are as explained in Table A.1.

Galaxy Name	RA (J2000)	Dec (J2000)	z	Reference
SDSS J100027.86+251750.9	10 ^h 00 ^m 27.87 ^s	+25° 17' 51.0''	0.0495	Le Fevre et al. (1995)
2MASX J09590595+2512006	09 ^h 59 ^m 05.97 ^s	+25° 12' 01.0''	0.0511	Adelman-McCarthy et al. (2008)
2MASX J09585969+2518276	09 ^h 58 ^m 59.70 ^s	+25° 18' 27.8''	0.0518	Adelman-McCarthy et al. (2008)
SDSS J095848.25+251116.9	09 ^h 58 ^m 48.25 ^s	+25° 11' 16.9''	0.0518	Adelman-McCarthy et al. (2008)
2MASX J09594076+2459301	09 ^h 59 ^m 40.76 ^s	+24° 59' 30.5''	0.0519	Adelman-McCarthy et al. (2008)
2MASX J10001346+2450242	10 ^h 00 ^m 13.49 ^s	+24° 50' 24.1''	0.0519	Adelman-McCarthy et al. (2008)
UGC 05361 2MASX J09590450+2527176	09 ^h 59 ^m 00.86 ^s	+25° 12' 08.2''	0.0519	Huchra et al. (2012)
2MASX J09590450+2527176	09 ^h 59 ^m 04.50 ^s	+25° 27' 18.2''	0.0519	Adelman-McCarthy et al. (2008)
SDSS J100144.49+250159.3	10 ^h 01 ^m 44.49 ^s	+25° 01' 59.3''	0.0526	Adelman-McCarthy et al. (2008)
2MASX J09591647+2509482	09 ^h 59 ^m 16.44 ^s	+25° 09' 48.8''	0.0528	Adelman-McCarthy et al. (2008)
SDSS J095900.71+251134.6	09 ^h 59 ^m 00.72 ^s	+25° 11' 34.7''	0.0529	Adelman-McCarthy et al. (2008)
2MASX J10010959+2520030	10 ^h 01 ^m 09.60 ^s	+25° 20' 03.3''	0.0542	Adelman-McCarthy et al. (2008)
SDSS J100105.06+245810.3	10 ^h 01 ^m 05.06 ^s	+24° 58' 10.4''	0.0549	Adelman-McCarthy et al. (2008)
SDSS J095938.75+251010.8	09 ^h 59 ^m 38.75 ^s	+25° 10' 10.9''	0.0555	Adelman-McCarthy et al. (2008)
2MASX J10000767+2514162	10 ^h 00 ^m 07.65 ^s	+25° 14' 16.4''	0.0556	Adelman-McCarthy et al. (2008)

Table A.8: XMMXCSJ095957.6+251629.0: All columns are as explained in Table A.1.

Galaxy Name	RA (J2000)	Dec (J2000)	z	Reference
SDSS J100052.66+013941.1	10 ^h 00 ^m 52.67 ^s	+01° 39' 41.2''	0.2166	Lilly et al. (2007)
zCOSMOS 805589 SDSS J100057.84+013637.1	10 ^h 00 ^m 33.07 ^s	+01° 41' 04.8''	0.2179	Lilly et al. (2007)
SDSS J100057.84+013637.1	10 ^h 00 ^m 57.84 ^s	+01° 36' 37.2''	0.2190	Lilly et al. (2007)
Continued on next page				

Table A.9 – continued from previous page

Galaxy Name	RA (J2000)	Dec (J2000)	z	Reference
2MASX J10004852+0139137	10 ^h 00 ^m 48.54 ^s	+01°39'13.9''	0.2190	Colless et al. (2003a)
SDSS J100037.77+014013.9	10 ^h 00 ^m 37.77 ^s	+01°40'14.0''	0.2194	Lilly et al. (2007)
SDSS J100057.85+013752.1	10 ^h 00 ^m 57.85 ^s	+01°37'52.2''	0.2195	Lilly et al. (2007)
SDSS J100045.29+013847.4	10 ^h 00 ^m 45.30 ^s	+01°38'47.4''	0.2205	Abazajian et al. (2004)
2MASX J100045.52+0139267	10 ^h 00 ^m 45.54 ^s	+01°39'26.5''	0.2207	Abazajian et al. (2003)
zCOSMOS 805608	10 ^h 00 ^m 32.16 ^s	+01°38'43.5''	0.2212	Lilly et al. (2007)
SDSS J100044.55+013942.0	10 ^h 00 ^m 44.55 ^s	+01°39'42.2''	0.2214	Trump et al. (2007)
SDSS J100038.81+013827.6	10 ^h 00 ^m 38.81 ^s	+01°38'27.6''	0.2219	Lilly et al. (2007)
SDSS J100049.03+013526.8	10 ^h 00 ^m 49.03 ^s	+01°35'26.9''	0.2220	Brusa et al. (2010)
SDSS J100103.45+014413.1	10 ^h 01 ^m 03.45 ^s	+01°44'13.1''	0.2220	Lilly et al. (2007)
zCOSMOS 805183	10 ^h 00 ^m 50.21 ^s	+01°43'20.6''	0.2224	Lilly et al. (2007)
zCOSMOS 805250	10 ^h 00 ^m 47.36 ^s	+01°37'41.6''	0.2235	Lilly et al. (2007)
SDSS J100108.66+013935.2	10 ^h 01 ^m 08.67 ^s	+01°39'35.2''	0.2278	Abazajian et al. (2004)

Table A.9: XMMXCSJ100047.4+013926.9: All columns are as explained in Table A.1.

Galaxy Name	RA (J2000)	Dec (J2000)	z	Reference
SDSS J100125.41+023145.1	10 ^h 01 ^m 25.42 ^s	+02°31'45.2''	0.1210	Abazajian et al. (2004)
SDSS J100131.47+022556.7	10 ^h 01 ^m 31.48 ^s	+02°25'56.7''	0.1211	Trump et al. (2007)
SDSS J100157.95+022746.1	10 ^h 01 ^m 57.96 ^s	+02°27'46.1''	0.1213	Lilly et al. (2007)
SDSS J100120.63+022601.5	10 ^h 01 ^m 20.63 ^s	+02°26'01.6''	0.1216	Lilly et al. (2007)
GALEXMSC J100120.08+022019.9	10 ^h 01 ^m 20.07 ^s	+02°20'20.0''	0.1224	Lilly et al. (2007)
SDSS J100131.65+022001.3	10 ^h 01 ^m 31.66 ^s	+02°20'01.3''	0.1224	Lilly et al. (2007)
SDSS J100135.32+022831.2	10 ^h 01 ^m 35.33 ^s	+02°28'31.2''	0.1225	Lilly et al. (2007)
SDSS J100138.98+022607.8	10 ^h 01 ^m 38.99 ^s	+02°26'07.8''	0.1228	Lilly et al. (2007)
SDSS J100130.65+022624.2	10 ^h 01 ^m 30.65 ^s	+02°26'24.2''	0.1228	Abazajian et al. (2004)
SDSS J100117.12+022919.1	10 ^h 01 ^m 17.13 ^s	+02°29'19.2''	0.1230	Lilly et al. (2007)
SDSS J100141.85+022519.5	10 ^h 01 ^m 41.86 ^s	+02°25'19.5''	0.1232	Abazajian et al. (2004)
2MASX J10013646+0226418	10 ^h 01 ^m 36.46 ^s	+02°26'42.2''	0.1234	Abazajian et al. (2003)
2MASX J10013692+0230318	10 ^h 01 ^m 36.93 ^s	+02°30'31.9''	0.1237	Abazajian et al. (2003)
SDSS J100119.77+022756.1	10 ^h 01 ^m 19.77 ^s	+02°27'56.1''	0.1237	Lilly et al. (2007)
zCOSMOS 830563 2MASX J10013974+0225487	10 ^h 01 ^m 20.30 ^s	+02°27'14.6''	0.1237	Lilly et al. (2007)
2MASX J10013974+0225487	10 ^h 01 ^m 39.76 ^s	+02°25'48.8''	0.1242	Abazajian et al. (2003)
SDSS J100143.45+022409.8	10 ^h 01 ^m 43.45 ^s	+02°24'09.9''	0.1245	Abazajian et al. (2004)
SDSS J100115.65+022423.0	10 ^h 01 ^m 15.66 ^s	+02°24'23.1''	0.1245	Lilly et al. (2007)
SDSS J100144.43+022654.0	10 ^h 01 ^m 44.43 ^s	+02°26'54.0''	0.1246	Trump et al. (2007)
SDSS J100132.33+023306.1	10 ^h 01 ^m 32.33 ^s	+02°33'06.2''	0.1253	Lilly et al. (2007)

Continued on next page

Table A.10 – continued from previous page

Galaxy Name	RA (J2000)	Dec (J2000)	z	Reference
SDSS J100123.59+022416.8	10 ^h 01 ^m 23.59 ^s	+02°24'16.8''	0.1264	Lilly et al. (2007)
SDSS J100135.42+022246.8	10 ^h 01 ^m 35.42 ^s	+02°22'46.8''	0.1265	Lilly et al. (2007)
SDSS J100147.06+022257.6	10 ^h 01 ^m 47.07 ^s	+02°22'57.7''	0.1269	Lilly et al. (2007)
SDSS J100123.20+022414.9	10 ^h 01 ^m 23.20 ^s	+02°24'14.9''	0.1273	Lilly et al. (2007)
SDSS J100154.07+021935.8	10 ^h 01 ^m 54.07 ^s	+02°19'35.9''	0.1281	Lilly et al. (2007)
SDSS J100127.72+023126.4	10 ^h 01 ^m 27.73 ^s	+02°31'26.5''	0.1298	Lilly et al. (2007)

Table A.10: XMMXCSJ100141.7+022539.8: All columns are as explained in Table A.1.

Galaxy Name	RA (J2000)	Dec (J2000)	z	Reference
2MASX J10403601+4002107	10 ^h 40 ^m 35.98 ^s	+40°02'10.8''	0.1331	Adelman-McCarthy et al. (2006)
SDSS J104045.34+395448.5	10 ^h 40 ^m 45.35 ^s	+39°54'48.6''	0.1341	Sánchez Almeida et al. (2011)
B3 1037+401	10 ^h 40 ^m 44.45 ^s	+39°54'54.9''	0.1341	Adelman-McCarthy et al. (2006)
SDSS J104126.57+395845.5	10 ^h 41 ^m 26.58 ^s	+39°58'45.5''	0.1352	Miller et al. (2002)
SDSS J104043.44+395705.3	10 ^h 40 ^m 43.44 ^s	+39°57'05.3''	0.1357	Adelman-McCarthy et al. (2006)
2MASX J10403391+4003497	10 ^h 40 ^m 33.96 ^s	+40°03'49.5''	0.1369	Miller et al. (2002)
2MASX J10405360+4001417	10 ^h 40 ^m 53.62 ^s	+40°01'42.0''	0.1374	Adelman-McCarthy et al. (2006)
SDSS J104044.49+395711.2	10 ^h 40 ^m 44.50 ^s	+39°57'11.3''	0.1380	Ofek et al. (2007)
SDSS J103943.42+400435.2	10 ^h 39 ^m 43.42 ^s	+40°04'35.2''	0.1384	Adelman-McCarthy et al. (2006)
2MASX J10414241+4000453	10 ^h 41 ^m 42.43 ^s	+40°00'45.8''	0.1385	Adelman-McCarthy et al. (2006)
2MASX J10404446+3957117	10 ^h 40 ^m 44.50 ^s	+39°57'11.3''	0.1386	Schaerer et al. (1999)

Continued on next page

Table A.11 – continued from previous page

Galaxy Name	RA (J2000)	Dec (J2000)	z	Reference
SDSS J104047.01+395551.8	10 ^h 40 ^m 47.01 ^s	+39°55'51.8''	0.1386	Adelman-McCarthy et al. (2006)
SDSS J104114.47+395901.6	10 ^h 41 ^m 14.48 ^s	+39°59'01.6''	0.1401	Adelman-McCarthy et al. (2006)
SDSS J104027.21+400459.3	10 ^h 40 ^m 27.22 ^s	+40°04'59.4''	0.1416	Adelman-McCarthy et al. (2006)
SDSS J104006.83+395356.8	10 ^h 40 ^m 06.84 ^s	+39°53'56.9''	0.1420	Adelman-McCarthy et al. (2006)
2MASX J10412053+3947284	10 ^h 41 ^m 20.49 ^s	+39°47'29.3''	0.1433	Adelman-McCarthy et al. (2006)
SDSS J103945.82+400047.0	10 ^h 39 ^m 45.83 ^s	+40°00'47.1''	0.1441	Adelman-McCarthy et al. (2006)

Table A.11: XMMXCSJ104044.4+395710.4: All columns are as explained in Table A.1.

Galaxy Name	RA (J2000)	Dec (J2000)	z	Reference
SDSS J111512.70+531930.5	11 ^h 15 ^m 12.71 ^s	+53°19'30.6''	0.4586	Bayliss et al. (2011)
SDSS J111520.84+532100.9	11 ^h 15 ^m 20.84 ^s	+53°21'01.0''	0.4601	Bayliss et al. (2011)
SDSS J111517.30+532115.2	11 ^h 15 ^m 17.30 ^s	+53°21'15.3''	0.4639	Bayliss et al. (2011)
SDSS J111517.85+531949.3	11 ^h 15 ^m 17.85 ^s	+53°19'49.4''	0.4640	Bayliss et al. (2011)
SDSS J111507.37+531955.7	11 ^h 15 ^m 07.38 ^s	+53°19'55.8''	0.4642	Bayliss et al. (2011)
SDSS J111505.53+532042.4	11 ^h 15 ^m 05.54 ^s	+53°20'42.4''	0.4654	Bayliss et al. (2011)
SDSS J111514.49+531948.8	11 ^h 15 ^m 14.49 ^s	+53°19'48.9''	0.4654	Bayliss et al. (2011)
SDSS J111514.51+531853.1	11 ^h 15 ^m 14.51 ^s	+53°18'53.1''	0.4660	Bayliss et al. (2011)
SDSS J111514.84+531954.3	11 ^h 15 ^m 14.85 ^s	+53°19'54.3''	0.4664	Abazajian et al. (2005)
SDSS J111519.70+531837.9	11 ^h 15 ^m 19.71 ^s	+53°18'37.9''	0.4670	Bayliss et al. (2011)
SDSS J111504.19+532100.4	11 ^h 15 ^m 04.20 ^s	+53°21'00.5''	0.4671	Bayliss et al. (2011)

Continued on next page

Table A.12 – continued from previous page

Galaxy Name	RA (J2000)	Dec (J2000)	z	Reference
SDSS J111518.75+531948.3	11 ^h 15 ^m 18.76 ^s	+53°19'48.4''	0.4686	Abazajian et al. (2005)
SDSS J111509.79+531925.2	11 ^h 15 ^m 09.79 ^s	+53°19'25.3''	0.4702	Bayliss et al. (2011)
SDSS J111515.10+532002.8	11 ^h 15 ^m 15.10 ^s	+53°20'02.8''	0.4708	Bayliss et al. (2011)
SDSS J111512.25+531830.8	11 ^h 15 ^m 12.26 ^s	+53°18'30.9''	0.4745	Bayliss et al. (2011)
(BHG2011) J111510.10+531939.9	11 ^h 15 ^m 10.11 ^s	+53°19'39.9''	0.4759	Bayliss et al. (2011)

Table A.12: XMMXCSJ111515.6+531949.5: All columns are as explained in Table A.1.

Galaxy Name	RA (J2000)	Dec (J2000)	z	Reference
2MASX J11511361+5507364	11 ^h 51 ^m 13.65 ^s	+55°07'36.5''	0.0757	Abazajian et al. (2005)
2MASX J11513633+5505433	11 ^h 51 ^m 36.33 ^s	+55°05'43.3''	0.0781	Abazajian et al. (2005)
SDSS J115109.52+550645.0	11 ^h 51 ^m 09.52 ^s	+55°06'45.1''	0.0782	Abazajian et al. (2005)
SDSS J115107.14+550839.1	11 ^h 51 ^m 07.14 ^s	+55°08'39.3''	0.0783	Abazajian et al. (2005)
2MASX J11510461+5510363	11 ^h 51 ^m 04.57 ^s	+55°10'36.0''	0.0787	Abazajian et al. (2005)
2MASX J11505351+5512012	11 ^h 50 ^m 53.45 ^s	+55°12'01.3''	0.0793	Abazajian et al. (2005)
2MASX J11511349+5506594	11 ^h 51 ^m 13.47 ^s	+55°06'59.2''	0.0794	Abazajian et al. (2005)
(KK81) 1 SDSS J115146.44+550644.2	11 ^h 51 ^m 25.80 ^s	+55°06'19.0''	0.0794	Schweizer (1996)
SDSS J115146.44+550644.2	11 ^h 51 ^m 46.45 ^s	+55°06'44.2''	0.0796	Abazajian et al. (2005)
2MASX J11515770+5508085	11 ^h 51 ^m 57.70 ^s	+55°08'08.4''	0.0797	Abazajian et al. (2005)
2MASX J11512829+5504483	11 ^h 51 ^m 28.30 ^s	+55°04'48.2''	0.0797	Abazajian et al. (2005)
SDSS J115132.91+550757.0	11 ^h 51 ^m 32.92 ^s	+55°07'57.1''	0.0798	Abazajian et al. (2005)

Continued on next page

Table A.13 – continued from previous page

Galaxy Name	RA (J2000)	Dec (J2000)	z	Reference
SDSS J115213.62+551312.7	11 ^h 52 ^m 13.62 ^s	+55°13'12.7''	0.0803	Abazajian et al. (2005)
2MASX J11512340+5506563	11 ^h 51 ^m 23.38 ^s	+55°06'56.0''	0.0806	Abazajian et al. (2005)
2MASX J11511641+5509594	11 ^h 51 ^m 16.45 ^s	+55°09'59.0''	0.0811	Abazajian et al. (2005)
SDSS J115201.62+550414.1	11 ^h 52 ^m 01.63 ^s	+55°04'14.2''	0.0814	Abazajian et al. (2005)

Table A.13: XMMXCSJ115112.0+550655.5: All columns are as explained in Table A.1.

Galaxy Name	RA (J2000)	Dec (J2000)	z	Reference
SDSS J123140.79+413626.3	12:31 ^m 40.80 ^s	+41°36'26.4''	0.1708	Adelman-McCarthy et al. (2006)
2MASX J12320414+4133324	12:32 ^m 04.12 ^s	+41°33'32.4''	0.1713	Adelman-McCarthy et al. (2006)
2MASX J12315661+4133582	12:31 ^m 56.59 ^s	+41°33'58.5''	0.1719	Adelman-McCarthy et al. (2006)
2MASX J12320054+4133322	12:32 ^m 00.56 ^s	+41°33'31.9''	0.1727	Adelman-McCarthy et al. (2006)
2MASX J12320463+4133362	12:32 ^m 04.68 ^s	+41°33'36.0''	0.1732	Adelman-McCarthy et al. (2007)
2MASX J12315296+4133182	12:31 ^m 52.98 ^s	+41°33'18.7''	0.1739	Adelman-McCarthy et al. (2006)
2MASX J12314144+4139361	12:31 ^m 41.46 ^s	+41°39'35.9''	0.1750	Adelman-McCarthy et al. (2006)
SDSS J123151.89+413434.7	12:31 ^m 51.90 ^s	+41°34'34.7''	0.1750	Adelman-McCarthy et al. (2006)
2MASX J12314386+4137341	12:31 ^m 43.90 ^s	+41°37'33.9''	0.1757	Adelman-McCarthy et al. (2006)
SDSS J123136.04+414314.0	12:31 ^m 36.05 ^s	+41°43'14.0''	0.1763	Adelman-McCarthy et al. (2006)

Table A.14: XMMXCSJ123144.4+413732.0: All columns are as explained in Table A.1.

Galaxy Name	RA (J2000)	Dec (J2000)	z	Reference
SDSS J151623.79+000156.4	15 ^h 16 ^m 23.79 ^s	+00°01'56.5''	0.1126	Stoughton et al. (2002)
SDSS J151626.35-000228.8	15 ^h 16 ^m 26.35 ^s	-00°02'28.9''	0.1142	Stoughton et al. (2002)
2MASX J15161900+0005067	15 ^h 16 ^m 19.00 ^s	+00°05'06.6''	0.1147	Abazajian et al. (2003)
2MASX J15162348+0006093	15 ^h 16 ^m 23.49 ^s	+00°06'09.1''	0.1154	Abazajian et al. (2003)
2MASX J15161563+0005291	15 ^h 16 ^m 15.63 ^s	+00°05'29.0''	0.1158	Abazajian et al. (2003)
2MASX J15162547+0003377	15 ^h 16 ^m 25.45 ^s	+00°03'37.6''	0.1167	Abazajian et al. (2003)
SDSS J151626.17+000707.4	15 ^h 16 ^m 26.18 ^s	+00°07'07.5''	0.1167	Stoughton et al. (2002)
2MASX J15161988+0003343	15 ^h 16 ^m 19.92 ^s	+00°03'34.5''	0.1174	Abazajian et al. (2003)
SDSS J151602.71+001518.3	15 ^h 16 ^m 02.71 ^s	+00°15'18.4''	0.1178	Abazajian et al. (2003)
2MASX J15160423+0002561	15 ^h 16 ^m 04.21 ^s	+00°02'56.4''	0.1183	Abazajian et al. (2003)
2MASX J15171323+0009193	15 ^h 17 ^m 13.25 ^s	+00°09'19.7''	0.1186	Abazajian et al. (2003)
SDSS J151640.19-000404.8	15 ^h 16 ^m 40.19 ^s	-00°04'04.8''	0.1188	Stoughton et al. (2002)
2MASX J15160950+0014541	15 ^h 16 ^m 09.53 ^s	+00°14'54.2''	0.1189	Abazajian et al. (2003)
2MASX J15170956+0007443	15 ^h 17 ^m 09.57 ^s	+00°07'44.7''	0.1190	Abazajian et al. (2003)
SDSS J151614.81+000022.5	15 ^h 16 ^m 14.81 ^s	+00°0'22.5''	0.1196	Abazajian et al. (2003)
SDSS J151615.10+000429.5	15 ^h 16 ^m 15.11 ^s	+00°04'29.6''	0.1201	Abazajian et al. (2003)
2MASX J15162640+0017507	15 ^h 16 ^m 26.38 ^s	+00°17'51.1''	0.1202	Abazajian et al. (2003)
SDSS J151629.25+000835.5	15 ^h 16 ^m 29.26 ^s	+00°08'35.6''	0.1203	Abazajian et al. (2003)
2MASX J15161210+0017401	15 ^h 16 ^m 12.12 ^s	+00°17'40.0''	0.1204	Abazajian et al. (2003)
2MASX J15160737+0020071	15 ^h 16 ^m 07.37 ^s	+00°20'07.1''	0.1206	Abazajian et al. (2003)

Continued on next page

Table A.15 – continued from previous page

Galaxy Name	RA (J2000)	Dec (J2000)	z	Reference
SDSS J151637.99+000718.7	15 ^h 16 ^m 38.00 ^s	+00°07'18.7''	0.1207	Abazajian et al. (2003)
2MASX J15161794+0005203	15 ^h 16 ^m 17.93 ^s	+00°05'20.5''	0.1208	Guzzo et al. (2009)
SDSS J151559.04-000323.8	15 ^h 15 ^m 59.04 ^s	-00°03'23.9''	0.1208	Stoughton et al. (2002)
SDSS J151709.75+001224.0	15 ^h 17 ^m 09.75 ^s	+00°12'24.1''	0.1210	Abazajian et al. (2003)
SDSS J151615.30-000325.4	15 ^h 16 ^m 15.3 ^s	-00°03'25.4''	0.1211	Abazajian et al. (2003)
SDSS J151649.45-000135.0	15 ^h 16 ^m 49.46 ^s	-00°01'35.0''	0.1215	Abazajian et al. (2003)
2MASX J15160803+0002011	15 ^h 16 ^m 08.06 ^s	+00°02'01.1''	0.1215	Abazajian et al. (2003)
SDSS J151624.58-000923.7	15 ^h 16 ^m 24.58 ^s	-00°09'23.7''	0.1216	Abazajian et al. (2003)
SDSS J151604.14+001024.8	15 ^h 16 ^m 04.15 ^s	+00°01'24.9''	0.1218	Abazajian et al. (2003)
2MASX J15160330+0008271	15 ^h 16 ^m 03.33 ^s	+00°08'27.5''	0.1223	Abazajian et al. (2003)
SDSS J151614.44+000508.3	15 ^h 16 ^m 14.45 ^s	+00°05'08.4''	0.1229	Guzzo et al. (2009)
SDSS J151613.19+000509.1	15 ^h 16 ^m 13.19 ^s	+00°05'09.1''	0.1239	Guzzo et al. (2009)
SDSS J151631.54+000648.1	15 ^h 16 ^m 31.54 ^s	+00°06'48.2''	0.1260	Abazajian et al. (2003)
2MASX J15155460+0002127	15 ^h 15 ^m 54.63 ^s	+00°02'13.0''	0.1266	Abazajian et al. (2003)
2MASX J15163414-0004296	15 ^h 16 ^m 34.14 ^s	-00°04'29.7''	0.1266	Jones et al. (2009)

Table A.15: XMMXCSJ151618.6+000531.3: All columns are as explained in Table A.1.

Galaxy Name	RA (J2000)	Dec (J2000)	z	Reference
SDSS J161126.49+541619.2	16 ^h 11 ^m 26.49 ^s	+54°16'19.2''	0.3310	Trichas et al. (2010)
SDSS J161131.39+541333.1	16 ^h 11 ^m 31.39 ^s	+54°13'33.2''	0.3330	Trichas et al. (2010)

Continued on next page

Table A.16 – continued from previous page

Galaxy Name	RA (J2000)	Dec (J2000)	z	Reference
SDSS J161147.78+541132.2	16 ^h 11 ^m 47.78 ^s	+54° 11' 32.3''	0.3340	Trichas et al. (2010)
ELAIS06S(R) J161127.5+541422	16 ^h 11 ^m 27.53 ^s	+54° 14' 22.7''	0.3350	Trichas et al. (2010)
SDSS J161122.54+541706.5	16 ^h 11 ^m 22.54 ^s	+54° 17' 06.6''	0.3360	Trichas et al. (2010)
SDSS J161134.91+541404.6	16 ^h 11 ^m 34.92 ^s	+54° 14' 04.7''	0.3360	Trichas et al. (2010)
SDSS J161135.93+541634.5	16 ^h 11 ^m 35.94 ^s	+54° 16' 34.5''	0.3380	Trichas et al. (2010)
SDSS J161138.50+541922.0	16 ^h 11 ^m 38.50 ^s	+54° 19' 22.1''	0.3390	Trichas et al. (2010)
SDSS J161128.25+541720.8	16 ^h 11 ^m 28.26 ^s	+54° 17' 20.8''	0.3400	Trichas et al. (2010)
SDSS J161140.23+541741.1	16 ^h 11 ^m 40.24 ^s	+54° 17' 41.1''	0.3410	Trichas et al. (2010)
SDSS J161143.52+541628.5	16 ^h 11 ^m 43.53 ^s	+54° 16' 28.5''	0.3410	Trichas et al. (2010)
SDSS J161115.41+541627.4	16 ^h 11 ^m 15.42 ^s	+54° 16' 27.4''	0.3420	Trichas et al. (2010)

Table A.16: XMMXCSJ161132.7+541628.3: All columns are as explained in Table A.1.

Galaxy Name	RA (J2000)	Dec (J2000)	z	Reference
SDSS J163057.87+243412.6	16 ^h 30 ^m 57.88 ^s	+24° 34' 12.7''	0.0560	Adelman-McCarthy et al. (2006)
CGCG 138-016 SDSS J162854.19+243138.5	16 ^h 28 ^m 36.04 ^s	+24° 33' 19.8''	0.0571	Freudling et al. (1992)
SDSS J162854.19+243138.5	16 ^h 28 ^m 54.20 ^s	+24° 31' 38.6''	0.0574	Adelman-McCarthy et al. (2006)
2MASX J16305968+2437076	16 ^h 30 ^m 59.72 ^s	+24° 37' 08.0''	0.0579	Adelman-McCarthy et al. (2007)
SDSS J163039.80+243938.2	16 ^h 30 ^m 39.80 ^s	+24° 39' 38.3''	0.0580	Adelman-McCarthy et al. (2006)
2MASX J16310298+2442456	16 ^h 31 ^m 03.00 ^s	+24° 42' 45.6''	0.0581	Adelman-McCarthy et al. (2006)
2MASX J16311876+2442442	16 ^h 31 ^m 18.75 ^s	+24° 42' 44.2''	0.0582	Adelman-McCarthy et al. (2006)

Continued on next page

Table A.17 – continued from previous page

Galaxy Name	RA (J2000)	Dec (J2000)	z	Reference
2MASX J16310320+2442586	16 ^h 31 ^m 03.26 ^s	+24°42'58.5"	0.0586	Adelman-McCarthy et al. (2007)
SDSS J163056.45+243816.4	16 ^h 30 ^m 56.45 ^s	+24°38'16.4"	0.0589	Adelman-McCarthy et al. (2006)
2MASX J16293963+2408563	16 ^h 29 ^m 39.59 ^s	+24°08'56.0"	0.0591	Adelman-McCarthy et al. (2007)
SDSS J163021.72+245911.6	16 ^h 30 ^m 21.73 ^s	+24°59'11.6"	0.0607	Adelman-McCarthy et al. (2006)
SDSS J163020.55+243457.6	16 ^h 30 ^m 20.56 ^s	+24°34'57.6"	0.0611	Adelman-McCarthy et al. (2006)
SDSS J163022.47+243215.9	16 ^h 30 ^m 22.48 ^s	+24°32'16.0"	0.0613	Adelman-McCarthy et al. (2006)
2MASX J16301853+2430424	16 ^h 30 ^m 18.54 ^s	+24°30'42.0"	0.0614	Adelman-McCarthy et al. (2007)
2MASX J16303722+2440374	16 ^h 30 ^m 37.21 ^s	+24°40'37.8"	0.0616	Adelman-McCarthy et al. (2006)
SDSS J163031.89+242519.5	16 ^h 30 ^m 31.89 ^s	+24°25'19.6"	0.0617	Adelman-McCarthy et al. (2006)
2MASX J16300229+2434054	16 ^h 30 ^m 02.28 ^s	+24°34'05.3"	0.0618	Adelman-McCarthy et al. (2007)
SDSS J163026.85+243652.1	16 ^h 30 ^m 26.86 ^s	+24°36'52.2"	0.0619	Adelman-McCarthy et al. (2006)
2MASX J16295863+2440084	16 ^h 29 ^m 58.65 ^s	+24°40'08.3"	0.0620	Adelman-McCarthy et al. (2006)
SDSS J163025.22+243517.2	16 ^h 30 ^m 25.23 ^s	+24°35'17.3"	0.0622	Adelman-McCarthy et al. (2006)
2MASX J16302666+2436404	16 ^h 30 ^m 26.65 ^s	+24°36'40.3"	0.0623	Adelman-McCarthy et al. (2006)
SDSS J163110.03+243637.9	16 ^h 31 ^m 10.04 ^s	+24°36'38.0"	0.0623	Adelman-McCarthy et al. (2006)
MCG +04-39-010 NED01	16 ^h 30 ^m 14.56 ^s	+24°34'38.0"	0.0626	Adelman-McCarthy et al. (2006)
SDSS J163046.39+245653.0	16 ^h 30 ^m 46.40 ^s	+24°56'53.1"	0.0629	Adelman-McCarthy et al. (2006)
2MASX J16300112+2432064	16 ^h 30 ^m 01.12 ^s	+24°32'06.8"	0.0630	Adelman-McCarthy et al. (2007)
CGCG 138-030	16 ^h 30 ^m 53.84 ^s	+24°33'43.6"	0.0632	Huchra et al. (2012)
SDSS J162854.70+244050.7	16 ^h 28 ^m 54.71 ^s	+24°40'50.8"	0.0632	Adelman-McCarthy et al. (2006)

Continued on next page

Table A.17 – continued from previous page

Galaxy Name	RA (J2000)	Dec (J2000)	z	Reference
SDSS J163042.59+242611.3	16 ^h 30 ^m 42.60 ^s	+24°26'11.3"	0.0633	Adelman-McCarthy et al. (2006)
2MASX J16314233+2445531	16 ^h 31 ^m 42.33 ^s	+24°45'53.1"	0.0634	Adelman-McCarthy et al. (2007)
MCG +04-39-010 NED07	16 ^h 30 ^m 16.11 ^s	+24°34'16.3"	0.0634	Adelman-McCarthy et al. (2007)
2MASX J16292467+2452082	16 ^h 29 ^m 24.69 ^s	+24°52'08.2"	0.0634	Adelman-McCarthy et al. (2007)
SDSS J163053.84+243147.2	16 ^h 30 ^m 53.84 ^s	+24°31'47.3"	0.0635	Adelman-McCarthy et al. (2006)
SDSS J163019.67+243330.0	16 ^h 30 ^m 19.68 ^s	+24°33'30.1"	0.0635	Adelman-McCarthy et al. (2006)
2MASX J16313042+2449302	16 ^h 31 ^m 30.39 ^s	+24°49'30.1"	0.0636	Adelman-McCarthy et al. (2007)
2MASX J16284192+2446279	16 ^h 28 ^m 41.91 ^s	+24°46'27.8"	0.0638	Adelman-McCarthy et al. (2006)
SDSS J163104.62+245719.8	16 ^h 31 ^m 04.62 ^s	+24°57'19.9"	0.0639	Adelman-McCarthy et al. (2006)
IC 4607 SDSS	16 ^h 30 ^m 15.87 ^s 16 ^h 31 ^m 06.45 ^s	+24°34'27.7" +24°12'48.7"	0.0639 0.0639	Huchra et al. (2012) Adelman-McCarthy et al. (2006)
J163106.44+241248.7 SDSS	16 ^h 31 ^m 10.31 ^s	+24°58'53.7"	0.0641	Adelman-McCarthy et al. (2006)
J163110.30+245853.6 SDSS	16 ^h 31 ^m 09.43 ^s	+24°22'02.8"	0.0642	Adelman-McCarthy et al. (2006)
J163109.43+242202.7 2MASX	16 ^h 30 ^m 15.43 ^s	+24°42'44.1"	0.0643	Adelman-McCarthy et al. (2007)
J16301543+2442443 2MASX	16 ^h 30 ^m 38.89 ^s	+24°30'59.2"	0.0643	Adelman-McCarthy et al. (2006)
J16303890+2430594 MCG +04-39-010	16 ^h 30 ^m 14.59 ^s	+24°35'13.2"	0.0643	Adelman-McCarthy et al. (2007)
NED03 SDSS	16 ^h 30 ^m 41.55 ^s	+24°58'53.0"	0.0644	Adelman-McCarthy et al. (2006)
J163041.54+245853.0 SDSS	16 ^h 28 ^m 36.56 ^s	+24°47'52.4"	0.0644	Adelman-McCarthy et al. (2006)
J162836.55+244752.4 2MASX	16 ^h 31 ^m 59.69 ^s	+24°28'55.4"	0.0645	Adelman-McCarthy et al. (2007)
J16315966+2428552 2MASX	16 ^h 30 ^m 14.50 ^s	+24°37'06.4"	0.0646	Adelman-McCarthy et al. (2006)
J16301449+2437063				

Continued on next page

Table A.17 – continued from previous page

Galaxy Name	RA (J2000)	Dec (J2000)	z	Reference
2MASX J16305028+2455226	16 ^h 30 ^m 50.28 ^s	+24°55'22.7"	0.0647	Adelman-McCarthy et al. (2006)
2MASX J16302886+2433164	16 ^h 30 ^m 28.83 ^s	+24°33'16.3"	0.0647	Adelman-McCarthy et al. (2006)
2MASX J16301215+2433473	16 ^h 30 ^m 12.17 ^s	+24°33'47.7"	0.0649	Adelman-McCarthy et al. (2006)
SDSS J163004.88+240409.2	16 ^h 30 ^m 04.89 ^s	+24°04'09.3"	0.0650	Adelman-McCarthy et al. (2006)
2MASX J16300743+2440363	16 ^h 30 ^m 07.44 ^s	+24°40'36.3"	0.0651	Adelman-McCarthy et al. (2006)
2MASX J16304317+2440386	16 ^h 30 ^m 43.18 ^s	+24°40'39.1"	0.0653	Adelman-McCarthy et al. (2006)
2MASX J16303509+2435324	16 ^h 30 ^m 35.09 ^s	+24°35'32.3"	0.0654	Adelman-McCarthy et al. (2007)
SDSS J162911.44+243413.9	16 ^h 29 ^m 11.45 ^s	+24°34'14.0"	0.0655	Adelman-McCarthy et al. (2006)
2MASX J16294712+2434194	16 ^h 29 ^m 47.10 ^s	+24°34'19.4"	0.0656	Adelman-McCarthy et al. (2007)
2MASX J16303981+2434546	16 ^h 30 ^m 39.85 ^s	+24°34'55.2"	0.0659	Adelman-McCarthy et al. (2007)
2MASX J16303606+2455434	16 ^h 30 ^m 36.06 ^s	+24°55'43.2"	0.0659	Adelman-McCarthy et al. (2006)
SDSS J163002.23+244721.6	16 ^h 30 ^m 02.24 ^s	+24°47'21.7"	0.0660	Adelman-McCarthy et al. (2006)
2MASX J16303737+2440154	16 ^h 30 ^m 37.41 ^s	+24°40'15.2"	0.0663	Adelman-McCarthy et al. (2007)
2MASX J16311982+2424422	16 ^h 31 ^m 19.80 ^s	+24°24'41.9"	0.0665	Adelman-McCarthy et al. (2006)
SDSS J163025.16+243528.7	16 ^h 30 ^m 25.17 ^s	+24°35'28.7"	0.0670	Adelman-McCarthy et al. (2006)

Table A.17: XMMXCSJ163015.6+243423.2: All columns are as explained in Table A.1.

Galaxy Name	RA (J2000)	Dec (J2000)	z	Reference
(W2011) J339.86728-05.76581	22 ^h 39 ^m 28.15 ^s	-05°45'56.9"	0.2402	Wegner (2011)
(W2011) J339.85526-05.78358	22 ^h 39 ^m 25.26 ^s	-05°47'00.9"	0.2405	Wegner (2011)
Continued on next page				

Table A.18 – continued from previous page

Galaxy Name	RA (J2000)	Dec (J2000)	z	Reference
(W2011) J339.85416-05.78444	22 ^h 39 ^m 25.00 ^s	-05°47'04.0''	0.2410	Wegner (2011)
(W2011) J339.84311-05.75219	22 ^h 39 ^m 22.35 ^s	-05°45'07.9''	0.2414	Wegner (2011)
(W2011) J339.85796-05.66972	22 ^h 39 ^m 25.91 ^s	-05°40'11.0''	0.2421	Wegner (2011)
(W2011) J339.91522-05.73214	22 ^h 39 ^m 39.65 ^s	-05°43'55.7''	0.2421	Wegner (2011)
(W2011) J339.92899-05.70703	22 ^h 39 ^m 42.96 ^s	-05°42'25.3''	0.2424	Wegner (2011)
APMUKS(BJ) B223649.45-060121.8	22 ^h 39 ^m 25.61 ^s	-05°45'43.1''	0.2425	Wegner (2011)
(W2011) J339.88293-05.68617	22 ^h 39 ^m 31.91 ^s	-05°41'10.2''	0.2425	Wegner (2011)
(W2011) J339.93253-05.72194	22 ^h 39 ^m 43.81 ^s	-05°43'19.0''	0.2427	Wegner (2011)
(W2011) J339.85922-05.77811	22 ^h 39 ^m 26.21 ^s	-05°46'41.2''	0.2434	Wegner (2011)
APMUKS(BJ) B223704.30-055906.2	22 ^h 39 ^m 40.49 ^s	-05°43'26.7''	0.2436	Wegner (2011)
(W2011) J339.91388-05.73789	22 ^h 39 ^m 39.33 ^s	-05°44'16.4''	0.2437	Wegner (2011)
(W2011) J339.93896-05.75525	22 ^h 39 ^m 45.35 ^s	-05°45'18.9''	0.2437	Wegner (2011)
APMUKS(BJ) B223702.94-060320.8	22 ^h 39 ^m 39.10 ^s	-05°47'41.7''	0.2441	Wegner (2011)
(W2011) J339.92871-05.74033	22 ^h 39 ^m 42.89 ^s	-05°44'25.2''	0.2441	Wegner (2011)
(W2011) J339.87462-05.69311	22 ^h 39 ^m 29.91 ^s	-05°41'35.2''	0.2441	Wegner (2011)
(W2011) J339.91187-05.63333	22 ^h 39 ^m 38.85 ^s	-05°38'00.0''	0.2442	Wegner (2011)
GALEXASC J223938.36-054401.5	22 ^h 39 ^m 38.36 ^s	-05°44'03.8''	0.2442	Wegner (2011)
(W2011) J339.82141-05.70861	22 ^h 39 ^m 17.14 ^s	-05°42'31.0''	0.2443	Wegner (2011)
APMUKS(BJ) B223656.20-055649.6	22 ^h 39 ^m 32.31 ^s	-05°41'10.7''	0.2443	Wegner (2011)
(W2011) J339.90479-05.74742	22 ^h 39 ^m 37.15 ^s	-05°44'50.7''	0.2445	Wegner (2011)

Continued on next page

Table A.18 – continued from previous page

Galaxy Name	RA (J2000)	Dec (J2000)	z	Reference
GALEXASC J223932.33-054544.9 (W2011)	22 ^h 39 ^m 32.36 ^s	-05°45'46.5''	0.2445	Wegner (2011)
J339.90805-05.72461 (W2011)	22 ^h 39 ^m 37.93 ^s	-05°43'28.6''	0.2445	Wegner (2011)
J339.88004-05.67217 (W2011)	22 ^h 39 ^m 31.21 ^s	-05°40'19.8''	0.2446	Wegner (2011)
J339.88586-05.68911 (W2011)	22 ^h 39 ^m 32.61 ^s	-05°41'20.8''	0.2446	Wegner (2011)
J339.91403-05.73167 (W2011)	22 ^h 39 ^m 39.37 ^s	-05°43'54.0''	0.2447	Wegner (2011)
J339.89958-05.70617 (W2011)	22 ^h 39 ^m 35.90 ^s	-05°42'22.2''	0.2448	Wegner (2011)
J339.90379-05.75611 (W2011)	22 ^h 39 ^m 36.91 ^s	-05°45'22.0''	0.2448	Wegner (2011)
J339.89209-05.80678 (W2011)	22 ^h 39 ^m 34.10 ^s	-05°48'24.4''	0.2448	Wegner (2011)
J339.85654-05.78022 (W2011)	22 ^h 39 ^m 25.57 ^s	-05°46'48.8''	0.2449	Wegner (2011)
J339.93542-05.67039 (W2011)	22 ^h 39 ^m 44.50 ^s	-05°40'13.4''	0.2451	Wegner (2011)
J339.83524-05.75508 (W2011)	22 ^h 39 ^m 20.46 ^s	-05°45'18.3''	0.2452	Wegner (2011)
J339.85291-05.78672 (W2011)	22 ^h 39 ^m 24.70 ^s	-05°47'12.2''	0.2452	Wegner (2011)
J340.00000-05.73803 2MASX	22 ^h 40 ^m 00.00 ^s	-05°44'16.9''	0.2453	Wegner (2011)
J22392454-0547173 APMUKS(BJ)	22 ^h 39 ^m 24.57 ^s	-05°47'17.4''	0.2453	Wegner (2011)
B223715.80-060103.5 (W2011)	22 ^h 39 ^m 51.98 ^s	-05°45'23.8''	0.2454	Wegner (2011)
J339.85626-05.78508 (W2011)	22 ^h 39 ^m 25.50 ^s	-05°47'06.3''	0.2454	Wegner (2011)
J339.95475-05.79149 (W2011)	22 ^h 39 ^m 49.14 ^s	-05°47'29.4''	0.2454	Wegner (2011)
J339.85004-05.74921 APMUKS(BJ)	22 ^h 39 ^m 24.01 ^s	-05°44'57.2''	0.2454	Wegner (2011)
B223651.70-060319.5 (W2011)	22 ^h 39 ^m 27.86 ^s	-05°47'40.2''	0.2455	Wegner (2011)
J339.88324-05.68225	22 ^h 39 ^m 31.98 ^s	-05°40'56.1''	0.2457	Wegner (2011)

Continued on next page

Table A.18 – continued from previous page

Galaxy Name	RA (J2000)	Dec (J2000)	z	Reference
(W2011) J339.84662-05.75625	22 ^h 39 ^m 23.19 ^s	-05°45'22.5"	0.2457	Wegner (2011)
(W2011) J339.90917-05.77036	22 ^h 39 ^m 38.20 ^s	-05°46'13.3"	0.2458	Wegner (2011)
(W2011) J339.89420-05.81267	22 ^h 39 ^m 34.61 ^s	-05°48'45.6"	0.2460	Wegner (2011)
(W2011) J339.94089-05.71742	22 ^h 39 ^m 45.81 ^s	-05°43'02.7"	0.2462	Wegner (2011)
(W2011) J339.94528-05.76256	22 ^h 39 ^m 46.87 ^s	-05°45'45.2"	0.2463	Wegner (2011)
(W2011) J339.90976-05.75339	22 ^h 39 ^m 38.34 ^s	-05°45'12.2"	0.2464	Wegner (2011)
(W2011) J339.87332-05.80614	22 ^h 39 ^m 29.60 ^s	-05°48'22.1"	0.2466	Wegner (2011)
(W2011) J339.89771-05.80597	22 ^h 39 ^m 35.45 ^s	-05°48'21.5"	0.2469	Wegner (2011)
2MASX J22392032-0544233	22 ^h 39 ^m 20.40 ^s	-05°44'23.1"	0.2469	Wegner (2011)
(W2011) J339.87396-05.76278	22 ^h 39 ^m 29.75 ^s	-05°45'46.0"	0.2470	Wegner (2011)
APMUKS(BJ) B223704.44-055858.1	22 ^h 39 ^m 40.60 ^s	-05°43'18.5"	0.2470	Wegner (2011)
(W2011) J339.90925-05.77828	22 ^h 39 ^m 38.22 ^s	-05°46'41.8"	0.2471	Wegner (2011)
(W2011) J339.94589-05.64414	22 ^h 39 ^m 47.01 ^s	-05°38'38.9"	0.2472	Wegner (2011)
(W2011) J339.84738-05.74164	22 ^h 39 ^m 23.37 ^s	-05°44'29.9"	0.2473	Wegner (2011)
APMUKS(BJ) B223710.40-055450.0	22 ^h 39 ^m 46.57 ^s	-05°39'11.1"	0.2475	Wegner (2011)
(W2011) J339.82697-05.74289	22 ^h 39 ^m 18.47 ^s	-05°44'34.4"	0.2475	Wegner (2011)
(W2011) J339.82428-05.74400	22 ^h 39 ^m 17.83 ^s	-05°44'38.4"	0.2475	Wegner (2011)
(W2011) J339.88842-05.80075	22 ^h 39 ^m 33.23 ^s	-05°48'02.7"	0.2478	Wegner (2011)
(W2011) J339.88092-05.75026	22 ^h 39 ^m 31.42 ^s	-05°45'00.9"	0.2489	Wegner (2011)
(W2011) J339.91043-05.69272	22 ^h 39 ^m 38.50 ^s	-05°41'33.8"	0.2490	Wegner (2011)

Continued on next page

Table A.18 – continued from previous page

Galaxy Name	RA (J2000)	Dec (J2000)	z	Reference
(W2011) J339.90521-05.68931	22 ^h 39 ^m 37.25 ^s	-05°41'21.5''	0.2492	Wegner (2011)
(W2011) J339.92203-05.73417	22 ^h 39 ^m 41.29 ^s	-05°44'03.0''	0.2492	Wegner (2011)
(W2011) J339.92083-05.73192	22 ^h 39 ^m 41.00 ^s	-05°43'54.8''	0.2497	Wegner (2011)
(W2011) J339.91183-05.68417	22 ^h 39 ^m 38.84 ^s	-05°41'03.0''	0.2500	Wegner (2011)
APMUKS(BJ) B223659.52-055721.9	22 ^h 39 ^m 35.71 ^s	-05°41'42.4''	0.2502	Wegner (2011)
(W2011) J339.90482-05.67711	22 ^h 39 ^m 37.16 ^s	-05°40'37.6''	0.2509	Wegner (2011)

Table A.18: XMMXCSJ223939.3-054327.4: All columns are as explained in Table A.1.

Galaxy Name	RA (J2000)	Dec (J2000)	z	Reference
AGC 331543	23 ^h 38 ^m 31.41 ^s	+27°13'48.2''	0.1218	Scoddeggio et al. (1995)
AGC 331535	23 ^h 37 ^m 55.52 ^s	+27°08'25.8''	0.1222	Scoddeggio et al. (1995)
2MASX J23380720+2715028	23 ^h 38 ^m 07.24 ^s	+27°15'02.9''	0.1222	Scoddeggio et al. (1995)
AGC 331529	23 ^h 37 ^m 41.99 ^s	+27°04'37.4''	0.1226	Scoddeggio et al. (1995)
AGC 331531	23 ^h 37 ^m 47.13 ^s	+27°09'29.5''	0.1226	Scoddeggio et al. (1995)
2MASX J23375415+2718448	23 ^h 37 ^m 54.16 ^s	+27°18'44.8''	0.1238	Scoddeggio et al. (1995)
2MASX J23375559+2711128	23 ^h 37 ^m 55.59 ^s	+27°11'13.1''	0.1245	Giovanelli et al. (1995)
AGC 331526	23 ^h 37 ^m 22.51 ^s	+27°06'32.6''	0.1246	Scoddeggio et al. (1995)
2MASX J23380218+2712088	23 ^h 38 ^m 02.18 ^s	+27°12'09.1''	0.1246	Smith et al. (2004)
2MASX J23382282+2717516	23 ^h 38 ^m 22.83 ^s	+27°17'51.6''	0.1263	Scoddeggio et al. (1995)
2MASX J23372726+2707408	23 ^h 37 ^m 27.26 ^s	+27°07'41.0''	0.1264	Scoddeggio et al. (1995)
BATC J233724.29+271434.14	23 ^h 37 ^m 24.10 ^s	+27°14'32.8''	0.1265	Pinkney et al. (1993)

Table A.19: XMMXCSJ233757.0+271121.0: All columns are as explained in Table A.1.

ID	RA (J2000)	Dec (J2000)	z	Reference	Member
1	10 ^h 57 ^m 03.77 ^s	-03°37'37.3"	0.8312	Nastasi et al. (2014) Tran et al. (1999)	✓
2	10 ^h 56 ^m 50.84 ^s	-03°37'37.4"	0.8390	Nastasi et al. (2014) Tran et al. (1999)	✓
3	10 ^h 57 ^m 04.10 ^s	-03°37'37.3"	0.8329	Nastasi et al. (2014) Tran et al. (1999)	✓
4	10 ^h 56 ^m 54.31 ^s	-03°37'37.4"	0.8380	Nastasi et al. (2014) Tran et al. (1999)	✓
5	10 ^h 56 ^m 51.77 ^s	-03°37'37.4"	0.8371	Nastasi et al. (2014) Tran et al. (1999)	✓
6	10 ^h 56 ^m 58.44 ^s	-03°37'37.4"	0.8353	Nastasi et al. (2014) Tran et al. (1999)	✓
7	10 ^h 56 ^m 56.37 ^s	-03°37'37.4"	0.8317	Nastasi et al. (2014) Tran et al. (1999)	✓
8	10 ^h 57 ^m 01.50 ^s	-03°37'37.3"	0.8346	Nastasi et al. (2014) Tran et al. (1999)	✓
9	10 ^h 56 ^m 56.90 ^s	-03°37'37.4"	0.8403	Nastasi et al. (2014) Tran et al. (1999)	✓
10	10 ^h 56 ^m 57.31 ^s	-03°37'37.4"	0.8175	Nastasi et al. (2014) Tran et al. (1999)	
11	10 ^h 57 ^m 02.97 ^s	-03°37'37.3"	0.8367	Nastasi et al. (2014) Tran et al. (1999)	✓
12	10 ^h 57 ^m 01.64 ^s	-03°37'37.3"	0.8239	Nastasi et al. (2014) Tran et al. (1999)	✓
13	10 ^h 57 ^m 01.04 ^s	-03°37'37.3"	0.8420	Nastasi et al. (2014) Tran et al. (1999)	✓
14	10 ^h 56 ^m 59.51 ^s	-03°37'37.4"	0.8454	Nastasi et al. (2014) Tran et al. (1999)	
15	10 ^h 56 ^m 59.90 ^s	-03°37'37.4"	0.8314	Nastasi et al. (2014) Tran et al. (1999)	✓
16	10 ^h 57 ^m 04.64 ^s	-03°37'37.3"	0.8282	Nastasi et al. (2014) Tran et al. (1999)	✓
17	10 ^h 57 ^m 03.37 ^s	-03°37'37.3"	0.8259	Nastasi et al. (2014) Tran et al. (1999)	✓
18	10 ^h 57 ^m 02.44 ^s	-03°37'37.3"	0.8397	Nastasi et al. (2014) Tran et al. (1999)	✓
19	10 ^h 57 ^m 02.44 ^s	-03°37'37.3"	0.8224	Nastasi et al. (2014) Tran et al. (1999)	✓
20	10 ^h 57 ^m 02.84 ^s	-03°37'37.3"	0.8314	Nastasi et al. (2014) Tran et al. (1999)	✓
21	10 ^h 57 ^m 02.17 ^s	-03°37'37.3"	0.8249	Nastasi et al. (2014) Tran et al. (1999)	✓
22	10 ^h 57 ^m 03.77 ^s	-03°37'37.3"	0.8392	Nastasi et al. (2014) Tran et al. (1999)	✓
23	10 ^h 57 ^m 03.84 ^s	-03°37'37.3"	0.8308	Nastasi et al. (2014) Tran et al. (1999)	✓
24	10 ^h 57 ^m 08.84 ^s	-03°37'37.3"	0.8250	Nastasi et al. (2014) Tran et al. (1999)	✓
25	10 ^h 57 ^m 01.97 ^s	-03°37'37.3"	0.8127	Nastasi et al. (2014) Tran et al. (1999)	
26	10 ^h 57 ^m 01.31 ^s	-03°37'37.3"	0.8213	Nastasi et al. (2014) Tran et al. (1999)	✓
27	10 ^h 56 ^m 57.97 ^s	-03°37'37.4"	0.8209	Nastasi et al. (2014) Tran et al. (1999)	✓
28	10 ^h 56 ^m 57.77 ^s	-03°37'37.4"	0.8286	Nastasi et al. (2014) Tran et al. (1999)	✓
29	10 ^h 56 ^m 57.37 ^s	-03°37'37.4"	0.8353	Nastasi et al. (2014) Tran et al. (1999)	✓

Continued on next page

Table A.20 – continued from previous page

ID	RA (J2000)	Dec (J2000)	z	Reference	Member
30	10 ^h 56 ^m 56.97 ^s	-03°37'37.4"	0.8332	Nastasi et al. (2014) Tran et al. (1999)	✓
31	10 ^h 56 ^m 54.44 ^s	-03°37'37.4"	0.8378	Nastasi et al. (2014) Tran et al. (1999)	✓
32	10 ^h 56 ^m 53.30 ^s	-03°37'37.4"	0.8319	Nastasi et al. (2014) Tran et al. (1999)	✓

Table A.20: XMMXCSJ105659.5-033728.0: Columns 2 - 5 are as explained in Table A.1. Column 1 gives an arbitrary ID for each galaxy and column 6 shows whether or not the galaxy was included as a member for the determination of the velocity dispersion.

ID	RA (J2000)	Dec (J2000)	z	Reference	Member
1	11 ^h 40 ^m 22.31 ^s	66°08'15.1"	0.7844	Nastasi et al. (2014) Donahue et al. (1999)	✓
2	11 ^h 40 ^m 22.01 ^s	66°08'12.1"	0.7903	Nastasi et al. (2014) Donahue et al. (1999)	✓
3	11 ^h 40 ^m 22.61 ^s	66°08'17.1"	0.7844	Nastasi et al. (2014) Donahue et al. (1999)	✓
4	11 ^h 40 ^m 22.01 ^s	66°08'19.0"	0.7927	Nastasi et al. (2014) Donahue et al. (1999)	✓
5	11 ^h 40 ^m 21.41 ^s	66°08'20.1"	0.7826	Nastasi et al. (2014) Donahue et al. (1999)	✓
6	11 ^h 40 ^m 17.70 ^s	66°08'23.0"	0.7808	Nastasi et al. (2014) Donahue et al. (1999)	✓
7	11 ^h 40 ^m 16.91 ^s	66°08'25.1"	0.7909	Nastasi et al. (2014) Donahue et al. (1999)	✓
8	11 ^h 40 ^m 17.21 ^s	66°08'29.1"	0.7916	Nastasi et al. (2014) Donahue et al. (1999)	✓
9	11 ^h 40 ^m 27.41 ^s	66°08'23.0"	0.7761	Nastasi et al. (2014) Donahue et al. (1999)	✓
10	11 ^h 40 ^m 27.01 ^s	66°08'09.0"	0.7760	Nastasi et al. (2014) Donahue et al. (1999)	✓
11	11 ^h 40 ^m 29.30 ^s	66°08'02.1"	0.7831	Nastasi et al. (2014) Donahue et al. (1999)	✓
12	11 ^h 40 ^m 24.50 ^s	66°07'26.1"	0.7823	Nastasi et al. (2014) Donahue et al. (1999)	✓
13	11 ^h 40 ^m 14.81 ^s	66°07'32.1"	0.7824	Nastasi et al. (2014) Donahue et al. (1999)	✓
14	11 ^h 40 ^m 30.80 ^s	66°09'03.0"	0.7900	Nastasi et al. (2014) Donahue et al. (1999)	✓
15	11 ^h 40 ^m 15.11 ^s	66°09'22.0"	0.7773	Nastasi et al. (2014) Donahue et al. (1999)	✓
16	11 ^h 40 ^m 17.40 ^s	66°09'14.1"	0.7909	Nastasi et al. (2014) Donahue et al. (1999)	✓
17	11 ^h 40 ^m 42.80 ^s	66°10'19.0"	0.7814	Nastasi et al. (2014) Donahue et al. (1999)	✓
18	11 ^h 40 ^m 40.40 ^s	66°07'52.0"	0.7889	Nastasi et al. (2014) Donahue et al. (1999)	✓
19	11 ^h 40 ^m 37.10 ^s	66°07'25.0"	0.7902	Nastasi et al. (2014) Donahue et al. (1999)	✓
20	11 ^h 40 ^m 10.31 ^s	66°07'18.1"	0.7898	Nastasi et al. (2014) Donahue et al. (1999)	✓
21	11 ^h 40 ^m 05.90 ^s	66°08'05.0"	0.7790	Nastasi et al. (2014) Donahue et al. (1999)	✓
22	11 ^h 39 ^m 58.91 ^s	66°07'60.0"	0.7792	Nastasi et al. (2014) Donahue et al. (1999)	✓
23	11 ^h 40 ^m 06.00 ^s	66°08'18.0"	0.7714	Nastasi et al. (2014) Donahue et al. (1999)	✓

Table A.21: XMMXCSJ114023.0+660819.0: All columns are as explained in Table A.20.

ID	RA (J2000)	Dec (J2000)	z	Reference	Member
1	18 ^h 21 ^m 16.61 ^s	68°30'25.0"	0.8151	Nastasi et al. (2014) Gioia et al. (2004)	✓
2	18 ^h 21 ^m 21.50 ^s	68°29'57.1"	0.8225	Nastasi et al. (2014) Gioia et al. (2004)	✓
3	18 ^h 21 ^m 26.21 ^s	68°29'31.0"	0.8206	Nastasi et al. (2014) Gioia et al. (2004)	✓
4	18 ^h 21 ^m 30.80 ^s	68°29'29.1"	0.8204	Nastasi et al. (2014) Gioia et al. (2004)	✓
5	18 ^h 21 ^m 27.90 ^s	68°28'43.0"	0.8229	Nastasi et al. (2014) Gioia et al. (2004)	✓
6	18 ^h 21 ^m 33.80 ^s	68°28'40.1"	0.8235	Nastasi et al. (2014) Gioia et al. (2004)	✓
7	18 ^h 21 ^m 32.60 ^s	68°27'54.1"	0.8167	Nastasi et al. (2014) Gioia et al. (2004)	✓
8	18 ^h 21 ^m 34.91 ^s	68°27'53.0"	0.8099	Nastasi et al. (2014) Gioia et al. (2004)	✓
9	18 ^h 21 ^m 37.20 ^s	68°27'51.1"	0.8153	Nastasi et al. (2014) Gioia et al. (2004)	✓
10	18 ^h 21 ^m 33.60 ^s	68°27'50.1"	0.8161	Nastasi et al. (2014) Gioia et al. (2004)	✓
11	18 ^h 21 ^m 35.21 ^s	68°27'34.0"	0.8115	Nastasi et al. (2014) Gioia et al. (2004)	✓
12	18 ^h 21 ^m 36.60 ^s	68°27'21.0"	0.8172	Nastasi et al. (2014) Gioia et al. (2004)	✓
13	18 ^h 21 ^m 37.50 ^s	68°27'07.0"	0.8231	Nastasi et al. (2014) Gioia et al. (2004)	✓
14	18 ^h 21 ^m 37.91 ^s	68°27'00.1"	0.8159	Nastasi et al. (2014) Gioia et al. (2004)	✓
15	18 ^h 21 ^m 18.20 ^s	68°27'00.1"	0.7942	Nastasi et al. (2014) Gioia et al. (2004)	✓
16	18 ^h 21 ^m 47.71 ^s	68°27'06.1"	0.8089	Nastasi et al. (2014) Gioia et al. (2004)	✓
17	18 ^h 21 ^m 51.11 ^s	68°27'17.0"	0.8060	Nastasi et al. (2014) Gioia et al. (2004)	✓
18	18 ^h 21 ^m 57.71 ^s	68°27'25.0"	0.8118	Nastasi et al. (2014) Gioia et al. (2004)	✓
19	18 ^h 21 ^m 50.81 ^s	68°26'09.0"	0.8152	Nastasi et al. (2014) Gioia et al. (2004)	✓
20	18 ^h 21 ^m 47.81 ^s	68°25'18.1"	0.8122	Nastasi et al. (2014) Gioia et al. (2004)	✓

Table A.22: XMMXCSJ182132.9+682755.0: All columns are as explained in Table A.20.

ID	Mask	RA (J2000)	Dec (J2000)	z	Quality	Identification	Member
1	GS-2012B-Q-011-03	00 ^h 56 ^m 46.52 ^s	-27°41'57.9"	0.6625	3	X	
2	GS-2012B-Q-011-03	00 ^h 56 ^m 47.54 ^s	-27°41'53.6"	0.6294	2	X	
3	GS-2012B-Q-011-03	00 ^h 56 ^m 47.56 ^s	-27°41'03.2"	0.5864	3	X	
5	GS-2012B-Q-011-03	00 ^h 56 ^m 47.54 ^s	-27°41'19.7"	0.5604	3	X	
6	GS-2012B-Q-011-03	00 ^h 56 ^m 54.47 ^s	-27°41'52.9"	0.5604	3	X	✓
7	GS-2012B-Q-011-03	00 ^h 56 ^m 52.73 ^s	-27°41'46.0"	0.5744	3	X	
9	GS-2012B-Q-011-03	00 ^h 56 ^m 53.45 ^s	-27°41'28.0"	0.5754	3	X	
11	GS-2012B-Q-011-03	00 ^h 56 ^m 53.03 ^s	-27°40'44.8"	0.5574	3	X	✓
12	GS-2012B-Q-011-03	00 ^h 56 ^m 57.06 ^s	-27°40'12.4"	0.8196	2	X	
13	GS-2012B-Q-011-03	00 ^h 56 ^m 58.95 ^s	-27°40'28.2"	0.5604	3	X	✓
14	GS-2012B-Q-011-03	00 ^h 56 ^m 55.93 ^s	-27°40'27.9"	0.5584	3	X	✓
16	GS-2012B-Q-011-03	00 ^h 56 ^m 54.31 ^s	-27°40'29.3"	0.5614	3	X	✓
17	GS-2012B-Q-011-03	00 ^h 56 ^m 57.48 ^s	-27°41'01.7"	0.5584	3	X	✓
18	GS-2012B-Q-011-03	00 ^h 56 ^m 59.35 ^s	-27°40'52.0"	0.5974	3	X	
19	GS-2012B-Q-011-03	00 ^h 56 ^m 57.03 ^s	-27°40'30.4"	0.5584	3	X	✓
20	GS-2012B-Q-011-03	00 ^h 56 ^m 56.80 ^s	-27°39'34.3"	0.6014	3	X	
23	GS-2012B-Q-011-03	00 ^h 56 ^m 59.28 ^s	-27°39'33.9"	0.8326	3	X	
25	GS-2012B-Q-011-03	00 ^h 57 ^m 02.36 ^s	-27°39'29.9"	0.6284	2	X	
26	GS-2012B-Q-011-03	00 ^h 57 ^m 01.73 ^s	-27°39'34.3"	0.5694	3	X	
27	GS-2012B-Q-011-03	00 ^h 57 ^m 00.36 ^s	-27°39'24.9"	0.8646	3	X	
28	GS-2012B-Q-011-03	00 ^h 57 ^m 02.35 ^s	-27°38'51.1"	0.5574	3	X	
29	GS-2012B-Q-011-03	00 ^h 57 ^m 03.56 ^s	-27°39'31.0"	0.5604	3	X	
31	GS-2012B-Q-011-03	00 ^h 57 ^m 04.76 ^s	-27°39'09.0"	0.6294	3	X	
32	GS-2012B-Q-011-03	00 ^h 57 ^m 03.51 ^s	-27°38'27.3"	0.2472	3	X	
1	GS-2012B-Q-011-04	00 ^h 56 ^m 46.96 ^s	-27°41'44.6"	1.0127	2	X	
2	GS-2012B-Q-011-04	00 ^h 56 ^m 46.52 ^s	-27°41'57.9"	0.6625	3	X	
3	GS-2012B-Q-011-04	00 ^h 56 ^m 49.75 ^s	-27°42'31.4"	0.8336	3	X	
4	GS-2012B-Q-011-04	00 ^h 56 ^m 44.95 ^s	-27°40'56.3"	0.7956	2	X	
5	GS-2012B-Q-011-04	00 ^h 56 ^m 46.64 ^s	-27°41'05.7"	0.5874	3	X	

Continued on next page

Table A.23 – continued from previous page

ID	Mask	RA (J2000)	Dec (J2000)	z	Quality	Identification	Member
6	GS-2012B-Q-011-04	00 ^h 56 ^m 47.56 ^s	-27°41'03.2''	0.5844	3	X	
7	GS-2012B-Q-011-04	00 ^h 56 ^m 48.10 ^s	-27°41'00.3''	0.8126	3	X	
8	GS-2012B-Q-011-04	00 ^h 56 ^m 52.46 ^s	-27°41'45.7''	0.2121	3	X	
10	GS-2012B-Q-011-04	00 ^h 56 ^m 54.96 ^s	-27°41'47.8''	0.5614	3	X	✓
11	GS-2012B-Q-011-04	00 ^h 56 ^m 50.57 ^s	-27°40'27.9''	0.5634	3	X	✓
12	GS-2012B-Q-011-04	00 ^h 56 ^m 53.08 ^s	-27°40'49.5''	0.8586	3	X	
13	GS-2012B-Q-011-04	00 ^h 56 ^m 58.35 ^s	-27°41'49.6''	0.6785	2	X	
14	GS-2012B-Q-011-04	00 ^h 56 ^m 52.88 ^s	-27°40'14.6''	0.7365	2	X	
15	GS-2012B-Q-011-04	00 ^h 56 ^m 54.90 ^s	-27°39'55.1''	0.5584	3	X	✓
16	GS-2012B-Q-011-04	00 ^h 56 ^m 54.76 ^s	-27°40'12.1''	0.5594	3	X	✓
17	GS-2012B-Q-011-04	00 ^h 56 ^m 54.76 ^s	-27°40'51.7''	0.5614	3	X	✓
18	GS-2012B-Q-011-04	00 ^h 56 ^m 56.82 ^s	-27°40'30.8''	0.5994	3	X	
19	GS-2012B-Q-011-04	00 ^h 56 ^m 59.12 ^s	-27°40'41.9''	0.5964	3	X	
20	GS-2012B-Q-011-04	00 ^h 56 ^m 56.89 ^s	-27°40'02.0''	1.1908	2	X	
23	GS-2012B-Q-011-04	00 ^h 56 ^m 58.05 ^s	-27°37'52.0''	0.7795	3	X	
24	GS-2012B-Q-011-04	00 ^h 56 ^m 59.04 ^s	-27°37'40.1''	0.6515	3	X	
25	GS-2012B-Q-011-04	00 ^h 56 ^m 57.22 ^s	-27°39'34.6''	0.6314	3	X	
26	GS-2012B-Q-011-04	00 ^h 56 ^m 59.03 ^s	-27°39'15.2''	0.6294	3	X	
27	GS-2012B-Q-011-04	00 ^h 57 ^m 07.97 ^s	-27°39'28.5''	0.6525	3	X	
28	GS-2012B-Q-011-04	00 ^h 57 ^m 04.24 ^s	-27°39'23.8''	0.5614	3	X	
29	GS-2012B-Q-011-04	00 ^h 57 ^m 04.76 ^s	-27°39'09.0''	0.6294	3	X	
30	GS-2012B-Q-011-04	00 ^h 57 ^m 03.46 ^s	-27°39'29.6''	0.4123	3	X	
31	GS-2012B-Q-011-04	00 ^h 57 ^m 02.17 ^s	-27°40'29.0''	0.5574	3	X	✓
32	GS-2012B-Q-011-04	00 ^h 57 ^m 02.74 ^s	-27°40'15.3''	0.5614	3	X	✓
33	GS-2012B-Q-011-04	00 ^h 57 ^m 01.02 ^s	-27°39'31.7''	0.3893	3	X	
35	GS-2012B-Q-011-04	00 ^h 57 ^m 02.94 ^s	-27°40'29.7''	0.5614	3	X	✓
Continued on next page							

Table A.23 – continued from previous page

ID	Mask	RA (J2000)	Dec (J2000)	<i>z</i>	Quality	Identification	Member
-----------	-------------	-------------------	--------------------	-----------------	----------------	-----------------------	---------------

Table A.23: XMMXCSJ005656.6-274031.9: Column 1 gives an ID for each galaxy in the mask given in column 2. Column 3 and 4 give the right ascension and declination respectively. Column 5 gives the redshift, column 6 gives the quality of the redshift according to the following scheme: $Q = 3$ corresponds to two or more strongly detected features; $Q = 2$ refers to one strongly detected or two weakly detected features; $Q = 1$ one weakly detected feature and $Q = 0$ when no features could be identified. Column 7 shows whether the redshift was found via visible inspection (V) or cross-correlation (X). Column 8 shows whether or not the galaxy was classified as a member and used in the calculation of the velocity dispersion.

ID	Mask	RA (J2000)	Dec (J2000)	z	Quality	Identification	Member
1	Nastasi et al. (2014)	01 ^h 52 ^m 41.30 ^s	-13°38'55.0"	0.8307	2		✓
3	Nastasi et al. (2014)	01 ^h 52 ^m 41.11 ^s	-13°39'07.9"	0.8303	3		✓
4	Nastasi et al. (2014)	01 ^h 52 ^m 42.71 ^s	-13°38'59.1"	0.8261	4		✓
5	Nastasi et al. (2014)	01 ^h 52 ^m 39.41 ^s	-13°38'55.8"	0.8233	3		✓
6	Nastasi et al. (2014)	01 ^h 52 ^m 40.70 ^s	-13°39'21.0"	0.8261	2		
7	Nastasi et al. (2014)	01 ^h 52 ^m 40.21 ^s	-13°39'24.1"	0.8307	3		✓
8	Nastasi et al. (2014)	01 ^h 52 ^m 43.20 ^s	-13°38'29.5"	0.8268	3		✓
9	Nastasi et al. (2014)	01 ^h 52 ^m 35.81 ^s	-13°39'15.0"	0.8326	2		✓
11	Nastasi et al. (2014)	01 ^h 52 ^m 47.21 ^s	-13°38'00.1"	0.8256	3		✓
13	Nastasi et al. (2014)	01 ^h 52 ^m 37.01 ^s	-13°40'15.0"	0.8324	2		✓
14	Nastasi et al. (2014)	01 ^h 52 ^m 36.00 ^s	-13°40'15.9"	0.8295	3		✓
15	Nastasi et al. (2014)	01 ^h 52 ^m 32.90 ^s	-13°40'01.9"	0.8279	3		✓
1	GS-2011B-Q-050-01	01 ^h 52 ^m 47.02 ^s	-13°41'18.3"	0.3772	2	X	
2	GS-2011B-Q-050-01	01 ^h 52 ^m 50.28 ^s	-13°39'20.2"	0.8277	3	X	
7	GS-2011B-Q-050-01	01 ^h 52 ^m 46.56 ^s	-13°39'37.1"	0.6377	2	X	
9	GS-2011B-Q-050-01	01 ^h 52 ^m 41.85 ^s	-13°40'19.6"	0.8149	2	X	✓
11	GS-2011B-Q-050-01	01 ^h 52 ^m 42.62 ^s	-13°39'50.4"	0.6160	2	X	
12	GS-2011B-Q-050-01	01 ^h 52 ^m 40.75 ^s	-13°39'20.9"	0.8250	3	X	✓
13	GS-2011B-Q-050-01	01 ^h 52 ^m 41.35 ^s	-13°38'56.1"	0.8290	3	X	✓
14	GS-2011B-Q-050-01	01 ^h 52 ^m 38.16 ^s	-13°38'54.3"	0.2460	3	X	
15	GS-2011B-Q-050-01	01 ^h 52 ^m 45.36 ^s	-13°38'38.5"	0.3533	3	X	
19	GS-2011B-Q-050-01	01 ^h 52 ^m 38.81 ^s	-13°38'28.0"	0.8211	3	X	✓
20	GS-2011B-Q-050-01	01 ^h 52 ^m 45.02 ^s	-13°39'26.0"	0.2756	3	X	
23	GS-2011B-Q-050-01	01 ^h 52 ^m 39.42 ^s	-13°38'02.8"	0.8211	2	X	✓
25	GS-2011B-Q-050-01	01 ^h 52 ^m 33.99 ^s	-13°38'48.2"	0.7724	3	X	
28	GS-2011B-Q-050-01	01 ^h 52 ^m 33.31 ^s	-13°38'45.3"	0.6357	3	X	
29	GS-2011B-Q-050-01	01 ^h 52 ^m 32.11 ^s	-13°38'28.7"	0.6345	3	X	
30	GS-2011B-Q-050-01	01 ^h 52 ^m 34.76 ^s	-13°37'58.5"	0.3948	3	X	
32	GS-2011B-Q-050-01	01 ^h 52 ^m 32.62 ^s	-13°37'44.1"	0.4942	2	X	

Continued on next page

Table A.24 – continued from previous page

ID	Mask	RA (J2000)	Dec (J2000)	z	Quality	Identification	Member
4	GS-2011B-Q-050-02	01 ^h 52 ^m 50.28 ^s	-13°39'20.2''	0.8276	2	X	✓
6	GS-2011B-Q-050-02	01 ^h 52 ^m 44.86 ^s	-13°40'14.2''	0.4947	2	V	
8	GS-2011B-Q-050-02	01 ^h 52 ^m 48.15 ^s	-13°38'53.9''	0.7398	2	X	
9	GS-2011B-Q-050-02	01 ^h 52 ^m 41.65 ^s	-13°39'42.5''	0.5290	3	X	
10	GS-2011B-Q-050-02	01 ^h 52 ^m 39.98 ^s	-13°39'22.4''	0.8294	3	X	✓
11	GS-2011B-Q-050-02	01 ^h 52 ^m 45.13 ^s	-13°39'09.0''	0.8313	2	X	✓
16	GS-2011B-Q-050-02	01 ^h 52 ^m 44.84 ^s	-13°38'24.8''	0.5340	2	X	
17	GS-2011B-Q-050-02	01 ^h 52 ^m 43.17 ^s	-13°38'29.5''	0.8258	3	X	
19	GS-2011B-Q-050-02	01 ^h 52 ^m 38.37 ^s	-13°39'22.7''	0.8290	2	X	✓
21	GS-2011B-Q-050-02	01 ^h 52 ^m 40.24 ^s	-13°39'00.4''	0.8193	3	X	✓
22	GS-2011B-Q-050-02	01 ^h 52 ^m 37.62 ^s	-13°38'30.5''	0.8202	2	X	✓
23	GS-2011B-Q-050-02	01 ^h 52 ^m 38.75 ^s	-13°38'24.1''	0.2813	3	X	
26	GS-2011B-Q-050-02	01 ^h 52 ^m 36.40 ^s	-13°36'50.5''	0.7283	3	X	
28	GS-2011B-Q-050-02	01 ^h 52 ^m 32.62 ^s	-13°37'44.1''	0.4941	2	X	
31	GS-2011B-Q-050-02	01 ^h 52 ^m 36.01 ^s	-13°37'45.2''	0.7848	2	X	
32	GS-2011B-Q-050-02	01 ^h 52 ^m 37.42 ^s	-13°37'45.5''	0.7858	2	X	
5606	KECK	01 ^h 52 ^m 44.13 ^s	-13°34'11.9''	0.8140			
5612	KECK	01 ^h 52 ^m 44.19 ^s	-13°34'49.9''	0.8209			
5638	KECK	01 ^h 52 ^m 42.02 ^s	-13°38'40.8''	0.8300			✓
5655	KECK	01 ^h 52 ^m 43.40 ^s	-13°38'24.1''	0.8348			✓
5688	KECK	01 ^h 52 ^m 42.88 ^s	-13°38'25.1''	0.8300			✓
5853	KECK	01 ^h 52 ^m 40.42 ^s	-13°38'20.7''	0.8297			✓
5900	KECK	01 ^h 52 ^m 39.78 ^s	-13°38'44.0''	0.8222			✓
5909	KECK	01 ^h 52 ^m 39.15 ^s	-13°40'35.3''	0.8213			✓
5922	KECK	01 ^h 52 ^m 39.52 ^s	-13°39'50.9''	0.8211			✓

Table A.24: XMMXCSJ015241.1-133855.9: All columns are as explained in Table A.23.

ID	Mask	RA (J2000)	Dec (J2000)	z	Quality	Identification	Member
2	GS-2012B-Q-011-06	02 ^h 17 ^m 30.50 ^s	-05°11'31.4''	0.5674	3	X	
3	GS-2012B-Q-011-06	02 ^h 17 ^m 28.40 ^s	-05°12'03.6''	0.9216	3	X	
6	GS-2012B-Q-011-06	02 ^h 17 ^m 27.60 ^s	-05°13'60.0''	0.6424	3	X	✓
8	GS-2012B-Q-011-06	02 ^h 17 ^m 34.35 ^s	-05°12'43.8''	0.6474	3	X	✓
10	GS-2012B-Q-011-06	02 ^h 17 ^m 33.72 ^s	-05°12'51.6''	0.6408	3	X	✓
11	GS-2012B-Q-011-06	02 ^h 17 ^m 35.84 ^s	-05°12'58.9''	0.8246	3	X	
12	GS-2012B-Q-011-06	02 ^h 17 ^m 30.52 ^s	-05°13'21.4''	0.8336	2	X	
13	GS-2012B-Q-011-06	02 ^h 17 ^m 35.79 ^s	-05°14'20.1''	0.6454	3	X	✓
15	GS-2012B-Q-011-06	02 ^h 17 ^m 32.55 ^s	-05°12'59.2''	0.6414	3	X	✓
16	GS-2012B-Q-011-06	02 ^h 17 ^m 33.02 ^s	-05°13'13.4''	0.6494	3	V	✓
17	GS-2012B-Q-011-06	02 ^h 17 ^m 34.18 ^s	-05°13'38.8''	0.4443	3	X	
18	GS-2012B-Q-011-06	02 ^h 17 ^m 34.97 ^s	-05°13'28.6''	0.6494	3	X	✓
19	GS-2012B-Q-011-06	02 ^h 17 ^m 35.92 ^s	-05°13'28.8''	1.0958	3	X	
20	GS-2012B-Q-011-06	02 ^h 17 ^m 41.81 ^s	-05°11'32.9''	0.4963	3	X	
22	GS-2012B-Q-011-06	02 ^h 17 ^m 38.72 ^s	-05°13'00.8''	0.6484	3	X	✓
23	GS-2012B-Q-011-06	02 ^h 17 ^m 39.37 ^s	-05°13'32.3''	0.7515	3	X	
24	GS-2012B-Q-011-06	02 ^h 17 ^m 37.16 ^s	-05°13'29.0''	0.6444	3	X	✓
25	GS-2012B-Q-011-06	02 ^h 17 ^m 38.01 ^s	-05°13'09.3''	0.6494	3	X	✓
26	GS-2012B-Q-011-06	02 ^h 17 ^m 40.15 ^s	-05°13'13.4''	0.7445	3	X	
27	GS-2012B-Q-011-06	02 ^h 17 ^m 43.39 ^s	-05°12'32.3''	0.6504	2	V	✓
28	GS-2012B-Q-011-06	02 ^h 17 ^m 42.49 ^s	-05°12'52.5''	0.4893	3	X	
29	GS-2012B-Q-011-06	02 ^h 17 ^m 41.00 ^s	-05°14'03.2''	0.6805	3	X	
30	GS-2012B-Q-011-06	02 ^h 17 ^m 44.89 ^s	-05°12'58.0''	0.4233	3	X	
31	GS-2012B-Q-011-06	02 ^h 17 ^m 45.25 ^s	-05°13'11.1''	0.2892	3	X	
32	GS-2012B-Q-011-06	02 ^h 17 ^m 43.79 ^s	-05°13'47.5''	0.6484	3	V	✓
33	GS-2012B-Q-011-06	02 ^h 17 ^m 46.73 ^s	-05°13'34.3''	0.6454	3	V	
34	GS-2012B-Q-011-06	02 ^h 17 ^m 46.01 ^s	-05°13'32.0''	0.5804	3	X	

Table A.25: XMMXCSJ021734.7-051326.9: All columns are as explained in Table A.23.

ID	Mask	RA (J2000)	Dec (J2000)	z	Quality	Identification	Member
1	GS-2010B-Q-46-06	02 ^h 50 ^m 22.92 ^s	-31°03'53.0"	0.8337	3	X	
8	GS-2010B-Q-46-06	02 ^h 50 ^m 15.25 ^s	-31°03'33.5"	0.7263	3	X	
9	GS-2010B-Q-46-06	02 ^h 50 ^m 13.27 ^s	-31°03'35.7"	0.6168	3	X	
10	GS-2010B-Q-46-06	02 ^h 50 ^m 12.05 ^s	-31°03'08.0"	0.7146	3	X	
14	GS-2010B-Q-46-06	02 ^h 50 ^m 06.63 ^s	-31°03'13.7"	0.8496	3	X	
15	GS-2010B-Q-46-06	02 ^h 50 ^m 08.70 ^s	-31°03'49.7"	0.9052	3	X	✓
16	GS-2010B-Q-46-06	02 ^h 50 ^m 03.78 ^s	-31°03'51.5"	0.3533	3	X	
17	GS-2010B-Q-46-06	02 ^h 50 ^m 06.89 ^s	-31°03'51.5"	0.9217	3	X	✓
18	GS-2010B-Q-46-06	02 ^h 50 ^m 05.48 ^s	-31°03'53.0"	0.6972	3	X	
19	GS-2010B-Q-46-06	02 ^h 50 ^m 04.50 ^s	-31°03'51.5"	0.9149	3	X	✓
21	GS-2010B-Q-46-06	02 ^h 50 ^m 02.79 ^s	-31°04'04.9"	0.9831	3	X	
22	GS-2010B-Q-46-06	02 ^h 50 ^m 06.48 ^s	-31°03'56.9"	0.9069	3	X	✓
23	GS-2010B-Q-46-06	02 ^h 50 ^m 09.04 ^s	-31°04'06.3"	0.7567	3	X	
25	GS-2010B-Q-46-06	02 ^h 50 ^m 03.83 ^s	-31°04'34.0"	0.8988	3	X	✓
26	GS-2010B-Q-46-06	02 ^h 50 ^m 04.24 ^s	-31°04'50.6"	0.9095	3	X	✓
28	GS-2010B-Q-46-06	02 ^h 50 ^m 04.59 ^s	-31°05'41.7"	0.6197	3	X	
34	GS-2010B-Q-46-06	02 ^h 50 ^m 04.26 ^s	-31°07'05.2"	0.1261	3	X	
1	GS-2012B-Q-011-09	02 ^h 50 ^m 22.92 ^s	-31°03'53.0"	0.5924	2	X	
2	GS-2012B-Q-011-09	02 ^h 50 ^m 18.11 ^s	-31°03'10.5"	0.9326	2	X	
4	GS-2012B-Q-011-09	02 ^h 50 ^m 16.05 ^s	-31°03'23.1"	1.0077	2	X	
5	GS-2012B-Q-011-09	02 ^h 50 ^m 14.89 ^s	-31°03'32.1"	0.7245	3	X	
6	GS-2012B-Q-011-09	02 ^h 50 ^m 14.94 ^s	-31°02'56.8"	0.9927	2	X	
9	GS-2012B-Q-011-09	02 ^h 50 ^m 08.98 ^s	-31°03'01.1"	0.9086	3	X	✓
10	GS-2012B-Q-011-09	02 ^h 50 ^m 10.24 ^s	-31°03'27.8"	0.9056	3	X	✓
11	GS-2012B-Q-011-09	02 ^h 50 ^m 07.01 ^s	-31°01'00.9"	0.5204	3	X	
13	GS-2012B-Q-011-09	02 ^h 50 ^m 06.54 ^s	-31°03'44.7"	0.9126	3	X	✓
17	GS-2012B-Q-011-09	02 ^h 50 ^m 03.99 ^s	-31°03'53.0"	0.9176	3	X	✓
18	GS-2012B-Q-011-09	02 ^h 50 ^m 07.33 ^s	-31°04'10.6"	0.9106	3	X	✓
19	GS-2012B-Q-011-09	02 ^h 50 ^m 02.67 ^s	-31°03'26.0"	0.9797	3	X	

Continued on next page

Table A.26 – continued from previous page

ID	Mask	RA (J2000)	Dec (J2000)	z	Quality	Identification	Member
20	GS-2012B-Q-011-09	02 ^h 50 ^m 07.38 ^s	-31°05'28.7''	0.6494	2	X	
21	GS-2012B-Q-011-09	02 ^h 49 ^m 58.10 ^s	-31°03'39.6''	0.8696	3	X	✓
22	GS-2012B-Q-011-09	02 ^h 50 ^m 05.48 ^s	-31°04'40.5''	0.9026	2	X	
27	GS-2012B-Q-011-09	02 ^h 49 ^m 58.68 ^s	-31°05'25.8''	0.6274	3	X	
28	GS-2012B-Q-011-09	02 ^h 49 ^m 59.99 ^s	-31°05'07.8''	0.8816	2	X	
29	GS-2012B-Q-011-09	02 ^h 49 ^m 58.60 ^s	-31°04'59.2''	0.9216	3	X	✓
30	GS-2012B-Q-011-09	02 ^h 50 ^m 00.51 ^s	-31°04'44.5''	0.5654	3	X	
31	GS-2012B-Q-011-09	02 ^h 50 ^m 04.26 ^s	-31°07'05.2''	0.9827	3	X	

Table A.26: XMMXCSJ025006.4-310400.8: All columns are as explained in Table A.23.

ID	Mask	RA (J2000)	Dec (J2000)	z	Quality	Identification	Member
1	GS-2011B-Q-050-03	03 ^h 02 ^m 13.84 ^s	-00°00'41.6''	0.4988	3	X	
7	GS-2011B-Q-050-03	03 ^h 02 ^m 13.04 ^s	00°00'41.5''	0.5958	3	X	
9	GS-2011B-Q-050-03	03 ^h 02 ^m 06.74 ^s	-00°00'06.1''	0.6432	3	X	✓
11	GS-2011B-Q-050-03	03 ^h 02 ^m 07.86 ^s	00°00'21.2''	0.6425	3	X	✓
12	GS-2011B-Q-050-03	03 ^h 02 ^m 06.20 ^s	-00°00'04.0''	0.6451	3	X	✓
13	GS-2011B-Q-050-03	03 ^h 02 ^m 08.78 ^s	00°00'39.9''	0.6486	3	X	✓
15	GS-2011B-Q-050-03	03 ^h 02 ^m 05.64 ^s	-00°00'00.5''	0.6452	3	X	✓
17	GS-2011B-Q-050-03	03 ^h 02 ^m 02.94 ^s	-00°00'53.1''	0.6503	3	X	✓
19	GS-2011B-Q-050-03	03 ^h 02 ^m 04.94 ^s	-00°00'33.0''	0.6477	2	X	✓
21	GS-2011B-Q-050-03	03 ^h 02 ^m 02.12 ^s	00°00'04.2''	0.6368	3	X	✓
22	GS-2011B-Q-050-03	03 ^h 02 ^m 00.91 ^s	-00°00'53.0''	0.4075	3	X	
23	GS-2011B-Q-050-03	03 ^h 02 ^m 00.40 ^s	-00°00'49.9''	0.6482	2	X	✓
25	GS-2011B-Q-050-03	03 ^h 01 ^m 59.56 ^s	00°00'31.0''	0.4688	2	X	
28	GS-2011B-Q-050-03	03 ^h 01 ^m 56.38 ^s	00°00'59.2''	0.4070	2	X	
31	GS-2011B-Q-050-03	03 ^h 01 ^m 55.80 ^s	-00°00'20.3''	0.7886	3	X	
5	GS-2011B-Q-050-04	03 ^h 02 ^m 11.53 ^s	00°00'46.1''	0.4094	2	X	
9	GS-2011B-Q-050-04	03 ^h 02 ^m 09.28 ^s	-00°01'04.8''	0.6700	3	X	
11	GS-2011B-Q-050-04	03 ^h 02 ^m 04.69 ^s	-00°00'32.1''	0.6435	2	X	✓
14	GS-2011B-Q-050-04	03 ^h 02 ^m 08.70 ^s	00°01'05.4''	0.6450	2	X	✓
15	GS-2011B-Q-050-04	03 ^h 02 ^m 07.94 ^s	00°00'30.1''	0.4770	3	X	
16	GS-2011B-Q-050-04	03 ^h 02 ^m 05.73 ^s	00°00'02.0''	0.6390	2	X	✓
17	GS-2011B-Q-050-04	03 ^h 02 ^m 05.26 ^s	00°00'09.0''	0.6454	2	X	✓
18	GS-2011B-Q-050-04	03 ^h 02 ^m 06.46 ^s	00°00'00.8''	0.6457	2	X	✓
23	GS-2011B-Q-050-04	03 ^h 02 ^m 00.18 ^s	-00°00'40.1''	0.4694	2	X	
24	GS-2011B-Q-050-04	03 ^h 02 ^m 00.65 ^s	00°00'21.3''	0.4051	3	X	
27	GS-2011B-Q-050-04	03 ^h 01 ^m 57.71 ^s	-00°00'34.4''	0.4944	2	X	
29	GS-2011B-Q-050-04	03 ^h 01 ^m 56.13 ^s	-00°00'20.8''	0.7888	3	X	
30	GS-2011B-Q-050-04	03 ^h 01 ^m 56.63 ^s	00°00'47.0''	0.9857	3	X	
17	GS-2011B-Q-050-05	03 ^h 02 ^m 06.06 ^s	-00°00'53.1''	0.6431	2	X	✓

Continued on next page

Table A.27 – continued from previous page

ID	Mask	RA (J2000)	Dec (J2000)	z	Quality	Identification	Member
18	GS-2011B-Q-050-05	03 ^h 02 ^m 02.64 ^s	-00°00'47.7''	0.6609	2	X	✓
20	GS-2011B-Q-050-05	03 ^h 02 ^m 04.82 ^s	-00°00'43.3''	0.6477	2	X	
21	GS-2011B-Q-050-05	03 ^h 02 ^m 06.50 ^s	-00°00'27.7''	0.4945	2	X	
26	GS-2011B-Q-050-05	03 ^h 01 ^m 59.29 ^s	00°00'43.5''	0.4070	3	X	
27	GS-2011B-Q-050-05	03 ^h 02 ^m 00.34 ^s	00°00'36.2''	0.4072	3	X	
28	GS-2011B-Q-050-05	03 ^h 01 ^m 57.26 ^s	-00°00'31.2''	0.5948	3	X	

Table A.27: XMMXCSJ030205.1-000003.6: All columns are as explained in Table A.23.

ID	Mask	RA (J2000)	Dec (J2000)	z	Quality	Identification	Member
2	GS-2010B-Q-046-01	09 ^h 59 ^m 41.78 ^s	02°33'39.1"	0.6964	3	X	
3	GS-2010B-Q-046-01	09 ^h 59 ^m 34.47 ^s	02°33'47.0"	0.6766	3	X	
4	GS-2010B-Q-046-01	09 ^h 59 ^m 43.01 ^s	02°32'32.0"	0.6963	3	X	
5	GS-2010B-Q-046-01	09 ^h 59 ^m 42.91 ^s	02°31'49.7"	0.7268	3	X	✓
7	GS-2010B-Q-046-01	09 ^h 59 ^m 39.41 ^s	02°33'00.1"	0.4701	3	X	
8	GS-2010B-Q-046-01	09 ^h 59 ^m 39.35 ^s	02°32'39.2"	0.6778	3	X	
9	GS-2010B-Q-046-01	09 ^h 59 ^m 38.13 ^s	02°32'11.0"	0.7296	3	X	✓
10	GS-2010B-Q-046-01	09 ^h 59 ^m 39.29 ^s	02°32'04.1"	0.7317	3	X	✓
11	GS-2010B-Q-046-01	09 ^h 59 ^m 35.47 ^s	02°31'56.0"	0.3317	3	X	
15	GS-2010B-Q-046-01	09 ^h 59 ^m 43.71 ^s	02°31'01.9"	0.2455	3	X	
16	GS-2010B-Q-046-01	09 ^h 59 ^m 43.04 ^s	02°31'08.7"	0.7314	3	X	✓
17	GS-2010B-Q-046-01	09 ^h 59 ^m 42.96 ^s	02°31'16.7"	0.7285	3	X	✓
18	GS-2010B-Q-046-01	09 ^h 59 ^m 40.88 ^s	02°30'34.2"	0.8369	3	X	
20	GS-2010B-Q-046-01	09 ^h 59 ^m 40.58 ^s	02°31'41.2"	0.7248	3	X	✓
21	GS-2010B-Q-046-01	09 ^h 59 ^m 41.64 ^s	02°31'29.9"	0.7307	3	X	✓
23	GS-2010B-Q-046-01	09 ^h 59 ^m 40.98 ^s	02°30'40.5"	0.8360	3	X	
24	GS-2010B-Q-046-01	09 ^h 59 ^m 40.40 ^s	02°30'54.6"	0.7169	3	X	
25	GS-2010B-Q-046-01	09 ^h 59 ^m 44.35 ^s	02°29'54.1"	0.7303	3	X	✓
27	GS-2010B-Q-046-01	09 ^h 59 ^m 41.46 ^s	02°30'18.2"	0.8352	3	X	
28	GS-2010B-Q-046-01	09 ^h 59 ^m 41.05 ^s	02°30'09.9"	0.7156	3	X	
30	GS-2010B-Q-046-01	09 ^h 59 ^m 35.91 ^s	02°29'13.4"	0.7149	3	X	
35	GS-2010B-Q-046-01	09 ^h 59 ^m 40.98 ^s	02°28'49.6"	0.4095	3	X	
6	GS-2012A-Q-046-01	09 ^h 59 ^m 38.44 ^s	02°33'13.9"	0.6603	2	X	
7	GS-2012A-Q-046-01	09 ^h 59 ^m 38.89 ^s	02°33'05.6"	0.7531	2	X	
8	GS-2012A-Q-046-01	09 ^h 59 ^m 43.03 ^s	02°32'00.1"	0.7259	2	X	✓
9	GS-2012A-Q-046-01	09 ^h 59 ^m 42.42 ^s	02°32'09.3"	0.7289	3	X	✓
10	GS-2012A-Q-046-01	09 ^h 59 ^m 42.27 ^s	02°31'34.6"	0.7265	2	X	✓
13	GS-2012A-Q-046-01	09 ^h 59 ^m 39.70 ^s	02°31'19.0"	0.7286	3	X	✓
14	GS-2012A-Q-046-01	09 ^h 59 ^m 42.19 ^s	02°32'36.8"	0.8893	3	X	

Continued on next page

Table A.28 – continued from previous page

ID	Mask	RA (J2000)	Dec (J2000)	z	Quality	Identification	Member
16	GS-2012A-Q-046-01	09 ^h 59 ^m 41.79 ^s	02°32'18.2''	0.5489	3	X	
17	GS-2012A-Q-046-01	09 ^h 59 ^m 40.25 ^s	02°31'10.9''	0.7332	3	X	✓
18	GS-2012A-Q-046-01	09 ^h 59 ^m 41.14 ^s	02°31'25.8''	0.7290	3	X	✓
19	GS-2012A-Q-046-01	09 ^h 59 ^m 42.36 ^s	02°30'45.3''	0.7270	3	X	✓
20	GS-2012A-Q-046-01	09 ^h 59 ^m 38.94 ^s	02°30'59.6''	0.7271	3	X	✓
21	GS-2012A-Q-046-01	09 ^h 59 ^m 39.66 ^s	02°30'52.1''	0.7186	3	X	✓
23	GS-2012A-Q-046-01	09 ^h 59 ^m 43.95 ^s	02°29'52.3''	0.7294	3	X	✓
25	GS-2012A-Q-046-01	09 ^h 59 ^m 40.35 ^s	02°30'19.2''	0.4748	2	X	
26	GS-2012A-Q-046-01	09 ^h 59 ^m 40.97 ^s	02°29'58.6''	0.7309	3	X	✓
29	GS-2012A-Q-046-01	09 ^h 59 ^m 40.95 ^s	02°29'16.9''	0.4053	3	X	
33	GS-2012A-Q-046-01	09 ^h 59 ^m 38.40 ^s	02°28'40.2''	0.7542	3	X	
35	GS-2012A-Q-046-01	09 ^h 59 ^m 40.88 ^s	02°28'46.8''	0.2494	3	X	
1	GS-2012A-Q-046-02	09 ^h 59 ^m 46.92 ^s	02°33'46.3''	0.6901	2	X	
5	GS-2012A-Q-046-02	09 ^h 59 ^m 43.78 ^s	02°31'54.5''	0.4687	3	X	
8	GS-2012A-Q-046-02	09 ^h 59 ^m 40.81 ^s	02°31'34.3''	0.7286	3	X	✓
11	GS-2012A-Q-046-02	09 ^h 59 ^m 39.41 ^s	02°33'00.1''	0.4703	3	X	
12	GS-2012A-Q-046-02	09 ^h 59 ^m 38.57 ^s	02°33'06.8''	0.7515	3	X	
15	GS-2012A-Q-046-02	09 ^h 59 ^m 39.41 ^s	02°32'20.4''	1.1040	3	X	
16	GS-2012A-Q-046-02	09 ^h 59 ^m 38.58 ^s	02°32'12.6''	0.4419	3	X	
19	GS-2012A-Q-046-02	09 ^h 59 ^m 40.65 ^s	02°31'15.9''	0.7295	3	X	✓
20	GS-2012A-Q-046-02	09 ^h 59 ^m 39.45 ^s	02°30'38.5''	0.7242	3	X	✓
23	GS-2012A-Q-046-02	09 ^h 59 ^m 42.80 ^s	02°30'08.8''	0.7248	3	X	✓
25	GS-2012A-Q-046-02	09 ^h 59 ^m 38.38 ^s	02°30'16.4''	0.7295	3	X	✓
26	GS-2012A-Q-046-02	09 ^h 59 ^m 40.52 ^s	02°30'02.4''	0.7308	3	X	✓
31	GS-2012A-Q-046-02	09 ^h 59 ^m 40.67 ^s	02°29'32.9''	0.9603	2	X	
33	GS-2012A-Q-046-02	09 ^h 59 ^m 39.64 ^s	02°28'37.8''	0.2489	3	X	
34	GS-2012A-Q-046-02	09 ^h 59 ^m 40.88 ^s	02°28'46.8''	0.2495	3	X	

Table A.28: XMMXCSJ095940.7+023113.4: All columns are as explained in Table A.23.

ID	Mask	RA (J2000)	Dec (J2000)	z	Quality	Identification	Member
2	GS-2010B-Q-046-03	11 ^h 24 ^m 00.44 ^s	05°27'13.8"	0.4726	3	X	
4	GS-2010B-Q-046-03	11 ^h 24 ^m 00.65 ^s	05°27'42.1"	0.3752	3	X	
5	GS-2010B-Q-046-03	11 ^h 24 ^m 00.16 ^s	05°27'43.0"	0.1554	3	X	
6	GS-2010B-Q-046-03	11 ^h 24 ^m 02.58 ^s	05°28'43.8"	0.3942	3	X	
11	GS-2010B-Q-046-03	11 ^h 23 ^m 58.50 ^s	05°28'10.8"	0.6544	3	X	
12	GS-2010B-Q-046-03	11 ^h 23 ^m 59.15 ^s	05°28'07.0"	0.5945	3	X	
13	GS-2010B-Q-046-03	11 ^h 23 ^m 57.11 ^s	05°28'34.9"	0.6514	3	X	✓
14	GS-2010B-Q-046-03	11 ^h 23 ^m 56.49 ^s	05°29'01.0"	0.6567	3	X	✓
15	GS-2010B-Q-046-03	11 ^h 23 ^m 59.97 ^s	05°29'13.0"	0.3750	3	X	
16	GS-2010B-Q-046-03	11 ^h 23 ^m 48.65 ^s	05°28'09.0"	0.5299	3	X	
17	GS-2010B-Q-046-03	11 ^h 23 ^m 51.43 ^s	05°28'49.7"	0.6569	3	X	✓
18	GS-2010B-Q-046-03	11 ^h 23 ^m 52.17 ^s	05°28'51.5"	0.6557	3	X	✓
19	GS-2010B-Q-046-03	11 ^h 23 ^m 50.28 ^s	05°29'13.9"	0.6557	3	X	✓
21	GS-2010B-Q-046-03	11 ^h 23 ^m 50.49 ^s	05°29'32.2"	0.6551	3	X	✓
25	GS-2010B-Q-046-03	11 ^h 23 ^m 53.46 ^s	05°29'04.3"	0.3747	3	X	
26	GS-2010B-Q-046-03	11 ^h 23 ^m 50.06 ^s	05°29'35.8"	0.6591	3	X	✓
27	GS-2010B-Q-046-03	11 ^h 23 ^m 43.65 ^s	05°28'04.6"	0.6552	3	X	✓
28	GS-2010B-Q-046-03	11 ^h 23 ^m 48.89 ^s	05°29'36.5"	0.6478	3	X	✓
30	GS-2010B-Q-046-03	11 ^h 23 ^m 46.52 ^s	05°29'52.2"	0.5826	3	X	
31	GS-2010B-Q-046-03	11 ^h 23 ^m 46.33 ^s	05°30'09.1"	0.6543	3	X	✓
32	GS-2010B-Q-046-03	11 ^h 23 ^m 47.45 ^s	05°29'57.6"	0.6389	3	X	
33	GS-2010B-Q-046-03	11 ^h 23 ^m 47.88 ^s	05°29'54.6"	0.6496	3	X	✓
2	GS2012AQ046-05	11 ^h 23 ^m 59.56 ^s	05°26'58.8"	0.4146	3	X	
7	GS2012AQ046-05	11 ^h 23 ^m 52.84 ^s	05°27'18.3"	0.6487	3	X	
14	GS2012AQ046-05	11 ^h 23 ^m 56.35 ^s	05°29'01.0"	0.2713	2	X	
15	GS2012AQ046-05	11 ^h 23 ^m 55.48 ^s	05°29'02.5"	0.6603	2	X	✓
16	GS2012AQ046-05	11 ^h 24 ^m 00.33 ^s	05°29'21.8"	0.6559	2	X	
19	GS2012AQ046-05	11 ^h 23 ^m 49.80 ^s	05°28'47.3"	0.6551	2	X	✓
20	GS2012AQ046-05	11 ^h 23 ^m 52.23 ^s	05°28'33.8"	0.2704	2	X	

Continued on next page

Table A.29 – continued from previous page

ID	Mask	RA (J2000)	Dec (J2000)	z	Quality	Identification	Member
23	GS2012AQ046-05	11 ^h 23 ^m 49.77 ^s	05°29'29.6"	0.6173	2	X	
26	GS2012AQ046-05	11 ^h 23 ^m 53.92 ^s	05°28'49.5"	0.6550	3	X	✓
32	GS2012AQ046-05	11 ^h 23 ^m 48.09 ^s	05°30'40.6"	0.2154	3	X	
3	GS2012AQ046-06	11 ^h 24 ^m 00.02 ^s	05°27'32.8"	0.4144	3	X	
6	GS2012AQ046-06	11 ^h 23 ^m 59.87 ^s	05°27'53.9"	0.4714	3	X	
12	GS2012AQ046-06	11 ^h 23 ^m 59.15 ^s	05°28'07.0"	0.5944	2	X	✓
13	GS2012AQ046-06	11 ^h 23 ^m 57.44 ^s	05°29'05.2"	0.6511	3	X	
14	GS2012AQ046-06	11 ^h 24 ^m 01.00 ^s	05°29'07.5"	0.3749	3	X	
15	GS2012AQ046-06	11 ^h 23 ^m 50.31 ^s	05°28'06.3"	0.6129	3	X	
17	GS2012AQ046-06	11 ^h 23 ^m 51.87 ^s	05°28'25.8"	0.5517	3	X	
18	GS2012AQ046-06	11 ^h 23 ^m 50.07 ^s	05°29'00.3"	0.6378	3	X	
19	GS2012AQ046-06	11 ^h 23 ^m 52.14 ^s	05°28'56.7"	0.6515	3	X	✓
20	GS2012AQ046-06	11 ^h 23 ^m 54.84 ^s	05°29'04.5"	0.6381	3	X	
23	GS2012AQ046-06	11 ^h 23 ^m 55.15 ^s	05°30'28.9"	0.3745	3	X	
27	GS2012AQ046-06	11 ^h 23 ^m 48.05 ^s	05°29'40.3"	0.8828	3	X	
28	GS2012AQ046-06	11 ^h 23 ^m 51.48 ^s	05°30'27.4"	0.4231	3	X	
30	GS2012AQ046-06	11 ^h 23 ^m 45.31 ^s	05°29'57.0"	0.5678	2	X	
32	GS2012AQ046-06	11 ^h 23 ^m 49.50 ^s	05°30'51.6"	0.6562	3	X	✓

Table A.29: XMMXCSJ112349.4+052955.1: All columns are as explained in Table A.23.

ID	Mask	RA (J2000)	Dec (J2000)	z	Quality	Identification	Member
3	GS-2012A-Q-046-07	11 ^h 35 ^m 58.38 ^s	-03°31'15.8"	1.0306	3	X	
5	GS-2012A-Q-046-07	11 ^h 35 ^m 59.26 ^s	-03°31'33.9"	0.8323	3	X	✓
6	GS-2012A-Q-046-07	11 ^h 35 ^m 59.51 ^s	-03°32'04.2"	0.8353	3	X	
8	GS-2012A-Q-046-07	11 ^h 36 ^m 01.95 ^s	-03°31'10.1"	0.8255	3	X	✓
9	GS-2012A-Q-046-07	11 ^h 36 ^m 02.76 ^s	-03°31'04.6"	0.8841	3	X	
11	GS-2012A-Q-046-07	11 ^h 36 ^m 01.15 ^s	-03°29'33.8"	0.8215	3	X	✓
12	GS-2012A-Q-046-07	11 ^h 36 ^m 04.68 ^s	-03°30'39.0"	0.8266	3	X	✓
13	GS-2012A-Q-046-07	11 ^h 36 ^m 04.36 ^s	-03°30'17.7"	0.8265	3	X	✓
14	GS-2012A-Q-046-07	11 ^h 36 ^m 03.15 ^s	-03°30'00.7"	0.8339	3	X	✓
15	GS-2012A-Q-046-07	11 ^h 36 ^m 04.33 ^s	-03°30'30.7"	0.8332	3	X	✓
16	GS-2012A-Q-046-07	11 ^h 36 ^m 06.69 ^s	-03°30'14.3"	0.7021	3	X	
17	GS-2012A-Q-046-07	11 ^h 36 ^m 04.13 ^s	-03°29'47.9"	0.8253	3	X	✓
18	GS-2012A-Q-046-07	11 ^h 36 ^m 03.74 ^s	-03°29'54.7"	0.8314	3	X	✓
20	GS-2012A-Q-046-07	11 ^h 36 ^m 00.34 ^s	-03°29'20.0"	0.8250	3	X	✓
21	GS-2012A-Q-046-07	11 ^h 36 ^m 01.38 ^s	-03°28'56.4"	0.9718	2	X	
22	GS-2012A-Q-046-07	11 ^h 36 ^m 01.43 ^s	-03°29'11.3"	0.8254	3	X	✓
23	GS-2012A-Q-046-07	11 ^h 36 ^m 10.03 ^s	-03°29'19.2"	0.6508	3	X	
24	GS-2012A-Q-046-07	11 ^h 36 ^m 09.58 ^s	-03°29'05.1"	0.6502	3	X	
25	GS-2012A-Q-046-07	11 ^h 36 ^m 05.87 ^s	-03°28'39.5"	0.8265	3	X	✓
26	GS-2012A-Q-046-07	11 ^h 36 ^m 04.83 ^s	-03°28'22.6"	0.8831	3	X	
28	GS-2012A-Q-046-07	11 ^h 36 ^m 03.95 ^s	-03°27'59.7"	0.8307	3	X	✓
34	GS-2012A-Q-046-07	11 ^h 36 ^m 02.55 ^s	-03°27'08.5"	0.6434	3	X	
36	GS-2012A-Q-046-07	11 ^h 36 ^m 04.01 ^s	-03°27'32.0"	0.8370	3	X	✓
9	GS-2012A-Q-046-08	11 ^h 36 ^m 04.48 ^s	-03°31'58.9"	0.5370	2	X	
11	GS-2012A-Q-046-08	11 ^h 35 ^m 58.58 ^s	-03°29'58.4"	0.2058	3	X	
12	GS-2012A-Q-046-08	11 ^h 36 ^m 00.27 ^s	-03°30'31.0"	0.7022	3	X	
13	GS-2012A-Q-046-08	11 ^h 36 ^m 03.65 ^s	-03°29'52.4"	0.8328	3	V	✓
15	GS-2012A-Q-046-08	11 ^h 36 ^m 02.47 ^s	-03°29'25.7"	0.6884	2	X	
16	GS-2012A-Q-046-08	11 ^h 36 ^m 05.41 ^s	-03°29'38.6"	0.8298	3	X	✓

Continued on next page

Table A.30 – continued from previous page

ID	Mask	RA (J2000)	Dec (J2000)	z	Quality	Identification	Member
17	GS-2012A-Q-046-08	11 ^h 36 ^m 04.64 ^s	-03°30'23.3''	0.8242	3	X	✓
18	GS-2012A-Q-046-08	11 ^h 36 ^m 06.05 ^s	-03°30'18.4''	0.8296	3	X	✓
19	GS-2012A-Q-046-08	11 ^h 36 ^m 02.55 ^s	-03°29'58.6''	0.8307	3	X	✓
20	GS-2012A-Q-046-08	11 ^h 36 ^m 02.67 ^s	-03°29'40.5''	0.8274	3	X	✓
22	GS-2012A-Q-046-08	11 ^h 36 ^m 03.71 ^s	-03°29'10.8''	0.4067	2	X	
24	GS-2012A-Q-046-08	11 ^h 36 ^m 04.25 ^s	-03°29'18.3''	0.8357	3	X	✓
30	GS-2012A-Q-046-08	11 ^h 36 ^m 04.70 ^s	-03°28'14.5''	0.1869	3	X	

Table A.30: XMMXCSJ113602.9-032943.2: All columns are as explained in Table A.23.

ID	Mask	RA (J2000)	Dec (J2000)	z	Quality	Identification	Member
4	GS-2012A-Q-046-10	13 ^h 42 ^m 58.07 ^s	-00°02'43.9"	0.8343	3	X	
5	GS-2012A-Q-046-10	13 ^h 42 ^m 59.51 ^s	00°00'08.0"	0.6925	3	X	✓
6	GS-2012A-Q-046-10	13 ^h 42 ^m 56.97 ^s	-00°00'47.4"	0.4383	3	X	
7	GS-2012A-Q-046-10	13 ^h 42 ^m 58.82 ^s	-00°00'53.6"	0.8342	3	X	
8	GS-2012A-Q-046-10	13 ^h 43 ^m 02.03 ^s	-00°01'17.4"	0.6829	3	X	✓
9	GS-2012A-Q-046-10	13 ^h 42 ^m 59.93 ^s	-00°01'20.0"	0.5510	3	X	
10	GS-2012A-Q-046-10	13 ^h 43 ^m 01.63 ^s	-00°01'41.7"	0.6833	3	X	✓
11	GS-2012A-Q-046-10	13 ^h 42 ^m 59.07 ^s	-00°01'45.5"	0.4123	3	X	
12	GS-2012A-Q-046-10	13 ^h 42 ^m 59.26 ^s	-00°01'33.3"	0.6865	3	X	✓
13	GS-2012A-Q-046-10	13 ^h 43 ^m 00.57 ^s	-00°01'23.8"	0.6962	3	X	✓
15	GS-2012A-Q-046-10	13 ^h 43 ^m 02.82 ^s	-00°00'28.3"	0.6956	3	X	✓
17	GS-2012A-Q-046-10	13 ^h 43 ^m 04.11 ^s	-00°01'50.1"	0.6896	3	X	✓
18	GS-2012A-Q-046-10	13 ^h 43 ^m 04.57 ^s	-00°00'56.4"	0.6912	3	X	✓
19	GS-2012A-Q-046-10	13 ^h 43 ^m 02.71 ^s	-00°01'13.1"	0.6913	3	X	✓
21	GS-2012A-Q-046-10	13 ^h 43 ^m 04.00 ^s	-00°00'55.2"	0.6849	3	X	✓
23	GS-2012A-Q-046-10	13 ^h 43 ^m 09.21 ^s	00°00'23.1"	0.6152	3	X	
24	GS-2012A-Q-046-10	13 ^h 43 ^m 06.79 ^s	00°00'09.5"	0.3847	2	X	
26	GS-2012A-Q-046-10	13 ^h 43 ^m 08.82 ^s	-00°00'04.8"	0.7017	2	X	
27	GS-2012A-Q-046-10	13 ^h 43 ^m 09.97 ^s	-00°01'11.0"	0.6906	3	X	✓
28	GS-2012A-Q-046-10	13 ^h 43 ^m 07.82 ^s	-00°00'51.4"	0.6911	3	X	✓
29	GS-2012A-Q-046-10	13 ^h 43 ^m 08.21 ^s	-00°00'30.5"	0.6958	3	X	✓
30	GS-2012A-Q-046-10	13 ^h 43 ^m 10.30 ^s	00°00'35.0"	0.6847	3	X	✓
31	GS-2012A-Q-046-10	13 ^h 43 ^m 09.80 ^s	00°00'25.8"	0.5491	3	X	
34	GS-2012A-Q-046-10	13 ^h 43 ^m 12.93 ^s	00°00'20.8"	0.2190	2	X	
35	GS-2012A-Q-046-10	13 ^h 43 ^m 13.05 ^s	-00°00'08.6"	0.6865	3	X	✓
36	GS-2012A-Q-046-10	13 ^h 43 ^m 13.85 ^s	-00°01'02.2"	0.7952	2	X	
3	GS-2012A-Q-046-11	13 ^h 42 ^m 54.94 ^s	-00°01'04.6"	0.8149	3	X	
8	GS-2012A-Q-046-11	13 ^h 43 ^m 02.43 ^s	-00°01'38.7"	0.6902	2	X	✓
10	GS-2012A-Q-046-11	13 ^h 43 ^m 00.20 ^s	-00°02'15.2"	0.6864	3	V	✓

Continued on next page

Table A.31 – continued from previous page

ID	Mask	RA (J2000)	Dec (J2000)	z	Quality	Identification	Member
11	GS-2012A-Q-046-11	13 ^h 43 ^m 00.10 ^s	-00°01'12.5''	0.6793	2	X	✓
13	GS-2012A-Q-046-11	13 ^h 42 ^m 59.42 ^s	-00°01'18.7''	0.6018	2	X	
14	GS-2012A-Q-046-11	13 ^h 43 ^m 02.31 ^s	-00°00'50.9''	0.6909	2	X	✓
15	GS-2012A-Q-046-11	13 ^h 43 ^m 03.97 ^s	-00°01'25.9''	0.6801	3	X	✓
16	GS-2012A-Q-046-11	13 ^h 43 ^m 05.18 ^s	-00°01'48.0''	0.5474	2	X	
18	GS-2012A-Q-046-11	13 ^h 43 ^m 04.65 ^s	-00°00'57.3''	0.6901	2	X	✓
19	GS-2012A-Q-046-11	13 ^h 43 ^m 04.77 ^s	-00°00'44.0''	0.6986	2	X	✓
21	GS-2012A-Q-046-11	13 ^h 43 ^m 07.84 ^s	00°00'19.6''	0.2707	2	X	
23	GS-2012A-Q-046-11	13 ^h 43 ^m 08.50 ^s	00°00'17.4''	0.7942	2	X	
30	GS-2012A-Q-046-11	13 ^h 43 ^m 12.41 ^s	00°01'23.7''	0.6895	2	X	✓
32	GS-2012A-Q-046-11	13 ^h 43 ^m 12.93 ^s	00°00'20.8''	0.8020	2	X	

Table A.31: XMMXCSJ134305.1-000056.8: All columns are as explained in Table A.23.

ID	Mask	RA (J2000)	Dec (J2000)	z	Quality	Identification	Member
1	Nastasi et al. (2014)	14 ^h 50 ^m 09.30 ^s	09°04'39.3''	0.6419	3		
2	Nastasi et al. (2014)	14 ^h 50 ^m 09.20 ^s	09°04'45.1''	0.6425	3		
3	Nastasi et al. (2014)	14 ^h 50 ^m 10.40 ^s	09°04'23.5''	0.6418	2		✓
4	Nastasi et al. (2014)	14 ^h 50 ^m 09.50 ^s	09°04'15.9''	0.6430	3		
5	Nastasi et al. (2014)	14 ^h 50 ^m 07.40 ^s	09°04'28.8''	0.6429	3		✓
6	Nastasi et al. (2014)	14 ^h 50 ^m 09.30 ^s	09°04'06.5''	0.6377	3		
7	Nastasi et al. (2014)	14 ^h 50 ^m 10.40 ^s	09°03'53.4''	0.6462	2		✓
8	Nastasi et al. (2014)	14 ^h 50 ^m 10.61 ^s	09°05'32.4''	0.6379	3		
9	Nastasi et al. (2014)	14 ^h 50 ^m 13.80 ^s	09°03'21.9''	0.6407	3		
10	Nastasi et al. (2014)	14 ^h 50 ^m 16.01 ^s	09°02'57.6''	0.6420	2		✓
11	Nastasi et al. (2014)	14 ^h 50 ^m 04.91 ^s	09°06'55.1''	0.6405	3		
3	GN-2012A-Q-070-05	14 ^h 50 ^m 12.84 ^s	09°02'45.1''	0.5093	3	X	
6	GN-2012A-Q-070-05	14 ^h 50 ^m 07.25 ^s	09°02'58.0''	0.5064	2	X	
9	GN-2012A-Q-070-05	14 ^h 50 ^m 10.22 ^s	09°02'50.9''	0.5889	3	X	
11	GN-2012A-Q-070-05	14 ^h 50 ^m 11.80 ^s	09°03'56.4''	0.6405	3	X	✓
12	GN-2012A-Q-070-05	14 ^h 50 ^m 09.37 ^s	09°04'06.5''	0.6367	2	X	✓
13	GN-2012A-Q-070-05	14 ^h 50 ^m 09.53 ^s	09°04'15.9''	0.6430	3	X	✓
14	GN-2012A-Q-070-05	14 ^h 50 ^m 09.97 ^s	09°04'36.0''	0.3242	3	X	
15	GN-2012A-Q-070-05	14 ^h 50 ^m 13.80 ^s	09°03'21.9''	0.6403	3	X	✓
16	GN-2012A-Q-070-05	14 ^h 50 ^m 09.86 ^s	09°04'27.2''	0.6412	2	X	✓
17	GN-2012A-Q-070-05	14 ^h 50 ^m 09.29 ^s	09°04'39.2''	0.6398	3	X	
22	GN-2012A-Q-070-05	14 ^h 50 ^m 11.94 ^s	09°05'40.3''	0.6455	3	X	✓
24	GN-2012A-Q-070-05	14 ^h 50 ^m 01.45 ^s	09°05'06.9''	0.6355	3	X	✓
27	GN-2012A-Q-070-05	14 ^h 50 ^m 02.90 ^s	09°05'45.5''	0.4828	3	X	
31	GN-2012A-Q-070-05	14 ^h 50 ^m 07.98 ^s	09°06'52.6''	0.3705	3	X	
1	GN-2012A-Q-070-06	14 ^h 50 ^m 09.49 ^s	09°01'54.0''	0.8757	2	X	
3	GN-2012A-Q-070-06	14 ^h 50 ^m 08.46 ^s	09°02'24.2''	0.2673	2	X	
4	GN-2012A-Q-070-06	14 ^h 50 ^m 09.14 ^s	09°02'21.3''	0.7059	2	X	
7	GN-2012A-Q-070-06	14 ^h 50 ^m 09.00 ^s	09°03'16.8''	0.6403	2	X	✓

Continued on next page

Table A.32 – continued from previous page

ID	Mask	RA (J2000)	Dec (J2000)	z	Quality	Identification	Member
10	GN-2012A-Q-070-06	14 ^h 50 ^m 09.73 ^s	09°04'11.7''	0.6372	3	X	✓
12	GN-2012A-Q-070-06	14 ^h 50 ^m 12.48 ^s	09°03'16.6''	0.5840	3	X	
15	GN-2012A-Q-070-06	14 ^h 50 ^m 09.12 ^s	09°04'25.8''	0.8099	3	X	
18	GN-2012A-Q-070-06	14 ^h 50 ^m 10.65 ^s	09°05'32.0''	0.6363	3	X	✓
21	GN-2012A-Q-070-06	14 ^h 50 ^m 14.62 ^s	09°05'46.7''	0.7252	3	X	
1	GN-2012A-Q-070-07	14 ^h 50 ^m 15.96 ^s	09°02'22.7''	0.5646	2	X	
6	GN-2012A-Q-070-07	14 ^h 50 ^m 07.24 ^s	09°02'45.5''	1.0768	3	X	
11	GN-2012A-Q-070-07	14 ^h 50 ^m 09.42 ^s	09°04'11.9''	0.6457	2	X	✓
12	GN-2012A-Q-070-07	14 ^h 50 ^m 13.56 ^s	09°03'51.6''	0.2948	3	X	
13	GN-2012A-Q-070-07	14 ^h 50 ^m 10.59 ^s	09°03'54.8''	0.2282	3	X	
14	GN-2012A-Q-070-07	14 ^h 50 ^m 08.87 ^s	09°04'18.6''	0.6444	3	X	✓
15	GN-2012A-Q-070-07	14 ^h 50 ^m 08.55 ^s	09°04'27.9''	0.7346	2	X	
16	GN-2012A-Q-070-07	14 ^h 50 ^m 09.51 ^s	09°03'59.3''	0.6413	2	X	✓
19	GN-2012A-Q-070-07	14 ^h 50 ^m 09.38 ^s	09°04'45.0''	0.6455	3	X	✓
22	GN-2012A-Q-070-07	14 ^h 50 ^m 01.03 ^s	09°04'50.5''	0.6417	3	X	✓
25	GN-2012A-Q-070-07	14 ^h 50 ^m 03.59 ^s	09°05'33.3''	0.6411	2	X	✓
26	GN-2012A-Q-070-07	14 ^h 50 ^m 03.83 ^s	09°06'15.5''	0.4833	3	X	
27	GN-2012A-Q-070-07	14 ^h 50 ^m 04.34 ^s	09°06'04.2''	0.6367	2	X	✓
32	GN-2012A-Q-070-07	14 ^h 50 ^m 07.98 ^s	09°06'52.6''	0.3702	3	X	

Table A.32: XMMXCSJ145009.3+090428.8: All columns are as explained in Table A.23.

ID	Mask	RA (J2000)	Dec (J2000)	z	Quality	Identification	Member
5	GS-2010B-Q-046-04	21 ^h 52 ^m 20.26 ^s	-27°28'46.6"	0.4662	2	X	
8	GS-2010B-Q-046-04	21 ^h 52 ^m 16.97 ^s	-27°28'39.8"	0.6330	3	X	
12	GS-2010B-Q-046-04	21 ^h 52 ^m 23.98 ^s	-27°30'29.9"	0.8217	3	X	✓
13	GS-2010B-Q-046-04	21 ^h 52 ^m 19.74 ^s	-27°30'32.1"	0.8262	2	X	✓
14	GS-2010B-Q-046-04	21 ^h 52 ^m 14.96 ^s	-27°30'00.0"	0.8293	3	X	✓
17	GS-2010B-Q-046-04	21 ^h 52 ^m 17.29 ^s	-27°29'22.2"	0.8297	2	X	✓
19	GS-2010B-Q-046-04	21 ^h 52 ^m 20.19 ^s	-27°29'52.9"	0.8281	2	X	✓
20	GS-2010B-Q-046-04	21 ^h 52 ^m 20.14 ^s	-27°30'22.7"	0.8203	2	X	✓
21	GS-2010B-Q-046-04	21 ^h 52 ^m 16.77 ^s	-27°29'44.6"	0.5923	3	X	
22	GS-2010B-Q-046-04	21 ^h 52 ^m 21.69 ^s	-27°30'05.5"	0.8308	2	X	✓
26	GS-2010B-Q-046-04	21 ^h 52 ^m 24.86 ^s	-27°30'59.8"	0.8076	3	X	
27	GS-2010B-Q-046-04	21 ^h 52 ^m 25.06 ^s	-27°31'42.7"	0.4450	3	X	
31	GS-2010B-Q-046-04	21 ^h 52 ^m 23.85 ^s	-27°31'20.3"	0.8287	2	X	✓
32	GS-2010B-Q-046-04	21 ^h 52 ^m 24.29 ^s	-27°32'05.7"	0.8240	3	X	
36	GS-2010B-Q-046-04	21 ^h 52 ^m 22.99 ^s	-27°32'50.7"	0.7358	3	X	
2	GS-2011B-Q-050-06	21 ^h 52 ^m 14.59 ^s	-27°28'22.5"	0.7984	2	X	
6	GS-2011B-Q-050-06	21 ^h 52 ^m 20.57 ^s	-27°29'08.9"	0.5914	3	X	
8	GS-2011B-Q-050-06	21 ^h 52 ^m 16.51 ^s	-27°28'45.2"	0.6038	3	X	
9	GS-2011B-Q-050-06	21 ^h 52 ^m 19.78 ^s	-27°28'45.5"	0.4569	3	X	
11	GS-2011B-Q-050-06	21 ^h 52 ^m 17.31 ^s	-27°29'43.8"	0.4667	2	X	
14	GS-2011B-Q-050-06	21 ^h 52 ^m 19.90 ^s	-27°29'23.0"	0.8057	2	X	
15	GS-2011B-Q-050-06	21 ^h 52 ^m 24.86 ^s	-27°30'54.4"	0.6334	3	X	
17	GS-2011B-Q-050-06	21 ^h 52 ^m 22.36 ^s	-27°29'59.0"	0.8292	3	X	✓
18	GS-2011B-Q-050-06	21 ^h 52 ^m 20.58 ^s	-27°30'26.0"	0.8264	3	X	✓
19	GS-2011B-Q-050-06	21 ^h 52 ^m 18.98 ^s	-27°30'50.1"	0.8271	2	X	✓
25	GS-2011B-Q-050-06	21 ^h 52 ^m 19.95 ^s	-27°31'28.2"	0.8251	3	X	✓
26	GS-2011B-Q-050-06	21 ^h 52 ^m 20.67 ^s	-27°30'18.8"	0.8240	3	X	✓
34	GS-2011B-Q-050-06	21 ^h 52 ^m 23.51 ^s	-27°32'34.8"	0.8111	2	X	
12	GS-2011B-Q-050-07	21 ^h 52 ^m 18.37 ^s	-27°30'18.4"	0.5314	3	X	

Continued on next page

Table A.33 – continued from previous page

ID	Mask	RA (J2000)	Dec (J2000)	z	Quality	Identification	Member
13	GS-2011B-Q-050-07	21 ^h 52 ^m 21.22 ^s	-27°30'21.3''	0.8305	3	X	✓
14	GS-2011B-Q-050-07	21 ^h 52 ^m 20.05 ^s	-27°30'34.2''	0.8313	3	X	✓
15	GS-2011B-Q-050-07	21 ^h 52 ^m 20.78 ^s	-27°29'43.1''	0.4419	3	X	
16	GS-2011B-Q-050-07	21 ^h 52 ^m 15.57 ^s	-27°29'12.9''	0.7362	3	X	
20	GS-2011B-Q-050-07	21 ^h 52 ^m 21.11 ^s	-27°30'37.5''	0.8383	3	X	
26	GS-2011B-Q-050-07	21 ^h 52 ^m 26.17 ^s	-27°31'26.5''	0.4950	2	X	

Table A.33: XMMXCSJ215221.0-273022.6: All columns are as explained in Table A.23.

ID	Mask	RA (J2000)	Dec (J2000)	z	Quality	Identification	Member
1	GN-2012A-Q-070-10	23 ^h 02 ^m 39.79 ^s	08°42'48.1''	0.7148	3	X	✓
2	GN-2012A-Q-070-10	23 ^h 02 ^m 38.96 ^s	08°42'33.7''	0.7141	3	X	✓
4	GN-2012A-Q-070-10	23 ^h 02 ^m 39.70 ^s	08°42'25.3''	0.7169	3	X	✓
9	GN-2012A-Q-070-10	23 ^h 02 ^m 42.62 ^s	08°43'57.4''	0.7235	2	X	✓
11	GN-2012A-Q-070-10	23 ^h 02 ^m 43.85 ^s	08°43'55.2''	0.7291	3	X	✓
12	GN-2012A-Q-070-10	23 ^h 02 ^m 42.24 ^s	08°42'57.6''	0.7231	3	X	✓
14	GN-2012A-Q-070-10	23 ^h 02 ^m 43.02 ^s	08°42'48.4''	0.6239	3	X	
16	GN-2012A-Q-070-10	23 ^h 02 ^m 47.41 ^s	08°44'10.3''	0.7152	3	X	✓
17	GN-2012A-Q-070-10	23 ^h 02 ^m 48.36 ^s	08°43'54.2''	0.7192	3	X	✓
18	GN-2012A-Q-070-10	23 ^h 02 ^m 49.81 ^s	08°43'45.2''	0.7181	3	X	✓
19	GN-2012A-Q-070-10	23 ^h 02 ^m 47.90 ^s	08°43'23.0''	0.7107	3	X	✓
20	GN-2012A-Q-070-10	23 ^h 02 ^m 47.40 ^s	08°43'13.9''	0.8648	3	X	
22	GN-2012A-Q-070-10	23 ^h 02 ^m 51.32 ^s	08°45'14.6''	0.6157	3	X	
23	GN-2012A-Q-070-10	23 ^h 02 ^m 52.81 ^s	08°45'17.2''	0.4820	3	X	
25	GN-2012A-Q-070-10	23 ^h 02 ^m 53.25 ^s	08°44'37.2''	0.7244	3	X	✓
27	GN-2012A-Q-070-10	23 ^h 02 ^m 52.60 ^s	08°44'00.3''	0.7261	3	X	✓
28	GN-2012A-Q-070-10	23 ^h 02 ^m 51.71 ^s	08°43'52.4''	0.7104	3	X	✓
29	GN-2012A-Q-070-10	23 ^h 02 ^m 51.41 ^s	08°43'38.7''	0.7166	3	X	✓
31	GN-2012A-Q-070-10	23 ^h 02 ^m 54.65 ^s	08°46'40.9''	0.7212	3	X	✓
33	GN-2012A-Q-070-10	23 ^h 02 ^m 56.04 ^s	08°45'03.7''	0.4818	3	X	
34	GN-2012A-Q-070-10	23 ^h 02 ^m 55.68 ^s	08°44'52.0''	0.7171	2	X	✓
11	GN-2012A-Q-070-11	23 ^h 02 ^m 41.64 ^s	08°43'44.2''	0.7157	3	X	✓
13	GN-2012A-Q-070-11	23 ^h 02 ^m 47.90 ^s	08°44'45.5''	0.7377	3	X	
14	GN-2012A-Q-070-11	23 ^h 02 ^m 45.49 ^s	08°44'30.1''	0.7209	3	X	✓
18	GN-2012A-Q-070-11	23 ^h 02 ^m 45.16 ^s	08°43'12.6''	0.7113	3	X	✓
19	GN-2012A-Q-070-11	23 ^h 02 ^m 47.95 ^s	08°43'58.1''	0.7283	3	X	✓
20	GN-2012A-Q-070-11	23 ^h 02 ^m 46.70 ^s	08°44'00.6''	0.7253	3	X	✓
21	GN-2012A-Q-070-11	23 ^h 02 ^m 48.54 ^s	08°43'60.0''	0.7253	3	X	✓
32	GN-2012A-Q-070-11	23 ^h 02 ^m 55.72 ^s	08°45'01.7''	0.4828	3	X	

Continued on next page

Table A.34 – continued from previous page

ID	Mask	RA (J2000)	Dec (J2000)	z	Quality	Identification	Member
33	GN-2012A-Q-070-11	23 ^h 03 ^m 00.05 ^s	08°43'00.9''	0.8772	2	X	

Table A.34: XMMXCSJ230247.7+084355.9: All columns are as explained in Table A.23.

APPENDIX B

VELOCITY HISTOGRAMS

In this appendix, we provide a visual view of Appendix A. We present velocity histograms for both samples, showing the possible and final chosen members. We also show 3D plots showing the position and redshift of the final members.

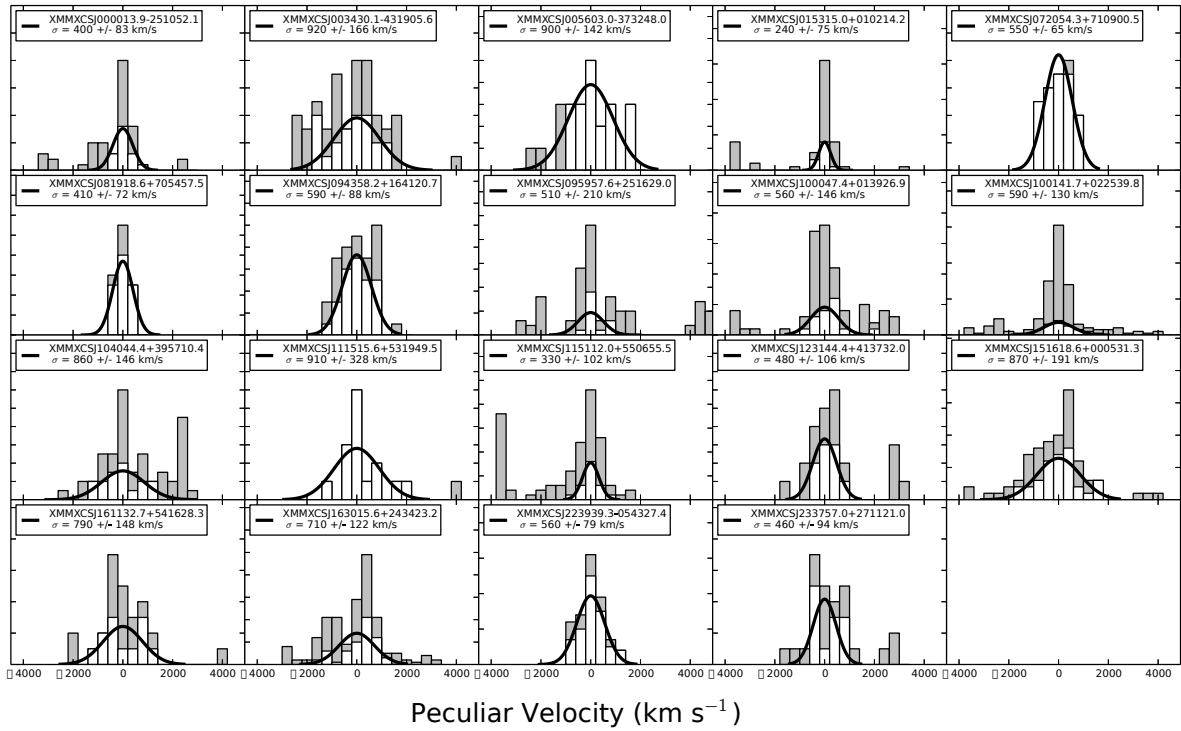


Figure B.1: We depict a synthetic view of the tables found in Appendix A in the form of histograms for the low redshift sample. The solid grey blocks depict all the galaxies considered as possible members while the white blocks are the final chosen members. The solid black line shows the velocity dispersion calculated using the method described in the paper.

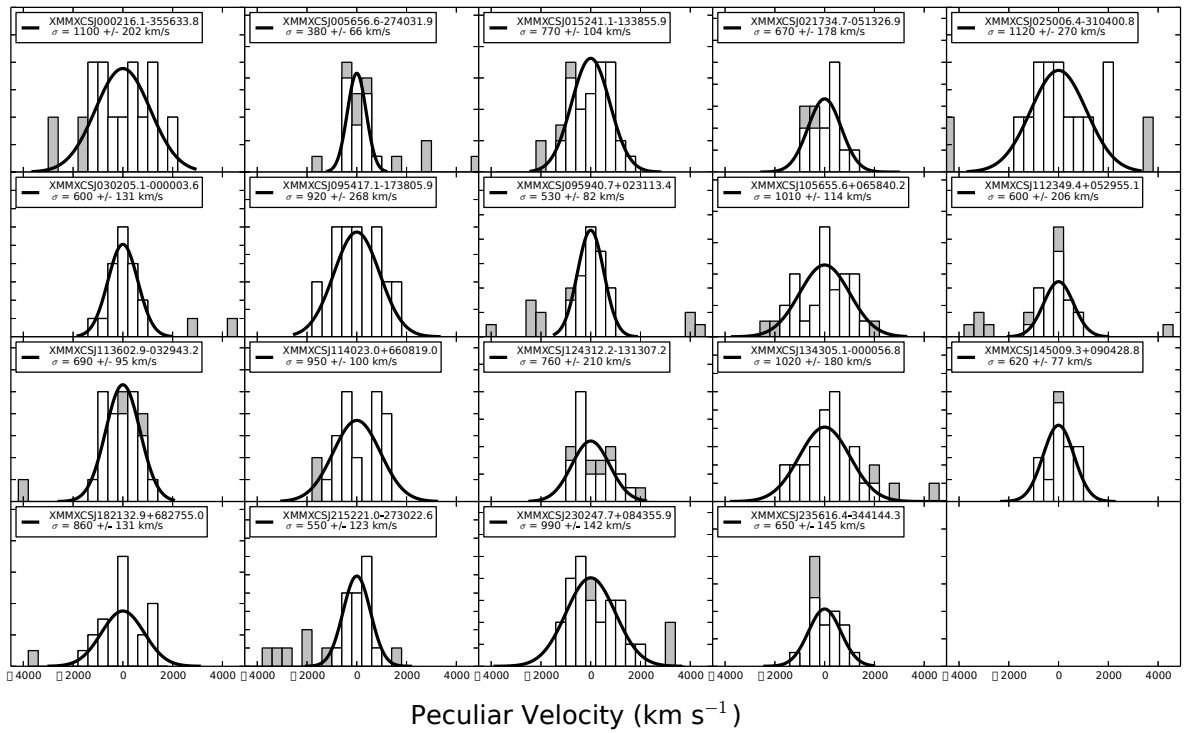


Figure B.2: We depict a synthetic view of the tables found in Appendix A in the form of histograms for the high redshift sample. All blocks and lines are as in Figure B.1.

BIBLIOGRAPHY

- Abazajian, K., Adelman-McCarthy, J. K., Agüeros, M. A., et al. (2004). The Second Data Release of the Sloan Digital Sky Survey. *AJ*, 128:502–512.
- Abazajian, K., Adelman-McCarthy, J. K., Agüeros, M. A., et al. (2005). The Third Data Release of the Sloan Digital Sky Survey. *AJ*, 129:1755–1759.
- Abazajian, K., Adelman-McCarthy, J. K., Agüeros, M. A., et al. (2003). The First Data Release of the Sloan Digital Sky Survey. *AJ*, 126:2081–2086.
- Abazajian, K. N., Adelman-McCarthy, J. K., Agüeros, M. A., et al. (2009). The Seventh Data Release of the Sloan Digital Sky Survey. *Astrophys. J. Supp.*, 182:543–558.
- Abell, G. O. (1958). The Distribution of Rich Clusters of Galaxies. *Astrophys. J. Supp.*, 3:211.
- Abell, G. O. (1975). *Clusters of Galaxies*, page 601. the University of Chicago Press.
- Adami, C., Mazure, A., Pierre, M., et al. (2011). The XMM-LSS survey: optical assessment and properties of different X-ray selected cluster classes. *Astron. Astrophys.*, 526:A18.
- Adelman-McCarthy, J. K., Agüeros, M. A., Allam, S. S., et al. (2008). The Sixth Data Release of the Sloan Digital Sky Survey. *ApJS*, 175:297–313.

- Adelman-McCarthy, J. K., Agüeros, M. A., Allam, S. S., et al. (2007). The Fifth Data Release of the Sloan Digital Sky Survey. *ApJS*, 172:634–644.
- Adelman-McCarthy, J. K., Agüeros, M. A., Allam, S. S., et al. (2006). The Fourth Data Release of the Sloan Digital Sky Survey. *ApJS*, 162:38–48.
- Akamatsu, H., de Plaa, J., Kaastra, J., Ishisaki, Y., Ohashi, T., Kawaharada, M., and Nakazawa, K. (2012a). Properties of the Intracluster Medium of Abell 3667 Observed with Suzaku XIS. *Pub. Astron. Soc. Japan*, 64:49.
- Akamatsu, H. and Kawahara, H. (2013). Systematic X-Ray Analysis of Radio Relic Clusters with Suzaku. *Pub. Astron. Soc. Japan*, 65:16.
- Akamatsu, H., Takizawa, M., Nakazawa, K., Fukazawa, Y., Ishisaki, Y., and Ohashi, T. (2012b). X-Ray View of the Shock Front in the Merging Cluster Abell 3376 with Suzaku. *Pub. Astron. Soc. Japan*, 64:67.
- Alam, S., Albareti, F. D., Allende Prieto, C., et al. (2015). The Eleventh and Twelfth Data Releases of the Sloan Digital Sky Survey: Final Data from SDSS-III. *Astrophys. J. Supp.*, 219:12.
- Allen, S. W. (2000). The properties of cooling flows in X-ray luminous clusters of galaxies. *Mon. Not. R. Astron. Soc.*, 315:269–295.
- Allen, S. W., Ettori, S., and Fabian, A. C. (2001). Chandra measurements of the distribution of mass in the luminous lensing cluster Abell 2390. *Mon. Not. R. Astron. Soc.*, 324:877–890.
- Allen, S. W., Evrard, A. E., and Mantz, A. B. (2011). Cosmological Parameters from Observations of Galaxy Clusters. *Annu. Rev. Astron. Astrophys.*, 49:409–470.
- Allen, S. W. and Fabian, A. C. (1998). The impact of cooling flows on the T_{X-L_Bol} relation for the most luminous clusters. *Mon. Not. R. Astron. Soc.*, 297:L57–L62.

- Allen, S. W., Rapetti, D. A., Schmidt, R. W., Ebeling, H., Morris, R. G., and Fabian, A. C. (2008). Improved constraints on dark energy from Chandra X-ray observations of the largest relaxed galaxy clusters. *Mon. Not. R. Astron. Soc.*, 383:879–896.
- Allen, S. W., Schmidt, R. W., and Fabian, A. C. (2002). Chandra observations of RX J1347.5-1145: the distribution of mass in the most X-ray-luminous galaxy cluster known. *Mon. Not. R. Astron. Soc.*, 335:256–266.
- Alpher, R. A., Bethe, H., and Gamow, G. (1948). The Origin of Chemical Elements. *Physical Review*, 73:803–804.
- Alpher, R. A. and Herman, R. C. (1948). On the Relative Abundance of the Elements. *Physical Review*, 74:1737–1742.
- Amodeo, S., Mei, S., Stanford, S. A., et al. (2017). Calibrating the Planck Cluster Mass Scale with Cluster Velocity Dispersions. *ArXiv e-prints*.
- Anderson, R. (2015). *The Cosmic Compendium: The Big Bang & the Early Universe*. LULU Press.
- Arnaud, M., Hughes, J. P., Forman, W., Jones, C., Lachieze-Rey, M., Yamashita, K., and Hatsuakade, I. (1992). A2163 - an exceptionally hot cluster of galaxies. *Astrophys. J.*, 390:345–349.
- Arnaud, M., Pointecouteau, E., and Pratt, G. W. (2005). The structural and scaling properties of nearby galaxy clusters. II. The M-T relation. *Astron. Astrophys.*, 441:893–903.
- Baade, W. (1956). The Period-Luminosity Relation of the Cepheids. *Pub. Astron. Soc. Pacific*, 68:5.
- Bacchi, M., Feretti, L., Giovannini, G., and Govoni, F. (2003). Deep images of cluster radio halos. *Astron. Astrophys.*, 400:465–476.
- Bagchi, J., Durret, F., Neto, G. B. L., and Paul, S. (2006). Giant Ringlike Radio Structures Around Galaxy Cluster Abell 3376. *Science*, 314:791–794.

- Bagchi, J., Sirothia, S. K., Werner, N., et al. (2011). Discovery of the First Giant Double Radio Relic in a Galaxy Cluster Found in the Planck Sunyaev-Zel'dovich Cluster Survey: PLCK G287.0+32.9. *Astrophys. J. Lett.*, 736:L8.
- Baker, J., Barr, J., and Bremer, M. (2005). Radio Sources as Probes of Distant Clusters. *Highlights of Astronomy*, 13:302.
- Baldry, I. K., Glazebrook, K., Brinkmann, J., Ivezić, Ž., Lupton, R. H., Nichol, R. C., and Szalay, A. S. (2004). Quantifying the Bimodal Color-Magnitude Distribution of Galaxies. *Astrophys. J.*, 600:681–694.
- Ballarati, B., Feretti, L., Ficarra, A., Giovannini, G., Nanni, M., Olori, M. C., and Gavazzi, G. (1981). 408 MHz observations of clusters of galaxies. I - Halo sources in the Coma-A 1367 supercluster. *Astron. Astrophys.*, 100:323–325.
- Balogh, M., Bower, R. G., Smail, I., Ziegler, B. L., Davies, R. L., Gaztelu, A., and Fritz, A. (2002). Galaxy properties in low X-ray luminosity clusters at $z=0.25$. *Mon. Not. R. Astron. Soc.*, 337:256–274.
- Balogh, M. L., Babul, A., Voit, G. M., McCarthy, I. G., Jones, L. R., Lewis, G. F., and Ebeling, H. (2006). An analytic investigation of the scatter in the integrated X-ray properties of galaxy groups and clusters. *Mon. Not. R. Astron. Soc.*, 366:624–634.
- Barrena, R., Boschin, W., Girardi, M., and Spolaor, M. (2007). Internal dynamics of the radio halo cluster Abell 773: a multiwavelength analysis. *Astron. Astrophys.*, 467:37–48.
- Bartelmann, M. and Schneider, P. (2001). Weak gravitational lensing. *Phys. Rep.*, 340:291–472.
- Basilakos, S., Plionis, M., Georgakakis, A., Georgantopoulos, I., Gaga, T., Kolokotronis, V., and Stewart, G. C. (2004). The XMM-Newton/2dF survey - III. Comparison between optical and X-ray cluster detection methods. *Mon. Not. R. Astron. Soc.*, 351:989–996.
- Basu, K. (2012). A Sunyaev-Zel'dovich take on cluster radio haloes - I. Global scaling and bi-modality using Planck data. *Mon. Not. R. Astron. Soc.*, 421:L112–L116.

- Bautz, L. P. and Morgan, W. W. (1970). On the Classification of the Forms of Clusters of Galaxies. *Astrophys. J. Lett.*, 162:L149.
- Bayliss, M. B., Hennawi, J. F., Gladders, M. D., Koester, B. P., Sharon, K., Dahle, H., and Oguri, M. (2011). Gemini/GMOS Spectroscopy of 26 Strong-lensing-selected Galaxy Cluster Cores. *ApJS*, 193:8.
- Beers, T. C., Flynn, K., and Gebhardt, K. (1990). Measures of location and scale for velocities in clusters of galaxies - A robust approach. *Astron. J.*, 100:32–46.
- Begeman, K. G. (1987). *HI rotation curves of spiral galaxies*. PhD thesis, , Kapteyn Institute, (1987).
- Bellagamba, F., Maturi, M., Hamana, T., Meneghetti, M., Miyazaki, S., and Moscardini, L. (2011). Optimal filtering of optical and weak lensing data to search for galaxy clusters: application to the COSMOS field. *Mon. Not. R. Astron. Soc.*, 413:1145–1157.
- Benjamin, J., Heymans, C., Semboloni, E., et al. (2007). Cosmological constraints from the 100-deg² weak-lensing survey. *Mon. Not. R. Astron. Soc.*, 381:702–712.
- Bennett, A. S. (1962). The revised 3C catalogue of radio sources. *Mem. R. Astron. Soc.*, 68:163.
- Bennett, C. L., Halpern, M., Hinshaw, G., et al. (2003). First-year wilkinson microwave anisotropy probe (wmap) observations: Preliminary maps and basic results. *The Astrophysical Journal Supplement Series*, 148(1):1.
- Berlind, A. A., Frieman, J., Weinberg, D. H., et al. (2006). Percolation Galaxy Groups and Clusters in the SDSS Redshift Survey: Identification, Catalogs, and the Multiplicity Function. *ApJS*, 167:1–25.
- Bernardi, M., Sheth, R. K., Nichol, R. C., Schneider, D. P., and Brinkmann, J. (2005). Colors, Magnitudes, and Velocity Dispersions in Early-Type Galaxies: Implications for Galaxy Ages and Metallicities. *Astron. J.*, 129:61–72.

- Bertschinger, E. (1998). Simulations of Structure Formation in the Universe. *Annu. Rev. Astron. Astrophys.*, 36:599–654.
- Bird, C. M., Mushotzky, R. F., and Metzler, C. A. (1995). The Velocity Dispersion–Temperature Correlation from a Limited Cluster Sample. *Astrophys. J.*, 453:40.
- Birkinshaw, M. (1999). The Sunyaev-Zel’dovich effect. *Phys. Rep.*, 310:97–195.
- Birkinshaw, M., Gull, S. F., and Northover, K. J. E. (1978a). Extent of hot intergalactic gas in the cluster Abell 2218. *Nature.*, 275:40.
- Birkinshaw, M., Gull, S. F., and Northover, K. J. E. (1978b). Measurements of the gas contents of clusters of galaxies by observations of the background radiation at 10.6 GHz. *Mon. Not. R. Astron. Soc.*, 185:245–262.
- Birkinshaw, M., Hughes, J. P., and Arnaud, K. A. (1991). A measurement of the value of the Hubble constant from the X-ray properties and the Sunyaev-Zel’dovich effect of Abell 665. *Astrophys. J.*, 379:466–481.
- Biviano, A. (2000). From Messier to Abell: 200 Years of Science with Galaxy Clusters. In *Constructing the Universe with Clusters of Galaxies*.
- Blanton, E. L. (2000). *Bent-double radio sources as tracers of clusters of galaxies*. PhD thesis, COLUMBIA UNIVERSITY.
- Blanton, E. L., Gregg, M. D., Helfand, D. J., Becker, R. H., and White, R. L. (2003). Discovery of a High-Redshift ($z=0.96$) Cluster of Galaxies Using a FIRST Survey Wide-Angle-Tailed Radio Source. *Astron. J.*, 125:1635–1641.
- Blasi, P. and Colafrancesco, S. (1999). Cosmic rays, radio halos and nonthermal X-ray emission in clusters of galaxies. *Astroparticle Physics*, 12:169–183.
- Bleem, L. E., Stalder, B., de Haan, T., et al. (2015). Galaxy Clusters Discovered via the Sunyaev-Zel’dovich Effect in the 2500-Square-Degree SPT-SZ Survey. *Astrophys. J. Supp.*, 216:27.

- Bliton, M., Rizza, E., Burns, J. O., Owen, F. N., and Ledlow, M. J. (1998). Cluster-subcluster mergers and the formation of narrow-angle tailed radio sources. *Mon. Not. R. Astron. Soc.*, 301:609–625.
- Boehringer, H., Voges, W., Fabian, A. C., Edge, A. C., and Neumann, D. M. (1993). A ROSAT HRI study of the interaction of the X-ray-emitting gas and radio lobes of NGC 1275. *Mon. Not. R. Astron. Soc.*, 264:L25–L28.
- Böhringer, H., Guzzo, L., Collins, C. A., et al. (1998). Probing the cosmic large-scale structure with the REFLEX Cluster Survey: profile of an ESO key programme. *The Messenger*, 94:21–25.
- Böhringer, H., Pratt, G. W., Arnaud, M., et al. (2010). Substructure of the galaxy clusters in the REXCESS sample: observed statistics and comparison to numerical simulations. *Astron. Astrophys.*, 514:A32.
- Böhringer, H., Schuecker, P., Guzzo, L., et al. (2004). The ROSAT-ESO Flux Limited X-ray (REFLEX) Galaxy cluster survey. V. The cluster catalogue. *Astron. Astrophys.*, 425:367–383.
- Böhringer, H., Voges, W., Huchra, J. P., et al. (2000). The Northern ROSAT All-Sky (NORAS) Galaxy Cluster Survey. I. X-Ray Properties of Clusters Detected as Extended X-Ray Sources. *Astrophys. J. Supp.*, 129:435–474.
- Boldt, E., McDonald, F. B., Riegler, G., and Serlemitsos, P. (1966). Extended Source of Energetic Cosmic X Rays. *Physical Review Letters*, 17:447–450.
- Bonafede, A., Giovannini, G., Feretti, L., Govoni, F., and Murgia, M. (2009). Double relics in Abell 2345 and Abell 1240. Spectral index and polarization analysis. *Astron. Astrophys.*, 494:429–442.
- Bonafede, A., Intema, H. T., Brügggen, M., et al. (2014). A giant radio halo in the cool core cluster CL1821+643. *Mon. Not. R. Astron. Soc.*, 444:L44–L48.

- Bonamente, M., Joy, M., LaRoque, S. J., Carlstrom, J. E., Nagai, D., and Marrone, D. P. (2008). Scaling Relations from Sunyaev-Zel'dovich Effect and Chandra X-Ray Measurements of High-Redshift Galaxy Clusters. *Astrophys. J.*, 675:106–114.
- Borgani, S. and Kravtsov, A. (2011). Cosmological Simulations of Galaxy Clusters. *Advanced Science Letters*, 4:204–227.
- Boschin, W., Girardi, M., Barrena, R., Biviano, A., Feretti, L., and Ramella, M. (2004). Internal dynamics of the radio-halo cluster A2219: A multi-wavelength analysis. *Astron. Astrophys.*, 416:839–851.
- Bosma, A. (1978). *The distribution and kinematics of neutral hydrogen in spiral galaxies of various morphological types*. PhD thesis, PhD Thesis, Groningen Univ., (1978).
- Bosma, A. (1981a). 21-cm line studies of spiral galaxies. I - Observations of the galaxies NGC 5033, 3198, 5055, 2841, and 7331. II - The distribution and kinematics of neutral hydrogen in spiral galaxies of various morphological types. *Astron. J.*, 86:1791–1846.
- Bosma, A. (1981b). 21-cm line studies of spiral galaxies. II. The distribution and kinematics of neutral hydrogen in spiral galaxies of various morphological types. *Astron. J.*, 86:1825–1846.
- Bower, R. G. (1997). The Entropy-Driven X-ray Evolution of Galaxy Clusters. *Mon. Not. R. Astron. Soc.*, 288:355–364.
- Bower, R. G., Lucey, J. R., and Ellis, R. S. (1992). Precision photometry of early-type galaxies in the Coma and Virgo clusters: A test of the universality of the colour-magnitude relation. I - The data. II. Analysis. *Mon. Not. R. Astron. Soc.*, 254:589–613.
- Bower, R. G., McCarthy, I. G., and Benson, A. J. (2008). The flip side of galaxy formation: a combined model of galaxy formation and cluster heating. *MNRAS*, 390:1399–1410.
- Bradford, J. D., Geha, M., Muñoz, R. R., et al. (2011). Structure and Dynamics of the Globular Cluster Palomar 13. *Astrophys. J.*, 743:167.

- Branchesi, M., Gioia, I. M., Fanti, C., and Fanti, R. (2007). High redshift X-ray galaxy clusters. II. The L_X -T relationship revisited. *Astron. Astrophys.*, 472:739–748.
- Bremer, M. N., Fabian, A. C., and Crawford, C. S. (1997). The onset of a powerful radio source in a central cluster galaxy. *Mon. Not. R. Astron. Soc.*, 284:213–224.
- Bridges, T., Gebhardt, K., Sharples, R., et al. (2006). The globular cluster kinematics and galaxy dark matter content of NGC 4649 (M60). *Mon. Not. R. Astron. Soc.*, 373:157–166.
- Bridle, A. H. (1969). Spectra of Extended Extragalactic Radio Sources. *Nature.*, 224:889–890.
- Brook, C. B. and Shankar, F. (2016). A matter of measurement: rotation velocities and the velocity function of dwarf galaxies. *Mon. Not. R. Astron. Soc.*, 455:3841–3847.
- Brown, S., Duisterhoeft, J., and Rudnick, L. (2011). Multiple Shock Structures in a Radio-selected Cluster of Galaxies. *Astrophys. J. Lett.*, 727:L25.
- Brunetti, G., Cassano, R., Dolag, K., and Setti, G. (2009). On the evolution of giant radio halos and their connection with cluster mergers. *Astron. Astrophys.*, 507:661–669.
- Brunetti, G., Giacintucci, S., Cassano, R., et al. (2008). A low-frequency radio halo associated with a cluster of galaxies. *Nature.*, 455:944–947.
- Brunetti, G. and Lazarian, A. (2011). Particle reacceleration by compressible turbulence in galaxy clusters: effects of a reduced mean free path. *Mon. Not. R. Astron. Soc.*, 412:817–824.
- Brunetti, G., Setti, G., Feretti, L., and Giovannini, G. (2001). Particle reacceleration in the Coma cluster: radio properties and hard X-ray emission. *Mon. Not. R. Astron. Soc.*, 320:365–378.
- Brunetti, G., Venturi, T., Dallacasa, D., Cassano, R., Dolag, K., Giacintucci, S., and Setti, G. (2007). Cosmic Rays and Radio Halos in Galaxy Clusters: New Constraints from Radio Observations. *Astrophys. J. Lett.*, 670:L5–L8.

- Brusa, M., Civano, F., Comastri, A., et al. (2010). The XMM-Newton Wide-field Survey in the Cosmos Field (XMM-COSMOS): Demography and Multiwavelength Properties of Obscured and Unobscured Luminous Active Galactic Nuclei. *ApJ*, 716:348–369.
- Bryan, G. L. and Norman, M. L. (1998). Statistical Properties of X-Ray Clusters: Analytic and Numerical Comparisons. *Astrophys. J.*, 495:80–99.
- Buote, D. A. (2001). On the Origin of Radio Halos in Galaxy Clusters. *Astrophys. J. Lett.*, 553:L15–L18.
- Buote, D. A. and Tsai, J. C. (1995). Quantifying the Morphologies and Dynamical Evolution of Galaxy Clusters. I. The Method. *Astrophys. J.*, 452:522.
- Buote, D. A. and Tsai, J. C. (1996). Quantifying the Morphologies and Dynamical Evolution of Galaxy Clusters. II. Application to a Sample of ROSAT Clusters. *Astrophys. J.*, 458:27.
- Burbidge, E. M., Burbidge, G. R., Fowler, W. A., and Hoyle, F. (1957). Synthesis of the Elements in Stars. *Reviews of Modern Physics*, 29:547–650.
- Burenin, R. A., Vikhlinin, A., Hornstrup, A., Ebeling, H., Quintana, H., and Mescheryakov, A. (2007). The 400 Square Degree ROSAT PSPC Galaxy Cluster Survey: Catalog and Statistical Calibration. *Astrophys. J. Supp.*, 172:561–582.
- Burnham, K. P. and Anderson, D. R. (2002). *Model Selection and Multimodel Inference: A Practical Information-Theoretic Approach*. Springer-Verlag, New York, 2 edition.
- Burns, J. O., Rhee, G., Roettiger, K., and Owen, F. N. (1993). Radio Galaxies, X-Ray Sub-clumps, and Mergers within Clusters of Galaxies. In Chincarini, G. L., Iovino, A., Maccacaro, T., and Maccagni, D., editors, *Observational Cosmology*, volume 51 of *Astronomical Society of the Pacific Conference Series*, page 407.
- Burns, J. O., Roettiger, K., Loken, C., Norman, M., and Bryan, G. (2000). Numerical Hydro/N-body Simulations of Galaxy Cluster Mergers and the Formation of Radio Halos. In *IAU Joint Discussion*, volume 10 of *IAU Joint Discussion*.

- Burns, J. O., Skillman, S. W., and O'Shea, B. W. (2010). Galaxy Clusters at the Edge: Temperature, Entropy, and Gas Dynamics Near the Virial Radius. *Astrophys. J.*, 721:1105–1112.
- Canning, R. E. A., Allen, S. W., Applegate, D. E., et al. (2015). A series of shocks and edges in Abell 2219. *ArXiv e-prints*.
- Cappi, A., Held, E. V., and Marano, B. (1998). Galaxy redshifts in 3 medium-distant clusters. *A&AS*, 129:31–40.
- Carlstrom, J. E., Holder, G. P., and Reese, E. D. (2002). Cosmology with the Sunyaev-Zel'dovich Effect. *Annu. Rev. Astron. Astrophys.*, 40:643–680.
- Carlstrom, J. E., Joy, M., and Grego, L. (1996). Interferometric Imaging of the Sunyaev-Zeldovich Effect at 30 GHz. *Astrophys. J. Lett.*, 456:L75.
- Carlstrom, J. E., Joy, M. K., Grego, L., Holder, G. P., Holzzapfel, W. L., Mohr, J. J., Patel, S., and Reese, E. D. (2000). Imaging the Sunyaev-Zel'dovich Effect. *Physica Scripta Volume T*, 85:148.
- Cash, W. (1979). Parameter estimation in astronomy through application of the likelihood ratio. *ApJ*, 228:939–947.
- Cassano, R. and Brunetti, G. (2005). Cluster mergers and non-thermal phenomena: a statistical magneto-turbulent model. *Mon. Not. R. Astron. Soc.*, 357:1313–1329.
- Cassano, R., Brunetti, G., and Setti, G. (2006). Statistics of giant radio haloes from electron reacceleration models. *Mon. Not. R. Astron. Soc.*, 369:1577–1595.
- Cassano, R., Brunetti, G., Setti, G., Govoni, F., and Dolag, K. (2007). New scaling relations in cluster radio haloes and the re-acceleration model. *Mon. Not. R. Astron. Soc.*, 378:1565–1574.
- Cassano, R., Brunetti, G., and Venturi, T. (2011). The Connection between Radio Halos and Cluster Mergers and the Statistical Properties of the Radio Halo Population. *Journal of Astrophysics and Astronomy*, 32:519–527.

- Cassano, R., Ettori, S., Brunetti, G., et al. (2013). Revisiting Scaling Relations for Giant Radio Halos in Galaxy Clusters. *Astrophys. J.*, 777:141.
- Cassano, R., Ettori, S., Giacintucci, S., Brunetti, G., Markevitch, M., Venturi, T., and Gitti, M. (2010). On the Connection Between Giant Radio Halos and Cluster Mergers. *Astrophys. J. Lett.*, 721:L82–L85.
- Castillo-Morales, A. and Schindler, S. (2003). Distribution of dark and baryonic matter in clusters of galaxies. *Astron. Astrophys.*, 403:433–442.
- Cavagnolo, K. W., Donahue, M., Voit, G. M., and Sun, M. (2008). Bandpass Dependence of X-Ray Temperatures in Galaxy Clusters. *Astrophys. J.*, 682:821–834.
- Chandler, C. (2016). The vla calibration pipeline. Slides of a talk given at a data reduction workshop in March 2016.
- Clerc, N., Adami, C., Lieu, M., et al. (2014). The XMM-LSS survey: the Class 1 cluster sample over the extended 11 deg² and its spatial distribution. *Mon. Not. R. Astron. Soc.*, 444:2723–2753.
- Clerc, N., Sadibekova, T., Pierre, M., Pacaud, F., Le Fèvre, J.-P., Adami, C., Altieri, B., and Valtchanov, I. (2012). The cosmological analysis of X-ray cluster surveys - II. Application of the CR-HR method to the XMM archive. *MNRAS*, 423:3561–3583.
- Clowe, D., Gonzalez, A., and Markevitch, M. (2004). Weak-Lensing Mass Reconstruction of the Interacting Cluster 1E 0657-558: Direct Evidence for the Existence of Dark Matter. *Astrophys. J.*, 604:596–603.
- Cohn, J. D. and White, M. (2005). The formation histories of galaxy clusters. *Astroparticle Physics*, 24:316–333.
- Colafrancesco, S. (1999). Cosmic Rays and Non-Thermal Emission in Galaxy Clusters. In Boehringer, H., Feretti, L., and Schuecker, P., editors, *Diffuse Thermal and Relativistic Plasma in Galaxy Clusters*, page 269.

- Colafrancesco, S. and Mele, B. (2001). Neutralinos and the Origin of Radio Halos in Clusters of Galaxies. *Astrophys. J.*, 562:24–41.
- Colless, M., Dalton, G., Maddox, S., et al. (2003a). VizieR Online Data Catalog: The 2dF Galaxy Redshift Survey 100k Data Release (2dFGRS Team, 2001). *VizieR Online Data Catalog*, 7226:0.
- Colless, M., Peterson, B. A., Jackson, C., et al. (2003b). The 2dF Galaxy Redshift Survey: Final Data Release. *ArXiv Astrophysics e-prints*.
- Collins, C. A., Stott, J. P., Hilton, M., et al. (2009). Early assembly of the most massive galaxies. *Nature*, 458:603–606.
- Condon, J. J., Cotton, W. D., Greisen, E. W., Yin, Q. F., Perley, R. A., Taylor, G. B., and Broderick, J. J. (1998). The NRAO VLA Sky Survey. *Astron. J.*, 115:1693–1716.
- Cornwell, T. J. and Wilkinson, P. N. (1981). A new method for making maps with unstable radio interferometers. *Mon. Not. R. Astron. Soc.*, 196:1067–1086.
- Costain, C. H. and Smith, F. G. (1960). The radio telescope for 7.9 meteres wavelength at the Mullard Observatory. *Mon. Not. R. Astron. Soc.*, 121:405.
- Covone, G., Kneib, J.-P., Soucail, G., Richard, J., Jullo, E., and Ebeling, H. (2006). VIMOS-IFU survey of $z \sim 0.2$ massive galaxy clusters. I. Observations of the strong lensing cluster Abell 2667. *Astron. Astrophys.*, 456:409–420.
- Coziol, R., Andernach, H., Caretta, C. A., Alamo-Martínez, K. A., and Tago, E. (2009). The Dynamical State of Brightest Cluster Galaxies and The Formation of Clusters. *AJ*, 137:4795–4809.
- Crawford, S. M., Wirth, G. D., and Bershady, M. A. (2014). Spatial and Kinematic Distributions of Transition Populations in Intermediate Redshift Galaxy Clusters. *ApJ*, 786:30.

- Croston, J. H., Arnaud, M., Pratt, G. W., and Böhringer, H. (2006). Gas Distributions in an Unbiased Sample of Low- z Galaxy Clusters. In Wilson, A., editor, *The X-ray Universe 2005*, volume 604 of *ESA Special Publication*, page 737.
- Croston, J. H., Hardcastle, M. J., and Birkinshaw, M. (2005). Evidence for radio-source heating of groups. *Mon. Not. R. Astron. Soc.*, 357:279–294.
- Croston, J. H., Hardcastle, M. J., Birkinshaw, M., and Worrall, D. M. (2003). XMM-Newton observations of the hot-gas atmospheres of 3C 66B and 3C 449. *Mon. Not. R. Astron. Soc.*, 346:1041–1054.
- Cuciti, V., Cassano, R., Brunetti, G., Dallacasa, D., Kale, R., Etori, S., and Venturi, T. (2015). Occurrence of radio halos in galaxy clusters. Insight from a mass-selected sample. *Astron. Astrophys.*, 580:A97.
- Dalcanton, J. J. (1996). A Proposal for Finding Clusters of Galaxies at $Z \text{pt} > -11.5\text{pt} - 3\text{pt} 1$. *Astrophys. J.*, 466:92.
- Dallacasa, D., Brunetti, G., Giacintucci, S., et al. (2009). Deep 1.4 GHz Follow-up of the Steep Spectrum Radio Halo in A521. *Astrophys. J.*, 699:1288–1292.
- Dalton, G. B., Efstathiou, G., Maddox, S. J., and Sutherland, W. J. (1992). Spatial correlations in a redshift survey of APM galaxy clusters. *Astrophys. J. Lett.*, 390:L1–L4.
- Dasadia, S., Sun, M., Sarazin, C., et al. (2016). A Strong Merger Shock in Abell 665. *Astrophys. J. Lett.*, 820:L20.
- de Gasperin, F., Ogrean, G. A., van Weeren, R. J., Dawson, W. A., Brüggén, M., Bonafede, A., and Simionescu, A. (2015). Abell 1033: birth of a radio phoenix. *Mon. Not. R. Astron. Soc.*, 448:2197–2209.
- De Grandi, S., Böhringer, H., Guzzo, L., et al. (1999). A Flux-limited Sample of Bright Clusters of Galaxies from the Southern Part of the ROSAT All-Sky Survey: The Catalog and LOG N-LOG S. *Astrophys. J.*, 514:148–163.

- De Lucia, G. and Blaizot, J. (2007). The hierarchical formation of the brightest cluster galaxies. *MNRAS*, 375:2–14.
- De Propriis, R., Couch, W. J., Colless, M., et al. (2002). The 2dF Galaxy Redshift Survey: a targeted study of catalogued clusters of galaxies. *MNRAS*, 329:87–101.
- de Vaucouleurs, G. (1982a). Five crucial tests of the cosmic distance scale using the Galaxy as fundamental standard. *Nature.*, 299:303–307.
- de Vaucouleurs, G. (1982b). The extragalactic distance scale and the Hubble constant. *The Observatory*, 102:178–194.
- de Vaucouleurs, G. and Bollinger, G. (1979). The extragalactic distance scale. VII - The velocity-distance relations in different directions and the Hubble ratio within and without the local supercluster. *Astrophys. J.*, 233:433–452.
- Dennison, B. (1980). Formation of radio halos in clusters of galaxies from cosmic-ray protons. *Astrophys. J. Lett.*, 239:L93–L96.
- Dicke, R. H. (1946). The measurement of thermal radiation at microwave frequencies. *Review of Scientific Instruments*, 17(7).
- Dicke, R. H., Peebles, P. J. E., Roll, P. G., and Wilkinson, D. T. (1965). Cosmic Black-Body Radiation. *Astrophys. J.*, 142:414–419.
- Dickey, J. M. (1990). Measuring atomic hydrogen masses using the 21-cm line. In Thronson, Jr., H. A. and Shull, J. M., editors, *The Interstellar Medium in Galaxies*, volume 161 of *Astrophysics and Space Science Library*, pages 473–481.
- Dolag, K. and Enßlin, T. A. (2000). Radio halos of galaxy clusters from hadronic secondary electron injection in realistic magnetic field configurations. *Astron. Astrophys.*, 362:151–157.
- Donahue, M., Voit, G. M., Scharf, C. A., Gioia, I. M., Mullis, C. R., Hughes, J. P., and Stocke, J. T. (1999). The Second Most Distant Cluster of Galaxies in the Extended Medium Sensitivity Survey. *ApJ*, 527:525–534.

- Donnert, J., Dolag, K., Brunetti, G., and Cassano, R. (2013). Rise and fall of radio haloes in simulated merging galaxy clusters. *Mon. Not. R. Astron. Soc.*, 429:3564–3569.
- Doroshkevich, A. G. and Novikov, I. D. (1964). Mean Density of Radiation in the Metagalaxy and Certain Problems in Relativistic Cosmology. *Soviet Physics Doklady*, 9:111.
- Douglass, E., Blanton, E. L., Randall, S. W., Clarke, T. E., and Wing, J. (2016). The Galaxy Cluster Environments of Wide Angle Tail Radio Sources. In *American Astronomical Society Meeting Abstracts*, volume 227 of *American Astronomical Society Meeting Abstracts*, page 235.14.
- Duffy, A. R., Schaye, J., Kay, S. T., and Dalla Vecchia, C. (2008). Dark matter halo concentrations in the Wilkinson Microwave Anisotropy Probe year 5 cosmology. *Mon. Not. R. Astron. Soc.*, 390:L64–L68.
- Dunn, R. J. H., Fabian, A. C., and Taylor, G. B. (2005). Radio bubbles in clusters of galaxies. *Mon. Not. R. Astron. Soc.*, 364:1343–1353.
- Ebeling, H., Barrett, E., Donovan, D., Ma, C.-J., Edge, A. C., and van Speybroeck, L. (2007). A complete sample of 12 very x-ray luminous galaxy clusters at $z > 0.5$. *The Astrophysical Journal Letters*, 661(1):L33.
- Ebeling, H., Edge, A. C., Allen, S. W., Crawford, C. S., Fabian, A. C., and Huchra, J. P. (2000). The ROSAT Brightest Cluster Sample - IV. The extended sample. *Mon. Not. R. Astron. Soc.*, 318:333–340.
- Ebeling, H., Edge, A. C., Bohringer, H., Allen, S. W., Crawford, C. S., Fabian, A. C., Voges, W., and Huchra, J. P. (1998). The ROSAT Brightest Cluster Sample - I. The compilation of the sample and the cluster log N-log S distribution. *Mon. Not. R. Astron. Soc.*, 301:881–914.
- Ebeling, H., Edge, A. C., and Henry, J. P. (2001). MACS: A Quest for the Most Massive Galaxy Clusters in the Universe. *Astrophys. J.*, 553:668–676.

- Ebeling, H., Voges, W., Bohringer, H., Edge, A. C., Huchra, J. P., and Briel, U. G. (1996). Properties of the X-ray-brightest Abell-type clusters of galaxies (XBACs) from ROSAT All-Sky Survey data - I. The sample. *Mon. Not. R. Astron. Soc.*, 281:799–829.
- Edge, A. C. and Stewart, G. C. (1991). EXOSAT Observations of Clusters of Galaxies - Part Two - X-Ray to Optical Correlations. *MNRAS*, 252:428.
- Edge, D. O., Shakeshaft, J. R., McAdam, W. B., Baldwin, J. E., and Archer, S. (1959). A survey of radio sources at a frequency of 159 Mc/s. *Mem. R. Astron. Soc.*, 68:37–60.
- Ellingson, E., Yee, H. K. C., Abraham, R. G., Morris, S. L., and Carlberg, R. G. (1998). The CNOG Cluster Redshift Survey Catalogs. VI. MS 0015.9+1609 and MS 0451.5-0305. *Astrophys. J. Supp.*, 116:247–262.
- Emerson, D. (2003). Why single dish? Slides of a talk given at NAIC-NRAO School on Single-Dish Radio Astronomy, August, Greenbank.
- Enßlin, T., Pfrommer, C., Miniati, F., and Subramanian, K. (2011). Cosmic ray transport in galaxy clusters: implications for radio halos, gamma-ray signatures, and cool core heating. *Astron. Astrophys.*, 527:A99.
- Enßlin, T. A. (1999). Radio Ghosts. In Boehringer, H., Feretti, L., and Schuecker, P., editors, *Diffuse Thermal and Relativistic Plasma in Galaxy Clusters*, page 275.
- Enßlin, T. A., Biermann, P. L., Klein, U., and Kohle, S. (1998). Cluster radio relics as a tracer of shock waves of the large-scale structure formation. *Astron. Astrophys.*, 332:395–409.
- Enßlin, T. A., Biermann, P. L., Klein, U., and Kohle, S. (1998). Cluster radio relics as a tracer of shock waves of the large-scale structure formation. *Astron. Astrophys.*, 332:395–409.
- Enßlin, T. A. and Gopal-Krishna (2001). Reviving fossil radio plasma in clusters of galaxies by adiabatic compression in environmental shock waves. *Astron. Astrophys.*, 366:26–34.
- Erickson, W. C. and Cronyn, W. M. (1965). The Spectra of Radio Sources at Decametric Wavelengths. *Astrophys. J.*, 142:1156.

- Ettori, S., De Grandi, S., and Molendi, S. (2002). Gravitating mass profiles of nearby galaxy clusters and relations with X-ray gas temperature, luminosity and mass. *Astron. Astrophys.*, 391:841–855.
- Ettori, S., Fabian, A. C., and White, D. A. (1998). ROSAT/SPC observations of the outer regions of the Perseus cluster of galaxies. *Mon. Not. R. Astron. Soc.*, 300:837–856.
- Ettori, S., Tozzi, P., Borgani, S., and Rosati, P. (2004). Scaling laws in X-ray galaxy clusters at redshift between 0.4 and 1.3. *A&A*, 417:13–27.
- Evans, D. A., Hardcastle, M. J., Croston, J. H., Worrall, D. M., and Birkinshaw, M. (2005). Chandra and XMM-Newton observations of NGC 6251. *Mon. Not. R. Astron. Soc.*, 359:363–382.
- Fabian, A. C. (1994). Cooling Flows in Clusters of Galaxies. *Annu. Rev. Astron. Astrophys.*, 32:277–318.
- Fadda, D., Girardi, M., Giuricin, G., Mardirossian, F., and Mezzetti, M. (1996). The Observational Distribution of Internal Velocity Dispersions in Nearby Galaxy Clusters. *ApJ*, 473:670.
- Farhang, M., Bond, J. R., and Chluba, J. (2012). Semi-blind Eigen Analyses of Recombination Histories Using Cosmic Microwave Background Data. *Astrophys. J.*, 752:88.
- Fassbender, R., Böhringer, H., Nastasi, A., et al. (2011). The x-ray luminous galaxy cluster population at $0.9 < z < 1.6$ as revealed by the XMM-Newton Distant Cluster Project. *New Journal of Physics*, 13(12):125014.
- Felten, J. E., Gould, R. J., Stein, W. A., and Woolf, N. J. (1966). X-Rays from the Coma Cluster of Galaxies. *Astrophys. J.*, 146:955–958.
- Feretti, L. (1999). Observational Results on Cluster Diffuse Emission. In Böhringer, H., Feretti, L., and Schuecker, P., editors, *Diffuse Thermal and Relativistic Plasma in Galaxy Clusters*, page 3.

- Feretti, L. (2003). Radio Observations of Clusters of Galaxies. In Bowyer, S. and Hwang, C.-Y., editors, *Matter and Energy in Clusters of Galaxies*, volume 301 of *Astronomical Society of the Pacific Conference Series*, page 143.
- Feretti, L., Brunetti, G., Giovannini, G., Govoni, F., and Setti, G. (2000). Non Thermal Emission from Galaxy Clusters: Radio Halos. In *Constructing the Universe with Clusters of Galaxies*.
- Feretti, L., Brunetti, G., Giovannini, G., Kassim, N., Orrú, E., and Setti, G. (2004). Properties and Spectral Behaviour of Cluster Radio Halos. *Journal of Korean Astronomical Society*, 37:315–322.
- Feretti, L., Fusco-Femiano, R., Giovannini, G., and Govoni, F. (2001). The giant radio halo in Abell 2163. *Astron. Astrophys.*, 373:106–112.
- Feretti, L., Giovannini, G., Govoni, F., and Murgia, M. (2011). Relativistic plasma and ICM/radio source interaction. In Bonanno, A., de Gouveia Dal Pino, E., and Kosovichev, A. G., editors, *Advances in Plasma Astrophysics*, volume 274 of *IAU Symposium*, pages 340–347.
- Feretti, L., Giovannini, G., Govoni, F., and Murgia, M. (2012). Clusters of galaxies: observational properties of the diffuse radio emission. *Astron. Astrophys. Rev.*, 20:54.
- Feretti, L., Schuecker, P., Böhringer, H., Govoni, F., and Giovannini, G. (2005). Diffuse radio emission in a REFLEX cluster. *Astron. Astrophys.*, 444:157–164.
- Ferrari, C., Govoni, F., Schindler, S., Bykov, A. M., and Rephaeli, Y. (2008). Observations of Extended Radio Emission in Clusters. *Space Sci. Rev.*, 134:93–118.
- Feruglio, C., Fiore, F., La Franca, F., et al. (2008). The XMM-Newton survey of the ELAIS-S1 field. II. Optical identifications and multiwavelength catalogue of X-ray sources. *A&A*, 488:417–428.
- Fesenko, B. I. (1979). Distortions in the Properties of galaxy clusters. II. The reality of Abell's clusters. *Soviet Astronomy*, 23:657.

- Finn, R. A., Zaritsky, D., McCarthy, Jr., D. W., et al. (2005). $H\alpha$ -derived Star Formation Rates for Three $z\sim 0.75$ EDisCS Galaxy Clusters. *ApJ*, 630:206–227.
- Finoguenov, A., Guzzo, L., Hasinger, G., et al. (2007). The XMM-Newton Wide-Field Survey in the COSMOS Field: Statistical Properties of Clusters of Galaxies. *Astrophys. J. Supp.*, 172:182–195.
- Finoguenov, A., Reiprich, T. H., and Böhringer, H. (2001). Details of the mass-temperature relation for clusters of galaxies. *Astron. Astrophys.*, 368:749–759.
- Finoguenov, A., Sarazin, C. L., Nakazawa, K., Wik, D. R., and Clarke, T. E. (2010). XMM-Newton Observation of the Northwest Radio Relic Region in A3667. *Astrophys. J.*, 715:1143–1151.
- Foley, R. J., Andersson, K., Bazin, G., et al. (2011). Discovery and Cosmological Implications of SPT-CL J2106-5844, the Most Massive Known Cluster at $z > 1$. *Astrophys. J.*, 731:86.
- Freedman, W. L., Madore, B. F., Gibson, B. K., et al. (2001). Final Results from the Hubble Space Telescope Key Project to Measure the Hubble Constant. *Astrophys. J.*, 553:47–72.
- Frenk, C. S., White, S. D. M., Efstathiou, G., and Davis, M. (1990). Galaxy clusters and the amplitude of primordial fluctuations. *Astrophys. J.*, 351:10–21.
- Freudling, W., Haynes, M. P., and Giovanelli, R. (1992). H I observations of galaxies in the Hercules supercluster. II - Additional UGC galaxies and galaxies in selected CGCG fields. *ApJS*, 79:157–182.
- Furusho, T., Yamasaki, N. Y., Ohashi, T., Shibata, R., and Ezawa, H. (2001). Temperature Map of the Perseus Cluster of Galaxies Observed with ASCA. *Astrophys. J. Lett.*, 561:L165–L169.
- Furuzawa, A., Tawara, Y., Kunieda, H., Yamashita, K., Sonobe, T., Tanaka, Y., and Mushotzky, R. (1998). ASCA Observation of the Distant Cluster of Galaxies Cl 0016+16 and Implication for H_0 . *Astrophys. J.*, 504:35–41.

- Gamow, G. (1946). Expanding Universe and the Origin of Elements. *Physical Review*, 70:572–573.
- Gawiser, E. and Silk, J. (2000). The cosmic microwave background radiation. *Phys. Rep.*, 333:245–267.
- Gelman, A. C., Stern, J. B., Rubin, H. S., et al. (2004). Bayesian data analysis. Technical report.
- Geman, S. and Geman, D. (1984). Stochastic relaxation, gibbs distributions, and the bayesian restoration of images. *IEEE Transactions on Pattern Analysis and Machine Intelligence*, PAMI-6(6):721–741.
- Gibbs, J. W. (1898). Fourier’s Series. *Nature.*, 59:200.
- Gilbank, D. G., Gladders, M. D., Yee, H. K. C., and Hsieh, B. C. (2011). The Red-sequence Cluster Survey-2 (RCS-2): Survey Details and Photometric Catalog Construction. *Astron. J.*, 141:94.
- Giodini, S., Lovisari, L., Pointecouteau, E., Ettori, S., Reiprich, T. H., and Hoekstra, H. (2013). Scaling Relations for Galaxy Clusters: Properties and Evolution. *Space Sci. Rev.*, 177:247–282.
- Gioia, I. M. (2000). Cluster Surveys. In *Constructing the Universe with Clusters of Galaxies*.
- Gioia, I. M. and Luppino, G. A. (1994). The EMSS catalog of X-ray-selected clusters of galaxies. 1: an atlas of CCD images of 41 distant clusters. *Astrophys. J. Supp.*, 94:583–614.
- Gioia, I. M., Maccacaro, T., Schild, R. E., Wolter, A., Stocke, J. T., Morris, S. L., and Henry, J. P. (1990). The Einstein Observatory Extended Medium-Sensitivity Survey. I - X-ray data and analysis. *Astrophys. J. Supp.*, 72:567–619.
- Gioia, I. M., Wolter, A., Mullis, C. R., Henry, J. P., Böhringer, H., and Briel, U. G. (2004). RX J1821.6+6827: A cool cluster at $z = 0.81$ from the ROSAT NEP survey. *A&A*, 428:867–875.

- Giovanelli, R. (1992). Clusters of galaxies, radio observations. In Maran, S. P., editor, *Astronomy and Astrophysics Encyclopedia*. Cambridge University Press, Cambridge.
- Giovanelli, R., Scodreggio, M., Solanes, J. M., Haynes, M. P., Arce, H., and Sakai, S. (1995). H I 2334+26: an extended H I cloud near Abell 2634. *AJ*, 109:1451–1457.
- Giovannini, G., Bonafede, A., Feretti, L., Govoni, F., Murgia, M., Ferrari, F., and Monti, G. (2009). Radio halos in nearby ($z < 0.4$) clusters of galaxies. *Astron. Astrophys.*, 507:1257–1270.
- Giovannini, G. and Feretti, L. (2000). Halo and relic sources in clusters of galaxies. *New Astron.*, 5:335–347.
- Giovannini, G. and Feretti, L. (2002). Diffuse Radio Sources and Cluster Mergers: Radio Halos and Relics. In Feretti, L., Gioia, I. M., and Giovannini, G., editors, *Merging Processes in Galaxy Clusters*, volume 272 of *Astrophysics and Space Science Library*, pages 197–227.
- Giovannini, G. and Feretti, L. (2004). Radio Relics in Clusters of Galaxies. *Journal of Korean Astronomical Society*, 37:323–328.
- Giovannini, G., Feretti, L., and Andernach, H. (1985). VLA observations of the extended source near Coma A. *Astron. Astrophys.*, 150:302–306.
- Giovannini, G., Feretti, L., and Stanghellini, C. (1991). The Coma cluster radio source 1253 + 275, revisited. *Astron. Astrophys.*, 252:528–537.
- Giovannini, G., Tordi, M., and Feretti, L. (1999). Radio halo and relic candidates from the NRAO VLA Sky Survey. *New Astron.*, 4:141–155.
- Girardi, M., Barrena, R., Boschin, W., and Ellingson, E. (2008). Cluster Abell 520: a perspective based on member galaxies. A cluster forming at the crossing of three filaments? *Astron. Astrophys.*, 491:379–395.
- Girardi, M., Fadda, D., Giuricin, G., Mardirossian, F., Mezzetti, M., and Biviano, A. (1996). Velocity Dispersions and X-Ray Temperatures of Galaxy Clusters. *ApJ*, 457:61.

- Girardi, M., Giuricin, G., Mardirossian, F., Mezzetti, M., and Boschin, W. (1998). Optical Mass Estimates of Galaxy Clusters. *ApJ*, 505:74–95.
- Girardi, M. and Mezzetti, M. (2001). Evolution of the Internal Dynamics of Galaxy Clusters. *Astrophys. J.*, 548:79–96.
- Gitti, M., Piffaretti, R., and Schindler, S. (2007). Mass distribution in the most X-ray-luminous galaxy cluster RX J1347.5-1145 studied with XMM-Newton. *Astron. Astrophys.*, 472:383–394.
- Gitti, M. and Schindler, S. (2004). XMM-Newton observation of the most X-ray-luminous galaxy cluster RX J1347.5-1145. *Astron. Astrophys.*, 427:L9–L12.
- Gladders, M. D. (2002). *The Red-Sequence Cluster Survey*. PhD thesis, Department of Astronomy and Astrophysics, University of Toronto.
- Gladders, M. D. and Yee, H. K. C. (2000). A New Method For Galaxy Cluster Detection. I. The Algorithm. *Astron. J.*, 120:2148–2162.
- Gladders, M. D. and Yee, H. K. C. (2001). The Red-Sequence Cluster Survey. In Clowes, R., Adamson, A., and Bromage, G., editors, *The New Era of Wide Field Astronomy*, volume 232 of *Astronomical Society of the Pacific Conference Series*, page 126.
- Gladders, M. D. and Yee, H. K. C. (2005). The Red-Sequence Cluster Survey. I. The Survey and Cluster Catalogs for Patches RCS 0926+37 and RCS 1327+29. *Astrophys. J. Supp.*, 157:1–29.
- Glazebrook, K. and Bland-Hawthorn, J. (2001). Microslit Nod-Shuffle Spectroscopy: A Technique for Achieving Very High Densities of Spectra. *PASP*, 113:197–214.
- Gómez, P. L., Hughes, J. P., and Birkinshaw, M. (2000). A Merger Scenario for the Dynamics of Abell 665. *Astrophys. J.*, 540:726–740.
- Gómez, P. L., Loken, C., Roettiger, K., and Burns, J. O. (2002). Do Cooling Flows Survive Cluster Mergers? *Astrophys. J.*, 569:122–133.

- Gómez, P. L., Pinkney, J., Burns, J. O., Wang, Q., Owen, F. N., and Voges, W. (1997). ROSAT X-Ray Observations of Abell Clusters with Wide-Angle Tailed Radio Sources. *Astrophys. J.*, 474:580–597.
- Gonzalez, A. H., Zaritsky, D., Dalcanton, J. J., and Nelson, A. (2001). The Las Campanas Distant Cluster Survey: The Catalog. *Astrophys. J. Supp.*, 137:117–138.
- Goto, T., Nichol, R. C., Okamura, S., et al. (2003). H δ -Strong Galaxies in the Sloan Digital Sky Survey: I. The Catalog. *PASJ*, 55:771–787.
- Govoni, F., Feretti, L., Giovannini, G., Böhringer, H., Reiprich, T. H., and Murgia, M. (2001). Radio and X-ray diffuse emission in six clusters of galaxies. *Astron. Astrophys.*, 376:803–819.
- Govoni, F., Markevitch, M., Vikhlinin, A., van Speybroeck, L., Feretti, L., and Giovannini, G. (2004). Chandra Temperature Maps for Galaxy Clusters with Radio Halos. *Astrophys. J.*, 605:695–708.
- Govoni, F., Murgia, M., Giovannini, G., Vacca, V., and Bonafede, A. (2011). The large-scale diffuse radio emission in A781. *Astron. Astrophys.*, 529:A69.
- Govoni, F., Murgia, M., Markevitch, M., Feretti, L., Giovannini, G., Taylor, G. B., and Carretti, E. (2009). A search for diffuse radio emission in the relaxed, cool-core galaxy clusters A1068, A1413, A1650, A1835, A2029, and Ophiuchus. *Astron. Astrophys.*, 499:371–383.
- Grego, L., Carlstrom, J. E., Joy, M. K., Reese, E. D., Holder, G. P., Patel, S., Cooray, A. R., and Holzappel, W. L. (2000). The Sunyaev-Zeldovich Effect in Abell 370. *Astrophys. J.*, 539:39–51.
- Grego, L., Carlstrom, J. E., Reese, E. D., Holder, G. P., Holzappel, W. L., Joy, M. K., Mohr, J. J., and Patel, S. (2001). Galaxy Cluster Gas Mass Fractions from Sunyaev-Zeldovich Effect Measurements: Constraints on Ω_M . *Astrophys. J.*, 552:2–14.
- Gull, S. F. and Northover, K. J. E. (1976). Detection of hot gas in clusters of galaxies by observation of the microwave background radiation. *Nature.*, 263:572.

- Gunn, J. E., Hoessel, J. G., and Oke, J. B. (1986). A systematic survey for distant galaxy clusters. *Astrophys. J.*, 306:30–37.
- Guzzo, L., Schuecker, P., Böhringer, H., et al. (2009). The REFLEX galaxy cluster survey. VIII. Spectroscopic observations and optical atlas. *A&A*, 499:357–369.
- Haines, C. P., Pereira, M. J., Smith, G. P., et al. (2015). LoCuSS: The Slow Quenching of Star Formation in Cluster Galaxies and the Need for Pre-processing. *Astrophys. J.*, 806:101.
- Hanisch, R. J. (1982). Common properties of clusters of galaxies containing radio halos and implications for models of radio halo formation. *Astron. Astrophys.*, 116:137–146.
- Hanisch, R. J., Strom, R. G., and Jaffe, W. J. (1985). The nature of the diffuse radio source near Coma A. *Astron. Astrophys.*, 153:9–12.
- Hao, J., McKay, T. A., Koester, B. P., et al. (2010). A GMBCG Galaxy Cluster Catalog of 55,424 Rich Clusters from SDSS DR7. *Astrophys. J. Supp.*, 191:254–274.
- Harris, D. E., Bahcall, N. A., and Strom, R. G. (1977). Radio and optical observations in the fields of five unidentified X-ray sources at high latitudes. *Astron. Astrophys.*, 60:27–38.
- Hartley, W. G., Gazzola, L., Pearce, F. R., Kay, S. T., and Thomas, P. A. (2008). Nature versus nurture: the curved spine of the galaxy cluster X-ray luminosity-temperature relation. *Mon. Not. R. Astron. Soc.*, 386:2015–2021.
- Hasselfield, M. et al. (2013). The Atacama Cosmology Telescope: Sunyaev-Zel’dovich selected galaxy clusters at 148 GHz from three seasons of data. *Journal of Cosmology and Astroparticle Physics.*, 7:8.
- Hennawi, J. F., Gladders, M. D., Oguri, M., et al. (2008). A New Survey for Giant Arcs. *Astron. J.*, 135:664–681.
- Henry, J. P., Gioia, I. M., Huchra, J. P., et al. (1995). Groups of Galaxies in the ROSAT North Ecliptic Pole Survey. *Astrophys. J.*, 449:422.

- Herbig, T., Lawrence, C. R., Readhead, A. C. S., and Gulkis, S. (1995). A Measurement of the Sunyaev-Zel'dovich Effect in the Coma Cluster of Galaxies. *Astrophys. J. Lett.*, 449:L5.
- Herschel, J. F. W. (1864). Catalogue of Nebulae and Clusters of Stars. *Royal Society of London Philosophical Transactions Series I*, 154:1–137.
- Heydon-Dumbleton, N. H., Collins, C. A., and MacGillivray, H. T. (1989). The Edinburgh/Durham Southern Galaxy Catalogue. II - Image classification and galaxy number counts. *Mon. Not. R. Astron. Soc.*, 238:379–406.
- Hill, G. J. and Lilly, S. J. (1991). A change in the cluster environments of radio galaxies with cosmic epoch. *Astrophys. J.*, 367:1–18.
- Hilton, M. et al. (2012). The XMM Cluster Survey: evidence for energy injection at high redshift from evolution of the X-ray luminosity-temperature relation. *Mon. Not. R. Astron. Soc.*, 424:2086–2096.
- Hilton, M., Lloyd-Davies, E., Stanford, S. A., et al. (2010). The XMM Cluster Survey: Active Galactic Nuclei and Starburst Galaxies in XMMXCS J2215.9-1738 at $z = 1.46$. *ApJ*, 718:133–147.
- Hilton, M., Stanford, S. A., Stott, J. P., et al. (2009). The XMM Cluster Survey: Galaxy Morphologies and the Color-Magnitude Relation in XMMXCS J2215.9 - 1738 at $z = 1.46$. *Astrophys. J.*, 697:436–451.
- Hinshaw, G., Larson, D., Komatsu, E., et al. (2013). Nine-year Wilkinson Microwave Anisotropy Probe (WMAP) Observations: Cosmological Parameter Results. *Astrophys. J. Supp.*, 208:19.
- Hoeft, M., Brüggén, M., and Yepes, G. (2004). Radio relics in a cosmological cluster merger simulation. *Mon. Not. R. Astron. Soc.*, 347:389–393.
- Högbom, J. A. (1974). Aperture Synthesis with a Non-Regular Distribution of Interferometer Baselines. *Astron. Astrophys. Supp.*, 15:417.

- Hogg, D. W., Bovy, J., and Lang, D. (2010). Data analysis recipes: Fitting a model to data. *ArXiv e-prints*.
- Holder, G. P., Mohr, J. J., Carlstrom, J. E., Evrard, A. E., and Leitch, E. M. (2000). Expectations for an Interferometric Sunyaev-Zeldovich Effect Survey for Galaxy Clusters. *Astrophys. J.*, 544:629–635.
- Holzappel, W. L., Wilbanks, T. M., Ade, P. A. R., Church, S. E., Fischer, M. L., Maukopf, P. D., Osgood, D. E., and Lange, A. E. (1997). The Sunyaev-Zeldovich Infrared Experiment: A Millimeter-Wave Receiver for Cluster Cosmology. *Astrophys. J.*, 479:17–30.
- Horner, D. J. (2001). *X-ray scaling laws for galaxy clusters and groups*. PhD thesis, University of Maryland College Park.
- Hoyle, F., Fowler, W. A., Burbidge, G. R., and Burbidge, E. M. (1956). Origin of the Elements in Stars. *Science*, 124:611–614.
- Hubble, E. (1929). A Relation between Distance and Radial Velocity among Extra-Galactic Nebulae. *Proceedings of the National Academy of Science*, 15:168–173.
- Hubble, E. and Humason, M. L. (1931). The Velocity-Distance Relation among Extra-Galactic Nebulae. *Astrophys. J.*, 74:43.
- Hubble, E. P. (1925). Cepheids in spiral nebulae. *The Observatory*, 48:139–142.
- Hubble, E. P. (1926). Extragalactic nebulae. *Astrophys. J.*, 64.
- Huchra, J. P., Macri, L. M., Masters, K. L., et al. (2012). The 2MASS Redshift Survey: Description and Data Release. *ApJS*, 199:26.
- Hughes, J. P. and Birkinshaw, M. (1998). Another X-Ray-discovered Poor Cluster of Galaxies Associated with CL 0016+16. *Astrophys. J.*, 497:645–649.
- Hughes, J. P., Birkinshaw, M., and Huchra, J. P. (1995). A New X-Ray-discovered Cluster of Galaxies Associated with CL 0016+16. *Astrophys. J. Lett.*, 448:L93.

- Humason, M. L., Mayall, N. U., and Sandage, A. R. (1956). Redshifts and magnitudes of extragalactic nebulae. *Astron. J.*, 61:97–162.
- Ikebe, Y., Reiprich, T. H., Böhringer, H., Tanaka, Y., and Kitayama, T. (2002). A new measurement of the X-ray temperature function of clusters of galaxies. *Astron. Astrophys.*, 383:773–790.
- Jaffe, W. J. (1977). Origin and transport of electrons in the halo radio source in the Coma cluster. *Astrophys. J.*, 212:1–7.
- Jaffe, W. J. and Rudnick, L. (1979). Observations at 610 MHz of radio halos in clusters of galaxies. *Astrophys. J.*, 233:453–462.
- Jeltema, T. E., Hallman, E. J., Burns, J. O., and Motl, P. M. (2008). Cluster Structure in Cosmological Simulations. I. Correlation to Observables, Mass Estimates, and Evolution. *Astrophys. J.*, 681:167–186.
- Jeltema, T. E., Mulchaey, J. S., Lubin, L. M., and Fassnacht, C. D. (2007). The Evolution of Galaxies in X-Ray-luminous Groups. *ApJ*, 658:865–883.
- Johnston-Hollitt, M., Ekers, R. D., Hunstead, R. W., Clay, R. W., and Wieringa, M. H. (2002). Cluster merger in A3667? New radio observations shed more light. *Highlights of Astronomy*, 12:535–536.
- Jones, D. H., Read, M. A., Saunders, W., et al. (2009). The 6dF Galaxy Survey: final redshift release (DR3) and southern large-scale structures. *MNRAS*, 399:683–698.
- Jones, M. and Saunders, R. (1996). Optimising H_0 determination from the X-ray plus Sunyaev-Zel'dovich route. In Zimmermann, H. U., Trümper, J., and Yorke, H., editors, *Roentgenstrahlung from the Universe*, pages 553–556.
- Jones, M., Saunders, R., Alexander, P., et al. (1993). An image of the Sunyaev-Zel'dovich effect. *Nature.*, 365:320–323.

- Jones, T. W. and Owen, F. N. (1979). Hot gas in elliptical galaxies and the formation of head-tail radio sources. *Astrophys. J.*, 234:818–824.
- Joy, M., LaRoque, S., Grego, L., et al. (2001). Sunyaev-Zeldovich Effect Imaging of Massive Clusters of Galaxies at Redshift $Z > 0.8$. *Astrophys. J. Lett.*, 551:L1–L4.
- Kaiser, N. (1986a). Evolution and clustering of rich clusters. *Mon. Not. R. Astron. Soc.*, 222:323–345.
- Kaiser, N. (1986b). Evolution and clustering of rich clusters. *Mon. Not. R. Astron. Soc.*, 222:323–345.
- Kale, R., Venturi, T., Giacintucci, S., Dallacasa, D., Cassano, R., Brunetti, G., Macario, G., and Athreya, R. (2013). The Extended GMRT Radio Halo Survey. I. New upper limits on radio halos and mini-halos. *Astron. Astrophys.*, 557:A99.
- Kay, S. T., da Silva, A. C., Aghanim, N., Blanchard, A., Liddle, A. R., Puget, J.-L., Sadat, R., and Thomas, P. A. (2007). The evolution of clusters in the CLEF cosmological simulation: X-ray structural and scaling properties. *MNRAS*, 377:317–334.
- Kelly, B. C. (2007). Some Aspects of Measurement Error in Linear Regression of Astronomical Data. *Astrophys. J.*, 665:1489–1506.
- Kempner, J. C., Blanton, E. L., Clarke, T. E., Enßlin, T. A., Johnston-Hollitt, M., and Rudnick, L. (2004). Conference Note: A Taxonomy of Extended Radio Sources in Clusters of Galaxies. In Reiprich, T., Kempner, J., and Soker, N., editors, *The Riddle of Cooling Flows in Galaxies and Clusters of galaxies*.
- Kempner, J. C. and Sarazin, C. L. (2001). Radio Halo and Relic Candidates from the Westerbork Northern Sky Survey. *Astrophys. J.*, 548:639–651.
- Kenderdine, S. (1963). A survey of galactic radiation at 38 Mc/s, I. *Mon. Not. R. Astron. Soc.*, 126:41.

- Keshet, U., Waxman, E., and Loeb, A. (2004). Imprint of Intergalactic Shocks on the Radio Sky. *Astrophys. J.*, 617:281–302.
- Khedekar, S. and Majumdar, S. (2013). Cosmology with the largest galaxy cluster surveys: going beyond Fisher matrix forecasts. *Journal of Cosmology and Astroparticle Physics.*, 2:030.
- Kim, K.-T., Kronberg, P. P., Giovannini, G., and Venturi, T. (1989). Discovery of intergalactic radio emission in the Coma-A1367 supercluster. *Nature.*, 341:720–723.
- Kirk, B., Hilton, M., Cress, C., et al. (2015). SALT spectroscopic observations of galaxy clusters detected by ACT and a type II quasar hosted by a brightest cluster galaxy. *Mon. Not. R. Astron. Soc.*, 449:4010–4026.
- Kitayama, T. (2014). Cosmological and astrophysical implications of the Sunyaev-Zel'dovich effect. *Progress of Theoretical and Experimental Physics*, 2014(6):06B111.
- Knowles, K. (2015). *OBSERVATIONAL PROBES OF MERGING GALAXY CLUSTERS*. PhD thesis, University of Kwa-Zulu Natal.
- Knowles, K., Intema, H. T., Baker, A. J., et al. (2016). A giant radio halo in a low-mass SZ-selected galaxy cluster: ACT-CL J0256.5+0006. *Mon. Not. R. Astron. Soc.*, 459:4240–4258.
- Koester, B. P., McKay, T. A., Annis, J., et al. (2007a). A MaxBCG Catalog of 13,823 Galaxy Clusters from the Sloan Digital Sky Survey. *Astrophys. J.*, 660:239–255.
- Koester, B. P., McKay, T. A., Annis, J., et al. (2007b). MaxBCG: A Red-Sequence Galaxy Cluster Finder. *Astrophys. J.*, 660:221–238.
- Komatsu, E., Smith, K. M., Dunkley, J., et al. (2011). Seven-year Wilkinson Microwave Anisotropy Probe (WMAP) Observations: Cosmological Interpretation. *Astrophys. J. Supp.*, 192:18.
- Komissarov, S. S. and Gubanov, A. G. (1994). Relic radio galaxies: evolution of synchrotron spectrum. *Astron. Astrophys.*, 285:27–43.

- Kravtsov, A. V. and Borgani, S. (2012). Formation of Galaxy Clusters. *Annu. Rev. Astron. Astrophys.*, 50:353–409.
- Kravtsov, A. V., Vikhlinin, A., and Nagai, D. (2006). A New Robust Low-Scatter X-Ray Mass Indicator for Clusters of Galaxies. *Astrophys. J.*, 650:128–136.
- Krivonos, R. A., Vikhlinin, A. A., Markevitch, M. L., and Pavlinsky, M. N. (2003). A Possible Shock Wave in the Intergalactic Medium of the Cluster of Galaxies A754. *Astronomy Letters*, 29:425–428.
- Kuo, P.-H., Hwang, C.-Y., and Ip, W.-H. (2004). The Evolution of Diffuse Radio Sources in Galaxy Clusters. *Astrophys. J.*, 604:108–115.
- Kurtz, M. J. and Mink, D. J. (1998). RVSAO 2.0: Digital Redshifts and Radial Velocities. *PASP*, 110:934–977.
- Large, M. I., Mathewson, D. S., and Haslam, C. G. T. (1959). A High-Resolution Survey of the Coma Cluster of Galaxies at 408 Mc./s. *Nature.*, 183:1663–1664.
- LaRoque, S. J., Carlstrom, J. E., Reese, E. D., Holder, G. P., Holzzapfel, W. L., Joy, M., and Grego, L. (2002). The Sunyaev-Zel’dovich Effect Spectrum of Abell 2163. *ArXiv Astrophysics e-prints*.
- Lau, E. T., Nagai, D., and Nelson, K. (2013). Weighing Galaxy Clusters with Gas. I. On the Methods of Computing Hydrostatic Mass Bias. *Astrophys. J.*, 777:151.
- Le Brun, A. M. C., McCarthy, I. G., Schaye, J., and Ponman, T. J. (2014). Towards a realistic population of simulated galaxy groups and clusters. *MNRAS*, 441:1270–1290.
- Le Fevre, O., Crampton, D., Lilly, S. J., Hammer, F., and Tresse, L. (1995). The Canada-France Redshift Survey. II. Spectroscopic Program: Data for the 0000-00 and 1000+25 Fields. *ApJ*, 455:60.
- Leccardi, A. and Molendi, S. (2008). Radial temperature profiles for a large sample of galaxy clusters observed with XMM-Newton. *Astron. Astrophys.*, 486:359–373.

- Lemaître, G. (1927). Un Univers homogène de masse constante et de rayon croissant rendant compte de la vitesse radiale des nébuleuses extra-galactiques. *Annales de la Société Scientifique de Bruxelles*, 47:49–59.
- Lemaître, G. (1931). Expansion of the universe, A homogeneous universe of constant mass and increasing radius accounting for the radial velocity of extra-galactic nebulae. *Mon. Not. R. Astron. Soc.*, 91:483–490.
- Lemze, D., Postman, M., Genel, S., et al. (2013). The Contribution of Halos with Different Mass Ratios to the Overall Growth of Cluster-sized Halos. *Astrophys. J.*, 776:91.
- Liang, H. (1999). A Radio Halo Found in the Hottest Known Cluster of Galaxies 1E0658-56. In Boehringer, H., Feretti, L., and Schuecker, P., editors, *Diffuse Thermal and Relativistic Plasma in Galaxy Clusters*, page 33.
- Liang, H., Hunstead, R. W., Birkinshaw, M., and Andreani, P. (2000). A Powerful Radio Halo in the Hottest Known Cluster of Galaxies 1E 0657-56. *Astrophys. J.*, 544:686–701.
- Lilly, S. J., Le Fèvre, O., Renzini, A., et al. (2007). zCOSMOS: A Large VLT/VIMOS Redshift Survey Covering $0 < z < 3$ in the COSMOS Field. *Astrophys. J. Supp.*, 172:70–85.
- Lindner, R. R., Baker, A. J., Hughes, J. P., et al. (2014). The Radio Relics and Halo of El Gordo, a Massive $z = 0.870$ Cluster Merger. *Astrophys. J.*, 786:49.
- Liu, J. and Hill, J. C. (2015). Cross-correlation of Planck CMB lensing and CFHTLenS galaxy weak lensing maps. *Physical Review D.*, 92(6):063517.
- Lloyd-Davies, E. J., Romer, A. K., Mehrrens, N., et al. (2011). The XMM Cluster Survey: X-ray analysis methodology. *MNRAS*, 418:14–53.
- Lovisari, L., Reiprich, T. H., and Schellenberger, G. (2015). Scaling properties of a complete X-ray selected galaxy group sample. *Astron. Astrophys.*, 573:A118.
- Lubin, L. M. and Bahcall, N. A. (1993). The relation between velocity dispersion and temperature in clusters - Limiting the velocity bias. *ApJ*, 415:L17–L20.

- Lucey, J. R. (1983). An assessment of the completeness and correctness of the Abell catalogue. *Mon. Not. R. Astron. Soc.*, 204:33–43.
- Lumb, D. H., Bartlett, J. G., Romer, A. K., et al. (2004). The XMM-NEWTON Ω project. I. The X-ray luminosity-temperature relation at $z > 0.4$. *A&A*, 420:853–872.
- Lumsden, S. L., Nichol, R. C., Collins, C. A., and Guzzo, L. (1992). The Edinburgh-Durham Southern Galaxy Catalogue. IV - The Cluster Catalogue. *Mon. Not. R. Astron. Soc.*, 258:1–22.
- Macario, G., Markevitch, M., Giacintucci, S., Brunetti, G., Venturi, T., and Murray, S. S. (2011). A Shock Front in the Merging Galaxy Cluster A754: X-ray and Radio Observations. *Astrophys. J.*, 728:82.
- Machacek, M. E., Bautz, M. W., Canizares, C., and Garmire, G. P. (2002). Chandra Observations of Galaxy Cluster A2218. *Astrophys. J.*, 567:188–201.
- Machacek, M. E., Jerius, D., Kraft, R., Forman, W. R., Jones, C., Randall, S., Giacintucci, S., and Sun, M. (2011). Deep Chandra Observations of Edges and Bubbles in the NGC 5846 Galaxy Group. *Astrophys. J.*, 743:15.
- Maddox, S. J., Efstathiou, G., and Loveday, J. (1988). The APM Galaxy Survey. In Audouze, J., Pelletan, M.-C., Szalay, A., Zel'dovich, Y. B., and Peebles, P. J. E., editors, *Large Scale Structures of the Universe*, volume 130 of *IAU Symposium*, page 151.
- Magnelli, B., Elbaz, D., Chary, R. R., Dickinson, M., Le Borgne, D., Frayer, D. T., and Willmer, C. N. A. (2009). The $0.4 < z < 1.3$ star formation history of the Universe as viewed in the far-infrared. *A&A*, 496:57–75.
- Mann, A. W. and Ebeling, H. (2012). X-ray-optical classification of cluster mergers and the evolution of the cluster merger fraction. *MNRAS*, 420:2120–2138.
- Mantz, A., Allen, S. W., Ebeling, H., Rapetti, D., and Drlica-Wagner, A. (2010a). The observed growth of massive galaxy clusters - II. X-ray scaling relations. *Mon. Not. R. Astron. Soc.*, 406:1773–1795.

- Mantz, A., Allen, S. W., Rapetti, D., and Ebeling, H. (2010b). The observed growth of massive galaxy clusters - I. Statistical methods and cosmological constraints. *Mon. Not. R. Astron. Soc.*, 406:1759–1772.
- Mao, M. Y., Johnston-Hollitt, M., Stevens, J. B., and Wotherspoon, S. J. (2009). Head-tail Galaxies: beacons of high-density regions in clusters. *Mon. Not. R. Astron. Soc.*, 392:1070–1079.
- Mao, M. Y., Sharp, R., Saikia, D. J., Norris, R. P., Johnston-Hollitt, M., Middelberg, E., and Lovell, J. E. J. (2010). Wide-angle tail galaxies in ATLAS. *Mon. Not. R. Astron. Soc.*, 406:2578–2590.
- Markevitch, M. (1996). Temperature Structure of Four Hot Clusters Obtained with ASCA Data. *Astrophys. J. Lett.*, 465:L1.
- Markevitch, M. (2006). Chandra Observation of the Most Interesting Cluster in the Universe. In Wilson, A., editor, *The X-ray Universe 2005*, volume 604 of *ESA Special Publication*, page 723.
- Markevitch, M., Forman, W. R., Sarazin, C. L., and Vikhlinin, A. (1998a). The Temperature Structure of 30 Nearby Clusters Observed with ASCA: Similarity of Temperature Profiles. *Astrophys. J.*, 503:77.
- Markevitch, M., Forman, W. R., Sarazin, C. L., and Vikhlinin, A. (1998b). The Temperature Structure of 30 Nearby Clusters Observed with ASCA: Similarity of Temperature Profiles. *Astrophys. J.*, 503:77–96.
- Markevitch, M., Gonzalez, A. H., Clowe, D., Vikhlinin, A., Forman, W., Jones, C., Murray, S., and Tucker, W. (2004). Direct Constraints on the Dark Matter Self-Interaction Cross Section from the Merging Galaxy Cluster 1E 0657-56. *Astrophys. J.*, 606:819–824.
- Markevitch, M., Gonzalez, A. H., David, L., Vikhlinin, A., Murray, S., Forman, W., Jones, C., and Tucker, W. (2002). A Textbook Example of a Bow Shock in the Merging Galaxy Cluster 1E 0657-56. *Astrophys. J. Lett.*, 567:L27–L31.

- Markevitch, M., Govoni, F., Brunetti, G., and Jerius, D. (2005). Bow Shock and Radio Halo in the Merging Cluster A520. *Astrophys. J.*, 627:733–738.
- Markevitch, M., Ponman, T. J., Nulsen, P. E. J., et al. (2000). Chandra Observation of Abell 2142: Survival of Dense Subcluster Cores in a Merger. *Astrophys. J.*, 541:542–549.
- Markevitch, M. and Vikhlinin, A. (2001). Merger Shocks in Galaxy Clusters A665 and A2163 and Their Relation to Radio Halos. *Astrophys. J.*, 563:95–102.
- Markevitch, M., Yamashita, K., Furuzawa, A., and Tawara, Y. (1994). Nonisothermality of the hottest cluster Abell 2163. *Astrophys. J. Lett.*, 436:L71–L74.
- Martini, P., Mulchaey, J. S., and Kelson, D. D. (2007). The Distribution of Active Galactic Nuclei in Clusters of Galaxies. *Astrophys. J.*, 664:761–776.
- Mason, B. S., Myers, S. T., and Readhead, A. C. S. (2001). A Measurement of H_0 from the Sunyaev-Zeldovich Effect. *Astrophys. J. Lett.*, 555:L11–L15.
- Mather, J. C., Cheng, E. S., Eplee, Jr., R. E., et al. (1990). A preliminary measurement of the cosmic microwave background spectrum by the Cosmic Background Explorer (COBE) satellite. *Astrophys. J. Lett.*, 354:L37–L40.
- Maughan, B. J. (2014). PICACS: self-consistent modelling of galaxy cluster scaling relations. *Mon. Not. R. Astron. Soc.*, 437:1171–1186.
- Maughan, B. J., Giles, P. A., Randall, S. W., Jones, C., and Forman, W. R. (2012). Self-similar scaling and evolution in the galaxy cluster X-ray luminosity-temperature relation. *MNRAS*, 421:1583–1602.
- Maughan, B. J., Jones, C., Forman, W., and Van Speybroeck, L. (2008). Images, Structural Properties, and Metal Abundances of Galaxy Clusters Observed with Chandra ACIS-I at $0.1 < z < 1.3$. *Astrophys. J. Supp.*, 174:117–135.

- Maughan, B. J., Jones, L. R., Ebeling, H., and Scharf, C. (2006). The evolution of the cluster X-ray scaling relations in the Wide Angle ROSAT Pointed Survey sample at $0.6 < z < 1.0$. *Mon. Not. R. Astron. Soc.*, 365:509–529.
- Maurogordato, S., Cappi, A., Ferrari, C., et al. (2008). A 2163: Merger events in the hottest Abell galaxy cluster. I. Dynamical analysis from optical data. *Astron. Astrophys.*, 481:593–613.
- Mauskopf, P. D., Ade, P. A. R., Allen, S. W., et al. (2000). A Determination of the Hubble Constant Using Measurements of X-Ray Emission and the Sunyaev-Zeldovich Effect at Millimeter Wavelengths in the Cluster Abell 1835. *Astrophys. J.*, 538:505–516.
- Mazzotta, P., Rasia, E., Moscardini, L., and Tormen, G. (2004). Comparing the temperatures of galaxy clusters from hydrodynamical N-body simulations to Chandra and XMM-Newton observations. *Mon. Not. R. Astron. Soc.*, 354:10–24.
- McCarthy, I. G., Balogh, M. L., Babul, A., Poole, G. B., and Horner, D. J. (2004). Models of the Intracluster Medium with Heating and Cooling: Explaining the Global and Structural X-Ray Properties of Clusters. *Astrophys. J.*, 613:811–830.
- McCarthy, I. G., Schaye, J., Bird, S., and Le Brun, A. M. C. (2016). The BAHAMAS project: Calibrated hydrodynamical simulations for large-scale structure cosmology. *ArXiv e-prints*.
- McMullin, J. P., Waters, B., Schiebel, D., Young, W., and Golap, K. (2007). CASA Architecture and Applications. In Shaw, R. A., Hill, F., and Bell, D. J., editors, *Astronomical Data Analysis Software and Systems XVI*, volume 376 of *Astronomical Society of the Pacific Conference Series*, page 127.
- McNamara, B. R., Wise, M. W., Nulsen, P. E. J., et al. (2001). Discovery of Ghost Cavities in the X-Ray Atmosphere of Abell 2597. *Astrophys. J. Lett.*, 562:L149–L152.
- Mehrtens, N., Romer, A. K., Hilton, M., et al. (2012). The XMM Cluster Survey: optical analysis methodology and the first data release. *MNRAS*, 423:1024–1052.

- Mei, S., Holden, B. P., Blakeslee, J. P., et al. (2009). Evolution of the color-magnitude relation in galaxy clusters at $z \sim 1$ from the ACS intermediate redshift cluster survey. *The Astrophysical Journal*, 690(1):42.
- Melin, J.-B., Bartlett, J. G., and Delabrouille, J. (2005). The selection function of SZ cluster surveys. *Astron. Astrophys.*, 429:417–426.
- Meneghetti, M., Rasia, E., Merten, J., Bellagamba, F., Ettori, S., Mazzotta, P., Dolag, K., and Marri, S. (2010). Weighing simulated galaxy clusters using lensing and X-ray. *Astron. Astrophys.*, 514:A93.
- Mercurio, A., Girardi, M., Boschin, W., Merluzzi, P., and Busarello, G. (2003). Structure and evolution of galaxy clusters: Internal dynamics of ABCG 209 at $z; \sim 0.21$. *Astron. Astrophys.*, 397:431–443.
- Merloni, A., Predehl, P., Becker, W., et al. (2012). eROSITA Science Book: Mapping the Structure of the Energetic Universe. *ArXiv e-prints*.
- Merten, J., Coe, D., Dupke, R., et al. (2011). Creation of cosmic structure in the complex galaxy cluster merger Abell 2744. *Mon. Not. R. Astron. Soc.*, 417:333–347.
- Messier, C. and Niles, P. H. (1981). *The Messier catalogue of Charles Messier*.
- Mewe, R. and Schrijver, C. J. (1986). A two-component model for the corona of Lambda Andromedae. *Astron. Astrophys.*, 169:178–184.
- Miley, G. (1980). The structure of extended extragalactic radio sources. *Annu. Rev. Astron. Astrophys.*, 18:165–218.
- Miller, C. J., Krughoff, K. S., Batuski, D. J., and Hill, J. M. (2002). The MX Northern Abell Cluster Survey II: The Abell/ACO Cluster Redshifts and Spatial Analyses. *AJ*, 124:1918–1933.
- Miller, C. J., Nichol, R. C., Reichart, D., et al. (2005). The C4 Clustering Algorithm: Clusters of Galaxies in the Sloan Digital Sky Survey. *Astron. J.*, 130:968–1001.

- Mills, B. Y. (1960). On the Identification of Extragalactic Radio Sources. *Australian Journal of Physics*, 13:550.
- Minkowski, R. L. and Abell, G. O. (1963). *The National Geographic Society-Palomar Observatory Sky Survey*, page 481. the University of Chicago Press.
- Moffet, A. T. and Birkinshaw, M. (1989). A VLA survey of the three clusters of galaxies 0016 + 16, Abell 665, and Abell 2218. *Astron. J.*, 98:1148–1174.
- Mohr, J. J., Geller, M. J., and Wegner, G. (1996). A Dynamical Analysis of the Poor Galaxy Clusters Abell 2626 and Abell 2440. *Astron. J.*, 112:1816.
- Morgan, W. W. (1961). The Classification of Clusters of Galaxies. *Proceedings of the National Academy of Science*, 47:905–906.
- Motl, P. M., Hallman, E. J., Burns, J. O., and Norman, M. L. (2005). The Integrated Sunyaev-Zeldovich Effect as a Superior Method for Measuring the Mass of Clusters of Galaxies. *Astrophys. J. Lett.*, 623:L63–L66.
- Mould, J. R., Huchra, J. P., Freedman, W. L., et al. (2000). The Hubble Space Telescope Key Project on the Extragalactic Distance Scale. XXVIII. Combining the Constraints on the Hubble Constant. *Astrophys. J.*, 529:786–794.
- Mulchaey, J. S., Lubin, L. M., Fassnacht, C., Rosati, P., and Jeltema, T. E. (2006). X-Ray-selected Intermediate-Redshift Groups of Galaxies. *ApJ*, 646:133–142.
- Mullis, C. R., McNamara, B. R., Quintana, H., et al. (2003). The 160 Square Degree ROSAT Survey: The Revised Catalog of 201 Clusters with Spectroscopic Redshifts. *Astrophys. J.*, 594:154–171.
- Munari, E., Biviano, A., Borgani, S., Murante, G., and Fabjan, D. (2013). The relation between velocity dispersion and mass in simulated clusters of galaxies: dependence on the tracer and the baryonic physics. *MNRAS*, 430:2638–2649.

- Murgia, M., Parma, P., Mack, K.-H., et al. (2011). Dying radio galaxies in clusters. *Astron. Astrophys.*, 526:A148.
- Myers, S. T., Baker, J. E., Readhead, A. C. S., Leitch, E. M., and Herbig, T. (1997). Measurements of the Sunyaev-Zeldovich Effect in the Nearby Clusters A478, A2142, and A2256. *Astrophys. J.*, 485:1–21.
- Nagai, D., Vikhlinin, A., and Kravtsov, A. V. (2007). Testing X-Ray Measurements of Galaxy Clusters with Cosmological Simulations. *Astrophys. J.*, 655:98–108.
- Narlikar, J. V. and Wickramasinghe, N. C. (1967). Microwave Background in a Steady-state Universe. *Nature.*, 216:43–44.
- Nastasi, A., Böhringer, H., Fassbender, R., et al. (2014). Kinematic analysis of a sample of X-ray luminous distant galaxy clusters. The $L_X - \sigma_v$ relation in the $z > 0.6$ universe. *A&A*, 564:A17.
- Navarro, J. F., Frenk, C. S., and White, S. D. M. (1997). A Universal Density Profile from Hierarchical Clustering. *Astrophys. J.*, 490:493–508.
- Nevalainen, J., Markevitch, M., and Forman, W. (2000). The Cluster M-T Relation from Temperature Profiles Observed with ASCA and ROSAT. *Astrophys. J.*, 532:694–699.
- Novicki, M. C., Sornig, M., and Henry, J. P. (2002). The Evolution of the Galaxy Cluster Luminosity-Temperature Relation. *Astron. J.*, 124:2413–2424.
- O’Dea, C. P. and Owen, F. N. (1985). The global properties of a representative sample of 51 narrow-angle-tail radio sources in the directions of Abell clusters. *Astron. J.*, 90:954–972.
- O’Donoghue, A. A., Eilek, J. A., and Owen, F. N. (1993). Flow dynamics and bending of wide-angle tailed radio sources. *Astrophys. J.*, 408:428–445.
- O’Donoghue, A. A., Owen, F. N., and Eilek, J. A. (1990). VLA observations of wide-angle tailed radio sources. *Astrophys. J. Supp.*, 72:75–131.

- Oemler, Jr., A. (1974). The Systematic Properties of Clusters of Galaxies. Photometry of 15 Clusters. *Astrophys. J.*, 194:1–20.
- Ofek, E. O., Oguri, M., Jackson, N., Inada, N., and Kayo, I. (2007). SDSS J131339.98+515128.3: a new gravitationally lensed quasar selected based on near-infrared excess. *MNRAS*, 382:412–418.
- Ogrean, G. A., Brüggén, M., van Weeren, R. J., Röttgering, H., Croston, J. H., and Hoeft, M. (2013). Challenges to our understanding of radio relics: X-ray observations of the Toothbrush cluster. *Mon. Not. R. Astron. Soc.*, 433:812–824.
- O’Hara, T. B., Mohr, J. J., Bialek, J. J., and Evrard, A. E. (2006). Effects of Mergers and Core Structure on the Bulk Properties of Nearby Galaxy Clusters. *Astrophys. J.*, 639:64–80.
- Oke, J. B., Postman, M., and Lubin, L. M. (1998). A Study of Nine High-Redshift Clusters of Galaxies. I. The Survey. *Astron. J.*, 116:549–559.
- Orrú, E., Murgia, M., Feretti, L., Govoni, F., Brunetti, G., Giovannini, G., Girardi, M., and Setti, G. (2007). Low-frequency study of two clusters of galaxies: A2744 and A2219. *Astron. Astrophys.*, 467:943–954.
- Ortiz-Gil, A., Guzzo, L., Schuecker, P., Böhringer, H., and Collins, C. A. (2004). The X-ray luminosity-velocity dispersion relation in the REFLEX cluster survey. *MNRAS*, 348:325–332.
- Ota, N., Nagayoshi, K., Pratt, G. W., Kitayama, T., Oshima, T., and Reiprich, T. H. (2014). Investigating the hard X-ray emission from the hottest Abell cluster A2163 with Suzaku. *Astron. Astrophys.*, 562:A60.
- Owen, F. N. and Rudnick, L. (1976). Radio sources with wide-angle tails in Abell clusters of galaxies. *Astrophys. J. Lett.*, 205:L1–L4.
- Owen, F. N., White, R. A., and Burns, J. O. (1992). A 20 centimeter VLA survey of Abell clusters of galaxies. II - Images and optical identifications. *Astrophys. J. Supp.*, 80:501–529.

- Owers, M. S., Randall, S. W., Nulsen, P. E. J., Couch, W. J., David, L. P., and Kempner, J. C. (2011). The Dissection of Abell 2744: A Rich Cluster Growing Through Major and Minor Mergers. *Astrophys. J.*, 728:27.
- Patel, S. K., Joy, M., Carlstrom, J. E., et al. (2000). The Distance and Mass of the Galaxy Cluster Abell 1995 Derived from Sunyaev-Zeldovich Effect and X-Ray Measurements. *Astrophys. J.*, 541:37–48.
- Paterno-Mahler, R., Blanton, E. L., Wing, J., Ashby, M. L. N., Brodwin, M., and Golden-Marx, E. (2016). The High-Redshift Clusters Occupied by Bent Radio AGN (COBRA) Survey. In Kaviraj, S., editor, *Galaxies at High Redshift and Their Evolution Over Cosmic Time*, volume 319 of *IAU Symposium*, pages 62–62.
- Peebles, P. J. E. (1982). Large-scale background temperature and mass fluctuations due to scale-invariant primeval perturbations. *Astrophys. J. Lett.*, 263:L1–L5.
- Peebles, P. J. E., Schramm, D. N., Kron, R. G., and Turner, E. L. (1991). The case for the relativistic hot big bang cosmology. *Nature.*, 352:769–776.
- Peebles, P. J. E. and Yu, J. T. (1970). Primeval Adiabatic Perturbation in an Expanding Universe. *Astrophys. J.*, 162:815.
- Pentericci, L., Röttgering, H. J. A., Miley, G. K., McCarthy, P., Spinrad, H., van Breugel, W. J. M., and Macchetto, F. (1999). HST images and properties of the most distant radio galaxies. *Astron. Astrophys.*, 341:329–347.
- Penzias, A. A. and Wilson, R. W. (1965). A Measurement of Excess Antenna Temperature at 4080 Mc/s. *Astrophys. J.*, 142:419–421.
- Peres, C. B., Fabian, A. C., Edge, A. C., Allen, S. W., Johnstone, R. M., and White, D. A. (1998). A ROSAT study of the cores of clusters of galaxies - I. Cooling flows in an X-ray flux-limited sample. *Mon. Not. R. Astron. Soc.*, 298:416–432.

- Perlman, E. S., Horner, D. J., Jones, L. R., Scharf, C. A., Ebeling, H., Wegner, G., and Malkan, M. (2002). The WARPS Survey. VI. Galaxy Cluster and Source Identifications from Phase I. *Astrophys. J. Supp.*, 140:265–301.
- Persic, M., Salucci, P., and Stel, F. (1996). The universal rotation curve of spiral galaxies - I. The dark matter connection. *Mon. Not. R. Astron. Soc.*, 281:27–47.
- Peterson, J. R., Kahn, S. M., Paerels, F. B. S., Kaastra, J. S., Tamura, T., Bleeker, J. A. M., Ferrigno, C., and Jernigan, J. G. (2003). High-Resolution X-Ray Spectroscopic Constraints on Cooling-Flow Models for Clusters of Galaxies. *Astrophys. J.*, 590:207–224.
- Petrosian, V. (2001). On the Nonthermal Emission and Acceleration of Electrons in Coma and Other Clusters of Galaxies. *Astrophys. J.*, 557:560–572.
- Pierre, M., Matsumoto, H., Tsuru, T., Ebeling, H., and Hunstead, R. (1999). ASCA observations of massive medium-distant clusters of galaxies. I. A 1300 and A 1732. *Astron. Astrophys. Supp.*, 136:173–177.
- Piffaretti, R. and Valdarnini, R. (2008). Total mass biases in X-ray galaxy clusters. *Astron. Astrophys.*, 491:71–87.
- Pinkney, J., Rhee, G., Burns, J. O., Hill, J. M., Oegerle, W., Batuski, D., and Hintzen, P. (1993). The Dynamics of the Galaxy Cluster Abell 2634. *ApJ*, 416:36.
- Planck Collaboration, Adam, R., Ade, P. A. R., et al. (2016a). Planck 2015 results. I. Overview of products and scientific results. *Astron. Astrophys.*, 594:A1.
- Planck Collaboration, Ade, P. A. R., Aghanim, N., et al. (2014a). Planck 2013 results. XXIX. The Planck catalogue of Sunyaev-Zeldovich sources. *Astron. Astrophys.*, 571:A29.
- Planck Collaboration, Ade, P. A. R., Aghanim, N., et al. (2014b). Planck 2013 results. XVI. Cosmological parameters. *Astron. Astrophys.*, 571:A16.
- Planck Collaboration, Ade, P. A. R., Aghanim, N., et al. (2014c). Planck 2013 results. XVI. Cosmological parameters. *Astron. Astrophys.*, 571:A16.

- Planck Collaboration, Ade, P. A. R., Aghanim, N., et al. (2014d). Planck 2013 results. XX. Cosmology from Sunyaev-Zeldovich cluster counts. *Astron. Astrophys.*, 571:A20.
- Planck Collaboration, Ade, P. A. R., Aghanim, N., et al. (2011). Planck early results. XI. Calibration of the local galaxy cluster Sunyaev-Zeldovich scaling relations. *Astron. Astrophys.*, 536:A11.
- Planck Collaboration, Ade, P. A. R., Aghanim, N., et al. (2016b). Planck 2015 results. XXVII. The second Planck catalogue of Sunyaev-Zeldovich sources. *Astron. Astrophys.*, 594:A27.
- Planck Collaboration, Ade, P. A. R., Aghanim, N., et al. (2015). Planck 2015 results. XXIV. Cosmology from Sunyaev-Zeldovich cluster counts. *ArXiv e-prints*.
- Planck Collaboration, Ade, P. A. R., Aghanim, N., et al. (2016c). Planck 2015 results. XIII. Cosmological parameters. *Astron. Astrophys.*, 594:A13.
- Planck Collaboration, Ade, P. A. R., Aghanim, N., et al. (2016d). Planck 2015 results. XIII. Cosmological parameters. *Astron. Astrophys.*, 594:A13.
- Pointecouteau, E., Giard, M., Benoit, A., Désert, F. X., Bernard, J. P., Coron, N., and Lamarre, J. M. (2001). Extended Sunyaev-Zeldovich Map of the Most Luminous X-Ray Cluster, RX J1347-1145. *Astrophys. J.*, 552:42–48.
- Ponman, T. J., Bourner, P. D. J., Ebeling, H., and Böhringer, H. (1996). A ROSAT survey of Hickson's compact galaxy groups. *MNRAS*, 283:690–708.
- Poole, G. B., Babul, A., McCarthy, I. G., Fardal, M. A., Bildfell, C. J., Quinn, T., and Mahdavi, A. (2007). The impact of mergers on relaxed X-ray clusters - II. Effects on global X-ray and Sunyaev-Zel'dovich properties and their scaling relations. *Mon. Not. R. Astron. Soc.*, 380:437–454.
- Poole, G. B., Fardal, M. A., Babul, A., McCarthy, I. G., Quinn, T., and Wadsley, J. (2006). The impact of mergers on relaxed X-ray clusters - I. Dynamical evolution and emergent transient structures. *Mon. Not. R. Astron. Soc.*, 373:881–905.

- Possenti, A. (2010). Why single dishes in future radio astronomy ? Slides of a talk given at Effelsberg Single Dish School, September 27, Bonn - MPIfR.
- Postman, M., Lubin, L. M., Gunn, J. E., Oke, J. B., Hoessel, J. G., Schneider, D. P., and Christensen, J. A. (1996). The Palomar Distant Clusters Survey. I. The Cluster Catalog. *Astron. J.*, 111:615.
- Pratt, G. W., Böhringer, H., Croston, J. H., Arnaud, M., Borgani, S., Finoguenov, A., and Temple, R. F. (2007). Temperature profiles of a representative sample of nearby X-ray galaxy clusters. *Astron. Astrophys.*, 461:71–80.
- Pratt, G. W., Croston, J. H., Arnaud, M., and Böhringer, H. (2009). Galaxy cluster X-ray luminosity scaling relations from a representative local sample (REXCESS). *Astron. Astrophys.*, 498:361–378.
- Pratt, N. (1977). The cosmos measuring machine. *Vistas in Astronomy*, 21:1 – 42.
- Prestage, R. M. and Peacock, J. A. (1988). The cluster environments of powerful radio galaxies. *Mon. Not. R. Astron. Soc.*, 230:131–160.
- Prestage, R. M. and Peacock, J. A. (1989). Erratum - the Cluster Environments of Powerful Radio Galaxies. *Mon. Not. R. Astron. Soc.*, 236:959.
- Quintana, H. and Melnick, J. (1982). The correlation between X-ray luminosity and velocity dispersion in clusters of galaxies. *AJ*, 87:972–979.
- Randall, S. W., Sarazin, C. L., and Ricker, P. M. (2002). The Effect of Merger Boosts on the Luminosity, Temperature, and Inferred Mass Functions of Clusters of Galaxies. *Astrophys. J.*, 577:579–594.
- Reese, E. D., Carlstrom, J. E., Joy, M., Mohr, J. J., Grego, L., and Holzappel, W. L. (2002). Determining the Cosmic Distance Scale from Interferometric Measurements of the Sunyaev-Zeldovich Effect. *Astrophys. J.*, 581:53–85.

- Reese, E. D., Mohr, J. J., Carlstrom, J. E., et al. (2000). Sunyaev-Zeldovich Effect-derived Distances to the High-Redshift Clusters MS 0451.6-0305 and CL 0016+16. *Astrophys. J.*, 533:38–49.
- Reichardt, C. L., Stalder, B., Bleem, L. E., et al. (2013). Galaxy Clusters Discovered via the Sunyaev-Zel'dovich Effect in the First 720 Square Degrees of the South Pole Telescope Survey. *Astrophys. J.*, 763:127.
- Reichert, A., Böhringer, H., Fassbender, R., and Mühlegger, M. (2011). Observational constraints on the redshift evolution of X-ray scaling relations of galaxy clusters out to $z \sim 1.5$. *Astron. Astrophys.*, 535:A4.
- Reid, I. N., Brewer, C., Brucato, R. J., et al. (1991). The second Palomar Sky Survey. *Pub. Astron. Soc. Pacific*, 103:661–674.
- Reiprich, T. H. and Böhringer, H. (2002). The Mass Function of an X-Ray Flux-limited Sample of Galaxy Clusters. *Astrophys. J.*, 567:716–740.
- Rines, K., Geller, M. J., Diaferio, A., and Kurtz, M. J. (2013). Measuring the Ultimate Halo Mass of Galaxy Clusters: Redshifts and Mass Profiles from the Hectospec Cluster Survey (HeCS). *Astrophys. J.*, 767:15.
- Ritchie, B. W. and Thomas, P. A. (2002). Hydrodynamic simulations of merging clusters of galaxies. *MNRAS*, 329:675–688.
- Rizza, E., Burns, J. O., Ledlow, M. J., Owen, F. N., Voges, W., and Bliton, M. (1998). X-ray observations of distant Abell clusters. *Mon. Not. R. Astron. Soc.*, 301:328–342.
- Robertson, H. P. (1929). On the Foundations of Relativistic Cosmology. *Proceedings of the National Academy of Science*, 15:822–829.
- Roettiger, K., Burns, J. O., and Stone, J. M. (1999). A Cluster Merger and the Origin of the Extended Radio Emission in Abell 3667. *Astrophys. J.*, 518:603–612.

- Roger, R. S., Costain, C. H., and Lacey, J. D. (1969). Spectral flux densities of radio sources at 22.25 MHz. I. *Astron. J.*, 74:366–372.
- Romer, A. K., Viana, P. T. P., Liddle, A. R., and Mann, R. G. (2001). A Serendipitous Galaxy Cluster Survey with XMM: Expected Catalog Properties and Scientific Applications. *Astrophys. J.*, 547:594–608.
- Rood, H. J. and Sastry, G. N. (1971). "Tuning Fork" Classification of Rich Clusters of Galaxies. *Pub. Astron. Soc. Pacific*, 83:313.
- Roos, M. (2008). Expansion of the Universe - Standard Big Bang Model. *ArXiv e-prints*.
- Rottgering, H. J. A., Wieringa, M. H., Hunstead, R. W., and Ekers, R. D. (1997). The extended radio emission in the luminous X-ray cluster A3667. *Mon. Not. R. Astron. Soc.*, 290:577–584.
- Rowley, D. R., Thomas, P. A., and Kay, S. T. (2004). The merger history of clusters and its effect on the X-ray properties of the intracluster medium. *Mon. Not. R. Astron. Soc.*, 352:508–522.
- Rozo, E., Rykoff, E. S., Bartlett, J. G., and Evrard, A. (2014). A comparative study of local galaxy clusters - I. Derived X-ray observables. *Mon. Not. R. Astron. Soc.*, 438:49–61.
- Rozo, E., Rykoff, E. S., Evrard, A., et al. (2009). Constraining the Scatter in the Mass-richness Relation of maxBCG Clusters with Weak Lensing and X-ray Data. *ApJ*, 699:768–781.
- Rozo, E., Wechsler, R. H., Rykoff, E. S., et al. (2010). Cosmological Constraints from the Sloan Digital Sky Survey maxBCG Cluster Catalog. *Astrophys. J.*, 708:645–660.
- Rubin, V. C., Ford, W. K. J., and Thonnard, N. (1980). Rotational properties of 21 SC galaxies with a large range of luminosities and radii, from NGC 4605 ($R = 4\text{kpc}$) to UGC 2885 ($R = 122\text{kpc}$). *Astrophys. J.*, 238:471–487.
- Rudnick, L. and Owen, F. N. (1976). Head-tail radio sources in clusters of galaxies. *Astrophys. J. Lett.*, 203:L107–L111.

- Russell, H. R., van Weeren, R. J., Edge, A. C., et al. (2011). A merger mystery: no extended radio emission in the merging cluster Abell 2146. *Mon. Not. R. Astron. Soc.*, 417:L1–L5.
- Rybicki, G. B. and Lightman, A. P. (1986). *Radiative Processes in Astrophysics*.
- Rykoff, E. S., Rozo, E., Busha, M. T., et al. (2014). redMaPPer. I. Algorithm and SDSS DR8 Catalog. *Astrophys. J.*, 785:104.
- Rykoff, E. S., Rozo, E., Hollowood, D., et al. (2016). The RedMaPPer Galaxy Cluster Catalog From DES Science Verification Data. *Astrophys. J. Supp.*, 224:1.
- Sacchi, N., La Franca, F., Feruglio, C., et al. (2009). Spectroscopic Identifications of Spitzer Sources in the SWIRE/XMM-Newton/ELAIS-S1 Field: A Large Fraction of Active Galactic Nucleus with High $F(24\ \mu\text{m})/F(R)$ Ratio. *ApJ*, 703:1778–1790.
- Sadat, R. (1997). Clusters of Galaxies and Mass Estimates. In Valls-Gabaud, D., Hendry, M. A., Molaro, P., and Chamcham, K., editors, *From Quantum Fluctuations to Cosmological Structures*, volume 126 of *Astronomical Society of the Pacific Conference Series*, page 349.
- Sadat, R., Blanchard, A., Kneib, J.-P., Mathez, G., Madore, B., and Mazzarella, J. M. (2004). Introducing BAX: A database for X-ray clusters and groups of galaxies. *Astron. Astrophys.*, 424:1097–1100.
- Sahlén, M., Viana, P. T. P., Liddle, A. R., et al. (2009). The XMM Cluster Survey: forecasting cosmological and cluster scaling-relation parameter constraints. *MNRAS*, 397:577–607.
- Sakelliou, I. and Merrifield, M. R. (1998). X-ray emission from the galaxies in Abell 2634. *Mon. Not. R. Astron. Soc.*, 293:489.
- Salucci, P., Lapi, A., Tonini, C., Gentile, G., Yegorova, I., and Klein, U. (2007). The universal rotation curve of spiral galaxies - II. The dark matter distribution out to the virial radius. *Mon. Not. R. Astron. Soc.*, 378:41–47.
- Sánchez Almeida, J., Aguerri, J. A. L., Muñoz-Tuñón, C., and Huertas-Company, M. (2011). Relationship between Hubble Type and Spectroscopic Class in Local Galaxies. *ApJ*, 735:125.

- Sandage, A. (1958). Current Problems in the Extragalactic Distance Scale. *Astrophys. J.*, 127:513.
- Sandage, A. and Tammann, G. A. (1974). Steps toward the Hubble constant. III - The distance and stellar content of the M101 group of galaxies. *Astrophys. J.*, 194:223–243.
- Santos, J. S., Rosati, P., Tozzi, P., Böhringer, H., Ettori, S., and Bignamini, A. (2008). Searching for cool core clusters at high redshift. *Astron. Astrophys.*, 483:35–47.
- Sarazin, C. L. (1988). *X-ray emission from clusters of galaxies*.
- Sarazin, C. L. and Boller, T. (1989). Book-Review - X-Ray Emission from Clusters of Galaxies. *Astronomische Nachrichten*, 310:362.
- Saunders, R., Kneissl, R., Grainge, K., et al. (2003). A measurement of H_0 from Ryle Telescope, ASCA and ROSAT observations of Abell 773. *Mon. Not. R. Astron. Soc.*, 341:937–940.
- Schaerer, D., Contini, T., and Pindao, M. (1999). New catalogue of Wolf-Rayet galaxies and high-excitation extra-galactic HII regions. *A&AS*, 136:35–52.
- Schafer, R. A. (1991). *XSPEC, an x-ray spectral fitting package : version 2 of the user's guide*.
- Scharf, C. A., Ebeling, H., Perlman, E., Malkan, M., and Wegner, G. (1997). The Wide-Angle ROSAT Pointed X-Ray Survey of Galaxies, Groups, and Clusters. I. Method and First Results. *Astrophys. J.*, 477:79–92.
- Schlickeiser, R., Sievers, A., and Thiemann, H. (1987). The diffuse radio emission from the Coma cluster. *Astron. Astrophys.*, 182:21–35.
- Schmidt, M. (1965). Optical Spectra and Redshifts of 31 Radio Galaxies. *Astrophys. J.*, 141:1.
- Schweizer, F. (1996). Colliding and Merging Galaxies. III. The Dynamically Young Merger Remnant NGC 3921. *AJ*, 111:109.

- Scodreggio, M., Solanes, J. M., Giovanelli, R., and Haynes, M. P. (1995). The spatial distribution, kinematics, and dynamics of the galaxies in the region of Abell 2634 and 2666. *ApJ*, 444:41–63.
- Sehgal, N., Trac, H., Acquaviva, V., et al. (2011). The Atacama Cosmology Telescope: Cosmology from Galaxy Clusters Detected via the Sunyaev-Zel’dovich Effect. *Astrophys. J.*, 732:44.
- Shectman, S. A. (1985). Clusters of galaxies from the Shane-Wirtanen counts. *Astrophys. J. Supp.*, 57:77–90.
- Shimwell, T. W., Brown, S., Feain, I. J., Feretti, L., Gaensler, B. M., and Lage, C. (2014). Deep radio observations of the radio halo of the bullet cluster 1E 0657-55.8. *Mon. Not. R. Astron. Soc.*, 440:2901–2915.
- Short, C. J., Thomas, P. A., Young, O. E., Pearce, F. R., Jenkins, A., and Muanwong, O. (2010). The evolution of galaxy cluster X-ray scaling relations. *MNRAS*, 408:2213–2233.
- Sifón, C., Battaglia, N., Menanteau, F., et al. (2015). The Atacama Cosmology Telescope: Dynamical masses for 44 SZ-selected galaxy clusters over 755 square degrees. *ArXiv e-prints*.
- Sifón, C., Menanteau, F., Hasselfield, M., et al. (2013). The Atacama Cosmology Telescope: Dynamical Masses and Scaling Relations for a Sample of Massive Sunyaev-Zel’dovich Effect Selected Galaxy Clusters. *ApJ*, 772:25.
- Silverman, J. D., Green, P. J., Barkhouse, W. A., et al. (2005). Hard X-Ray-emitting Active Galactic Nuclei Selected by the Chandra Multiwavelength Project. *ApJ*, 618:123–138.
- Slee, O. B., Roy, A. L., Murgia, M., Andernach, H., and Ehle, M. (2001). Four Extreme Relic Radio Sources in Clusters of Galaxies. *Astron. J.*, 122:1172–1193.
- Smith, G. P., Kneib, J.-P., Smail, I., Mazzotta, P., Ebeling, H., and Czoske, O. (2005). A Hubble Space Telescope lensing survey of X-ray luminous galaxy clusters - IV. Mass, structure and thermodynamics of cluster cores at $z=0.2$. *Mon. Not. R. Astron. Soc.*, 359:417–446.

- Smith, R. J., Hudson, M. J., Nelan, J. E., et al. (2004). NOAO Fundamental Plane Survey. I. Survey Design, Redshifts, and Velocity Dispersion Data. *AJ*, 128:1558–1569.
- Smith, S. (1936). The Mass of the Virgo Cluster. *Astrophys. J.*, 83:23.
- Solovyeva, L., Anokhin, S., Feretti, L., Sauvageot, J. L., Teyssier, R., Giovannini, G., Govoni, F., and Neumann, D. (2008). The dynamical state of A548 from XMM-Newton data: X-ray and radio connection. *Astron. Astrophys.*, 484:621–630.
- Springel, V. (2004). Studying clusters of galaxies with hydrodynamical simulations. In Diaferio, A., editor, *IAU Colloq. 195: Outskirts of Galaxy Clusters: Intense Life in the Suburbs*, pages 260–266.
- Springel, V., White, S. D. M., Jenkins, A., et al. (2005). Simulations of the formation, evolution and clustering of galaxies and quasars. *Nature*, 435:629–636.
- Stocke, J. T., Morris, S. L., Gioia, I. M., Maccacaro, T., Schild, R., Wolter, A., Fleming, T. A., and Henry, J. P. (1991). The Einstein Observatory Extended Medium-Sensitivity Survey. II - The optical identifications. *Astrophys. J. Supp.*, 76:813–874.
- Stott, J. P., Collins, C. A., Sahlén, M., et al. (2010). The XMM Cluster Survey: The Build-up of Stellar Mass in Brightest Cluster Galaxies at High Redshift. *ApJ*, 718:23–30.
- Stoughton, C., Lupton, R. H., Bernardi, M., et al. (2002). Sloan Digital Sky Survey: Early Data Release. *AJ*, 123:485–548.
- Struble, M. F. and Rood, H. J. (1999). A Compilation of Redshifts and Velocity Dispersions for ACO Clusters. *Astrophys. J. Supp.*, 125:35–71.
- Sunyaev, R. A. and Zeldovich, Y. B. (1970a). Small-Scale Fluctuations of Relic Radiation. *Astrophys. Space Sci.*, 7:3–19.
- Sunyaev, R. A. and Zeldovich, Y. B. (1970b). The Spectrum of Primordial Radiation, its Distortions and their Significance. *Comments on Astrophysics and Space Physics*, 2:66.

- Sunyaev, R. A. and Zeldovich, Y. B. (1972). The Observations of Relic Radiation as a Test of the Nature of X-Ray Radiation from the Clusters of Galaxies. *Comments on Astrophysics and Space Physics*, 4:173.
- Sweet, S. M., Drinkwater, M. J., Meurer, G., Kilborn, V., Audcent-Ross, F., Baumgardt, H., and Bekki, K. (2016). Kinematics of dwarf galaxies in gas-rich groups, and the survival and detectability of tidal dwarf galaxies. *Mon. Not. R. Astron. Soc.*, 455:2508–2528.
- Takey, A., Schwobe, A., and Lamer, G. (2011). The 2XMMi/SDSS Galaxy Cluster Survey. I. The first cluster sample and X-ray luminosity-temperature relation. *Astron. Astrophys.*, 534:A120.
- Takey, A., Schwobe, A., and Lamer, G. (2013). The 2XMMi/SDSS Galaxy Cluster Survey. II. The optically confirmed cluster sample and the L_X - T relation. *Astron. Astrophys.*, 558:A75.
- Thompson, A. R., Moran, J. M., and Swenson, Jr., G. W. (2001). *Interferometry and Synthesis in Radio Astronomy, 2nd Edition*.
- Tinker, J. L., Sheldon, E. S., Wechsler, R. H., et al. (2012). Cosmological Constraints from Galaxy Clustering and the Mass-to-number Ratio of Galaxy Clusters. *Astrophys. J.*, 745:16.
- Tonry, J. and Davis, M. (1979). A survey of galaxy redshifts. I - Data reduction techniques. *AJ*, 84:1511–1525.
- Tortora, C., Napolitano, N. R., Saglia, R. P., Romanowsky, A. J., Covone, G., and Capaccioli, M. (2014). Evolution of central dark matter of early-type galaxies up to $z \sim 0.8$. *Mon. Not. R. Astron. Soc.*, 445:162–174.
- Tran, K.-V. H., Kelson, D. D., van Dokkum, P., Franx, M., Illingworth, G. D., and Magee, D. (1999). The Velocity Dispersion of MS 1054-03: A Massive Galaxy Cluster at High Redshift. *ApJ*, 522:39–45.
- Tribble, P. C. (1993). Radio haloes, cluster mergers, and cooling flows. *Mon. Not. R. Astron. Soc.*, 263:31–36.

- Trichas, M., Rowan-Robinson, M., Georgakakis, A., et al. (2010). Spectroscopic identifications of SWIRE sources in ELAIS-N1. *MNRAS*, 405:2243–2252.
- Trump, J. R., Impey, C. D., McCarthy, P. J., et al. (2007). Magellan Spectroscopy of AGN Candidates in the COSMOS Field. *ApJS*, 172:383–395.
- Tukey, J. W. (1977). *Exploratory data analysis*.
- Uson, J. M. (1986). The Sunyaev-Zel'dovich effect - Measurements and implications. *National Radio Astronomy Observatory Workshop*, 16:255–260.
- Šuhada, R., Fassbender, R., Nastasi, A., et al. (2011). Exploring the galaxy cluster-group transition regime at high redshifts. Physical properties of two newly detected $z > 1$ systems. *Astron. Astrophys.*, 530:A110.
- van den Bergh, S. (1961). Radio Sources and Clusters of Galaxies. *Astrophys. J.*, 134:970.
- van den Bergh, S. (1970). Extra-galactic Distance Scale. *Nature.*, 225:503–505.
- van den Bergh, S. (1972). A New Method for Estimating the Hubble Constant. *Astron. Astrophys.*, 20:469.
- van den Bergh, S. (1975). *The Extragalactic Distance Scale*, page 509. the University of Chicago Press.
- van den Bosch, F. C. and Swaters, R. A. (2001). Dwarf galaxy rotation curves and the core problem of dark matter haloes. *Mon. Not. R. Astron. Soc.*, 325:1017–1038.
- van der Marel, R. P., Besla, G., Cox, T. J., Sohn, S. T., and Anderson, J. (2012). The M31 Velocity Vector. III. Future Milky Way M31-M33 Orbital Evolution, Merging, and Fate of the Sun. *Astrophys. J.*, 753:9.
- van Dokkum, P. G., Franx, M., Kelson, D. D., Illingworth, G. D., Fisher, D., and Fabricant, D. (1998). The Color-Magnitude Relation in CL 1358+62 at $Z = 0.33$: Evidence for Significant Evolution in the S0 Population. *Astrophys. J.*, 500:714–737.

- van Haarlem, M. P., Frenk, C. S., and White, S. D. M. (1997). Projection effects in cluster catalogues. *Mon. Not. R. Astron. Soc.*, 287:817–832.
- van Weeren, R. J., Brüggén, M., Röttgering, H. J. A., Hoeft, M., Nuza, S. E., and Intema, H. T. (2011). Radio continuum observations of new radio halos and relics from the NVSS and WENSS surveys. Relic orientations, cluster X-ray luminosity, and redshift distributions. *Astron. Astrophys.*, 533:A35.
- van Weeren, R. J., Röttgering, H. J. A., Brüggén, M., and Hoeft, M. (2010). Particle Acceleration on Megaparsec Scales in a Merging Galaxy Cluster. *Science*, 330:347.
- Vanderlinde, K., Crawford, T. M., de Haan, T., et al. (2010). Galaxy Clusters Selected with the Sunyaev-Zel'dovich Effect from 2008 South Pole Telescope Observations. *Astrophys. J.*, 722:1180–1196.
- Ventimiglia, D. A., Voit, G. M., Donahue, M., and Ameglio, S. (2008). Substructure and Scatter in the Mass-Temperature Relations of Simulated Clusters. *Astrophys. J.*, 685:118–127.
- Venturi, T., Giacintucci, S., Brunetti, G., Cassano, R., Bardelli, S., Dallacasa, D., and Setti, G. (2007). GMRT radio halo survey in galaxy clusters at $z = 0.2-0.4$. I. The REFLEX sub-sample. *Astron. Astrophys.*, 463:937–947.
- Venturi, T., Giacintucci, S., Dallacasa, D., Cassano, R., Brunetti, G., Bardelli, S., and Setti, G. (2008). GMRT radio halo survey in galaxy clusters at $z = 0.2-0.4$. II. The eBCS clusters and analysis of the complete sample. *Astron. Astrophys.*, 484:327–340.
- Verdugo, M., Ziegler, B. L., and Gerken, B. (2008). The galaxy populations from the centers to the infall regions in $z > 0.25$ clusters. *A&A*, 486:9–24.
- Vikhlinin, A. et al. (2009). Chandra Cluster Cosmology Project III: Cosmological Parameter Constraints. *Astrophys. J.*, 692:1060–1074.

- Vikhlinin, A., Kravtsov, A., Forman, W., Jones, C., Markevitch, M., Murray, S. S., and Van Speybroeck, L. (2006a). Chandra Sample of Nearby Relaxed Galaxy Clusters: Mass, Gas Fraction, and Mass-Temperature Relation. *ApJ*, 640:691–709.
- Vikhlinin, A., Kravtsov, A., Forman, W., Jones, C., Markevitch, M., Murray, S. S., and Van Speybroeck, L. (2006b). Chandra Sample of Nearby Relaxed Galaxy Clusters: Mass, Gas Fraction, and Mass-Temperature Relation. *Astrophys. J.*, 640:691–709.
- Vikhlinin, A., McNamara, B. R., Forman, W., Jones, C., Quintana, H., and Hornstrup, A. (1998). A Catalog of 200 Galaxy Clusters Serendipitously Detected in the ROSAT PSPC Pointed Observations. *ApJ*, 502:558–581.
- Vikhlinin, A., van Speybroeck, L., Markevitch, M., Forman, W. R., and Grego, L. (2002). Evolution of the Cluster X-Ray Scaling Relations since $z > 0.4$. *ApJ*, 578:L107–L111.
- Visvanathan, N. and Sandage, A. (1977). The color-absolute magnitude relation for E and S0 galaxies. I - Calibration and tests for universality using Virgo and eight other nearby clusters. *Astrophys. J.*, 216:214–226.
- Vogelsberger, M., Genel, S., Springel, V., et al. (2014). Properties of galaxies reproduced by a hydrodynamic simulation. *Nature.*, 509:177–182.
- Voit, G. M. (2005). Tracing cosmic evolution with clusters of galaxies. *Reviews of Modern Physics*, 77:207–258.
- Wegner, G. A. (2011). The double galaxy cluster Abell 2465 - I. Basic properties: optical imaging and spectroscopy. *MNRAS*, 413:1333–1352.
- Wen, Z. L., Han, J. L., and Liu, F. S. (2009). Galaxy Clusters Identified from the SDSS DR6 and Their Properties. *Astrophys. J. Supp.*, 183:197–213.
- White, D. A. (2000). Deconvolution of ASCA X-ray data - II. Radial temperature and metallicity profiles for 106 galaxy clusters. *Mon. Not. R. Astron. Soc.*, 312:663–688.

- White, D. A., Jones, C., and Forman, W. (1997). An investigation of cooling flows and general cluster properties from an X-ray image deprojection analysis of 207 clusters of galaxies. *MNRAS*, 292:419.
- White, M., editor (1999). *Anisotropies in the CMB*.
- Willson, M. A. G. (1970). Radio observations of the cluster of galaxies in Coma Berenices - the 5C4 survey. *Mon. Not. R. Astron. Soc.*, 151:1–44.
- Wilson, A. S., Young, A. J., and Shopbell, P. L. (2000). Chandra Observations of Cygnus A: Magnetic Field Strengths in the Hot Spots of a Radio Galaxy. *Astrophys. J. Lett.*, 544:L27–L30.
- Witz, Stephan W. (2015). VLA observational status summary 2015a.
- Wojtak, R., Łokas, E. L., Mamon, G. A., and Gottlöber, S. (2009). The mass and anisotropy profiles of galaxy clusters from the projected phase-space density: testing the method on simulated data. *Mon. Not. R. Astron. Soc.*, 399:812–821.
- Worrall, D. M. and Birkinshaw, M. (2003). The temperature and distribution of gas in cl 0016+16 measured with xmm-Newton. *Monthly Notices of the Royal Astronomical Society*, 340(4):1261–1268.
- Wu, X.-P., Fang, L.-Z., and Xu, W. (1998). Updating the σ -T relationship for galaxy clusters. *A&A*, 338:813–818.
- Wu, X.-P., Xue, Y.-J., and Fang, L.-Z. (1999). The L_X -T and L_X - σ Relationships for Galaxy Clusters Revisited. *ApJ*, 524:22–30.
- Xu, H., Li, H., Collins, D. C., Li, S., and Norman, M. L. (2010). Evolution and Distribution of Magnetic Fields from Active Galactic Nuclei in Galaxy Clusters. I. The Effect of Injection Energy and Redshift. *Astrophys. J.*, 725:2152–2165.
- Xue, Y.-J. and Wu, X.-P. (2000). The L_X -T, L_X - σ , and σ -T Relations for Groups and Clusters of Galaxies. *ApJ*, 538:65–71.

- Yee, H. K. C. and Gladders, M. D. (2002). Optical Surveys for Galaxy Clusters. In Chen, L.-W., Ma, C.-P., Ng, K.-W., and Pen, U.-L., editors, *AMiBA 2001: High-Z Clusters, Missing Baryons, and CMB Polarization*, volume 257 of *Astronomical Society of the Pacific Conference Series*, page 109.
- Yee, H. K. C., Gladders, M. D., Gilbank, D. G., Majumdar, S., Hoekstra, H., and Ellingson, E. (2007). The Red-Sequence Cluster Surveys. In Metcalfe, N. and Shanks, T., editors, *Cosmic Frontiers*, volume 379 of *Astronomical Society of the Pacific Conference Series*, page 103.
- Yoon, J. H., Schawinski, K., Sheen, Y.-K., Ree, C. H., and Yi, S. K. (2008). A Spectrophotometric Search for Galaxy Clusters in SDSS. *Astrophys. J. Supp.*, 176:414–423.
- Zaritsky, D., Gonzalez, A. H., Nelson, A. E., and Dalcanton, J. J. (2002). An Overview of the Las Campanas Distant Cluster Survey. In Chen, L.-W., Ma, C.-P., Ng, K.-W., and Pen, U.-L., editors, *AMiBA 2001: High-Z Clusters, Missing Baryons, and CMB Polarization*, volume 257 of *Astronomical Society of the Pacific Conference Series*, page 133.
- ZuHone, J. A., Markevitch, M., Brunetti, G., and Giacintucci, S. (2013). Turbulence and Radio Mini-halos in the Sloshing Cores of Galaxy Clusters. *Astrophys. J.*, 762:78.
- Zwicky, F. (1933). Die Rotverschiebung von extragalaktischen Nebeln. *Helvetica Physica Acta*, 6:110–127.
- Zwicky, F. (1937). On the Masses of Nebulae and of Clusters of Nebulae. *Astrophys. J.*, 86:217.
- Zwicky, F., Herzog, E., and Wild, P. (1968). *Catalogue of galaxies and of clusters of galaxies*.